OTTO VON GUERICKE UNIVERSITÄT MAGDEBURG

FAKULTÄT FÜR MASCHINENBAU

3D-Vibration Testing for Automotive Components

Dissertation

zur Erlangung des akademischen Grades

Doktoringenieur
(Dr.-Ing.)

von M.Sc. Kurthan Kersch

geb. am 29.08.1990 in München

genehmigt durch die Fakultät Maschinenbau
der Otto-von-Guericke-Universität Magdeburg

Gutachter:

1. Jun.-Prof. Dr.-Ing. Elmar Woschke
2. Prof. Dr.-Ing. Thomas Kuttner
3. Dr. Christian Dindorf

Promotionskolloquium am 05.10.2020

Kurzfassung

In der vorliegenden Arbeit wird eine ganzheitliche Methodik zur Auslegung und Bewertung multiaxialer Vibrationstests für Fahrzeugkomponenten entwickelt. Ziel ist es dabei ein Schädigungsvergleich zwischen herkömmlich sequentiell uniaxialen und multiaxialen Tests zu ermöglichen.
Die Schädigungen werden durch das Strukturspannungskonzept beschrieben. In der Praxis wird häufig aus Zeit- und Kostengründen auf detaillierte Simulationen und auch auf die Verwendung von Dehnungsmessstreifen zur Bestimmung lokaler mechanischer Spannungen verzichtet.
Zunächst soll eine sinnvolle Berechnungsgröße gefunden werden, welches die Ermüdung ausreichend genau beschreibt. Hierfür wird eine bestehende Vergleichsspannungsformulierung verwendet, welche in Abhängigkeit von modalen Geschwindigkeiten und Geometriefaktoren aus vereinfachten Finite Elemente Modellen beschrieben wird. Modale Geschwindigkeiten, bei denen gezeigt werden kann, dass sie in guter Näherung proportional zu lokalen mechanischen Spannungen sind, können effizient durch Beschleunigungsaufnehmer und anschließende Integration ermittelt werden. Die allgemeine Beziehung zwischen Geschwindigkeiten und Schädigung wird durch Ermüdungstests an einfachen Bauteilen bestätigt.
Im Rahmen der Arbeit wird der Prototyp eines elektrodynamischen, tri-axialen Schwingtischs verwendet, welcher auf die Anforderungen der Automobilindustrie zugeschnitten und somit kein allgemein verfügbarer Standard ist. Es werden Modifikationen an der Aufspannvorrichtung vorgenommen, um die Regelgüte zu erhöhen und den hierauf negativen Einfluss der Resonanzen der Lagereinheit abzuschwächen. Fahrzeugmessdaten sollen dadurch in zufriedenstellendem Umfang qualitativ abgebildet werden können.
Im weiteren Vorgehen werden Überlegungen zur Ableitung von multiaxialen Prüfprofilen durchgeführt. Die vorhandenen Methoden für die Definition uniaxialer und multiaxialer Profile werden untersucht und nach Möglichkeit erweitert. Dabei sollen die in der Automobilindustrie verwendeten praktischen Herangehensweisen beibehalten und um die notwendigen, aus Fahrzeugmessdaten erhaltenen Phaseninformationen erweitert werden.
Die komplette Methodik wird an drei mechanischen Komponenten demonstriert. Als Ergebnis wird der Unterschied in der Schädigung im Vergleich zur herkömmlichen Erprobung evaluiert.

Abstract

The present work aims at implementing a full multi-axis vibration testing methodology for automotive components. A key objective is the fatigue damage comparison between common sequentially applied uniaxial and multiaxial vibration tests on a given shaker system with realistic test profiles.

In practice, time consuming and costly simulations and the application of strain gauges are to be avoided for the prediction of local stresses causing fatigue damage. Therefore, a reliable measurement quantity to predict local stresses is to be found. An equivalent stress concept based on modal velocities and geometric factors obtained from simplified finite element models is proposed. Velocities, that sufficiently relate to local stresses, are easily to be extracted from accelerometers, which are widely established in vibration testing, and a subsequent numerical integration. The general relationship between modal velocities and fatigue damage is further proven through end of life tests of simple specimens.

All vibration tests are to be conducted on an electrodynamic triaxial shaker prototype which was developed regarding the requirements of the automotive industry. Respective shaker systems are not widely available as standard test equipment. Fixture modifications are conducted in order to ensure an effective control and to overcome the resonances of the bearing unit. Thereby, the goal is to sufficiently replicate field measurements.

In further procedure, considerations are made regarding multiaxial test profile derivation based on available field data. Several existing approaches for both uniaxial and multiaxial profile definition are investigated and extended. Thereby, the goal is to maintain the current practice in uniaxial vibration testing of automotive components and to include relevant phase information obtained from field data.

The entire multi-axis testing methodology is demonstrated on three mechanical structures. Furthermore, an evaluation regarding the difference to common sequential uniaxial tests is performed.

Table of Contents

List of Figures

List of Tables

Table of Acronyms

Acronym	Description
CoG	Center Of Gravity
CSD	Cross Spectral Density
CSDM	Cross Spectral Density Matrix
CSDP	Complex Semidefinite Programming
DP	Damage Potential
DUT	Device Under Test
EB	Euler Bernoulli
EOL	End of Life
MDOF	Multiple Degree Of Freedom
MIL-STD	Military Standard
MIMO	Multiple Input Multiple Output
EMA	Experimental Modal Analysis
EVMS	Equivalent Von Mises
FDS	Fatigue Damage Spectrum
FEM	Finite Element Method
FFT	Fast Fourier Transform
FRF	Frequency Response Function
HCF	High Cycle Fatigue
IFFT	Inverse Fast Fourier Transform
ISO	International Organization for Standardization
LCF	Low Cycle Fatigue
LP	Linear Programming
LTI	Linear Time Invariant
ODS	Operational Deflection Shape
ODE	Ordinary Differential Equation
PDE	Partial Differential Equation
PSD	Power Spectral Density
RMS	Root Mean Square
SDM	Spectral Density Matrix
SDOF	Single Degree Of Freedom
SISO	Single Input Single Output
SoR	Sine on Random
SDP	Semidefinite Programming
SVD	Singular Value Decomposition

SWT	Smith Watson Topper
TWR	Time Waveform Replication
VHCF	Very High Cycle Fatigue

Table of Symbols

Latin Letters	
Symbol	**Description**
a	Relative acceleration
$\hat{a}$	Amplitude
A	Cross-sectional area
$\hat{A}$	Amplitude
$\boldsymbol{A}$	Design matrix
b	Basquin exponent
$\hat{b}$	Amplitude
$\tilde{b}$	Body force
$\boldsymbol{B}(f)$	Optimized matrix
$\hat{\boldsymbol{B}}$	Gradient matrix
c	Damping factor
c'	Cyclical ductility exponent
$\hat{c}$	Constant
$\boldsymbol{c}$	Modal damping matrix
C	Basquin constant
$\hat{C}$	Constant of integration
$\boldsymbol{C}$	Damping matrix
$\hat{\boldsymbol{C}}$	Material matrix
d	Partial damage
D	Pseudo damage
$\hat{D}$	Fatigue damage
$\boldsymbol{D}(f)$	Drives spectral density matrix
e	Euler number
E	Young's modulus
$\hat{E}$	Constant
$\boldsymbol{E}(f)$	Error matrix
f	Frequency
$f(t)$	Force
f_n	Natural frequency
$\boldsymbol{f}(t)$	Force vector
$\boldsymbol{F}(f), \boldsymbol{F}(j\Omega)$	Fourier transform of force vector
$\hat{\boldsymbol{F}}(f)$	Hermitian matrix out of transfer functions
G	Shear modulus

$G_{xx}(f)$	Spectral density
$G_{xy}(f)$	Cross-spectral density
$G_\sigma(f), G_\tau(f)$	Stress spectral densities
$\boldsymbol{G}(f)$	Spectral density matrix
$\boldsymbol{G}_{xx}(f)$	Input spectral density matrix
$\boldsymbol{G}_{yy}(f)$	Output spectral density matrix
$[G]$	Set of tests
$h(t)$	Impulse response function
$\hat{h}(t)$	Analytic signal
$\tilde{h}(t)$	Phase shifted analytic signal
$\boldsymbol{h}(t)$	Vector of impulse response function
$H(f)$	Transfer function
$\hat{H}(f)$	Inverse transfer function
$\boldsymbol{H}(f)$	Transfer matrix
$\hat{\boldsymbol{H}}(f)$	Inverse transfer matrix
I	Area moment of inertia
$\hat{I}$	Modified Bessel function of the first kind
I_1	First invariant
I_2	Second invariant
I_3	Third invariant
I_p	Polar area moment of inertia
I_t	Torsional constant
$\boldsymbol{I}$	Identity matrix
j	Complex number
J	Moment of inertia
$\hat{J}$	Bessel function of the first kind
k	Stiffness
k_d	Displacement factor
k_e	Static factor
$k_{e,\phi}$	Static factor for torsion
k_v	Velocity factor
k_σ	Factor of proportionality for normal stress
k_τ	Factor of proportionality for shear stress
k_ω	Dynamic factor
$k_{\omega,\phi}$	Dynamic factor for torsion
$\boldsymbol{k}$	Modal stiffness matrix
K	Geometric factor

K'	Cyclical strain hardening coefficient
$\hat{K}$	Modified Bessel function of the second kind
$\boldsymbol{K}$	Stiffness matrix
L	Length
$\hat{\boldsymbol{L}}$	Linear differential operator matrix
$\boldsymbol{L}(f)$	Lower triangular matrix of Cholesky decomposition
m	Mass
m_i	Statistical moment
$m_t(x)$	Distributed moment
$\tilde{m}$	Number of modes
$\boldsymbol{m}$	Modal mass matrix
$\boldsymbol{M}$	Mass matrix
n	Number of cycles
n'	Cyclical strain hardening exponent
$\hat{n}$	Number of tests
$\tilde{n}$	Order of cross-section
N	Number of maximum endurable cycles
N_D	Number of cycles at fatigue limit point
$\boldsymbol{N}$	Matrix of shape functions
$p(x)$	Probability density function
$\boldsymbol{p}(t)$	Modal force vector
$P(f)$	Trace of drives matrix
P_{SWT}	Smith Watson Topper damage parameter
$q(x)$	Distributed load
$\hat{q}(f)$	Iteration gain
Q	Quality factor
$\boldsymbol{Q}$	Matrix of constants
$\hat{\boldsymbol{Q}}$	Diagonal matrix of iteration gains
r	Radius
$\boldsymbol{r}$	Spatial vector
$\boldsymbol{r}(f)$	Reference vector
R_m	Ultimate tensile strength
$R(f)$	Reference Fourier spectrum
$\boldsymbol{R}(f)$	Reference spectral density matrix
R_{xx}	Auto-correlation
R_{xy}	Cross-correlation
$\hat{s}$	Severity

S_a	Stress cycle amplitude
S'_a	Mean stress corrected cycle amplitude
S_D	Stress cycle amplitude at fatigue limit point
S_m	Stress cycle mean value
$\boldsymbol{S}(f)$	Diagonal matrix
t	Time
T	Time period
$\boldsymbol{u}(t)$	Modal displacement vector
$\boldsymbol{U}(f)$	Eigenvector matrix
v	Relative velocity
$\hat{v}$	Amplitude of relative velocity
v^*	Phase shifted analytic velocity signal
v_{rot}	Relative rotational velocity
$\boldsymbol{v}$	Design vector
V	Volume
w	Deflection
$\hat{w}$	Weighting function
$\boldsymbol{w}(f)$	Vector of independent noise sources
W_t	Torsional resistance moment
x, X	Position, direction
$\dot{x}, \ddot{x}$	Derivatives of position
$\tilde{x}$	Gamma function variable
$x(t)$	Input time signal, position w.r.t. time
$\hat{x}$	Amplitude
$x_b(t)$	Time signal of base excitation
$\boldsymbol{x}(f)$	Vector of input Fourier spectrum
$\boldsymbol{x}(t)$	Vector of input time signal, vector of positions
$\dot{\boldsymbol{x}}(t), \ddot{\boldsymbol{x}}(t)$	Vector of derivatives of positions
$X(f), X(j\Omega)$	Fourier transform of $x(t)$
$X(s)$	Laplace transform of $x(t)$
$X_b(s)$	Laplace transform of $x_b(t)$
$\hat{X}$	Function depending on eigenfrequencies
y, Y	Direction
$y(t)$	Output time signal
$\boldsymbol{y}(f)$	Vector of output Fourier spectrum
$\hat{\boldsymbol{y}}(f)$	Vector of predicted output Fourier spectrum
$\boldsymbol{y}(t)$	Vector of output time signal

$Y(f)$	Fourier transform of $y(t)$
$\hat{Y}$	Bessel function of the second kind
z, Z	Direction
$\hat{z}$	Distance to neutral fiber
$\tilde{z}$	Complex variable
$\boldsymbol{Z}(f)$	Inverse transfer matrix voltage to acceleration
$\hat{Z}_{\hat{\nu}}$	Linear combination of Bessel functions
Greek Letters	
Symbol	**Description**
α	Rotation angle
γ	Coherence
$\tilde{\gamma}$	Shear strain
Γ	Gamma function
δ	Damping constant
Δ	Difference operator
Δf	Frequency band
ε	Strain
ε'	Cyclical ductility coefficient
$\hat{\zeta}$	Direction
η	Frequency ratio
$\hat{\eta}$	Direction
θ	Phase angle
λ	Eigenvalue
ν	Poisson's ratio
ν_0	Positive zero-crossing rate
ν_p	Positive extreme value rate
ξ	Damping ratio
$\hat{\xi}$	Direction
ρ	Density
σ	(Normal) stress
σ'	Fatigue strength coefficient
$\hat{\sigma}$	Stress amplitude
$\tilde{\sigma}$	Standard deviation
$\boldsymbol{\sigma}$	Stress tensor
$\hat{\boldsymbol{\sigma}}$	Stress vector
τ	Shear stress
$\hat{\tau}$	Time lag

τ_t	Torsional shear stress
ϕ	Angle
$\mathbf{\Phi}$	Modal matrix of eigenvectors
φ	Angle of hermitian matrix out of transfer functions
ω	Circular frequency
ω_0	Circular eigenfrequency
ω_d	Damped circular eigenfrequency
Ω	Excitation circular frequency

Notation	
Symbol	**Description**
a, A	Scalar
$a(f), A(f)$	Spectrum
$\boldsymbol{a}$	Vector
$\boldsymbol{a}(f)$	Vector of Spectra
$\boldsymbol{A}$	Matrix
$\boldsymbol{A}(f)$	Spectral matrix
$[a]$	Set of scalars

Indices and superscripts	
Symbol	**Description**
0	Initial value
1	First value
$1D$	Uniaxial excitation
2	Second value
3	Third value
$3D$	Simultaneous excitation
4	Fourth value
a	Amplitude
b	Base
e	Element
el	Elastic
env	Envelope
aa	Acceleration
D	Fatigue limit
eq	Equivalent
F	Frobenius norm
i	i'th value, i'th order
k	k'th value, k'th order
lon	Longitudinal
L	Position $x = L$
n	n'th value
max	Maximum value
pl	Plastic
ref	Reference
rot	Rotational
v, vv	Velocity
x, y, z	Spatial directions
$\hat{\nu}$	Order
σ	Related to stress
σ_{max}, τ_{max}	Position of maximum stress

1 Introduction

Vibration testing is an indispensable step for the validation of newly developed automotive parts and structures. Load collectives are usually obtained from different field measurements and combined into a meaningful test profile to cover all possible load situations. Test profiles are created out of different load cases and driving scenarios. Especially within the automotive industry, the service times range from years to decades which makes an accelerated testing unavoidable in most cases. This is achieved by appropriately scaling-up the vibration profiles. Within the automotive industry, the approval of structures is usually conducted on uniaxial shakers on which all relevant industrial standards are based.

Figure 1.1: 3D-shaker testing

1.1 Motivation

Gradually, the need to perform more multi-axis testing has arisen among the respective manufacturers. The motivation is to achieve a more realistic testing condition in order to reproduce the original failure mode. Thereby, the design of products can be accomplished in a more efficient way due to a precise estimation of the reliability. Furthermore, a reduction of testing time by 66% is theoretically accomplishable. On contrary to the aerospace industry, multi-axis testing is not established within the automotive industry which results in a lack of respective standards and methods.
The difference in fatigue damage and failure modes between multiaxial and commonly performed sequential uniaxial excitation is hardly investigated in literature regarding real products under realistic test conditions. A respective evaluation is thus a major objective of the thesis. An apparent disagreement between scientific publications, reference books and standards regarding the correct measurement quantity relating to fatigue damage shall be investigated and clarified in the course of the evaluation.
Multiaxial shaker systems with the respective requirements of automotive testing are not available as standard test equipment. The test system of the current research is an electrodynamic 3D-shaker prototype (see fig. (1.1)). All investigations are to be performed on this system which requires a preliminary implementation and modification regarding the desired test conditions.
Current methods for the derivation of vibration test profiles are either for uniaxial purposes or limited in their processing of phase information. According to the requirements of automotive testing, existing methods shall be enhanced based on available vehicle measurement data.
The overall motivation of this work is to implement a full multi-axis testing methodology including the handling of the shaker system, the definition of relevant vibration profiles and its evaluation with respect to the introduced damage. Fundamental investigations shall be performed in order to go beyond the state of the art and elaborate proposals for new methods regarding multi-axis test design and evaluation.

1.2 State of the Art

Difference between uniaxial and multiaxial shaker testing

The general difference in fatigue damage caused between multiaxial and sequential uniaxial testing has been discussed in literature extensively. Multi-axis testing is widely considered as being more realistic than performing sequential uniaxial tests. Early investigations of triaxial excitation on aerospace hardware concluded in twice the fatigue damage from sequential uniaxial excitation, as explained in [31]. In [24], it has been shown experimentally and in simulation, that differences in maximum stresses and their respective locations occur with multiaxial testing. The simultaneous excitation of plate structures may result in either higher or lower response energy than sequential uniaxial tests, depending on the excitation level as described in [60]. Further nonlinear effects occurring with simultaneous excitation have also been investigated in [17]. Thereby, real electronic components were used which emphasizes the need for multi-axis testing. Different failure modes have been experimentally proven with End of Life (EOL) tests using simple specimens, conducted in [20]. Inadequacies in sequential uniaxial testing regarding sequence effects have been investigated in [98] by performing EOL tests.

Evaluation of vibrational environments

To evaluate the severity of different vibrational environments (for example uniaxial and multi-axial), an appropriate indicator to obtain a fatigue damage related quantity has to be chosen. The direct measurement of strains using strain gauges is costly and requires access to the location of interest. As explained in [42], this is not always possible and thus easily measurable vibrational quantities have been considered. Quantities such as relative displacement, relative velocity or relative acceleration can be obtained from accelerometers which can easily be applied on most structures. Regarding electronic equipment, relative displacement and acceleration are directly related to stress for conductor plates, as proposed in [80]. In relevant standards such as [35], structural failures of electronic equipment, particularly for road vehicles, are related to acceleration. On the contrary, it is argued in [83] that velocity is most appropriate for indicating structural fatigue. Acceleration in turn, may only be used for electrical relays and quasi-static acceleration (low frequency) excitation. Furthermore, displacement shall be used for structures composed of several subassemblies, position-sensitive equipment or if the amplitude is important when mounted near other structures. A rough relation between normal stress and translational velocity is found in [21] which was derived using the differential equations for plane and axial vibrations. The derivations are based on clamped-free configurations for both a long-thin rod and an Euler-Bernoulli beam. Further qualitative considerations about structures with variable cross sections are made in [13],[32]. A direct comparison of velocity, acceleration and strain data obtained from field measurements is accomplished in [97], concluding with a better fit between strain and velocity. Experimental tests are conducted in [37] to estimate the factor between stress and velocity, resulting in a narrow bandwidth over frequency. Further preliminary considerations on the factor between stress and velocity are accomplished in [89], [65] and [19] resulting in approximate estimates of the value range. Simple absolute value calculations of velocity spectral density responses under three-dimensional excitation are performed in [31] which further supports the usage of velocities.

Multi-axis shaker systems

On contrary to the aerospace industry, partially higher acceleration levels and frequency ranges up to 2000 Hz are common within the scope of automotive testing, as can be seen in [35]. For electric vehicles, even higher frequencies are to be expected for future vibration testing. Multiaxial shaker systems with the respective requirements are no widely available standard equipment. The systems used in literature are mostly prototypes which serve for a scientific purpose. Both implementation and handling of the system is thereby usually described sparely. The main challenge of multi-axis shakers is the construction and handling of the bearing unit that couples the different shaker axes. For large industrial shakers, such as needed by the automotive industry, resonances of the bearing unit due to the low stiffness are unavoidable which may violate testing results, as indicated in [24]. A six-degree-of-freedom shaker is investigated [77], where both occurring system modes are left unconsidered for testing. As conclusion, for every shaker model a qualification test has to be undertaken.

Profile derivation methods

Vibrations from road excitation are mostly described in terms of random vibrations using Power Spectral Densities (PSD). In the multiaxial case, the input profile can be specified as a fully populated Spectral Density Matrix (SDM), as described in [86]. A simple approach to merge different profiles from different scenarios is performing a weighted average of different PSDs or entire SDMs, as described in [27]. Averaging the cross-diagonal terms results in mean values for the phases and coherences. Generally, care has to be taken when performing manipulations of the SDM since the matrix is required to be positive definite in order to remain physically realizable. Another possibility for profile derivation is the usage of enveloping techniques over a set of PSDs which describes a worst case excitation. Examples are only available for uniaxial cases. However, it is mentioned in [33] that envelopes may not be practical for cross spectral terms.
Another widely used approach for the combination of PSDs is the Fatigue Damage Spectrum (FDS), described in [30] and [100]. It tries to maintain damage equivalency, considering the structure as a sequence of single-degree-of-freedom systems for each frequency and using their respective frequency response functions. The FDS approach is thereby strictly restricted to the uniaxial case. The FDS may also be used to perform accelerated testing by upscaling the acceleration levels. A commonly used procedure is the usage of standard profiles. For the uniaxial case, examples are given in [35] and [90]. Especially in case of using standard profiles, no field data and thus respective information about the cross-correlation is available. In order not to choose the cross terms arbitrarily a minimum drives approach is proposed in [74] and extended by phase relationships in [55]. Further work on determining phases and coherences properly is described in [50].

1.3 Objectives and Structure

The objectives of this thesis are:

- To evaluate the difference in fatigue damage (apart from other failure mechanisms) between multiaxial and sequential uniaxial testing using realistic scenarios within the scope of automotive testing
- To define an appropriate measurement quantity along its respective measurement locations for the evaluation of multiaxial fatigue damage introduced by a vibrational environment, avoiding full simulations in order to perform a fast and efficient evaluation
- To develop a methodology for the implementation and modification of a specific 3D-shaker system with respect to common requirements of automotive vibration testing
- To enhance appropriate profile derivation methods for automotive applications including a correct processing of phase information
- To develop a new multi-axis testing methodology which may contribute to future standards

The structure of the thesis is described as follows. Chapter 2 initially introduces the theoretical background on several scientific fields which are forming the base for the entire vibration testing methodology. The main chapters are 3, 4, 5 and 6 (see fig. (1.2)). The entire fatigue damage

evaluation methodology is developed in the main chapter 3. All investigations and modifications on the 3D-shaker system are accomplished in chapter 4. The development of an appropriate profile derivation method is explained in chapter 5. Being the core objective of the thesis, an evaluation of fatigue damage due to uniaxial and multiaxial excitation using different realistic scenarios is performed in chapter 6. It can be seen as the interface of the preceding three chapters which all contribute to the entire testing methodology. Finally, chapter 7 summarizes the thesis and gives conclusions and an outlook of future steps.

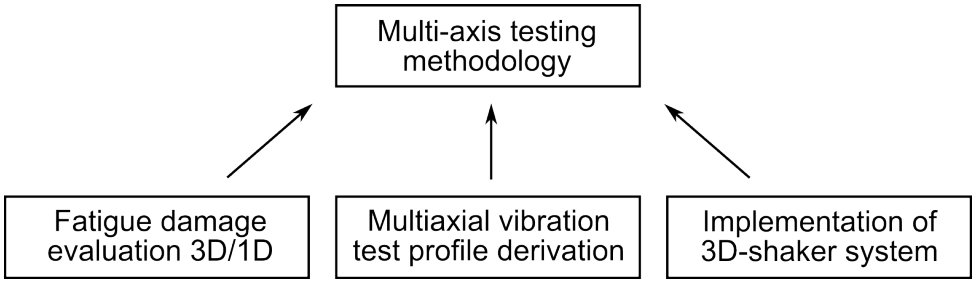

Figure 1.2: Multi-axis testing methodology

2 Theoretical Background

The design of vibration tests requires knowledge of a wide scope of scientific fields. Thus, an initial chapter shall introduce basic theory which is necessary for the understanding of the subsequently presented work. It is partitioned into three major subjects: Signal processing and structural dynamics, structural durability calculation including operational strength analysis and vibration testing methodologies including vibration control and test profile derivation.

2.1 Signal Processing and Linear Systems

This section explains basic theory of signal processing and structural dynamics. Thereby, signals are considered solely, as well as their input-output relationships involving linear systems. The fundamental modeling of the dynamic behavior of linear systems is presented. Further information and more detailed explanation can be found in [2], [51] and [46] for signal processing and in [51], [82], [58] and [95] for structural dynamics. The following content is based on the respective references.

2.1.1 Multidimensional Signal Analysis

Dynamic signals are divided into deterministic (periodic, aperiodic/transient) and stochastic, respectively random signals (stationary, non-stationary). Periodic signals $x(t)$ can be written in form of a sum of sine and cosine terms, known as Fourier series, to be broken down into its frequency components. They are given in eq. (2.1) with the respective amplitudes (coefficients) $\hat{a}$, $\hat{b}$ and the angular frequency ω as

$$x(t) = \frac{\hat{a}_0}{2} + \sum_{i=1}^{\infty} \left(\hat{a}_i \sin(\omega_i t) + \hat{b}_i \cos(\omega_i t) \right) \quad . \tag{2.1}$$

During further notation, $x(t)$ is referred to as system input and $y(t)$ as system output. Using the assumption of infinite periodicity, transient signals of a time period T can be converted into a frequency spectrum $X(f)$ using a Fourier transformation $\mathcal{F}$ as

$$X(f) = \mathcal{F}\left(x(t)\right) = \int_{-\infty}^{\infty} x(t)\, e^{-j\omega t} \mathrm{d}t \quad . \tag{2.2}$$

The Fourier transform of a system output is described analogously and referred to as $Y(f)$. A commonly used discrete version of the Fourier transform is the so-called Fast Fourier Transform (FFT). The process can be fully reversed through an Inverse Fast Fourier Transform (IFFT).
In Linear Time Invariant (LTI) systems, frequency inputs and outputs are coupled through a transfer function $H_{xy}(f)$ as

$$Y(f) = H_{xy}(f)\, X(f) \quad . \tag{2.3}$$

In the multidimensional case, the input, respectively output vectors $\boldsymbol{x}(f), \boldsymbol{y}(f)$ are coupled through a transfer matrix $\boldsymbol{H}(f)$ as

$$\boldsymbol{y}(f) = \boldsymbol{H}(f)\, \boldsymbol{x}(f) \ . \tag{2.4}$$

In the time domain, the inputs $\boldsymbol{x}(t)$ and outputs $\boldsymbol{y}(t)$ are coupled through a convolution with the vector of impulse response functions $\boldsymbol{h}(t)$ as

$$\boldsymbol{y}(t) = \boldsymbol{h}(t) * \boldsymbol{x}(t) \ . \tag{2.5}$$

For a three-dimensional linear system which is mainly considered in this thesis, the input-output relation in the frequency domain is given as

$$\left\{ \begin{array}{c} Y_1(f) \\ Y_2(f) \\ Y_3(f) \end{array} \right\} = \left[\begin{array}{ccc} H_{11}(f) & H_{12}(f) & H_{13}(f) \\ H_{21}(f) & H_{22}(f) & H_{23}(f) \\ H_{31}(f) & H_{32}(f) & H_{33}(f) \end{array} \right] \left\{ \begin{array}{c} X_1(f) \\ X_2(f) \\ X_3(f) \end{array} \right\} \ . \tag{2.6}$$

Real life signals are often varying and have to be treated differently than true deterministic signals. Thus, a holistic description of signals is needed using stochastic properties. Therefore, the auto-correlation function $R_{xx}(\hat{\tau})$ is introduced as a measure of how an instantaneous amplitude value of a signal depends upon previously occurring values. It can be interpreted as the area of a signal multiplied with itself shifted by the time $\hat{\tau}$ and is described as

$$R_{xx}(\hat{\tau}) = \lim_{T\to\infty} \frac{1}{2T} \int_{-T}^{T} x(t)x(t+\hat{\tau})\mathrm{d}t \ . \tag{2.7}$$

The same calculation can also be performed for two different time signals $x(t)$ and $y(t)$, defined as the so-called cross-correlation function $R_{xy}(\hat{\tau})$, given as

$$R_{xy}(\hat{\tau}) = \lim_{T\to\infty} \frac{1}{2T} \int_{-T}^{T} x(t)y(t+\hat{\tau})\mathrm{d}t \ . \tag{2.8}$$

Using the Fourier transform, the correlation functions can be described in the frequency domain as the Power Spectral Density (PSD) $G_{xx}(f)$ and the Cross Spectral Density (CSD) $G_{xy}(f)$

$$G_{xx}(f) = \mathcal{F}\left(R_{xx}(\hat{\tau})\right) = X^*(f)X(f) = |X(f)|^2 \tag{2.9}$$

and

$$G_{xy}(f) = \mathcal{F}\left(R_{xy}(\hat{\tau})\right) = X^*(f)Y(f) \ . \tag{2.10}$$

In contrary to the Fourier spectrum, the spectral densities describe the power distribution over all frequency bands. The equivalent harmonic amplitude to a certain spectral density of a frequency band Δf with the same signal power can be calculated as

$$\hat{A} = \sqrt{2G_{xx}\Delta f} \ . \tag{2.11}$$

For both inputs and outputs the spectral densities and cross spectral densities can be merged into a Spectral Density Matrix (SDM) $\boldsymbol{G}(f)$, given for the three-dimensional case according to [84] as

$$\boldsymbol{G}(f) = \begin{bmatrix} G_{11}(f) & G_{12}(f) & G_{13}(f) \\ G_{21}(f) & G_{22}(f) & G_{23}(f) \\ G_{31}(f) & G_{32}(f) & G_{33}(f) \end{bmatrix} \quad . \tag{2.12}$$

The SDM can be generalized to a Cross Spectral Density Matrix (CSDM) when all spectral densities are calculated between two different locations [88]. In terms of vibration control this is commonly used between excitation and response spectra.
The diagonal and off-diagonal terms of the SDM are connected through the phase angle θ and coherence γ, respectively the magnitude squared coherence γ^2, as given in eq. (2.13) as

$$G_{12}(f) = \sqrt{\gamma_{12}^2(f)\, G_{11}(f)\, G_{22}(f)}\, e^{j\theta_{12}(f)} \quad . \tag{2.13}$$

The coherence is a direct measure for the correlation[1] of two signals and ranges between 0 (uncorrelated) to 1 (fully correlated). The coherence can also be described in another form using only absolute values as

$$\gamma_{12}(f) = \sqrt{\frac{|G_{12}(f)|^2}{G_{11}(f) G_{22}(f)}} \tag{2.14}$$

which is similar to the correlation coefficient. The SDM is a conjugate symmetric (hermitian), positive definite matrix. The condition for positive definiteness using an arbitrary vector $\boldsymbol{v}$ and an arbitrary matrix $\boldsymbol{A}$ is $\boldsymbol{v}^T \boldsymbol{A} \boldsymbol{v} > 0$ for real matrices and $\boldsymbol{v}^H \boldsymbol{A} \boldsymbol{v} > 0$ for hermitian ones. Positive definite matrices contain real eigenvalues and real diagonal elements resulting in a positive trace [33], [55].
For a linear system, the input and output spectral densities, respectively cross-spectral densities, are again coupled through the system transfer functions with

$$G_{yy}(f) = |H_{xy}(f)|^2\, G_{xx}(f) \tag{2.15}$$

and

$$G_{xy}(f) = H_{xy}(f)\, G_{xx}(f) \tag{2.16}$$

and

$$G_{yy}(f) = H_{xy}(f)\, G_{xy}(f) \quad . \tag{2.17}$$

Eq. (2.15) can also be merged into a matrix yielding a CSDM

$$\boldsymbol{G}_{yy}(f) = \boldsymbol{H}(f)\, \boldsymbol{G}_{xx}(f)\, \boldsymbol{H}^*(f) \quad . \tag{2.18}$$

All transformations between frequency and time domain and between system input and output are summarized in fig. (2.1).

[1] The correlation describes how much two signals resemble to each other

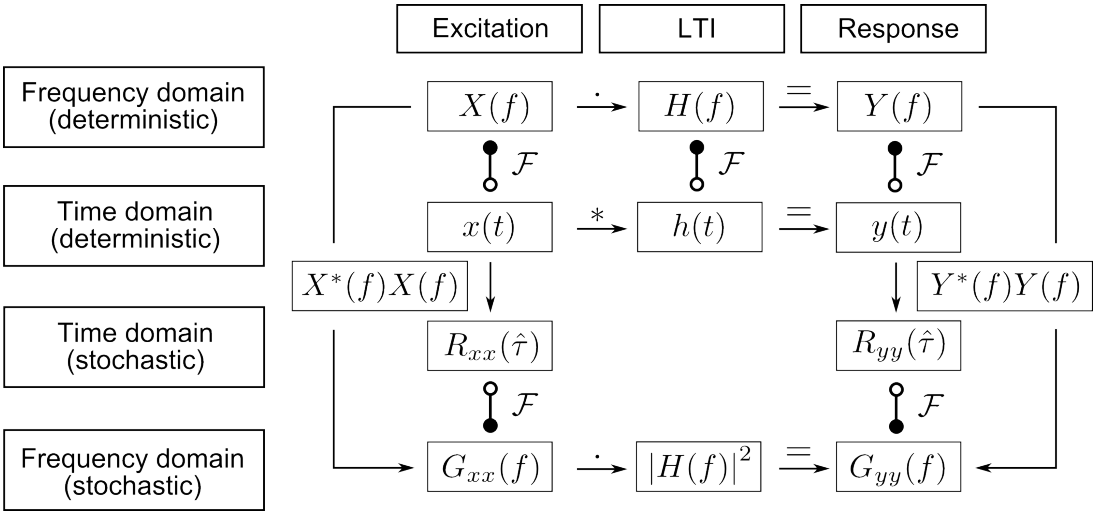

Figure 2.1: Chart of signal processing in LTI systems

So far, relevant quantities of signal processing were introduced. Regarding random processes, its properties can also be expressed in stochastical terms which will be discussed in the next subsection. The stochastical expressions are helpful to perform fatigue damage calculations without the direct consideration of entire time signals, as will be seen later.

2.1.2 Stochastic Signal Description

A random vibration signal is considered to be an ergodic[2] stationary stochastic process if it is long enough to create a (Gaussian) probability density function $p(x)$ with stationary stochastic properties. Those properties are called the statistical moments m_i and can be extracted from the time series $x(t)$ according to [46] as

$$m_i(x(t)) = \int_{-\infty}^{\infty} x^i \, p(x) \, \mathrm{d}x \quad . \tag{2.19}$$

For a value of $i = 0$ eq. (2.19) yields the area of the probability density function that has a value of 1. For $i = 1$ the expected value is obtained which is 0 for centered signals. The second statistical moment ($i = 2$) is the variance, the third ($i = 3$) is a measure for the skewness, and the fourth statistical moment ($i = 4$) is a measure for the so-called kurtosis. Eq. (2.19) can be expressed in terms of the spectral density as

$$m_i = \int_{-\infty}^{\infty} f^i \, G_{xx}(f) \, \mathrm{d}f \quad . \tag{2.20}$$

Thereby, the $2i$'th moment equals the variance of the i'th derivative of the random signal $x(t)$. The variances of the derivatives contain information about the distribution of extreme values and turning points. For a value of $i = 0$ the variance is obtained which yields the standard deviation $\tilde{\sigma}$ by extracting its root as shown in eq. 2.21 as

[2] The measured process is sufficiently long to obtain correct statistical properties

$$\tilde{\sigma} = \sqrt{m_0} = \sqrt{\int_{-\infty}^{+\infty} G_{xx}(f)\,\mathrm{d}f} \quad . \tag{2.21}$$

In case of an overall zero mean amplitude, the standard deviation equals the Root Mean Square (RMS). The expression of time signals in stochastic terms can be applied to the load cycle domain which has a focus on amplitude and mean value distributions. Commonly used in terms of mechanical stresses, the amplitude is expressed as S_a and the mean value as S_m. For the cycle distribution, the positive zero-crossing rate (eq. (2.22)) and the rate of positive extreme values (eq. (2.23)) are used for its calculation [46].

$$\nu_0 = \sqrt{\frac{m_2}{m_0}} \tag{2.22}$$

$$\nu_p = \sqrt{\frac{m_4}{m_2}} \tag{2.23}$$

For a narrowband process, i.e. a random time signal that contains only one narrow frequency band, the expression $\nu_0 \approx \nu_p$ is valid. The cycle distribution of a narrowband process follows a Rayleigh distribution, given as

$$p_{\mathrm{rayleigh}}(S_a) = \frac{S_a}{\tilde{\sigma}^2} e^{-\frac{S_a^2}{2\tilde{\sigma}^2}} \quad . \tag{2.24}$$

The moments of a narrowband process are given as

$$m_{i,\mathrm{rayleigh}}(S_a) = \int_0^{\infty} S_a^i \left(\frac{S_a}{\tilde{\sigma}^2} e^{-\frac{S_a^2}{2\tilde{\sigma}^2}}\right) \mathrm{d}S_a = \left(\sqrt{2}\,\tilde{\sigma}\right)^i \,\Gamma\left(1+\frac{i}{2}\right) \tag{2.25}$$

using the Gamma function $\Gamma(\tilde{z})$ containing the Gamma function variable $\tilde{x}$ and the complex variable $\tilde{z}$ with $\mathrm{Re}(z) > 0$, described as

$$\Gamma(\tilde{z}) = \int_0^{\infty} \tilde{x}^{\tilde{z}-1}\, e^{-\tilde{x}}\, \mathrm{d}\tilde{x} \quad . \tag{2.26}$$

For calculating the cycle distribution of a broadband process, i.e. a random time signal containing frequency information of several frequency bands, different approaches can be found in literature [54], [62].

2.1.3 Modeling in Structural Dynamics

In this subsection, the focus is put on the dynamic behavior of linear systems which is described by its respective transfer functions. At first, a simple oscillatory system is presented for initial considerations. Then, an extension to more complex systems is performed, also including the usage of finite elements.

2.1.3.1 Single Degree of Freedom systems

An oscillatory system is usually modeled containing a mass m, a spring with the stiffness k, a damper with the damping factor c and an excitation force $f(t)$ (see fig. (2.2) according to [51]). The homogeneous differential equation $(f(t) = 0)$ of the Single Degree of Freedom (SDOF) system is known as

$$m\ddot{x}(t) + c\dot{x}(t) + kx(t) = 0 \quad . \tag{2.27}$$

Using the exponential approach $\hat{x}e^{\lambda t}$ with the amplitude $\hat{x}$ and the eigenvalue λ, the solution of the damped system can be stated as

$$\lambda_{1,2} = -\frac{c}{2m} \pm j\sqrt{\frac{k}{m} - \left(\frac{c}{2m}\right)^2} = -\delta \pm j\omega_d \tag{2.28}$$

where δ is the damping constant and ω_d the damped circular eigenfrequency. For the undamped case which is a system without damper and the respective damping factor, the undamped circular eigenfrequency is defined as $\omega_0 = \sqrt{\frac{k}{m}}$. The damping ratio ξ is defined as the ratio between the damping constant and the undamped angular eigenfrequency $\xi = \frac{\delta}{\omega_0} = \frac{c}{2\sqrt{km}}$. To describe the damping of a system, often the Q-factor is used that is defined as $Q = \frac{1}{2\xi}$.
Within the scope of vibration testing, forced vibration is commonly modeled with a base excitation $x_b(t)$ that applies a spring and damping force component to the mass. The equilibrium of forces then yields

$$\ddot{x}(t) + 2\xi\omega_0\ \dot{x}(t) + \omega_0^2\ x(t) = 2\xi\omega_0\ \dot{x}_b(t) + \omega_0^2\ x_b(t) \quad . \tag{2.29}$$

In order to show the amplitude ratio of the absolute input and output displacement, the transfer function is calculated. To obtain the particular (stationary) solution, either the exponential approach or the Laplace transformation $\mathcal{L}(x(t)) = X(s)$ using the complex frequency parameter s can be applied. Using the latter yields eq. (2.30) which is plotted in fig. (2.2):

$$H(s) = \frac{X(s)}{X_b(s)} = \frac{2\xi\omega_0\ s + \omega_0^2}{s^2 + 2\xi\omega_0\ s + \omega_0^2} \quad . \tag{2.30}$$

For the steady state case it applies $s = j\omega$ and the transfer function becomes the Frequency Response Function (FRF) with the excitation circular frequency Ω

$$H(j\Omega) = \frac{2\xi\omega_0\ j\Omega + \omega_0^2}{(j\Omega)^2 + 2\xi\omega_0\ j\Omega + \omega_0^2} \quad . \tag{2.31}$$

The ratio between excitation circular frequency and circular eigenfrequency is known as $\eta = \frac{\Omega}{\omega_0}$.

The FRF for the strain proportional relative displacement response $x(t) - x_b(t)$ caused by an input displacement is

$$H(j\Omega) = \frac{X(j\Omega) - X_b(j\Omega)}{X_b(j\Omega)} = \frac{\Omega^2}{(j\Omega)^2 + 2\xi\omega_0\ j\Omega + \omega_0^2} \quad . \tag{2.32}$$

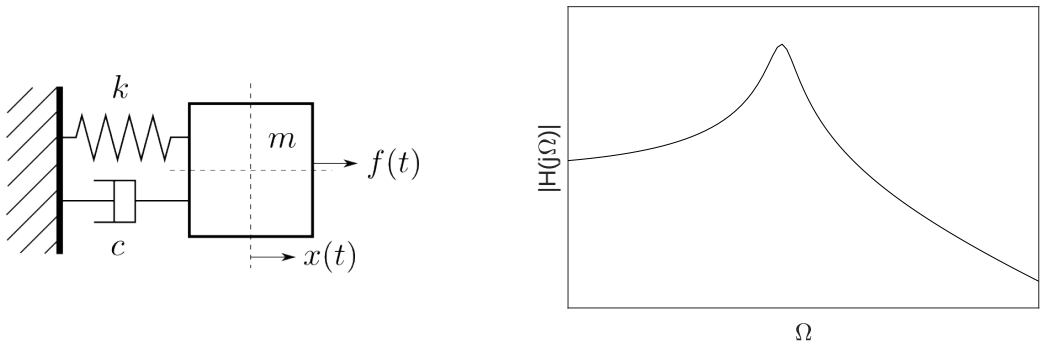

Figure 2.2: SDOF system and corresponding FRF of absolute displacement response

In terms of random vibration, the response of a SDOF system can be expressed stochastically. Eq. (2.15) and (2.21) are combined from zero to infinity and with $H(f)$ being the transfer function of the SDOF system, it can be stated for the standard deviation that

$$\tilde{\sigma} = \int_0^\infty \sqrt{|H(f)|^2 \, G_{xx}(f)} \, \mathrm{d}f \quad . \tag{2.33}$$

As mentioned before, the RMS equals the standard deviation for zero mean time signals. Under the assumption of a relatively flat excitation PSD (almost ideal white noise process), the so-called Miles equation (see [99]) can be derived as

$$\tilde{\sigma}_{aa} = \sqrt{\frac{\pi}{2} \, f_n \, Q \, G_{xx}(f) \, (1 + Q^{-2})} \approx \sqrt{\frac{\pi}{2} \, f_n \, Q \, G_{xx}(f)} \tag{2.34}$$

with the natural frequency $f_n = \frac{\omega_0}{2\pi}$. In case of a non-flat PSD, eq. (2.33) has to be approximated with a discrete integration. Eq. (2.34) can be transformed into other vibrational quantities such as velocity, given as

$$\tilde{\sigma}_{vv} = \sqrt{\frac{\pi}{2} \, f_n \, Q \, \frac{G_{xx}(f)}{(2\pi f)^2}} \quad . \tag{2.35}$$

2.1.3.2 Multiple Degree of Freedom systems

For Multi Degree of Freedom (MDOF) systems, eq. (2.27) is extended to a matrix formulation using the mass matrix $\boldsymbol{M}$, the damping matrix $\boldsymbol{C}$ and the stiffness matrix $\boldsymbol{K}$ as

$$\boldsymbol{M}\ddot{\boldsymbol{x}}(t) + \boldsymbol{C}\dot{\boldsymbol{x}}(t) + \boldsymbol{K}\boldsymbol{x}(t) = \boldsymbol{f}(t) \quad . \tag{2.36}$$

External forces, such as introduced through base excitation, are given as $\boldsymbol{f}(t)$. In case of a single set of rigid body motions it holds $\boldsymbol{f}(t) = -\boldsymbol{M}\ddot{x}_b(t)$ which is called primary base excitation. The eigenvalue problem of an undamped system is

$$\left[\boldsymbol{K} - \omega_{0,i}^2 \boldsymbol{M}\right] \boldsymbol{\Phi} = 0 \tag{2.37}$$

with the eigenvector matrix $\boldsymbol{\Phi}$. In order to decouple the differential eq. (2.36) into SDOF systems expressed with the modal displacement vector $\boldsymbol{u}(t)$, a modal transformation

$$\boldsymbol{x}(t) = \boldsymbol{\Phi}\boldsymbol{u}(t) \tag{2.38}$$

is applied using the eigenvector matrix. Each system is then described in its modal coordinates (modal space). The mass, stiffness and damping matrices, as well as the force vector are normalized by $\boldsymbol{\Phi}$ resulting in the modal mass matrix $\boldsymbol{m}$, modal stiffness matrix $\boldsymbol{k}$, modal damping matrix $\boldsymbol{c}$ and the modal force vector $\boldsymbol{p}(t)$, described as

$$\boldsymbol{m}_i = \boldsymbol{\Phi}_i^T \boldsymbol{M} \boldsymbol{\Phi}_i \tag{2.39}$$

and

$$\boldsymbol{k}_i = \boldsymbol{\Phi}_i^T \boldsymbol{K} \boldsymbol{\Phi}_i \tag{2.40}$$

and

$$\boldsymbol{c}_i = \boldsymbol{\Phi}_i^T \boldsymbol{C} \boldsymbol{\Phi}_i \tag{2.41}$$

and

$$\boldsymbol{p}_i(t) = \boldsymbol{\Phi}_i^T \boldsymbol{f}(t) \ . \tag{2.42}$$

The modal damping $\boldsymbol{c}$ is independently defined for each mode directly. The decoupled equations of motion can then be expressed as

$$\boldsymbol{m}_i \ddot{\boldsymbol{u}}(t) + \boldsymbol{c}_i \dot{\boldsymbol{u}}(t) + \boldsymbol{k}_i \boldsymbol{u}(t) = \boldsymbol{p}_i(t) \ . \tag{2.43}$$

Applying a Fourier transformation on both input and output and performing a back transformation using eq. (2.38) and (2.42) yields the modal FRF between the n'th and k'th position

$$H_{nk}(j\Omega) = \frac{X_n(j\Omega)}{F_k(j\Omega)} = \sum_i^{\tilde{m}} \frac{\Phi_{i,n} \Phi_{i,k}^T}{-\Omega^2 \boldsymbol{m}_i + j\Omega \boldsymbol{c}_i + \boldsymbol{k}_i} \ . \tag{2.44}$$

The FRF is the superimposition of all $\tilde{m}$ modes.

2.1.3.3 Spatial discretization with finite elements

Real structures which can be simplified by MDOF systems are continuums. Most technical processes are thereby described by Partial Differential Equations (PDE). Analytically, they have to be solved using initial and boundary conditions. A numerical approach is the Finite-Element Method (FEM) using linear dynamics. It performs a discretization of the structure which leads to a system of Ordinary Differential Equations (ODE) that is in turn easier to solve. For a continuum, the conservation of momentum and angular momentum has to be valid at each point. Its local formulation is known as the Cauchy-Euler equation of motion, given as

$$\rho \, \ddot{\boldsymbol{x}} = \mathrm{div}(\boldsymbol{\sigma}) + \tilde{b} \tag{2.45}$$

in its strong formulation with the stress tensor $\boldsymbol{\sigma}$ and body forces $\tilde{b}$. Both sides of the equation are time-dependent and describe the connection between local stresses and accelerations. For FEM calculations a weak formulation of eq. (2.45) is used in order to remain feasible. The

integral of the differential equation allows a solution in an average sense without forcing the equation to be fulfilled at every local point. The weak formulation is expressed with a weighting function $\hat{w}$ and the volume V as

$$\int_V \hat{w}\ \rho\ \ddot{\boldsymbol{x}}\ \mathrm{d}V = \int_V \hat{w}\ \mathrm{div}(\boldsymbol{\sigma}) + \hat{w}\ \tilde{b}\ \mathrm{d}V \quad . \tag{2.46}$$

In FEM linear dynamics the local stresses are calculated with a partial integration of (2.46). Thereby, the numerical solution of eq. (2.43) is used which is obtained from a previous steady-state harmonic analysis.

Real MDOF systems are usually irregularly shaped structures. In order to obtain the system matrices the entire structure is meshed with finite elements. For simple geometries (plane, axially symmetric), structural elements such as rods and beams are used for 1D-analyses and plates and shells for 2D-analyses. Full 3D-calculations are accomplished with volume elements, mostly hexahedral and tetrahedral as shown in fig. (2.3) according to [95]. They allow the most general simulation in terms of a continuum and require a higher computing time.

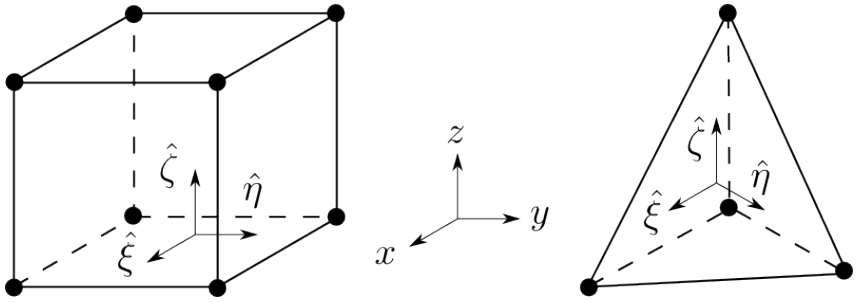

Figure 2.3: Hexahedral and tetrahedral element

Each element is described in its own local coordinate system ($\hat{\xi}$, $\hat{\eta}$, $\hat{\zeta}$). To determine the displacement of every point within the respective element, shape functions $\boldsymbol{N}_i$ are defined for each i'th node. The shape functions can be for example of a linear or quadratic nature and have a value of 1 at their associated node and a value of 0 at any other node. The shape functions for a linear hexahedron element are defined as

$$\boldsymbol{N}_i = \frac{1}{8}\left[(1+\hat{\xi}\hat{\xi}_i)(1+\hat{\eta}\hat{\eta}_i)(1+\hat{\zeta}\hat{\zeta}_i)\right] \tag{2.47}$$

where $\hat{\xi}_i$, $\hat{\eta}_i$, $\hat{\zeta}_i$ are the respective coordinates of the i'th node. Linear elements (tetrahedral: C3D4, hexahedral: C3D8) can be used for preliminary investigations, while quadratic elements (tetrahedral: C3D10, hexahedral: C3D20) are to be preferred for precise stress analyses and linear dynamics [58]. The reason for the latter is computing time efficiency due to good convergency with a limited number of nodes. Generally, the usage of hexahedrals is to be preferred for structure calculations due to the overestimated stiffness of tetrahedral elements. Using the matrix of shape functions $\boldsymbol{N}$ and the gradient matrix $\hat{\boldsymbol{B}}$, the linear differential operator matrix $\hat{L}$ can be calculated as

$$\hat{\boldsymbol{B}} = \hat{\boldsymbol{L}}\boldsymbol{N} = \begin{bmatrix} \frac{\partial}{\partial x} & 0 & 0 \\ 0 & \frac{\partial}{\partial y} & 0 \\ 0 & 0 & \frac{\partial}{\partial z} \\ \frac{\partial}{\partial y} & \frac{\partial}{\partial x} & 0 \\ 0 & \frac{\partial}{\partial z} & \frac{\partial}{\partial y} \\ \frac{\partial}{\partial z} & 0 & \frac{\partial}{\partial x} \end{bmatrix} \begin{bmatrix} \boldsymbol{N}_1 & 0 & 0 & ... & \boldsymbol{N}_n & 0 & 0 \\ 0 & \boldsymbol{N}_1 & 0 & ... & 0 & \boldsymbol{N}_n & 0 \\ 0 & 0 & \boldsymbol{N}_1 & ... & 0 & 0 & \boldsymbol{N}_n \end{bmatrix} . \tag{2.48}$$

The number of columns of $\hat{\boldsymbol{N}}$ is 3 times the number of nodal points for each element. The stiffness matrix $\boldsymbol{K}_e$ of each element can be calculated as

$$\boldsymbol{K}_e = \int_{V_e} \hat{\boldsymbol{B}}^T \hat{\boldsymbol{C}} \hat{\boldsymbol{B}} \, \mathrm{d}V \tag{2.49}$$

with the material matrix $\hat{\boldsymbol{C}}$ which will be introduced in the next section 2.2.1.
The numerical integration of eq. (2.49) is performed at the supporting points, also called integration points. The mass matrix is calculated as

$$\boldsymbol{M}_e = \int_{V_e} \boldsymbol{N}^T \rho \boldsymbol{N} \, \mathrm{d}V \tag{2.50}$$

with the material density ρ. Both the global stiffness and global mass matrix are obtained through summation of all element matrices.

So far, the dynamics of linear systems were introduced. In the next section, a link to the calculation of fatigue damage due to vibrational loads will be created.

2.2 Structural Durability Calculation

There are many reasons for the structural failure of mechanical components (see fig. (2.4) according to [29]). This thesis treats the influence of vibrational loads on the durability of components over their life time (fatigue loading). However, depending on the application other failure mechanisms such as for example abrasion in connectors can be most severe. It is generally distinguished between fatigue failures, abrasion, creeping and special loads due to buckling or shock events.

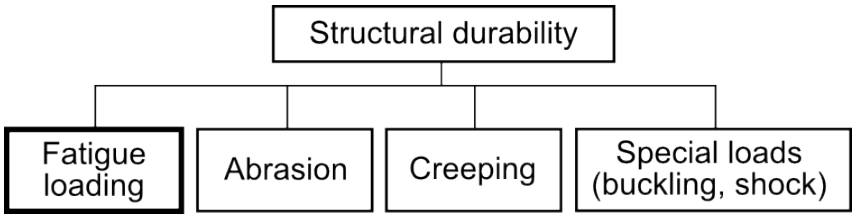

Figure 2.4: Classification of structural durability

In this section, the basic theory which is necessary for fatigue damage calculation is presented. At first, general stress and strain states are introduced together with linear-elastic theory. Equivalent stress formulations and material properties are then considered as a base for the subsequent fatigue damage calculation. Further information on continuum mechanics and FEM

can be found in [36] and [58]. As a detailed reference work on operational strength and fatigue damage [26] and [45] can be consulted.

2.2.1 General Stress and Strain States

In continuums mechanics, the stress tensor $\boldsymbol{\sigma}$ is a second order tensor of symmetric nature. It contains normal stresses σ on its diagonal and shear stresses τ on the off-diagonal entries, described as

$$\boldsymbol{\sigma} = \begin{bmatrix} \sigma_x & \tau_{xy} & \tau_{xz} \\ \tau_{yx} & \sigma_y & \tau_{yz} \\ \tau_{zx} & \tau_{zy} & \sigma_z \end{bmatrix} \quad . \tag{2.51}$$

The general stress state described by the tensor is illustrated in fig. (2.5) according to [3]. Normal stresses are a result of tension, compression and bending in structures, shear stresses are produced by shear forces and torsional loading.

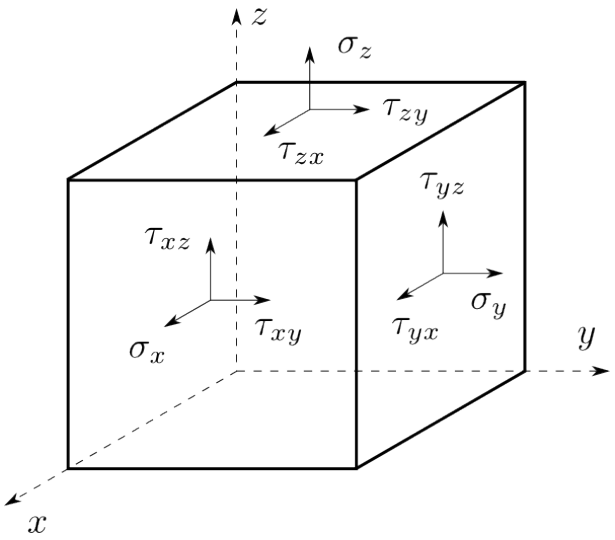

Figure 2.5: General stress state

The eigenvalues of the stress tensor are called principal stresses σ_1, σ_2 and σ_3, the respective eigenvectors are the principal directions. When the stress tensor is rotated in direction of the principal directions, all shear components dissolve to zero. Based on the principal stresses, the invariants of the stress tensor I_1, I_2, I_3 can be defined as

$$I_1 = \sigma_1 + \sigma_2 + \sigma_3 = \sigma_x + \sigma_y + \sigma_z = \sigma_{\hat{\xi}} + \sigma_{\hat{\eta}} + \sigma_{\hat{\zeta}} \tag{2.52}$$

and

$$I_2 = \sigma_1\,\sigma_2 + \sigma_2\,\sigma_3 + \sigma_3\,\sigma_1 \tag{2.53}$$

and

$$I_3 = \sigma_1\,\sigma_2\,\sigma_3 \quad . \tag{2.54}$$

Furthermore, using the constraint $\sigma_1 \geq \sigma_2 \geq \sigma_3$ it can be stated that

$$\tau_{max} = \frac{1}{2}(\sigma_1 - \sigma_3) \quad . \tag{2.55}$$

In case of a bi-axial stress state (plane stress), the expression in eq. (2.51) is reduced to

$$\boldsymbol{\sigma} = \begin{bmatrix} \sigma_x & \tau_{xy} \\ \tau_{yx} & \sigma_y \end{bmatrix} \quad . \tag{2.56}$$

The plane stress expression will be used in section 3.1 due to the assumption that crack initiations usually start at the (plane) surface of a structure. In order to rotate a plane by the angle α in $\hat{\xi}$ and $\hat{\eta}$ direction which can be for example the surface of a structure, following transformation has to be accomplished:

$$\begin{bmatrix} \sigma_{\hat{\xi}} & \tau_{\hat{\xi}\hat{\eta}} \\ \tau_{\hat{\xi}\hat{\eta}} & \sigma_{\hat{\eta}} \end{bmatrix} = \begin{bmatrix} \cos\alpha & \sin\alpha \\ -\sin\alpha & \cos\alpha \end{bmatrix} \begin{bmatrix} \sigma_x & \tau_{xy} \\ \tau_{yx} & \sigma_y \end{bmatrix} \begin{bmatrix} \cos\alpha & -\sin\alpha \\ \sin\alpha & \cos\alpha \end{bmatrix} \quad . \tag{2.57}$$

Using the linear elastic theory for continuous isotropic media, the relation between local stresses and local strains ε, respectively shear $\tilde{\gamma}$, can be expressed as

$$\begin{aligned} \varepsilon_x &= \frac{1}{E}\,\sigma_x - \frac{\nu}{E}\,\sigma_y - \frac{\nu}{E}\,\sigma_z \\ \varepsilon_y &= -\frac{\nu}{E}\,\sigma_x + \frac{1}{E}\,\sigma_y - \frac{\nu}{E}\,\sigma_z \\ \varepsilon_z &= -\frac{\nu}{E}\,\sigma_x - \frac{\nu}{E}\,\sigma_y + \frac{1}{E}\,\sigma_z \end{aligned} \tag{2.58}$$

and

$$\begin{aligned} \tilde{\gamma}_{xy} &= \frac{1}{G}\,\tau_{xy} \\ \tilde{\gamma}_{xz} &= \frac{1}{G}\,\tau_{xz} \\ \tilde{\gamma}_{yz} &= \frac{1}{G}\,\tau_{yz} \end{aligned} \tag{2.59}$$

with the Young's modulus E, the shear modulus G and the Poisson's ratio ν. Furthermore, it is $E = 2G(1+\nu)$ and $\tilde{\gamma}_{ik} = 2\varepsilon_{ik}$. Eq. (2.58) and (2.59) can be combined into

$$\begin{bmatrix} \sigma_x \\ \sigma_y \\ \sigma_z \\ \tau_{xy} \\ \tau_{xz} \\ \tau_{yz} \end{bmatrix} = \frac{E}{(1+\nu)(1-2\nu)} \begin{bmatrix} 1-\nu & \nu & \nu & 0 & 0 & 0 \\ \nu & 1-\nu & \nu & 0 & 0 & 0 \\ \nu & \nu & 1-\nu & 0 & 0 & 0 \\ 0 & 0 & 0 & \frac{1-2\nu}{2} & 0 & 0 \\ 0 & 0 & 0 & 0 & \frac{1-2\nu}{2} & 0 \\ 0 & 0 & 0 & 0 & 0 & \frac{1-2\nu}{2} \end{bmatrix} \begin{bmatrix} \varepsilon_x \\ \varepsilon_y \\ \varepsilon_z \\ \tilde{\gamma}_{xy} \\ \tilde{\gamma}_{xz} \\ \tilde{\gamma}_{yz} \end{bmatrix} \tag{2.60}$$

where the matrix is called material matrix $\hat{C}$ which was already mentioned in eq. (2.49). The tensor of strains is equivalent to the stress tensor (see eq. (2.51)) including principal strains and their directions.

2.2.2 Equivalent Dynamic Stress Formulations

Multiaxial stress loadings which basically include six different stress time series are complicated to be evaluated regarding their damaging influence. According to [6] there are three major multiaxial criteria: Stress-component based criteria including the calculation of an equivalent uniaxial stress, critical plane criteria which often consider the plane of the highest shear stress during the initial crack growth, and stress invariant based concepts. In this thesis the focus is put on the concept of equivalent stresses due to its analytic expandability to other vibrational quantities, as will be seen in section 3.2. Assuming a correct application of an equivalent stress criterion to the respective case, no worse accuracy is accomplished in comparison to other multiaxial concepts. The most common equivalent stress is the von Mises criterion σ_{vM} which describes the difference between the elastic and the hydrostatic energy that is responsible for a deformation. It is used for reasonably ductile materials, mostly metals and plastics. For the plane static case it is expressed as

$$\sigma_{vM} = \sqrt{\sigma_x^2 + \sigma_y^2 - \sigma_x\sigma_y + 3\tau_{xy}^2} \ . \tag{2.61}$$

For ideally ductile materials the equivalent stress according to Tresca is often proposed, for ideally brittle materials the equivalent stress according to Rankine can be used (see [48]). Whatever criterion is used, the original formulations are only valid for the static case and have to be translated into a meaningful dynamic form. In the following, the most popular equivalent dynamic stress formulations are presented for both time and frequency domain using the plane stress case.

2.2.2.1 Time domain

An intuitive approach of translating the von Mises stress into a dynamic equivalent is the so-called signed von Mises stress, as explained in [63]. In order to obtain an alternating time signal a signum function is applied determining the sign by the first stress invariant (eq. (2.52)) which yields

$$\sigma_{vM}(t) = \mathrm{sgn}(I_1)\sqrt{\sigma_x^2(t) + \sigma_y^2(t) - \sigma_x(t)\sigma_y(t) + 3\tau_{xy}^2(t)} \tag{2.62}$$

for the plane stress case. A different concept is the Multiaxial Rainflow[3] method originally proposed in [8]. It is not limited to stress time signals only and can be used for all kinds of loads. Remaining in terms of stresses, the equivalent stress is found by performing a scan on all possible linear combinations of

$$\sigma_{eq}(t) = \hat{c}_1\sigma_x(t) + \hat{c}_2\sigma_y(t) + \hat{c}_3\tau_{xy}(t) \tag{2.63}$$

by changing the constants $\hat{c}_1$, $\hat{c}_2$, $\hat{c}_3$ with respect to $\hat{c}_1^2 + \hat{c}_2^2 + \hat{c}_3^2 = 1$. For each combination a Rainflow cycle counting is performed and a fatigue damage value calculated. The most damaging equivalent stress time signal is then chosen. Further details on the general fatigue damage calculation procedure will be given in section 2.2.4.

[3] The Rainflow counting is a stress time signal based identification method of stress cycles and will be introduced in 2.2.4

2.2.2.2 Frequency domain

The most common approach for translating the von Mises criterion into the frequency domain is the so-called Equivalent von Mises Stress (EVMS) introduced in [66]. Due to the quadratic nature of the stress components they are assumed to be zero mean Gaussian random processes. Therefore, the original von Mises equation is reformulated into

$$\sigma_{vM}^2 = \sigma_x^2 + \sigma_y^2 - \sigma_x\sigma_y + 3\tau_{xy}^2 = \hat{\boldsymbol{\sigma}}^T \boldsymbol{Q} \hat{\boldsymbol{\sigma}} = \operatorname{trace}\left(\boldsymbol{Q}\left[\hat{\boldsymbol{\sigma}}\hat{\boldsymbol{\sigma}}^T\right]\right) \tag{2.64}$$

with $\hat{\boldsymbol{\sigma}}$ being the stress vector and $\boldsymbol{Q}$ being a matrix of constants defined as

$$\boldsymbol{Q} = \begin{bmatrix} 1 & -0.5 & 0 \\ -0.5 & 1 & 0 \\ 0 & 0 & 3 \end{bmatrix} \quad . \tag{2.65}$$

On both sides of eq. (2.64) the expected value is taken and eq. (2.21) is applied which leads to a PSD formulation of the signed von Mises stress

$$G_{\sigma_{vM}}(f) = \operatorname{trace}\left(\boldsymbol{Q}\boldsymbol{G}_{\sigma}(f)\right) \quad . \tag{2.66}$$

Taking the trace of eq. (2.66) and considering only the real part of the cross-spectral density term G_{σ_x,σ_y}, as proposed in [6], yields following expression

$$G_{\sigma_{vM}}(f) = G_{\sigma_x}(f) + G_{\sigma_y}(f) - \operatorname{Re}\left(G_{\sigma_x,\sigma_y}(f)\right) + 3G_{\tau_{xy}}(f) \quad . \tag{2.67}$$

Since the obtained expression does not consider any phase information between the individual stress components, the approach was extended in [10] using a harmonic oscillation

$$\sigma(t) = \hat{\sigma}\,\cos\left(\omega t + \theta\right) \tag{2.68}$$

for each stress component. Eq. (2.68) is inserted into eq. (2.64) and after some geometric reformulations the von Mises PSD can be described for each frequency as

$$\begin{aligned} G_{\sigma_{vM}} = 0.5\left(\hat{\sigma}_x^2 + \hat{\sigma}_y^2 - \hat{\sigma}_x\hat{\sigma}_y\cos(\theta_x - \theta_y) + 3\hat{\tau}_{xy}^2\right) + \\ 0.5\,\operatorname{abs}\left(\hat{\sigma}_x^2 + \hat{\sigma}_y^2 e^{2j(\theta_y-\theta_x)} - \hat{\sigma}_x\hat{\sigma}_y e^{j(\theta_y-\theta_x)} + 3\hat{\tau}_{xy}^2 e^{2j(\theta_{xy}-\theta_x)}\right) \quad . \end{aligned} \tag{2.69}$$

Expressed in terms of PSDs, eq. (2.69) becomes

$$\begin{aligned} G_{\sigma_{vM}} = 0.5\left(G_{\sigma_x} + G_{\sigma_y} - \sqrt{G_{\sigma_x}G_{\sigma_y}}\cos(\theta_x - \theta_y) + 3G_{\tau_{xy}}\right) + \\ 0.5\,\operatorname{abs}\left(G_{\sigma_x} + G_{\sigma_y} e^{2j(\theta_y-\theta_x)} - \sqrt{G_{\sigma_x}G_{\sigma_y}}\; e^{j(\theta_y-\theta_x)} + 3G_{\tau_{xy}} e^{2j(\theta_{xy}-\theta_x)}\right) \quad . \end{aligned} \tag{2.70}$$

Another von Mises based formulation in frequency domain can be found in [70].

2.2.3 Material Properties

In the previous subsection, the general description of component loads was considered. Complementary to that, considerations on the component strength, respectively the material properties, have to be made as well.
Basically, it has to be distinguished between static and dynamic material properties. Static material properties such as the ultimate tensile strength R_m are determined with tensile tests. To obtain cyclical properties so-called Wöhler fatigue tests are conducted until failure. The cyclical strain consists of a plastic and an elastic part, given as

$$\varepsilon = \varepsilon_{el} + \varepsilon_{pl} = \frac{\sigma}{E} + \left(\frac{\sigma}{K'}\right)^{n'} \tag{2.71}$$

with the cyclical strain hardening coefficient K' and the cyclical strain hardening exponent n'. The latter one is defined as $n' = c'/b$ with the cyclical ductility exponent c' and the Basquin exponent b. They are both used following the notation of [45] which is using the inverse values as in opposite to many other references. Furthermore, the fatigue strength coefficient σ' and the cyclical ductility coefficient ε' can be obtained by the fatigue tests. In terms of the maximum endurable cycles N and the strain amplitudes ε_a, the strain-cycle correlation is expressed as

$$\varepsilon_a = \varepsilon_{a,el} + \varepsilon_{a,pl} = \frac{\sigma'}{E}\,(2N)^{1/b} + \varepsilon'\,(2N)^{1/c'} \quad . \tag{2.72}$$

It is shown in fig. (2.6) together with a stress-strain hysteresis including both elastic and plastic strain, according to [26]. The left part shows the overall behavior considering all cycles until failure (S-N curve) while the right part illustrates an individual cycle including an elastic and plastic contribution. The right part can be seen as a doubled version of the cyclical stress-strain curve. Generally, each type of loading, as for example bending or torsion, produces a different S-N curve.

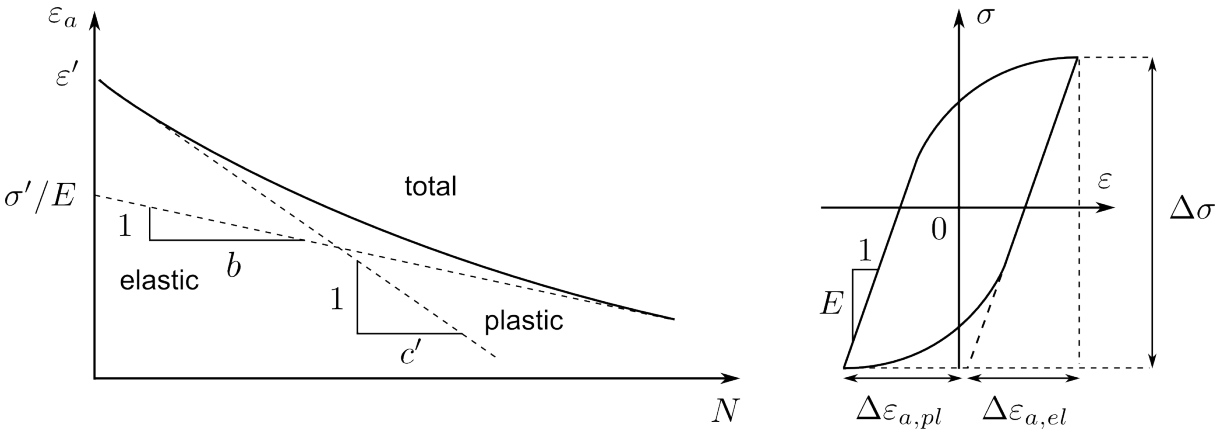

Figure 2.6: Cyclical material behavior: S-N curve and stress-strain hysteresis

According to the load cycles, the S-N curve can be divided into three domains: The Low Cycle Fatigue (LCF) range, typically for a number of cycles lower than around 10^4, the limited endurance domain also called High Cycle Fatigue (HCF) range covering load cycles roughly

between 1×10^4 (in some references 5×10^4) and 2×10^6, and the unlimited endurance domain called Very High Cycle Fatigue (VHCF) range for a cycle number higher than 10^7. The LCF range is dominated by plastic deformation while the HCF and VHCF ranges are dominated by linear elastic deformation. Fig. (2.7) shows the idealized S-N curve that primarily accounts for the HCF and VHCF range and is typically represented in terms of stress amplitudes S_a. The relation between the stress amplitude and the cycle number until failure (endurance strength) is given as

$$N = C\ S_a^{-b} \tag{2.73}$$

with the Basquin constant C that is defined as

$$C = N_D\ S_D^b\ . \tag{2.74}$$

The values for S_D and N_D are obtained at the fatigue limit point which defines the transition point between the HCF and the VHCF range. The Basquin exponent b represents the slope of the S-N curve. For different materials and structures (including notches and welded joints) the value typically ranges between $3 - 13$, but also higher values are possible. A summary of different examples is given in [45]. As shown in fig. (2.7), different approaches exist to describe the S-N curve within the VHCF range. The conservative, elementary Miner rule is a linear extension of the HCF that assumes that even small cycle amplitudes contribute to the fatigue damage. On the contrary, the original Miner considers only amplitudes of $S_a > S_D$. Cycle amplitudes below the fatigue limit do not contribute to the fatigue damage at all. A modified approach, also known as Haibach extension, considers all cycle amplitudes $S_a < S_D$ according to

$$N = C\ S_a^{-(2b-1)}\ . \tag{2.75}$$

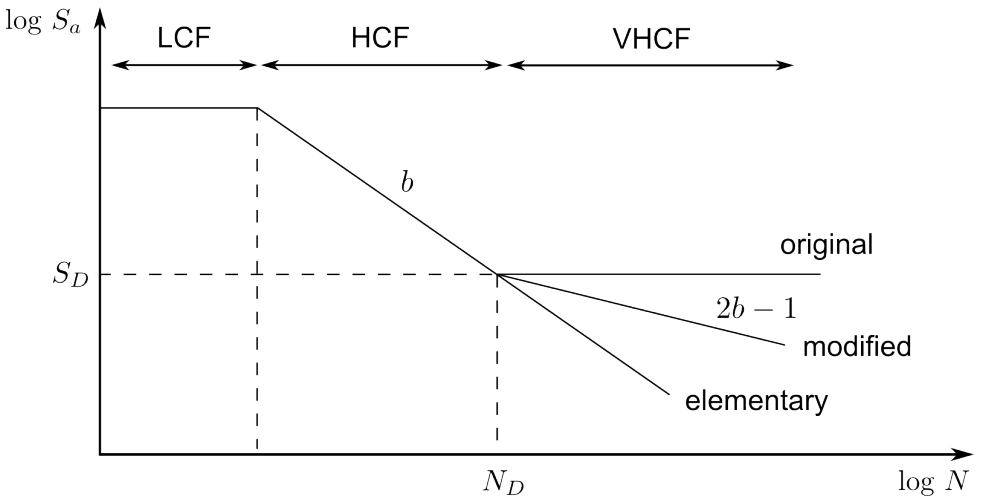

Figure 2.7: Idealized S-N curve

Within operational strength analysis two major approaches are commonly used: The nominal stress concept and the local concept, also called notch concept. The first one is giving

fatigue life estimations based on experimental data of smooth test bars that are applied with different factors considering following effects: Form (notch) effect, scale effect, surface effects, temperature effects and further various effects considering for example the stress frequency and corrosion. The local concept is a mostly FEM based method performing the fatigue life calculation directly at the failure location (hot spot) using locally obtained stresses and strains. Furthermore, the structural stress concept is known as an extension of the nominal stress concept focusing on the hot spot stress.
The strong difference between the nominal stress concept and the local concept can be demonstrated with the respective handling of the mean stress influence. Generally, the mean stress sensitivity depends on the materials, especially on the material strength. For metals, the mean stress sensitivity typically increases with its strength. Using the nominal concept, a mean stress correction can be applied on the stress amplitudes according to the Goodman line, described in [52] as

$$S'_a = \frac{S_a}{1 - \frac{S_m}{R_m}} \tag{2.76}$$

where S'_a is the mean stress corrected cycle amplitude. The concept only uses the ultimate tensile stress of the respective material. For the local concept, a damage equivalent parameter such as proposed by Smith, Watson and Topper (SWT) has to be applied. Therefore, local stress and strain information is used to calculate the damage parameter P_{SWT} as

$$P_{SWT} = \sqrt{(S_a + S_m)\, \varepsilon_a\, E} \ . \tag{2.77}$$

The modification has also to be performed on the respective S-N curve, where both LCF and HCF domain are taken into account. Generally, the S-N curve is shifted downwards with tensile mean stress and upwards with compressive mean stress.
Considering the effect of notches, the nominal concept uses experimentally determined notch factors while the local concept performs further corrections on the stress-strain curve such as proposed by Neuber [26]. The S-N curve of a notched specimen is usually shifted downwards while the Basquin exponent decreases.
Another effect to be considered is due to load history: If small stress amplitudes are applied first and high stress amplitudes subsequent, the fatigue life tends to increase. In the opposite case the fatigue life decreases. While those sequence effects cannot be considered using the nominal concept, there are existing approaches with the local concept. However, in random vibration the influence is found to be much lower than for sinusoidal excitation due to the unordered sequences [45].

2.2.4 Fatigue Damage Calculation

In this subsection, the considerations on both component loads and strength are combined to make statements on the fatigue damage.
The first step in the determination of fatigue damage values is the identification of stress cycles. Therefore, usually a Rainflow counting is performed on the stress time signals after the extraction of turning points according to [4]. It is based on two concepts, masing behavior and material memory. The masing hypothesis states that a doubling of the cyclical stress-strain

curve, as shown in fig. (2.6), results in the stress hystereses to be obtained. The stress-strain hysteresis that is produced during reloading was previously shown in fig. (2.6). The assumption of the memory effect of a material comprises the influence of the load sequence. Thus, both stress hysteresis amplitudes and mean values are to be extracted according to an appropriate counting method.
In a next step, the obtained stress amplitudes have to be transferred into a fatigue damage value. This is commonly achieved using a linear damage accumulation, also called Palmgren-Miner damage accumulation according to [26]. It assumes that the total fatigue damage $\hat{D}$ introduced into a structure can be expressed as a sum of all individual cycles n_i divided by their respective number of maximum endurable cycles N_i, which yields

$$\hat{D} = \sum_i d_i = \sum_i \frac{n_i}{N_i} \leq 1 \ . \tag{2.78}$$

The virtual fatigue damage value at failure is defined as 1. In principle there are two major states of life time, the crack initiation and the crack propagation. In the strict sense the linear damage accumulation is only appropriate to calculate fatigue damage through crack propagation, since crack initiation is the result of microscopic effects. However, linear damage accumulation is used widely for the entire fatigue life since it is often not possible to distinct both states adequately.
Combining eq. (2.78) and eq. (2.73) yields an expression including the stress amplitudes

$$\hat{D} = \frac{1}{C} \sum_i n_i \ S_{a,i}^b \leq 1 \ . \tag{2.79}$$

It has to be noted that linear damage accumulation does not account for mean stresses if no prior amplitude correction was performed. Eq. (2.79) is often written in a simplified form ignoring the Basquin constant and without a classification of the stress amplitudes which removes the specific cycle number n_i. Each stress amplitude is then evaluated individually. Eq. (2.80) then describes an artificial pseudo damage value D as

$$D = \sum_i S_{a,i}^b \ . \tag{2.80}$$

which is mainly used for fatigue damage evaluation due to the lack of need to determine C. For random vibration environments, the fatigue damage in eq. (2.79) per time unit T can be expressed generally in a stochastic manner according to [5] as

$$\hat{D} = \frac{\nu_0}{C} \int_0^\infty p(S_a) \ S_a^b \, \mathrm{d}S_a \ . \tag{2.81}$$

Equation (2.81) is the base for various spectral fatigue damage estimators which mainly differ in the assumed probability density function $p(S_a)$. As discussed in (2.1.2), for narrowband processes the stress cycles are underlying a Rayleigh distribution. For broadband processes, common approaches are named after Dirlik, Lalanne, Tovo and Benasciutti, Zhao and Baker, etc. (see [62] and [54]). All approaches are using different combinations of distributions, such as Gaussian, Rayleigh, Rice, Weibull and the exponential distribution. A comparison of those

approaches is performed in [62]. A novel approach for the estimation of the Rainflow distribution out of a broadband process can be found in [70].

In the following section the focus is put on vibration testing. Thereby, it is distinguished between vibration control and the definition of vibration test profiles. While the first topic only requires the introduced theory of signal processing, the latter requires both signal processing as well as the theory of structural dynamics and fatigue damage calculation.

2.3 Vibration Testing

Vibration testing is essential for the release of newly developed machines and structures. Thereby, a sufficient resistance to expected loads over the entire service life has to be ensured. Usually, measured field data is used to obtain meaningful load collectives which are then reproduced on a shaker table. In most cases accelerated testing is unavoidable if the original service time ranges from years to decades, as it is within the automotive as well as the aerospace industry. Therefore, the vibrational loads of each driving, respectively flight scenario are scaled up appropriately.
For commercial vehicles, typical environmental conditions regarding vibration are road excitations which are modeled as random and shock, and run-ups especially of combustion engines and electric motors that can be described as a harmonic excitation. To obtain respective random load collectives, rides are performed on different tracks such as for example on rough road or cobblestone tracks, but also on highways and country roads, depending on the expected utilization. Engine run-ups are usually performed on roller dynamometer test benches in order to obtain completely decoupled information of the internal excitations.
The load collectives of fixed wing aircrafts are primarily obtained from engine noise, (turbulent) aerodynamic flow and maneuvers such as landing and taxi. Rotary wing aircrafts are dominated by sinusoids from the rotating components. For military applications a focus is put on specific shock scenarios such as gunfire, but also on road specific aspects of transport protection.
Typical vibration test types that are performed by controlled shaker excitation can be divided into three main groups: Random, sine and shock (see fig. (2.8)). Further test types are combinations as for example Sine on Random (SoR) or the exact replication of measured time signals which is called Time Waveform Replication (TWR).
Within the automotive industry vibration tests are mainly conducted on uniaxial shaker tables, while within military and aerospace multi-axis testing is already state of the art. This is in particular due to the limitation of facilities regarding the frequency range which tends to be lower in aerospace applications.
Further information on the load collectives and testing procedures of transportation vehicles, as well as aircraft and military applications can be found in [90] and [59], for passenger and commercial vehicles in [35].

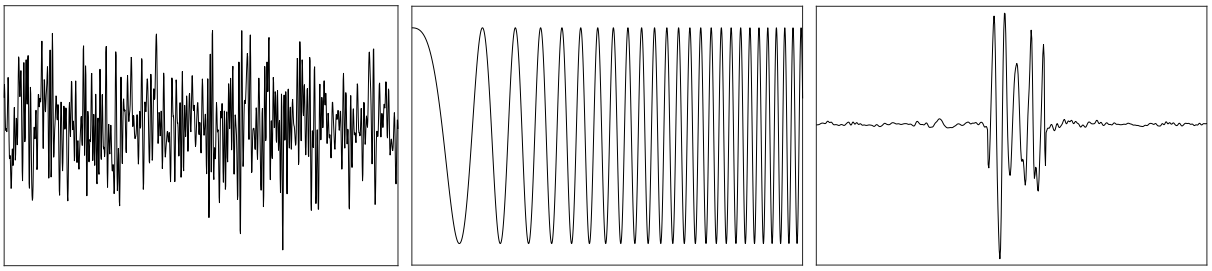

Figure 2.8: Illustrations of different vibration test types (random, sine, shock)

In this section vibration testing methodologies are introduced. The first part aims at explaining necessary vibration control theory for all relevant test types. Thereby, it is distinguished between the control of random and deterministic time signals. The second part is focused on the definition of meaningful test profiles as a reference for the control loop. Both existing uniaxial and multiaxial test profile derivation methods are presented, as well as standard profiles proposed by the aforementioned literature references.

2.3.1 Multi-Input-Multi-Output Control

Linear vibration control is usually designed with a feedback control loop for each frequency independently. Thereby, the control process is realized with a P-control element speaking in terms of automation control. Within the scope of this thesis only Multi Input Multi Output (MIMO) control is treated as an extended version of the uniaxial Single Input Single Output (SISO) control. In case of an equal number of drives and control transducers the configuration is referred to as square control, in any other cases as rectangular control which is described in [88] and [87]. Starting point for all control methods is an initial measurement of the systems transfer matrix $\boldsymbol{H}(f)$, usually on a low excitation level.

2.3.1.1 Random vibration control

In the following, the random vibration control process for a square configuration is explained in detail, according to [64], [14] and [76] amongst others. A flow chart of the feedback control loop for random vibration is given in fig. (2.9) according to [64].
The control reference for the random time signals is a positive definite SDM $\boldsymbol{R}(f)$. The aim of the entire process is to match the output spectrum $\boldsymbol{G}(f)$ with the reference as

$$\boldsymbol{G}(f) = \boldsymbol{R}(f) \ . \tag{2.82}$$

As an initial step, a spectral decomposition is performed on $\boldsymbol{R}(f)$ as

$$\boldsymbol{R}(f) = \boldsymbol{U}_0(f)\ \boldsymbol{S}_0(f)\ \boldsymbol{U}_0^*(f) \ . \tag{2.83}$$

resulting in the initial eigenvector matrix $\boldsymbol{U}_0(f)$ and the initial diagonal matrix $\boldsymbol{S}_0(f)$. According to [78] any spectral decomposition can be used as long as it can be expressed in the form of eq. (2.83). An eigenvalue decomposition can be used, as well as the singular value decomposition which is equivalent in case of a symmetric matrix $\boldsymbol{R}(f)$. All relationships are described detailed in [81]. Commonly, a Cholesky decomposition is used, as explained in [73], which yields

$$\boldsymbol{R}(f) = \boldsymbol{L}_0(f)\boldsymbol{L}_0^*(f) \ . \tag{2.84}$$

The lower triangular matrix $\boldsymbol{L}(f)$ is also referred to as Cholesky factor. Eq. (2.83) can be transformed into eq. (2.84) if $\boldsymbol{S}(f) = \boldsymbol{I}$. All decompositions are possible as long as the matrix is positive definite. During the control process the decomposition is performed on $\boldsymbol{G}(f)$.
As a next step, the predicted output Fourier spectrum $\hat{\boldsymbol{y}}(f)$ is calculated based on a random part and a reference part which can be characterized as decoupled inputs [103]. The random part $\boldsymbol{w}(f)$ is a vector of independent noise sources that are realized with a uniformly distributed random phase $e^{j\phi(f)}$ for each entry. The noise source is also known as pseudo random, as described in [64] and [78]. Using a Cholesky decomposition to obtain the reference part $\boldsymbol{L}(f)$ yields

$$\hat{\boldsymbol{y}}(f) = \boldsymbol{L}(f)\ \boldsymbol{w}(f) \tag{2.85}$$

which can also be derived with an eigenvalue decomposition and its resulting reference part $\boldsymbol{U}(f)\sqrt{\boldsymbol{S}(f)}$ as

$$\hat{\boldsymbol{y}}(f) = \boldsymbol{U}(f)\ \sqrt{\boldsymbol{S}(f)}\ \boldsymbol{w}(f) \ . \tag{2.86}$$

Being the third decoupled input, the inverse of the transfer matrix $\hat{\boldsymbol{H}}(f)$ is then multiplied to eq. (2.86) which yields the input spectrum $\boldsymbol{x}(f)$, expressed as

$$\boldsymbol{x}(f) = \hat{\boldsymbol{H}}(f)\ \hat{\boldsymbol{y}}(f) = \hat{\boldsymbol{H}}(f)\ \boldsymbol{L}(f)\ \boldsymbol{w}(f) \tag{2.87}$$

in case of a Cholesky decomposition and

$$\boldsymbol{x}(f) = \hat{\boldsymbol{H}}(f)\ \hat{\boldsymbol{y}}(f) = \hat{\boldsymbol{H}}(f)\ \boldsymbol{U}(f)\ \sqrt{\boldsymbol{S}(f)}\ \boldsymbol{w}(f) \tag{2.88}$$

using an eigenvalue decomposition. To obtain the drive time signals $\boldsymbol{x}(t)$, an IFFT is applied:

$$\boldsymbol{x}(t) = \mathrm{ifft}\left(\boldsymbol{x}(f)\right) \ . \tag{2.89}$$

Depending on the SDM, they can be fully, partly or not correlated. In practice, a time domain randomization is then performed on the drive time signals. Therefore, several data blocks are generated and manipulated through windowing, overlapping and coupling in order to achieve different signals each loop, as described in [25]. If time domain randomization is applied, the random part $\boldsymbol{w}(f)$ has to be the same for all signals in order to maintain the coherences. Otherwise, the random part can change in every control loop.
The core of the control action is the algorithm that updates the decoupled inputs $\boldsymbol{L}(f)$, respectively $\boldsymbol{U}(f)\sqrt{\boldsymbol{S}(f)}$. Two basic approaches exist: The update of the reference part $\boldsymbol{L}(f) \rightarrow \boldsymbol{L}(f) + \Delta\boldsymbol{L}(f)$ as described in [64] and updating the transfer matrix $\hat{\boldsymbol{H}}(f) \rightarrow \hat{\boldsymbol{H}}(f) + \Delta\hat{\boldsymbol{H}}(f)$ as described in [79] and [72]. Both approaches can also be used together as performed in [76]. The first approach numerically finds an update for both amplitude and phase based on the error $\boldsymbol{R}(f) - \boldsymbol{G}(f)$. The second one continuously recalculates the transfer matrix based on eq. (2.16) and (2.17).

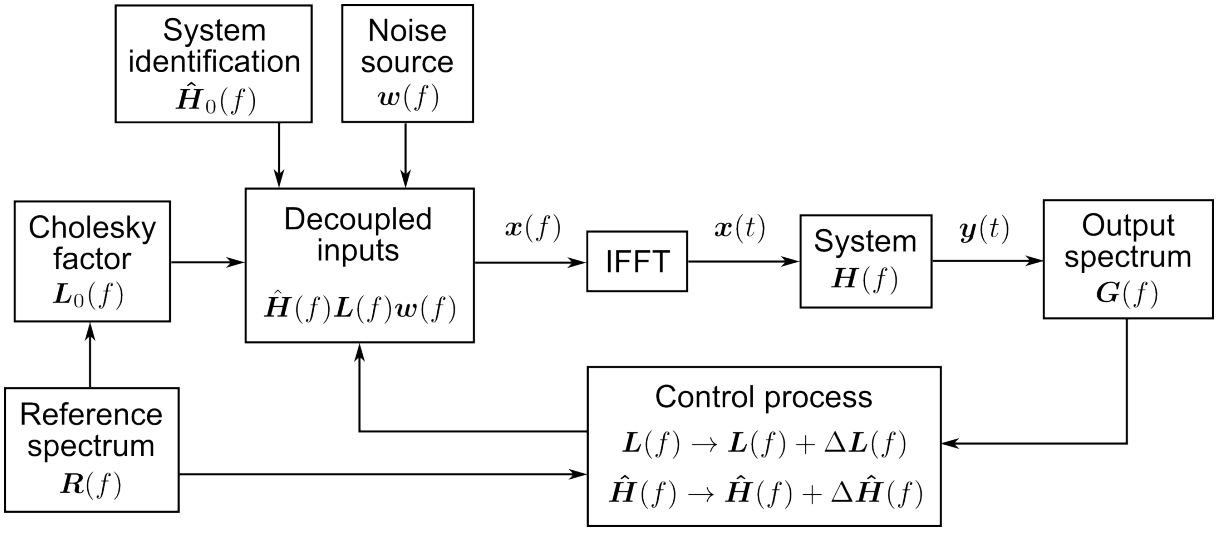

Figure 2.9: Flow chart of random vibration control algorithm

For rectangular control applications some further considerations have to be made. The fundamental control problem is solved by an error minimization using the matrix error norm

$$|\boldsymbol{E}(f)|^2 = |\boldsymbol{R}(f) - \boldsymbol{H}(f)\ \boldsymbol{G}(f)\ \boldsymbol{H}^*(f)|^2 \tag{2.90}$$

with the error matrix $\boldsymbol{E}(f)$. Since the transfer matrix not being symmetric anymore, its inversion has to be accomplished using for example the Moore-Penrose pseudo inverse[4] yielding $H^\dagger$. Furthermore, an ordinary coherence calculation as performed with eq. (2.13) is not possible anymore. For responses caused by several drives, partial coherences need to be considered as explained in [88].

2.3.1.2 Deterministic vibration control

The square control of deterministic signals requires a control process based on the acceleration levels. A flow chart of the feedback control loop for deterministic vibration is given in fig. (2.10). The reference spectrum is a vector of Fourier transforms $\boldsymbol{r}(f)$, that has to match the output spectrum $\boldsymbol{y}(f)$ according to

$$\boldsymbol{y}(f) = \boldsymbol{r}(f) \quad . \tag{2.91}$$

Based on the error $\boldsymbol{r}(f) - \boldsymbol{y}(f)$ the drives of the i'th loop $\boldsymbol{x}_i(f)$ are updated iteratively according to

$$\boldsymbol{x}_i(f) = \boldsymbol{x}_{i-1}(f) + \Delta\boldsymbol{x}_i(f) \quad . \tag{2.92}$$

The control process uses the error to recalculate the diagonal matrix $\hat{\boldsymbol{Q}}(f)$ which contains the so-called iteration gains $\hat{q}(f)$ (with $0 \leq \hat{q} \leq 1$) on its entries, described as

$$\Delta\boldsymbol{x}_i(f) = \hat{\boldsymbol{Q}}(f)\ \hat{\boldsymbol{H}}(f)\,(\boldsymbol{r}(f) - \boldsymbol{y}_{i-1}(f)) \quad . \tag{2.93}$$

[4] The pseudo inverse is a least squares solution for the inversion of a non-symmetric or singular matrix

Initially, it is $\hat{\boldsymbol{Q}}_0(f) = \boldsymbol{I}$. In opposite to random vibration control where a (permanently changing) noise source is given, the drives can be updated directly based on each other. Furthermore, the transfer matrix can also be updated according to $\hat{\boldsymbol{H}}(f) \rightarrow \hat{\boldsymbol{H}}(f) + \Delta\hat{\boldsymbol{H}}(f)$.

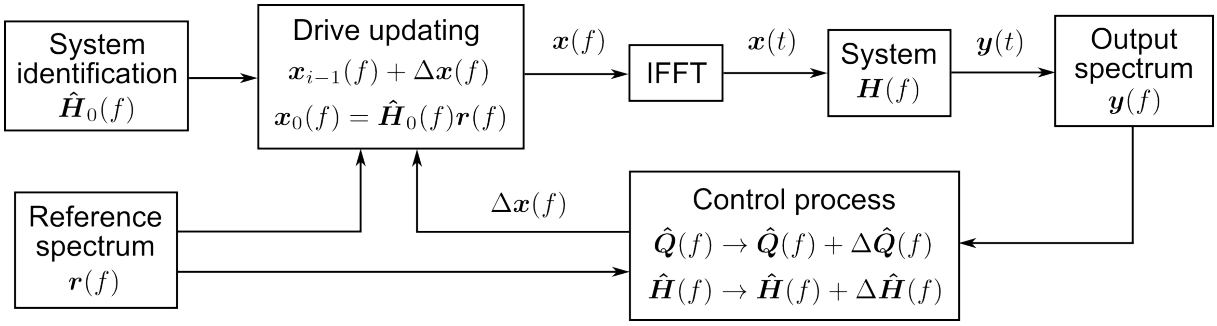

Figure 2.10: Flow chart of sine vibration control algorithm

The first application for deterministic control is the sine sweep. It is commonly used for preliminary resonance investigations, as well as for the simulation of engine run-ups. A linear sweep (or chirp) between the frequencies f_0 and f_1 over a duration of T with an amplitude $\hat{A}(t)$ and a phase $\theta(t)$ is defined as

$$x(t) = \hat{A}(t)\,\sin\left[\theta(t) + 2\pi\left(f_0 t + \frac{1}{2}\,\frac{f_1 - f_0}{T}\,t^2\right)\right] \tag{2.94}$$

according to [11], rearranged including a phase term. To accelerate at higher frequencies, usually an exponential (or logarithmic) sweep is used which is defined as

$$x(t) = \hat{A}(t)\,\sin\left[\theta(t) + 2\pi f_0\left(\frac{\left(\frac{f_1}{f_0}\right)^{t/T} - 1}{\ln\left[\left(\frac{f_1}{f_0}\right)^{1/T}\right]}\right)\right] \quad . \tag{2.95}$$

The application of MIMO sine control is further explained in [68].

Apart from sine, another application in deterministic vibration control is the Time Waveform Replication (TWR). As the name indicates, the TWR performs an exact replication of a measured or generated time signal. It is commonly used for special load cases and for shock tests. Thereby, the iteration process shown in fig. (2.10) is calculated offline before the test. All calculations are usually performed in the frequency domain despite the suggestion of the time domain. However, for specific cases such as shocks also a direct error calculation in time domain is feasible. In its basic version, once the initial transfer matrix is estimated and the drive signals are computed, the test runs through without any further control actions. After a single test, the transfer matrix can be updated optionally to achieve improvements for the next run. This procedure is referred to as adaptive modeling, as explained in [12]. To account for nonlinear effects, also a real time (online) update of the transfer matrix is possible which is referred to as adaptive control, as described in [85]. The main limitation of the method is its requirement of a large data storage space, especially for time signals with high sampling rates.

2.3.2 Test Profile Derivation Methods

Several approaches exist to obtain load collectives and thus vibration profiles from field measurements. They are introduced in the following subsections. Prior to the combination of different scenarios or maneuvers to a single profile, the underlying signal processing of each one has to be determined. Within the automotive industry, a common procedure is the division of the time signals into windows of 2048 samples using a sampling rate of 12500 Hz, as described in [35]. Thereby, the Nyquist criterion is considered which states that the sampling frequency should be 2.5 times[5] the maximum observed frequency. For stationary signals a Hanning window function can be applied on each window in order to reduce spectral leakage. For random profiles, an average PSD is then usually calculated over all windows. Depending on the aim of the profile (average or worst case), a certain percentage of windows containing extremely large or low values can be omitted. Differences in steady state and transient field data are analyzed and evaluated in [92]. For sine profiles, usually peak hold FFT values $X_{max}(f)$ are obtained which always use the maximum values of all windows for each frequency. For highly instationary signals, [90] proposes the maximum expected environment where additional confidence limits are added to the profile.
After the determination of all $\hat{n}$ scenario profiles, they are combined into a test profile as illustrated in fig. (2.11). The underlying methods will be explained in the following.

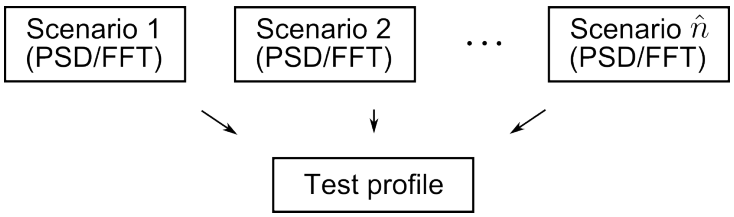

Figure 2.11: Profile derivation

2.3.2.1 Techniques using field data directly (averaging and enveloping)

In terms of random vibration the most intuitive approach is the averaging method, where all individual scenario PSDs are combined in an average sense. According to the respective expected service times this can also be accomplished in a weighted average form. For multiaxial profiles the averaging can also be performed on the entire SDM, according to [27]. Thereby, the obtained mean SDM $\bar{\boldsymbol{G}}(f)$, described as

$$\bar{\boldsymbol{G}}(f) = \frac{1}{\hat{n}} \sum_{i=1}^{\hat{n}} \boldsymbol{G}_i(f) \tag{2.96}$$

remains positive definite. Exemplary given in eq. (2.97), the mean PSD and CSD terms can be used to obtain mean phases $\bar{\theta}(f)$ and mean coherences $\bar{\gamma}(f)$ according to

$$\bar{G}_{12}(f) = \sqrt{\bar{\gamma}_{12}^2(f)\, \bar{G}_{11}(f)\, \bar{G}_{22}(f)}\, e^{j\bar{\theta}_{12}(f)} \quad . \tag{2.97}$$

[5] The original Nyquist theorem requires a factor of 2 but commonly 2.5 is used including a safety factor

For the calculation of a sine profile, the amplitudes can be obtained analogously from the average of all individual peak hold FFTs

$$\bar{\boldsymbol{x}}(f) = \frac{1}{\hat{n}} \sum_{i=1}^{\hat{n}} \boldsymbol{x}_{max,i}(f) \quad . \tag{2.98}$$

During the peak hold calculation the phase information in each time window gets lost for each scenario. For multiaxial tests, the phase can be of higher importance to qualitatively maintain the vibrational environment. Therefore, the phase information is obtained from the particular mean FFTs which can then be combined respectively as

$$\bar{\boldsymbol{x}}(f) = \frac{1}{\hat{n}} \sum_{i=1}^{\hat{n}} \boldsymbol{x}_{i}(f) \quad . \tag{2.99}$$

Another approach are enveloping techniques in order to directly construct the worst case for all frequencies. Envelopes are also often applied to overcome resonance frequency shifts or an unknown mounting orientation [90]. Frequency shifts of both the product itself as well as the substructure can occur due to variable material and boundary conditions. Differences in the boundary stiffness between shaker and vehicle is a common issue in practice. Furthermore, straight-line specifications support an easier handling. The enveloping can be performed on both PSD and FFT profile sets. For a set of PSD profiles $\hat{N}$, the enveloping technique is defined as

$$G_{env}(f) = \text{envelope} \left[\bigcup_{i \in \hat{N}} G_i(f) \right] \quad . \tag{2.100}$$

It can be used analogue for FFT profiles. According to [27] no enveloping should be performed on SDM terms to avoid violations of the positive definiteness.

The final step of profile derivation is a scaling in case of accelerated testing is needed. The exposure time, and thus the damage, is related to the stress amplitudes through the S-N slope b, as given in eq. (2.80). Using the relation between amplitude and RMS value from eq. (2.11) yields also an expression for random vibration

$$\frac{T_{\text{service}}}{T_{\text{test}}} = \left(\frac{S_{a,\text{test}}}{S_{a,\text{service}}} \right)^{b} = \left(\frac{\hat{s}_{\text{test}}}{\hat{s}_{\text{service}}} \right)^{b/2} \tag{2.101}$$

with the severity $\hat{s}$ that is equivalent to the RMS level of the PSD (see [27]). It doesn't matter which vibrational quantity is expressed as PSD since only an amplification factor is described. Mostly, the acceleration PSD of the profile is used. Eq. (2.101) is based on several assumptions, such as a constant slope value, the validity of the linear damage accumulation and a constant cycle number over time.
Considering an entire SDM, a scaling on an individual DOF-basis is proposed in [27]. For deterministic time signals, eq. (2.101) is called load amplification method according to [28]. Thereby, frequency, phase and cycle sequence remain the same and only the amplitude changes. Another approach for the acceleration is the so-called compressed time testing where non-damaging cycles are removed from the original time signal.

2.3.2.2 Techniques using a substituted mechanical system - Fatigue Damage Spectrum

Instead of creating a vibration profile directly from field data, a substituted mechanical system can be used for a better consideration of a system's behavior. The most common approach is the Fatigue Damage Spectrum (FDS) which considers any mechanical system as sequence of SDOF systems as shown in fig. (2.12). Each frequency is thereby assumed to be a potential eigenfrequency with its own SDOF system.

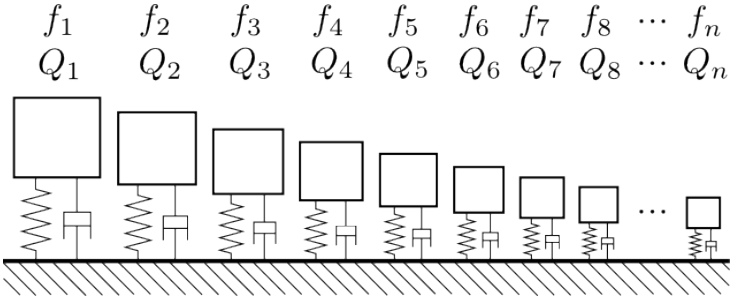

Figure 2.12: Concept of FDS using spring-mass-damper systems

Any vibration profile is first translated into an FDS representing the damage domain. For random vibrations, a narrowband process is assumed for each SDOF system and eq. (2.25), (2.81) and (2.34) are combined yielding

$$D(f,T) = \frac{f_n k_d^b T}{C}\left[\pi f_n Q \frac{G_{xx}(f)}{(2\pi f_n)^4}\right]^{b/2} \Gamma\left(1+\frac{b}{2}\right) \tag{2.102}$$

according to [100] with k_d being an artificial factor between stress and displacement. Furthermore, it is $\nu_0 = f_n$ considering the narrowband assumption and $f = f_n$ since each frequency is considered as potential eigenfrequency. Another formulation uses the relationship between stress and velocity expressed with the factor k_v according to

$$D(f,T) = \frac{f_n k_v^b T}{C}\left[\frac{Q G_{xx}(f)}{4\pi f_n}\right]^{b/2} \Gamma\left(1+\frac{b}{2}\right) \quad . \tag{2.103}$$

Thereby, eq. (2.35) is used for the derivation. The relationship between stress and velocity will be investigated in detail in the next chapter.
As indicated in [91], it doesn't matter which quantity is used since always narrowband responses are calculated for the translation into a damage spectrum. A simplified formulation of eq. (2.103) is given in [30] neglecting all constants which yields the so-called Damage Potential (DP), described as

$$DP(f,T) = f_n T\left[\frac{2Q G_{xx}(f)}{f_n}\right]^{b/2} \quad . \tag{2.104}$$

Commonly, values of $Q = 10$ and $b = 8$ are used in practice, as proposed in [100].
The actual profile derivation happens in the fatigue domain, where all profiles can be summed up to a single one. Thereby, each profile is already weighted with its respective exposure time. As a next step, a backwards calculation of eq. (2.104) is accomplished as illustrated in fig.

(2.13) using a desired test time T_{test}. The FDS relates to the weighted averaging method when considering low values for b. Considering higher values for b, the FDS calculation gets more influenced by the highest PSD level at each frequency.

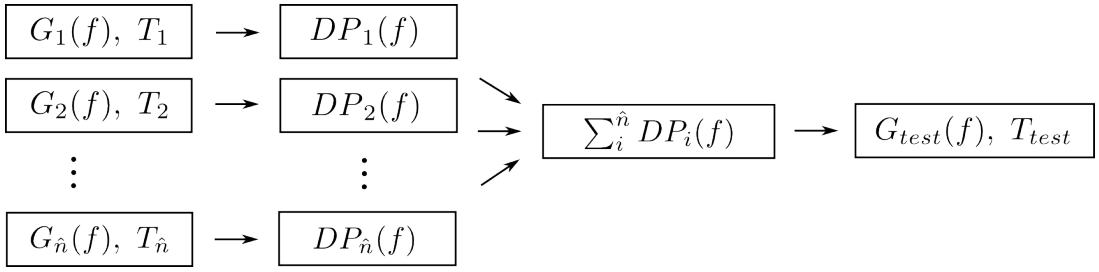

Figure 2.13: Profile derivation using FDS approach

The FDS of a single sine excitation at eigenfrequency is introduced in [47] as

$$D(f,T) = \frac{f_n k_d^b T}{C} \left[\frac{QS_a(f)}{(2\pi f_n)^2}\right]^b \tag{2.105}$$

where $QS_a(f)$ can be expressed by the amplitude of the excitation acceleration $\hat{A}(f)$. The FDS expressions for linear and logarithmic sine sweeps are given in [47]. The sine FDS can also be added to a random FDS if a damage equivalent random profile shall be created based on both sine and random. A formulation for the sine based DP can be consequently stated as

$$DP(f,T) = f_n T \left[\frac{QS_a(f)}{f_n^2}\right]^b \tag{2.106}$$

with all constants being neglected.

2.3.3 International Standards

The methods introduced in the previous subsection are partly included in different international standards. The US Military Standard (MIL-STD) 810 [90] proposes an FDS for the combination of different spectra and further includes the averaging method for multiaxial profiles from eq. (2.96). In cases where no field data is available, standard profiles are given for different military and aerospace applications. Fig. (2.14) shows direction specific standard profiles for common carriers driving on US highways. Thereby, only a lower frequency range up to 500 Hz is excited. The test time is given as 60 minutes per axis. If the mounting orientation is unclear, an envelope should be used to cover the worst case. However, no extension to multi-axis shaker testing is mentioned. Further standard profiles are considering two wheelers, composite wheeled vehicles and helicopters amongst others.

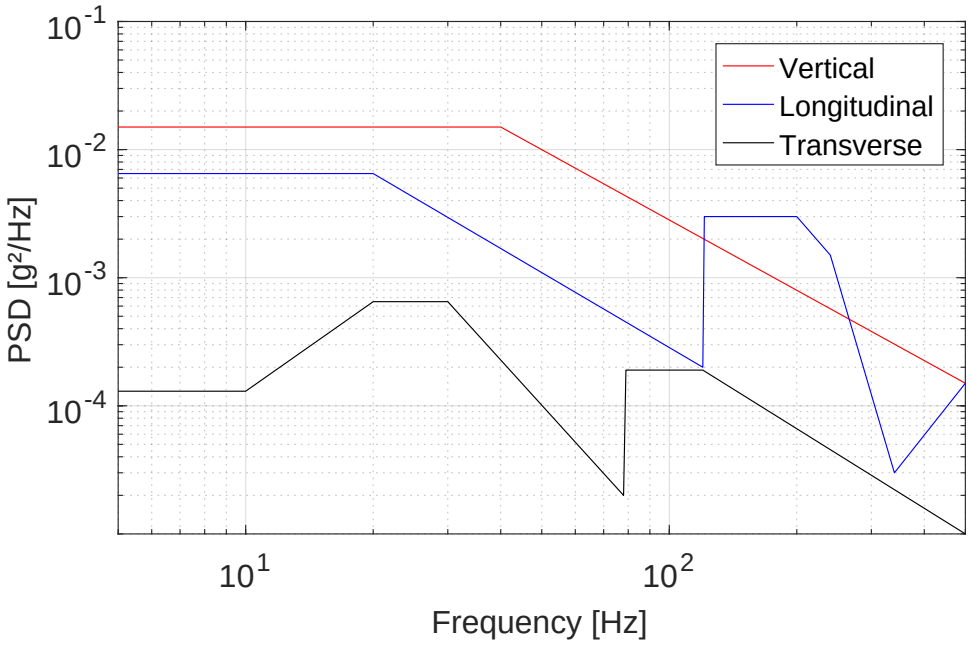

Figure 2.14: Standard profile for common carriers on US highways

The International Organization for Standardization (ISO) 16750-3 [35] provides standards for passenger and commercial vehicles. Standard profiles are given for sprung and unsprung masses, engine components, the gearbox, etc. The standard profile for sprung masses is shown in fig. (2.15). The associated testing time is 8 hours per axis. No proposals for multi-axis testing are given. To evaluate the fatigue damage of both field and shaker test, a cycle counting on the acceleration responses is proposed. Thereby, the field data is extrapolated to the complete service time. It is stated that this procedure is only valid for structures with a single dominant mode (where the narrowband assumption holds). A peak counting, which is a simplified form of the Rainflow counting, is then applied to determine the cycle amplitudes. For the fatigue damage calculation 12 different S-N curve models are used together with the Haibach extension. All combinations for an exponent b out of $[3, 5, 7, 10]$ and number of cycles at the fatigue point limit N_D out of $[2 \times 10^6, 10 \times 10^6, 50 \times 10^6]$ have to be considered. If the damage based on the shaker test is always higher than based on the field data, the test succeeded.

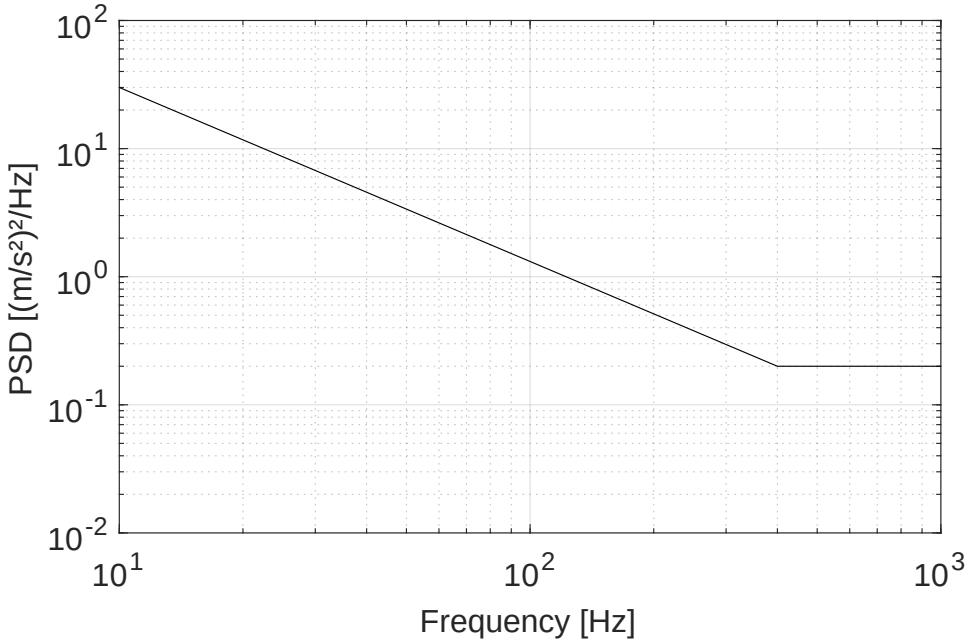

Figure 2.15: Standard profile for sprung masses on passenger cars

3 Multiaxial Fatigue Damage Calculation

The core of this thesis is the comparison of fatigue damage between sequential uniaxial and multiaxial (simultaneous) vibration tests. Therefore, relevant considerations are made in this chapter resulting in a new evaluation concept. Existing fatigue damage calculation procedures and models are reviewed and basic effects of sequential and simultaneous excitation are discussed. An easily measurable damage equivalent quantity is determined and applied to the previously specified calculation procedure. The geometric influence on the methodology is then investigated extensively.

3.1 Preliminary Considerations

The first step is to define a general approach for the quantification of fatigue damage. Thereby, both sides, loading and material strength, are to be considered. An equivalent stress concept, an appropriate handling of the respective cycle amplitudes and mean values, as well as reasonable S-N curve models are chosen. Different effects resulting from both sequential and simultaneous excitation are considered: The influence of narrowband and broadband response, the excitation phase and resulting failure locations, and the influence of coherence.

3.1.1 Fatigue Damage Evaluation Methodology

An initial assumption is the crack initiation at the surface of a structure which justifies the usage of plane stress simplifications. As equivalent stress criterion, the von Mises PSD in eq. (2.70), also referred to as Bonte PSD, is used due to its consequent consistency with the static von Mises criterion. The PSD is then used as a base for the generation of a white noise signal (see eq. (2.85) and (2.86)), that in turn can be used for a subsequent fatigue damage calculation. As indicated in [71], the time signal has to be sufficiently long in order to neglect fluctuations. Therefore, a minimum of 10^6 cycles should be used which results in a time signal of 200 minutes to cover components with a first eigenfrequency at around 100 Hz. Thereby, a sampling rate of 12500 Hz is used. Since accurate results shall be obtained, none of the spectral fatigue damage estimators that were mentioned in 2.2.4 are used. Instead, a Rainflow counting is performed on the generated signals to obtain the stress cycles. A flow chart of the entire method is given in fig. (3.1). For an underlying stationary random process, the obtained cycles from the Bonte PSD can be directly used as absolute values for a fatigue damage calculation. For underlying deterministic signals, such as for example sine sweeps which are transformed into a Bonte PSD, only a relative damage comparison between two profiles can be performed using the obtained cycles. The high amplitudes that occur are usually lowered through the averaging process which is violating the contribution to the actual fatigue damage, however in the same manner for both profiles.

Apart from the Bonte PSD, existing time domain methods (see subsection 2.2.2.1) are found to be not appropriate: The multiaxial Rainflow approach is an artificial concept which requires a high computing time. The signed von Mises is a simple method that applies its sign according to the first invariant. In case of higher out-of-phase components, such as shear stresses, the results can get highly violated due to the respective components being forced to the sign of the

normal stresses.

The fatigue damage calculation is based on linear damage accumulation ignoring the mean stress values. According to investigations performed in [44], mean stresses obtained from symmetric random time signals with an expected value of zero have hardly influence on fatigue life. Due to the dominance of resonant vibration, the time signals used in this thesis are all of symmetric nature. Furthermore, the mean stress sensitivity strongly depends on the material. Structural effects such as counter effects on the loss of fatigue strength introduced by notches may occur with higher mean stress sensitivities. Thus, a general fatigue damage evaluation method cannot include mean stresses.
To evaluate all kinds of materials and structures, all calculations are performed using different S-N models with exponents of $b = 3 - 13$. For the pseudo fatigue damage calculation the conservative elementary Miner rule of eq. (2.80) is used. Due to the exponential consideration, the influence of low amplitudes is neglectable. In [44], the lower 50 percent of the amplitudes are left out. Furthermore it is stated in [45] that other approaches than the elementary Miner rule are too specific and bring complexity into the method that is not justified by the results.
The small difference between the three approaches of the Miner rule shall be demonstrated using an arbitrary white noise time signal. It is Rainflow counted and the cycle amplitudes are applied with the different exponents b according to the different Miner rules. Thereby, the percentiles of stress amplitudes lower than the fatigue limit S_D are increased from 90% to 99%. As number of cycles at the fatigue limit point $N_D = 2 \times 10^6$ is chosen arbitrarily, since it is canceled out during further procedure. The maximum fatigue damage values which are those from the elementary approach are divided by the minimum values which come from the original approach to find the largest discrepancy. The results using the Haibach extension are logically lying between both approaches. All results for $D_{\mathrm{elementary}}/D_{\mathrm{original}}$ are given in table (3.1) and show a maximum discrepancy of a factor of 3.78 for an absolute worst case scenario which is still acceptable within the scope of fatigue damage calculation where uncertainties of up to 10 are common (see [7] and [43]).

Table 3.1: Ratio of maximum and minimum fatigue damage values for different percentiles of stress amplitudes less than the fatigue limit

b	3	4	5	6	7	8	9	10	11	12	13
$90\% < S_D$	1.34	1.14	1.05	1.02	1.01	1.00	1.00	1.00	1.00	1.00	1.00
$95\% < S_D$	1.72	1.33	1.16	1.07	1.03	1.01	1.01	1.00	1.00	1.00	1.00
$97\% < S_D$	2.14	1.55	1.28	1.14	1.07	1.03	1.02	1.01	1.00	1.00	1.00
$98\% < S_D$	2.60	1.79	1.41	1.22	1.12	1.06	1.03	1.02	1.01	1.00	1.00
$99\% < S_D$	3.78	2.39	1.75	1.43	1.25	1.14	1.09	1.05	1.03	1.02	1.01

The entire methodology is illustrated in fig. (3.1) using results obtained from simulation. The stress FRFs are multiplied with the FFT of a generated white noise random input in order to get stress response FFTs which can be processed further according to the figure. The stress time signal of the Bonte PSD is generated according to subsection 2.3.1.1 including an IFFT. Thereby, a random phase is introduced to the Bonte PSD.

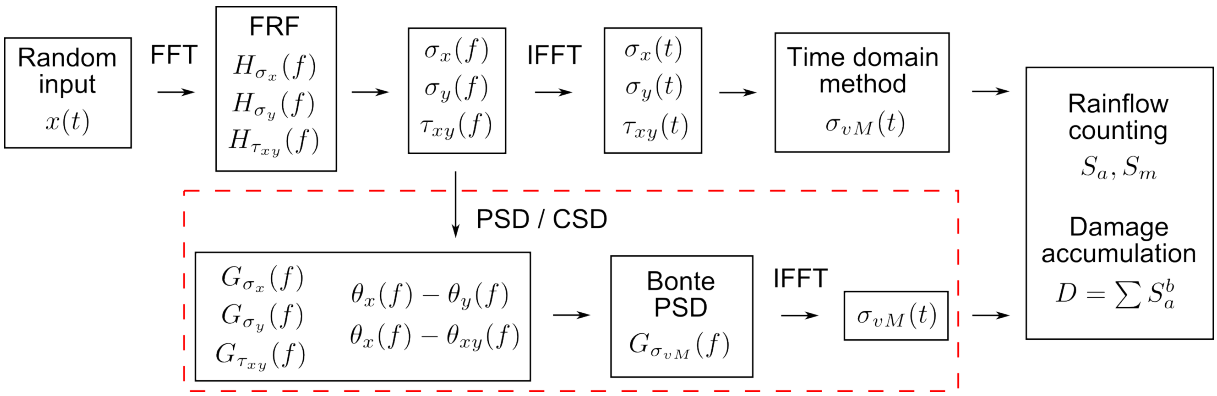

Figure 3.1: Flow chart of fatigue damage calculation using simulation

3.1.2 Effects of Sequential and Simultaneous Excitation

3.1.2.1 Frequency bandwidth

Simultaneous excitation goes basically hand in hand with the superimposition of several modes and thus interaction of the resulting stress cycles. In order to separate the effect of different cycle formation from multiaxial loading, an example using two independent SDOF systems is considered, as given in fig. (3.2).

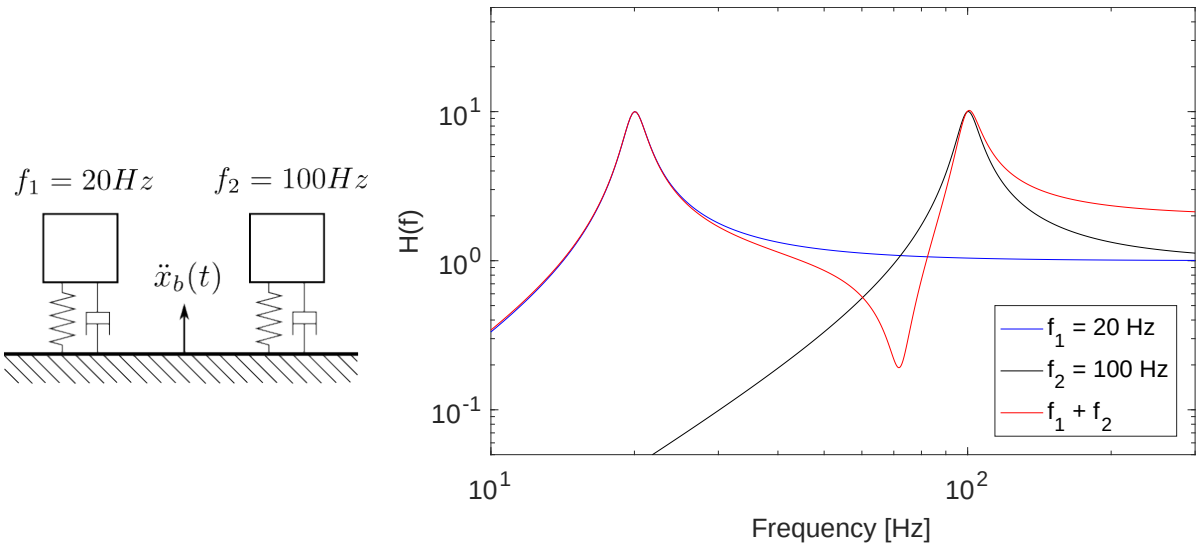

Figure 3.2: Exemplary narrowband and broadband relative displacement responses of two SDOF systems

Based on the relative displacement response time signals (200 min) caused by a random excitation with a flat displacement PSD (1 [mm²/Hz], $10 - 2000$ Hz), the uniaxial fatigue damage is then calculated for each SDOF system independently and for both SDOF systems superimposed, i.e. their response time signals are superimposed. The Rainflow counting is performed directly on the uniaxial relative displacement responses due to its equivalency to strain. Fig. (3.3) shows the typical difference between the cycles of a narrowband and broadband response. Due to the interactions between two frequencies resulting in amplitude and mean

values, broadband cycles contain more higher and less lower amplitudes than narrowband cycles.

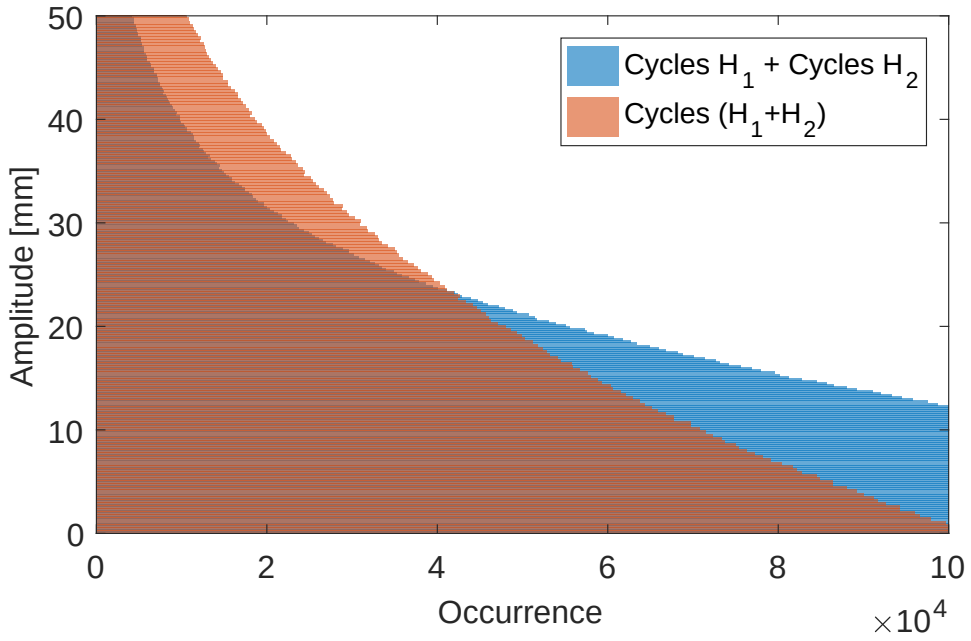

Figure 3.3: Hysteresis cycles for different excitation of the SDOF systems

The fatigue damage is given in fig. (3.4) for different slope values b. The broadband response yields the largest fatigue damage by nearly two orders of magnitude for $b = 13$. Summing up the fatigue damage values of each SDOF system is almost equal to the greater value of the two.

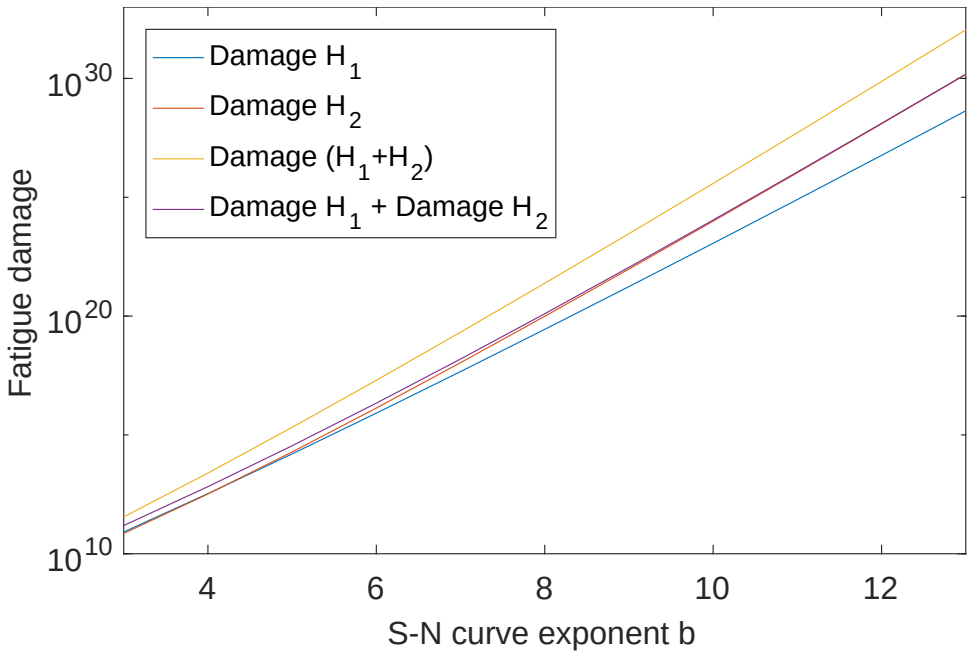

Figure 3.4: Fatigue damage values for different excitation of the SDOF systems

3.1.2.2 Excitation phase and different failure locations

To show the influence of the excitation phase on the fatigue damage, as well as on the respective failure locations, an example cantilever beam is introduced, given in fig. (3.5). It has a circular cross section with a radius of $r = 10$ mm and a length of $L = 500$ mm. An FEM steady state harmonic analysis is performed in order to obtain the stress FRFs from the respective locations 1, 2 and 3 at the clamped end. The beam is modelled with C3D20 volume elements to maintain generality through the subsequent analysis.

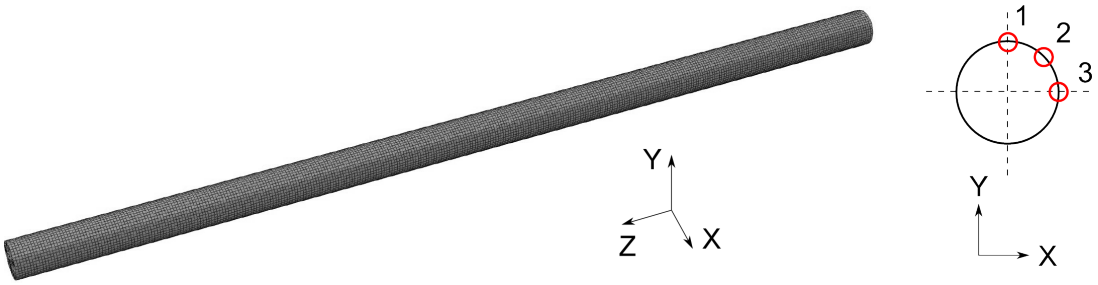

Figure 3.5: Simulated example beam

The results of a fatigue damage calculation according to the methodology previously shown in fig. (3.1) are given in fig. (3.6). Therefore, three different coherent excitation phase angles $\theta_{xy} = 0$ (in-phase excitation in positive x- and y-direction), $\pi/2$ ($90°$ phase shift), π (in-phase excitation in negative x- and positive y-direction) between the x- and y-axis are applied for the simultaneous excitation. In addition, a sequential excitation in x- and y-direction is performed for a comparison.

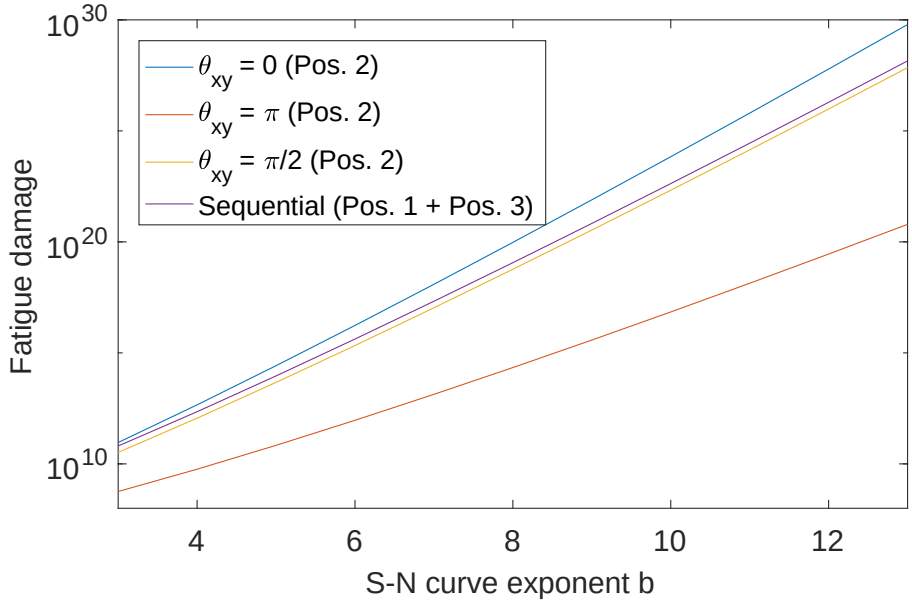

Figure 3.6: Fatigue damage values of example beam for simultaneous excitation with different phases and sequential excitation

It can be seen that the fatigue damage at position 2 has its largest value for an in-phase bending motion in its respective direction ($\theta_{xy} = 0$) and the lowest value for a perpendicular in-phase bending motion ($\theta_{xy} = \pi$). For a tumbling motion through an out-of-phase excitation ($\theta_{xy} = \pi/2$), the fatigue damage appears to be the same at every location due to the evenly distributed loading caused by the tumbling. Thus, it is half as much the summed value of a sequential excitation evaluated at positions 1 and 3, which are the respective hot spots of the uniaxial excitations. Thereby, its summation provides an artificial pseudo damage since two different locations are considered. The phase influence is distinct especially when two damaging modes are close to each other.

3.1.2.3 Coherence of excitation phase

The influence of the excitation coherence, which gives information about the stability of the phase, is investigated using the same beam. For all three phase values, coherences of $\gamma_{xy} = [0.01,\ 0.5,\ 0.99]$ are applied. Absolute values of 0 and 1 are not used to avoid numerical issues. Fig. (3.8) shows the result for the respective fatigue damage calculations at position 2. It can be seen that with lower coherence the phase information gets lost and the damage appears to be the same for each phase. Thereby, it ranges in the same dimension as the damage obtained from a coherent excitation with a phase shift of $\pi/2$ as previously shown in fig. (3.6). An example time signal (10 minutes divided in 3515 time windows) is used to show the distribution of the phase angles over the time windows used for calculation. Fig. (3.7) shows the actual phase angle occurrences when a phase angle of $\theta = 0$ rad with a coherence of $\gamma = 0.5$ is set.

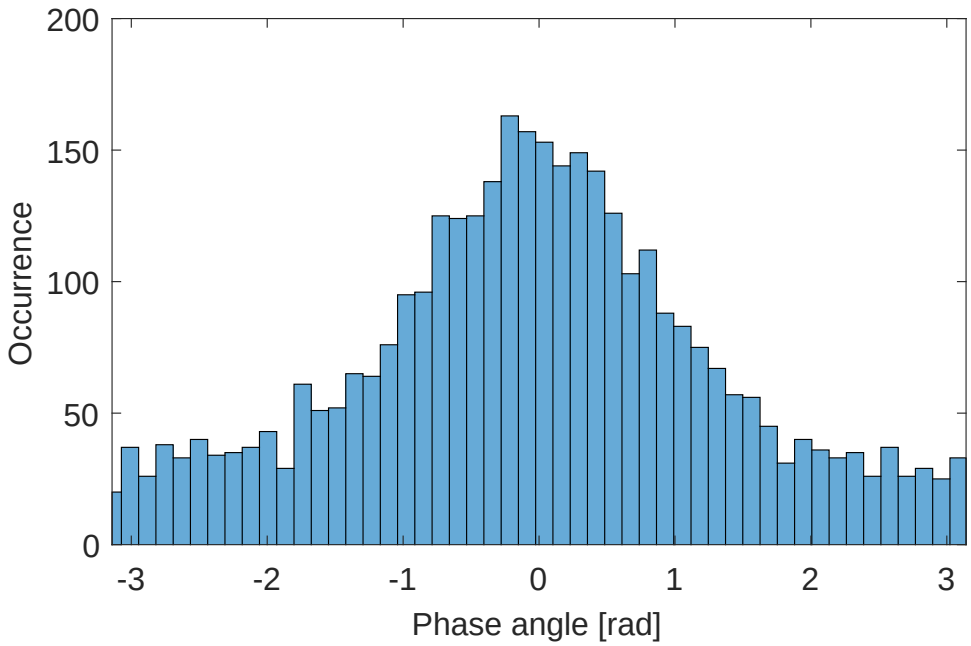

Figure 3.7: Phase distribution of white noise signals with a phase of $\theta = 0$ rad and a coherence of $\gamma = 0.5$ (time signal of 10 minutes, evaluated with 3515 time windows)

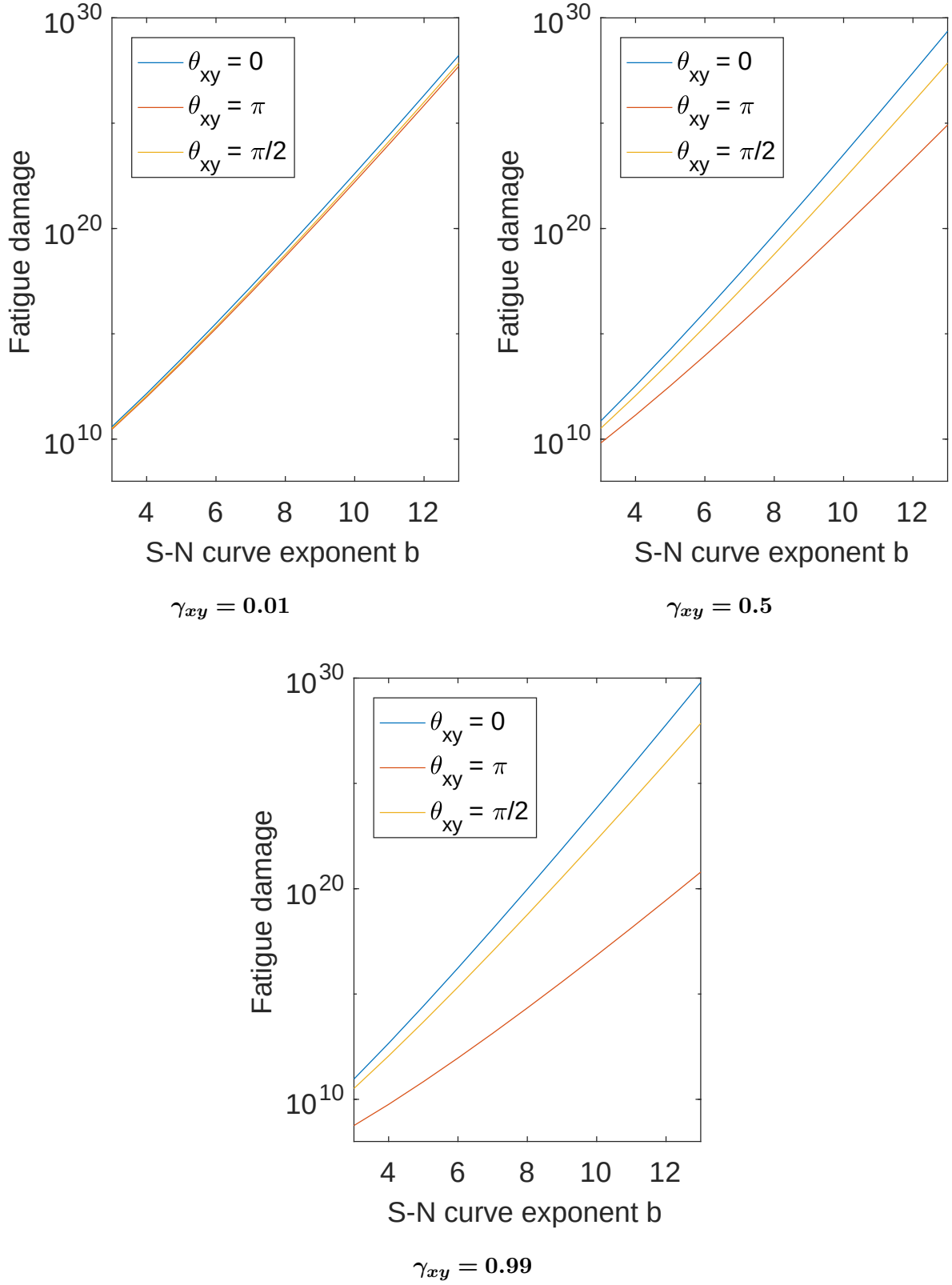

$\gamma_{xy} = 0.01$ $\gamma_{xy} = 0.5$

$\gamma_{xy} = 0.99$

Figure 3.8: Fatigue damage values of example beam for different excitation phases and coherences

So far, a multiaxial fatigue damage calculation methodology was introduced along different effects that occur with multiaxial loadings. As a next step, an appropriate measurement quantity apart from local stresses shall be elaborated.

3.2 Relationship Between Stresses and Different Vibrational Quantities

As stated in the introduction, strain gauge measurements should be avoided due to their complexity in application and the possible lack of accessibility which may occur for example at bolted mounting locations. In this section, an indicator is found that relates to fatigue damage which is in turn caused by local stresses. Thereby, it is sufficient to identify a scaled quantity carrying all necessary information about frequency, amplitude and phase. An analytic relationship between stress and velocity is the starting point of the theoretical investigation. Mechanical loads consist of both normal and shear stresses. For each stress component a particular relationship is formulated using simple structures such as rods and Euler-Bernoulli (EB) beams. Effects of transverse shear strain are thus neglected. Parts of this section, especially 3.2.1, 3.2.2 and 3.2.3.1, have been published previously in [38].

3.2.1 Translational Motion

The EB beam differential equation for a uniform beam with the deflection curve $w(x)$, the bending stiffness EI and the cross-sectional area A is known as

$$\frac{\partial^4 w(x,t)}{\partial x^4} = -\frac{\rho A}{EI}\,\frac{\partial^2 w(x,t)}{\partial t^2} \tag{3.1}$$

according to [53]. For the static case the deflection curve is expressed depending on the distributed load $q(x)$ with

$$w(x)EI = \int\int\int\int q(x)\mathrm{d}x^4 \tag{3.2}$$

which is illustrated in fig. (3.9).

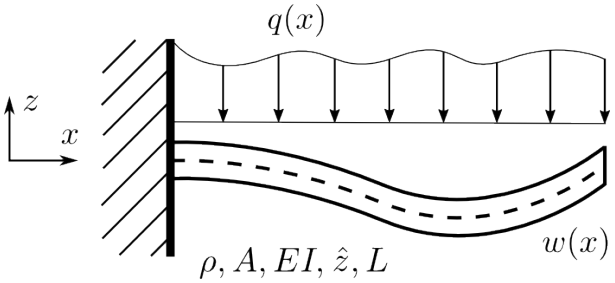

Figure 3.9: Euler-Bernoulli beam [38]

Deriving eq. (3.2) two times leads to the bending moment and thus to the normal stress with the area moment of inertia I and the distance to the neutral fiber $\hat{z}$, described as

$$\frac{\mathrm{d}^2 w(x)}{\mathrm{d}x^2}\,EI = \int\int q(x)\mathrm{d}x^2 = \frac{I}{\hat{z}}\,\sigma(x) \quad . \tag{3.3}$$

For a constant $q(x)$, the solution of the deflection curve is stated in eq. (3.4) with the constants of integration $\hat{C}_1$, $\hat{C}_2$, $\hat{C}_3$ and $\hat{C}_4$ which depend on the boundary conditions of the beam.

$$w(x)EI = \frac{qx^4}{24} + \hat{C}_1\frac{x^3}{6} + \hat{C}_2\frac{x^2}{2} + \hat{C}_3 x + \hat{C}_4 \tag{3.4}$$

The distributed load q is eliminated in order to obtain an equation for the maximum normal stress as a function of maximum deflection. Thereby, eq. (3.3) and (3.4) are solved for q, resulting in

$$\sigma_{max} = k_e \; w_{max} \; \frac{\hat{z}E}{L^2} \tag{3.5}$$

with the beam length L and the static factor k_e that depends on the distributed load and the boundary conditions. As an example, a constant $q(x)$ on a clamped-free configuration yields $k_e = 4$. In general, the position of the maximum deflection is not the same as of the maximum normal stress.

In a next step, the static description is extended to dynamic analyses. Equalizing the kinetic and the strain energy of the beam yields

$$\frac{1}{2EI}\int_0^L \left(EI\,\frac{\mathrm{d}^2 w(x)}{\mathrm{d}x^2}\right)^2 \mathrm{d}x = \frac{1}{2}\rho A \int_0^L \dot{w}^2(x)\mathrm{d}x \quad . \tag{3.6}$$

The time derivative of the deflection curve $\dot{w}$ can be described as

$$\dot{w}(x) = v(x) = \sum_i^{\tilde{m}} \omega_i \; w_i(x) \tag{3.7}$$

using the assumption of a harmonic oscillation, where ω_i is the i-th circular eigenfrequency out of $\tilde{m}$ modes and $w_i(x)$ its corresponding eigenform. The superposition of all eigenforms yields the total deflection curve. Solving eq. (3.6) for a single ω then yields

$$\omega = k_\omega \; \frac{1}{L^2} \; \sqrt{\frac{EI}{\rho A}} \tag{3.8}$$

with the dynamic factor k_ω defined as

$$k_\omega = L^2 \sqrt{\frac{\int_0^L \left(\frac{\mathrm{d}^2 w(x)}{\mathrm{d}x^2}\right)^2 \mathrm{d}x}{\int_0^L w^2(x)\;\mathrm{d}x}} \quad . \tag{3.9}$$

Eq. (3.8) and (3.9) can only be formulated for each eigenfrequency independently. The final relationship between maximum stress and maximum velocity is obtained by combining eq. (3.5), (3.7) and (3.8), yielding

$$\sigma_{max} = \frac{k_e}{k_\omega} \; \hat{z} \; \sqrt{\frac{\rho A E}{I}} \; v_{max} = k_\sigma \; v_{max} \quad . \tag{3.10}$$

The factor of proportionality is thereby labelled as k_σ. The equation describes a relation to the maximum occurring stress which may serve as a base for fatigue damage calculation. Eq. (3.10) is valid for each eigenfrequency. The location of w_{max} is logically equal to the location of v_{max}. Evaluating the EB beam differential eq. (3.1) shows that k_e/ω and thus k_e/k_ω are nearly

constant for each eigenfrequency. For a hinged-hinged configuration the assumption of the modeshape $w(x)$ being a sine wave can be made which leads to the obviously valid statement

$$\frac{\left(\frac{\mathrm{d}^2 w(x)}{\mathrm{d}x^2}\right)_{max}}{(w(x))_{max}} = \frac{\sqrt{\int \left(\frac{\mathrm{d}^2 w(x)}{\mathrm{d}x^2}\right)^2 \mathrm{d}x}}{\sqrt{\int w^2(x)\,\mathrm{d}x}} \quad . \tag{3.11}$$

In principle, the relation between k_e and k_ω is comparable. Eq. (3.11) shows the special case of a sinusoidal shape and is therefore not valid in general, nonetheless the deviation for other boundary conditions is still constant for each eigenfrequency. Table (3.2) shows the approximate values of k_e/k_ω for different boundary conditions which are similar to the ones obtained in [89]. For the hinged-hinged configuration, the waveform has exactly the shape of a sinusoid and thus an expected factor of $k_e/k_\omega = 1$.

Table 3.2: Factors for different boundary conditions

Boundary condition	k_e/k_ω
Clamped-free	1.00
Hinged-free	0.76
Clamped-clamped	$1/0.76$
Hinged-hinged	1.00
Clamped-hinged	$1/0.76$

The other two vibrational quantities acceleration and displacement can now be derived from eq. (3.10). The maximum acceleration is obtained by $a_{max} = v_{max}\ \omega$ and the maximum displacement by $w_{max} = v_{max}/\omega$ using the same assumption of a harmonic oscillation.
Apart from transversal motion, the derivation for longitudinal motion was accomplished in [21] based on the differential equation of a longitudinal vibrating rod. The relationship between maximum longitudinal velocity and maximum normal stress is given as

$$\sigma_{max} = \sqrt{\rho E}\ v_{max} = k_{\sigma,lon}\ v_{max} \quad . \tag{3.12}$$

3.2.2 Rotational Motion

A similar relationship is derived for the rotational motion using a torsional element as illustrated in fig. (3.10). The torsional eigenforms have the same characteristics as the longitudinal ones. The differential equation is given in [53] as

$$\frac{\partial^2 \phi(x,t)}{\partial x^2} = \frac{\rho I_p}{G I_t}\ \frac{\partial^2 \phi(x,t)}{\partial t^2} \tag{3.13}$$

with the torsion angle $\phi(x)$, the torsional stiffness GI_t and the polar area moment of inertia I_p. For circular cross sections the polar area moment of inertia is equal to the torsional constant I_t. As indicated above, the differential equation is similar for the longitudinal vibrating rod. Analogue to eq. (3.2) and (3.3), the deflection curve for the static case can be expressed as

$$\phi(x) G I_t = \int \int -m_t(x) \mathrm{d}x^2 \quad . \tag{3.14}$$

The equation for the torsional resistance moment W_t and the torsional shear stress τ_t can be derived as

$$\frac{\mathrm{d}\phi(x)}{\mathrm{d}x}\, GI_t = \int -m_t(x)\mathrm{d}x = W_t\, \tau_t(x) \tag{3.15}$$

with the distributed moment $m_t(x)$.

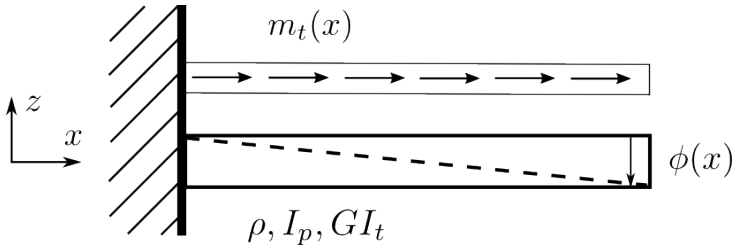

Figure 3.10: Torsion rod [38]

Eliminating the distributed moment yields the maximum torsional shear stress expressed with the maximum angle of twist

$$\tau_{t,max} = k_{e,\phi}\, \phi_{max}\, \frac{GI_t}{W_t L} \tag{3.16}$$

including the static factor for torsion $k_{e,\phi}$, analogue to the static factor obtained for bending. Again, kinetic and strain energy are equalized as

$$\frac{1}{2GI_t} \int_0^L \left(GI_t\, \frac{\mathrm{d}\phi(x)}{\mathrm{d}x} \right)^2 \mathrm{d}x = \frac{1}{2}\omega^2 \int_0^L J\phi^2(x)\mathrm{d}x \tag{3.17}$$

with the moment of inertia J that is constant over the entire rod. The resulting equation for ω is given as

$$\omega = k_{\omega,\phi}\, \sqrt{\frac{GI_t}{JL}} \tag{3.18}$$

and for the dynamic factor for torsion $k_{\omega,\phi}$ as

$$k_{\omega,\phi} = L \sqrt{\frac{\int_0^L \left(\frac{\mathrm{d}\phi(x)}{\mathrm{d}x} \right)^2 \mathrm{d}x}{\int_0^L \phi^2(x)\, \mathrm{d}x}} \tag{3.19}$$

The final relationship between maximum torsional shear stress and maximum angular velocity can be obtained using eq. (3.16), (3.17) and the assumption of a harmonic oscillation $\dot{\phi}_{max} = \omega\, \phi_{max}$, described as

$$\tau_{t,max} = \frac{k_{e,\phi}}{k_{\omega,\phi}}\, \sqrt{\frac{JGI_t}{{W_t}^2 L}}\, \dot{\phi}_{max} \quad . \tag{3.20}$$

The angular velocity can be expressed as $\dot{\phi}_{max} = v_{rot,max}/r$ and the entire factor of proportionality can be labelled as k_τ which yields

$$\tau_{t,max} = \frac{k_{e,\phi}}{k_{\omega,\phi}} \sqrt{\frac{JGI_t}{{W_t}^2 Lr^2}}\, v_{rot,max} = k_\tau\, v_{rot,max} \quad . \tag{3.21}$$

Evaluating the differential equation of a constant rod formulated in eq. (3.13) yields $k_{e,\phi}/k_{\omega,\phi} = 1$ for all configurations which simplifies eq. (3.20) to

$$\tau_{t,max} = \sqrt{\frac{JGI_t}{{W_t}^2 Lr^2}}\, v_{rot,max} \quad . \tag{3.22}$$

The relation to angular acceleration and displacement can be found by applying a factor of ω, as previously described in 3.2.1.

3.2.3 Evaluation of Different Vibrational Quantities

3.2.3.1 Maximum positions

In order to verify the analytic expressions found for the different vibrational quantities, the cantilever beam of the previous section (see fig. (3.5)) is used for an FEM simulation. Its clamped-free configuration ensures the same position of maximum velocity for each frequency. Acceleration, velocity and displacement are measured at the tip while the stress is obtained near the clamped end, as shown in fig. (3.11).

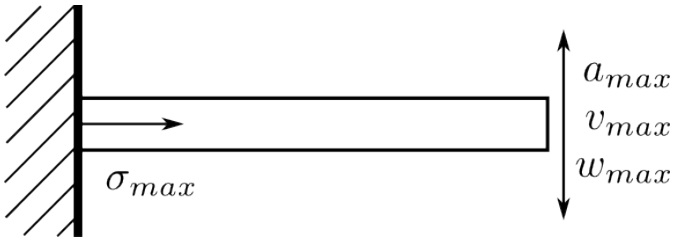

Figure 3.11: Maximum positions on the cantilever beam [38]

Fig. (3.12) shows the normalized absolute values of the respective FRFs of a uniform acceleration excitation for translational motion. The corresponding FRFs for rotational motion are given in fig. (A1) within the appendix. The best match is detected between stress and velocity which verifies the analytically derived relationships in the subsections 3.2.1 and 3.2.2. However, the relationship is only valid for the absolute values and only at the eigenfrequencies. As shown in fig. (3.13), the phase values do not match at the eigenfrequencies and are shifted by $\pm\pi/2$. However, the first bending modes in each direction and the first torsional mode which are usually most severe are of the same phase shift. The same consideration can be made for configurations other than clamped-free, where the velocity measurement should be performed at the estimated position of the first eigenfrequency's antinode. The theoretical case of higher eigenmodes of a complex structure where the predicted hot spot is facing more motion than the actual measurement position can also not be covered sufficiently. However, this is only a theoretical consideration and usually not the case for real technical systems, as well as of little damage contribution. Within the scope of this thesis, fatigue damage caused by resonant vibration is considered which serves as legitimation to further process with the investigation on

the stress-velocity relationship. Furthermore, acceleration and displacement differ by a factor of frequency which inevitably leads to an over- or underestimation of the fatigue damage.

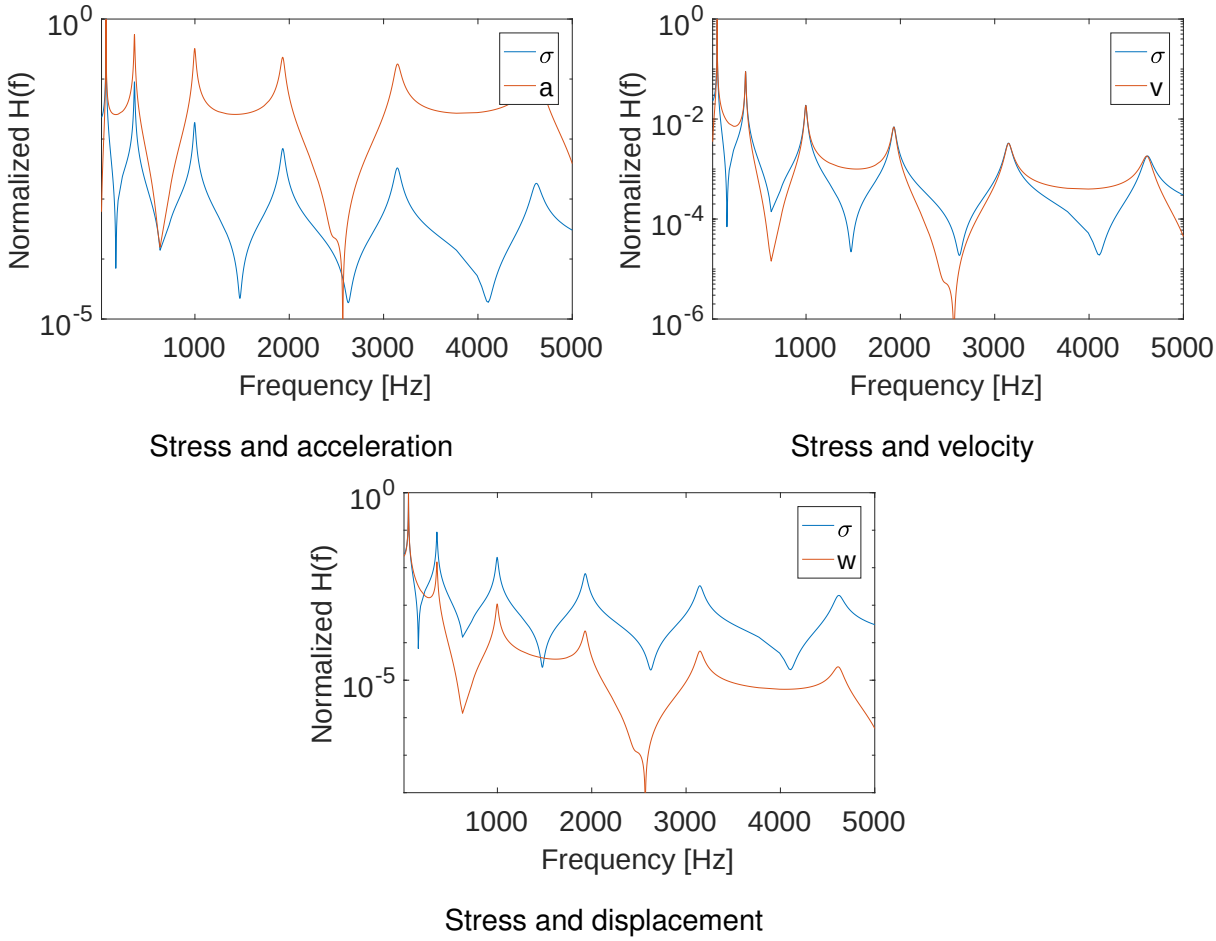

Figure 3.12: Frequency responses of normalized stress and different vibrational quantities at maximum positions

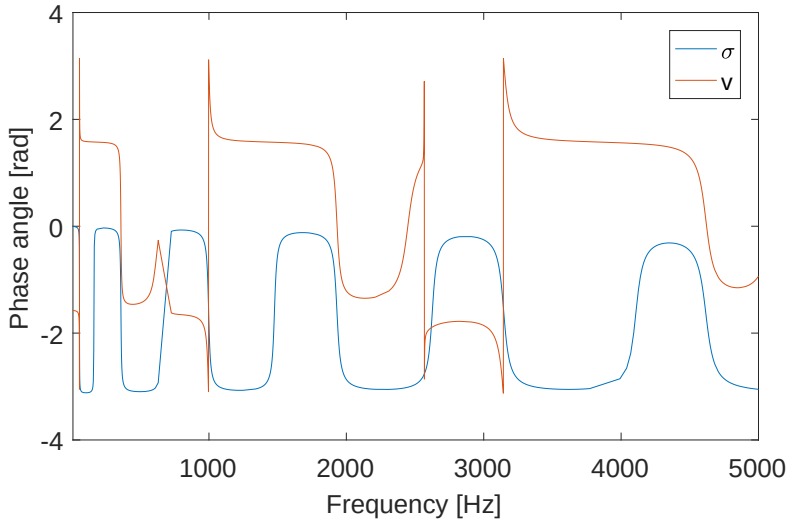

Figure 3.13: Stress and velocity response phases

3.2.3.2 Same positions

Beyond the maximum value positions, the relationship between stress and velocity also holds at the so-called farfield regions, as described in [37]. On these regions, the normal stress can be directly obtained from the velocity at the same position, as illustrated in fig. (3.14). The phase shift has the same value of $\pi/2$ for each eigenfrequency as shown in fig. (3.16).
A similar relationship can be detected between normal stress in direction of motion and acceleration near the free end, and between stress and displacement near the clamped end, as shown in fig. (3.15). The first relationship can be explained by a high influence of the inertia at the free end where the normal stress is nearly zero and only caused by acceleration. The second one is due to the high influence of stiffness and the similarity between displacement and strain at the clamped end. This quantity can only be measured with strain gauges and access to the respective location.

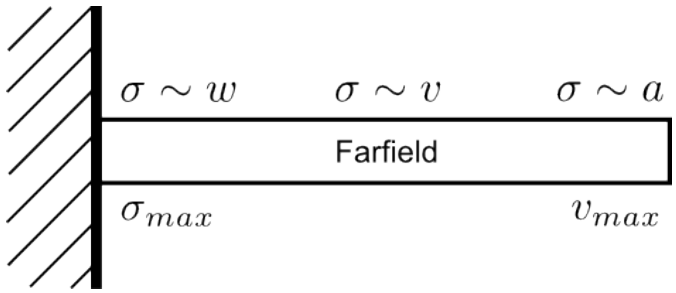

Figure 3.14: Evaluation positions on the cantilever beam

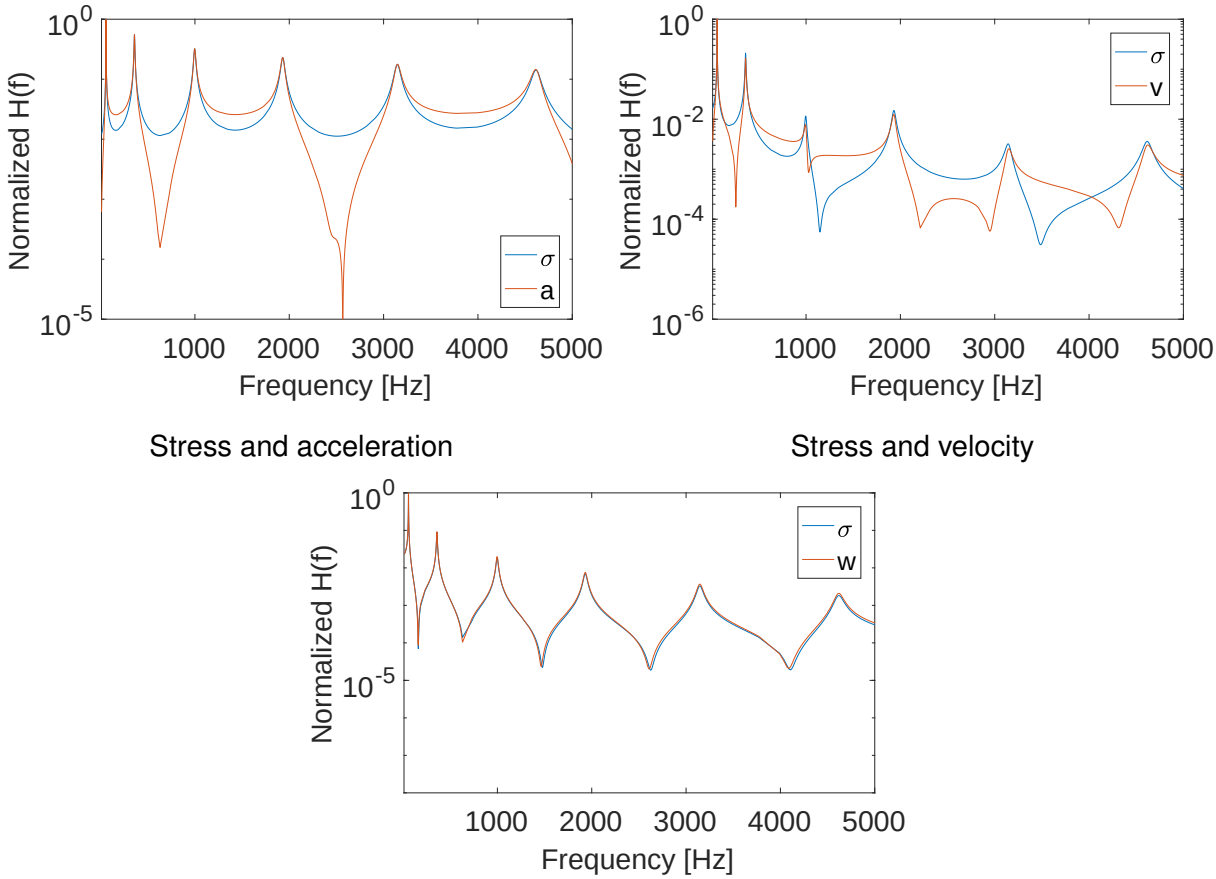

Figure 3.15: Frequency responses of normalized stress and different vibrational quantities obtained at the same locations

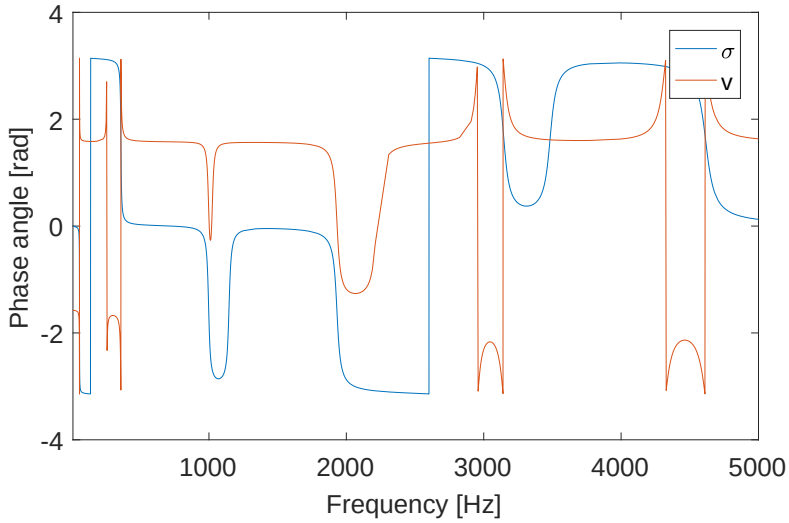

Figure 3.16: Stress and velocity response phases in farfield region

The constant phase shift can be removed in order to replicate the stress time signals accurately. In order to provide phase information to a real-valued time signal, a Hilbert transformation as described in [18] is applied. It is defined as

$$\mathcal{H}(x(t)) = \frac{1}{\pi} \int_{-\infty}^{\infty} \frac{x(\hat{\tau})}{t - \hat{\tau}} \, \mathrm{d}\hat{\tau} \quad . \tag{3.23}$$

Then, an analytic signal representation of the original time signal $\hat{h}(t)$ is used where its imaginary part is the Hilbert transformed of the real part. It is described as

$$\hat{h}(t) = x(t) + j\mathcal{H}(x(t)) \quad . \tag{3.24}$$

The analytic signal can be brought in an amplitude-phase form, where the phase $\angle\hat{h}(t)$ is manipulable. Then, a constant phase shift of $\pi/2$ is applied which yields $\tilde{h}(t)$, described as

$$\tilde{h}(t) = |\hat{h}(t)| \cos\left(\angle\hat{h}(t) + \frac{\pi}{2}\right) \quad . \tag{3.25}$$

Eq. (3.25) is applied on a velocity signal generated from the FRF shown in fig. (3.15). The normalized stress and the Hilbert transformed and phase shifted velocity signal v^* are shown in fig. (3.17). Depending on the accuracy of the farfield localization, the normal stress signal can be sufficiently replicated from the velocity signal.

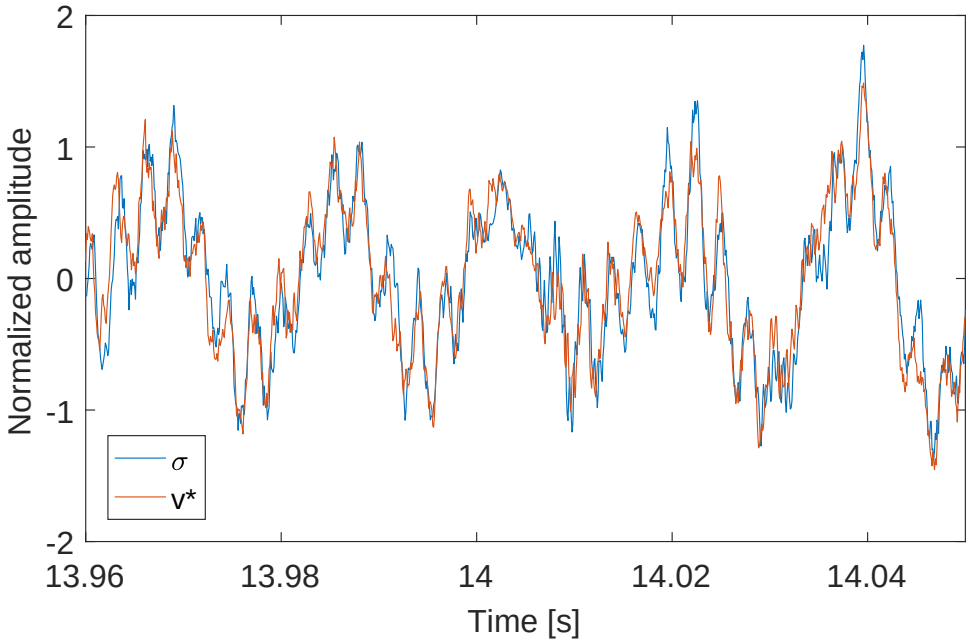

Figure 3.17: Stress and phase shifted velocity time signal v^*

However, the normal stress obtained at the farfield location is not equal to the maximum stress in the beam and the amplitude proportions of the eigenfrequencies are generally different. Therefore, this approach is not useful for a general fatigue damage evaluation methodology.

3.3 Fatigue Damage Evaluation Using Velocities

To perform a fatigue damage evaluation based on velocities, the respective components first have to be combined in a meaningful way through reasonable geometric factors. After the relative weighting they can be incorporated into an equivalent stress formulation to obtain a fatigue damage related quantity. Parts of this section have been published previously in [38].

3.3.1 Combination of Velocity Components

For the application of geometric factors only transversal and rotational velocities are considered. The damaging effect of longitudinal motion can usually be neglected for most real applications. The geometric term within the factor of proportionality k_σ for transversal motion is referred to as geometric factor $K = \sqrt{\frac{A\hat{z}^2}{I}}$. For each bending direction another factor of proportionality can be calculated. In case of uniform cross sections, like rectangular or circular beams, the values for $\hat{z}$ and the square root of the reciprocal radius of gyration I/A compensate each other and the factor K always remains constant. For a rectangular shape it is $K = \sqrt{3}$ and for a round shape $K = 2$. For complex equipment a geometrical factor of 4 to 8 is proposed in [65], probably justified by the largest possible geometric factor which is obtained from a constant triangular cross section with $K = 2\sqrt{2}$ times a factor of three. The factor of three might be derived assuming a three-sigma limit of a normal distribution.
According to the proposed values, a maximum deviation by a factor of 2 is considered. The possible influence on the resulting fatigue damage is investigated using an H-section cantilever beam, shown in fig. (3.18). The H-section is designed respectively, resulting in a proportion of $k_{\sigma,x}/k_{\sigma,y} = 3.05/1.45 \approx 2$ which is equivalent to a structure with $K = 4$ and $K = 8$ for different directions. It has a height and width of 20 mm and a length of 500 mm. A FEM simulation yields the FRF for normal stresses and transversal velocities with the eigenmodes alternating between both bending directions x and y. Thereby, $k_{\sigma,x} = k_{\sigma,y}$ is used to obtain the maximum error as can be seen in fig. (3.18). Every second peak amplitude has a deviation of roughly 50%. A uniaxial fatigue damage calculation is performed according to the methodology explained in subsection 3.1.1 using only normal stress and the sum of both translational velocities $k_{\sigma,x}v_x + k_{\sigma,y}v_y$. Both generated stress and velocity white noise response time signals are normalized with respect to the RMS value of their PSD to be comparable. Table (3.3) shows the ratio D_v/D_σ for different slope values of the S-N curve. The phase difference between some higher eigenfrequencies have a neglectable influence on the results. The deviations are of a maximum value of 1.12 which is absolutely acceptable within the scope of fatigue calculation. However, this investigation only addressed beams with a constant cross section.

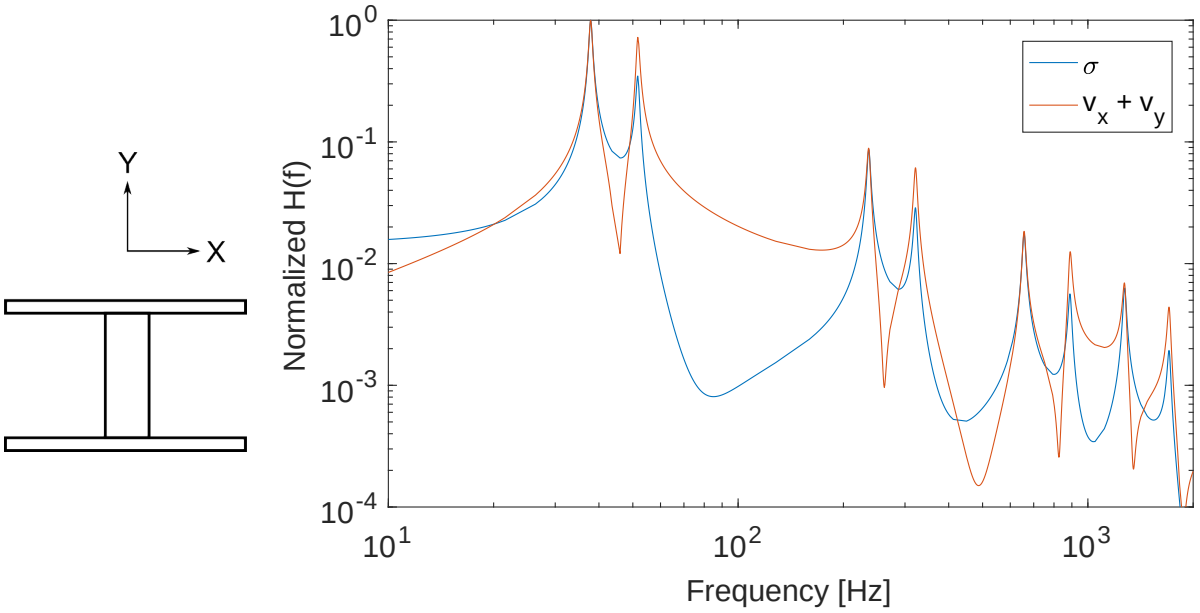

Figure 3.18: Normalized frequency responses of normal stress and translational velocities of an exemplary H-section beam, assuming $k_{\sigma,x} = k_{\sigma,y}$

b	3	4	5	6	7	8	9	10	11	12	13
D_v/D_σ	0.95	0.97	0.99	1.00	1.02	1.03	1.05	1.07	1.09	1.10	1.12

Table 3.3: Deviation of the fatigue damage values for an H-section

In order to determine a rough proportion between the factors for normal stress and torsional shear stress, equal transversal factors of proportionality $k_\sigma = k_{\sigma,x} = k_{\sigma,y} = k_{\sigma,z}$ are assumed. For beams with a constant circular cross section it is

$$\frac{k_\sigma}{k_\tau} = \frac{k_e}{k_\omega} \sqrt{\frac{\frac{\rho A E \hat{z}^2}{I}}{\frac{JGI_t}{{W_t}^2 L r^2}}} \quad . \tag{3.26}$$

Thereby, the values for $\hat{z}$ and the radius r are equal. In case of ideal elastic, isotropic and metallic material, a Poisson's ratio[1] of $\nu = 0.3$ can be used. Then, a value of $k_\sigma/k_\tau = 3.225$ is obtained for a clamped-free configuration and $k_\sigma/k_\tau = 4.2$ for a clamped-clamped configuration. These results show similarities with investigations on pipe structures in [19]. In case of rectangular cross sections, I_T and W_T are calculated numerically yielding values of $k_\sigma/k_\tau = 1.9 - 2.7$ for ratios of height to width of 1 to 10. However, circular cross sections are emphasized since the severity of their torsional modes is much larger than for rectangular ones. As a conservative approach, both maximum normal and torsional shear stress are assumed to have the same location. The proposed value of $k_\sigma/k_\tau = 3.225$ is verified with the FE beam model given in fig. (3.5) resulting in the FRFs shown in fig. (3.19). For both transversal and torsional modes the FRFs are in a close match. Absolute values are used due to the phase shift of the different components.

[1] Used for the relation $E = 2G(1 + \nu)$ introduced in section 2.2.1

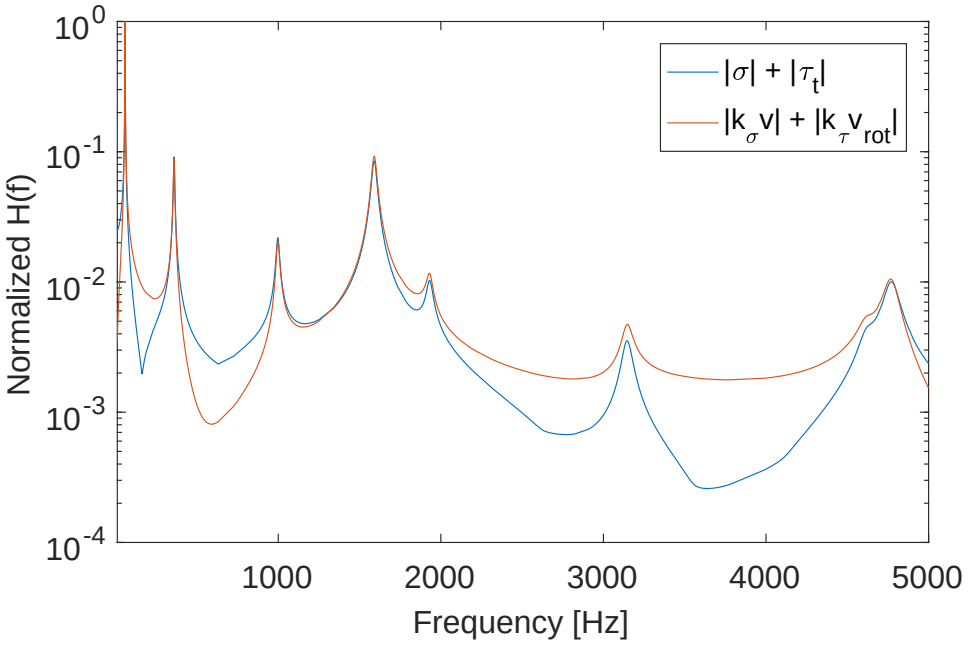

Figure 3.19: Normalized frequency response of sum of normal and torsional shear stress, respectively velocity and rotational velocity

The same considerations can also be made for the ratio of transversal and longitudinal velocities resulting in $k_\sigma/k_{\sigma,\mathrm{lon}} = 2$ for a circular beam in a clamped-free configuration which is not relevant for further engineering. If no information about the geometry is available, an overall standard value of $k_\sigma/k_\tau = 3$ is proposed for clamped-free configurations and $k_\sigma/k_\tau = 4$ for clamped-clamped configurations. Further investigations on geometric factors for non-uniform structures are performed in the next subsection 3.3.2.

3.3.2 Composition of an Equivalent Stress out of Velocities

As equivalent stress, again the Bonte PSD from eq. (2.70) is considered as discussed in subsection 3.1.1. Its main advantage is the correct processing of out-of-phase components, such as transversal and rotational velocities. For the subsequent formulation, the x-axis is defined as the longitudinal direction of the beam and the y-, respectively z-axis as the cross axis directions. The coupling through lateral contraction leads to the assumption of a rough proportionality between the normal stresses $\sigma_x \sim \sigma_y \sim \sigma_z$ which can be confirmed by simple beam simulations. Thus, eq. (2.70) becomes

$$\begin{aligned} G_{\sigma_{vM}} = 0.5 \left(G_{\sigma_x} \left[1 + \frac{G_{\sigma_y}}{G_{\sigma_x}} - \sqrt{\frac{G_{\sigma_y}}{G_{\sigma_x}}} \cos(\theta_x - \theta_y) \right] + 3 G_{\tau_{xy}} \right) + 0.5 \ \mathrm{abs} \\ \left(G_{\sigma_x} \left[1 + \frac{G_{\sigma_y}}{G_{\sigma_x}} \, e^{2j(\theta_y - \theta_x)} - \sqrt{\frac{G_{\sigma_y}}{G_{\sigma_x}}} \, e^{j(\theta_y - \theta_x)} \right] + 3 G_{\tau_{xy}} e^{2j(\theta_{xy} - \theta_x)} \right) \quad . \end{aligned} \tag{3.27}$$

Based on the assumption of slender beams, a dominating normal stress $\sigma_x \gg \sigma_y$, respectively $\sigma_x \gg \sigma_z$ is settled. Then, the term in squared brackets in eq. (3.27) becomes 1 which yields

$$G_{\sigma_{vM}} = 0.5 \left(G_{\sigma_x} + 3 G_{\tau_{xy}} \right) + 0.5 \ \mathrm{abs} \left(G_{\sigma_x} + 3 G_{\tau_{xy}} e^{2j(\theta_{xy} - \theta_x)} \right) \quad . \tag{3.28}$$

All three transversal velocities contribute to the same axial normal stress σ_x as derived in the previous section. Thus, it is $\sigma_x \approx k_{\sigma,x}v_x + k_{\sigma,y}v_y + k_{\sigma,z}v_z$ to cover for all possibilities which is a valid statement considering the assumed proportionality of the stress components. Furthermore, during vibration all kinetic energy stored in velocity is transformed into potential energy stored as stress. It can be argued that stress caused by contraction is also included in the velocity. Considering shear stress, a relationship between torsional shear stress and rotational velocities was derived. Shear stress induced by shear force cannot be reasonably represented by an oscillation. Based on the slender beam theory its contribution is neglected. Thus it is $\tau_{xy} = \tau_t$ which is incorporated into eq. (3.28) together with the assumptions above, yielding

$$G_{\sigma_{vM}} = 0.5\,(G_{kv} + 3G_{kv_{rot}}) \;+\; 0.5\,\mathrm{abs}\left(G_{kv} + 3G_{kv_{rot}}e^{2j(\theta_v - \theta_{v_{rot}})}\right) \quad . \tag{3.29}$$

Thereby, the normal stress proportional PSD G_{kv} is calculated from $k_{\sigma,x}v_x(t) + k_{\sigma,y}v_y(t) + k_{\sigma,z}v_z(t)$ and the torsional shear stress proportional PSD $G_{kv_{rot}}$ from $k_\tau v_{rot}(t)$. Considering the standard factor of $k_\sigma/k_\tau = 3$ proposed in section 3.3.1, eq. (3.29) is simplified to

$$\begin{aligned} G_{\sigma_{vM}} &= 0.5\,k_\sigma^2\left(G_v + \frac{1}{3}G_{v_{rot}}\right) \;+ \\ &0.5\,k_\sigma^2\,\mathrm{abs}\left(G_v + \frac{1}{3}G_{v_{rot}}e^{2j(\theta_v - \theta_{v_{rot}})}\right) \end{aligned} \tag{3.30}$$

where the transversal velocity PSD G_v is calculated from $v_x(t) + v_y(t) + v_z(t)$ and the rotational velocity PSD $G_{v_{rot}}$ from $v_{rot}(t)$. Based on a few assumptions and basically the summation of velocities, the derived equivalent stress formulation eq. (3.30) yields good estimations for real structures, as evaluated in [38]. The new fatigue damage calculation procedure is illustrated in fig. (3.20). The velocities can also be applied to any other equivalent stress formulations in the same manner.

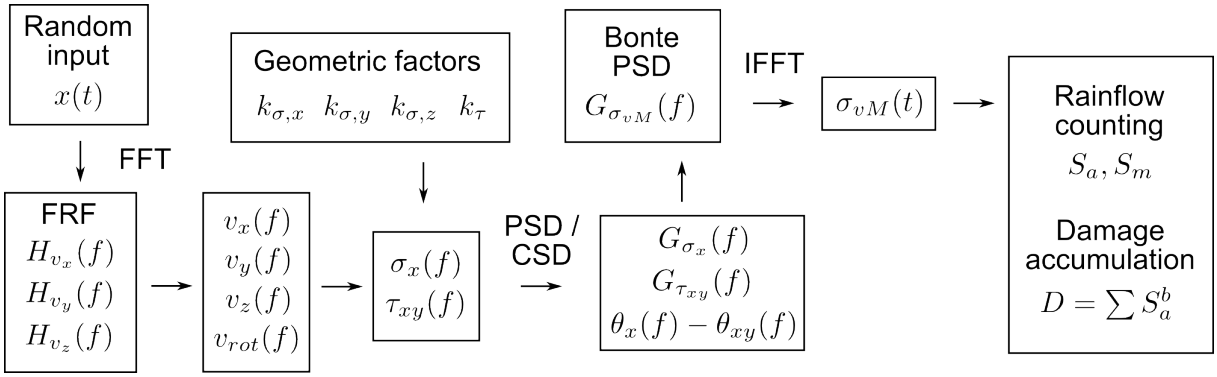

Figure 3.20: Flow chart of fatigue damage calculation using velocities from a simulation model

For a relative damage comparison of two different environments, the factor of k_σ^2 in eq. (3.30) can be removed. The fatigue damage calculation then results in an artificial pseudo damage. The linear damage accumulation according to the original Miner rule is the only meaningful approach using velocities directly, since the contribution of velocity amplitudes to either the HCF or the UHCF range is usually unknown. In cases where a mean stress contribution is

to be considered, it is questionable to perform reasonable mean stress corrections directly on velocity signals.

3.4 Geometry Influence on the Stress-Velocity Relationship

In this section, the investigation on the geometric factors of the stress-velocity relationship is extended to non-constant cross sections. Thereby, the analytical derivation in the subsections 3.2.1 and 3.2.2 is repeated accordingly. A procedure for obtaining factors from FE models is presented. Furthermore, a FE model simplification is proposed for the estimation of the respective factors using different examples. Parts of this section have been published previously in [40].

3.4.1 Non-Constant Cross Sections

3.4.1.1 Translational motion

According to [69], the EB beam differential equation for a non-uniform beam is known as

$$\frac{\partial^2}{\partial x^2}\left(EI(x)\frac{\partial^2 w(x,t)}{\partial x^2}\right) = -\rho A(x)\,\frac{\partial^2 w(x,t)}{\partial t^2} \tag{3.31}$$

with the deflection curve $w(x)$. The left hand side of eq. (3.31) represents the potential energy while the right hand side represents the kinetic energy. The deflection curve is expressed as

$$w(x) = x^{-\tilde{n}/2}\left(\hat{C}_1\hat{J}_{\tilde{n}}(\lambda\sqrt{x}) + \hat{C}_2\hat{Y}_{\tilde{n}}(\lambda\sqrt{x}) + \hat{C}_3\hat{I}_{\tilde{n}}(\lambda\sqrt{x}) + \hat{C}_4\hat{K}_{\tilde{n}}(\lambda\sqrt{x})\right) \tag{3.32}$$

using the Bessel function of the first kind $J_{\tilde{n}}$, the modified Bessel function of the first kind $I_{\tilde{n}}$, the Bessel function of the second kind $Y_{\tilde{n}}$, the modified Bessel function of the second kind $K_{\tilde{n}}$, the constants of integration C_1, C_2, C_3 and C_4, the eigenvalue λ and the index of the beam section variation $\tilde{n}$. A circular cone is expressed with $\tilde{n} = 2$ due to the quadratic variation of the cross section. The relationship of the eigenvalue λ to the circular eigenfrequency ω is given as

$$\lambda^4 = \frac{16\rho A_L \omega^2 L^2}{EI_L} \tag{3.33}$$

where A_L and I_L are obtained at the position $x = L$, according to [69]. As performed in subsection 3.2.1, a static consideration is done at first. The static relationship for the maximum normal stress is similar to eq. (3.5) except a varying distance to the neutral fiber $\hat{z}_{\sigma_{max}}$ which depends on the location of maximum normal stress. It is

$$\sigma_{max} = k_e\, w_{max}\,\frac{\hat{z}_{\sigma_{max}} E}{L^2}\quad . \tag{3.34}$$

Again, the kinetic and strain energy are equalized using eq. (3.31) and the assumption of a harmonic oscillation which yields

$$\frac{E}{2}\int_0^L I(x)\left(\frac{\mathrm{d}^2 w(x)}{\mathrm{d}x^2}\right)^2 \mathrm{d}x = \frac{1}{2}\rho\omega^2\int_0^L A(x)w^2(x)\mathrm{d}x\quad . \tag{3.35}$$

Solving eq. (3.35) for ω yields

$$\omega = k_\omega \, \frac{1}{L} \sqrt{\frac{E}{\rho}} \tag{3.36}$$

expressed with the dimensionless dynamic factor k_ω which is described as

$$k_\omega = L \, \sqrt{\frac{\int_0^L I(x) \left(\frac{\mathrm{d}^2 w(x)}{\mathrm{d}x^2} \right)^2 \mathrm{d}x}{\int_0^L A(x) w^2(x) \, \mathrm{d}x}} \tag{3.37}$$

including the terms $I(x)$ and $A(x)$. The final relationship between maximum stress and velocity from eq. (3.10) extended for non-constant cross sections can then be stated as

$$\sigma_{max} = \frac{k_e}{k_\omega} \, \sqrt{\rho E} \, \frac{1}{L} \, \hat{z}_{\sigma_{max}} \, v_{max} \quad . \tag{3.38}$$

The information of $A(x)$ and $I(x)$ is now included in the term $\frac{k_e}{k_\omega}$.
The same derivation can be made for longitudinal motion using the solutions of [1] and [49]. However, due to its neglectable influence on fatigue damage it is not considered further. Parts of this subsection have been investigated in [96].

3.4.1.2 Rotational motion

Using a non-constant torsional rod for the rotational motion, its differential equation can be described according to [67] as

$$\frac{\partial}{\partial x} \left(G I_t(x) \frac{\partial \phi(x,t)}{\partial x} \right) = \rho I_p(x) \, \frac{\partial^2 \phi(x,t)}{\partial t^2} \tag{3.39}$$

with the polar area moment of inertia I_p and the torsional constant I_t. The left hand side of eq. (3.39) represents the potential energy while the right hand side represents the kinetic energy. Again, Bessel functions are used to describe the torsion angle line $\phi(x)$ which yields

$$\phi(x) = \left(\hat{E} + x/L \right)^{-\hat{\nu}} \hat{Z}_{\hat{\nu}}(\hat{X}) \tag{3.40}$$

with a geometric constant $\hat{E}$, a linear combination of Bessel functions $\hat{Z}_{\hat{\nu}}$, the equation order $\hat{\nu}$ and an eigenfrequency-dependent function X. Further explanations of the respective terms can be found in [67].
The static relationship for $\tau_{t,max}$ is similar to eq. (3.16) except a varying torsional resistance moment $W_{t,\tau_{max}}$ and torsional constant $I_{t,\tau_{max}}$ which depend on the location of maximum torsional shear stress. Then, it is

$$\tau_{t,max} = k_{e,\phi} \, \phi_{max} \, \frac{G I_{t,\tau_{max}}}{L W_{t,\tau_{max}}} \tag{3.41}$$

with the dimensionless static factor for torsion $k_{e,\phi}$. Again, an energy equalization is performed using eq. (3.39) and the assumption of a harmonic oscillation analogue to the translational motion which yields

$$\frac{G}{2} \int_0^L I_t(x) \left(\frac{\mathrm{d}\phi(x)}{\mathrm{d}x} \right)^2 \mathrm{d}x = \frac{1}{2} \omega^2 \int_0^L J(x) \phi^2(x) \mathrm{d}x \tag{3.42}$$

with the integral of the non-constant moment of inertia $\int J = \int \frac{1}{2}\rho r^2(x)A(x)$. Solving for ω gives

$$\omega = k_{\omega,\phi}\,\frac{1}{L}\sqrt{\frac{2G}{\rho}} \tag{3.43}$$

including the dimensionless dynamic factor for torsion $k_{\omega,\phi}$ given as

$$k_{\omega,\phi} = L\,\sqrt{\frac{\int_0^L I_t(x)\left(\frac{\mathrm{d}\phi(x)}{\mathrm{d}x}\right)^2 \mathrm{d}x}{\int_0^L r^2(x)A(x)\phi^2(x)\,\mathrm{d}x}}\quad . \tag{3.44}$$

The final relationship of eq. (3.21) for non-constant cross sections is then stated as

$$\tau_{t,max} = \frac{k_{e,\phi}}{k_{\omega,\phi}}\,\sqrt{\frac{\rho G}{2}}\,\frac{I_{t,\tau_{max}}}{W_{t,\tau_{max}}}\frac{v_{rot,max}}{r_{v_{rot,max}}}\quad . \tag{3.45}$$

The information about the geometry is now included in the term $\frac{k_{e,\phi}}{k_{\omega,\phi}}$.

3.4.1.3 Exemplary truncated circular cone

To evaluate the influence of the non-constant cross section, an example cone with structural steel material parameters is considered, as shown in fig. (3.21). Thereby, the large radius is defined as $r_2 = 3$ m, the small radius as $r_1 = 1$ m and the cone length as $L = 4$ m. Both a clamped-free configuration with the small radius at the clamped end, and a clamped-clamped configuration are considered.

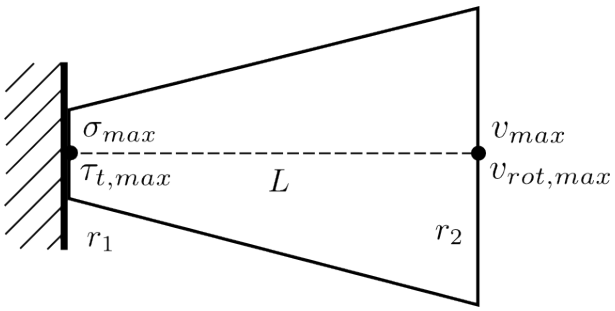

Figure 3.21: Clamped-free truncated circular cone [40]

The results for $\frac{k_e}{k_\omega}$ and $\frac{k_{e,\phi}}{k_{\omega,\phi}}$ are shown in tables (3.4) and (3.5) for the first three bending modes and the first three torsional modes. Due to the inclusion of geometric properties both factors are not constant over frequency anymore.

Table 3.4: Factors for a clamped-free configuration

Bending mode	k_e/k_ω	Torsional mode	$k_{e,\phi}/k_{\omega,\phi}$
55 Hz	52.67	422 Hz	17.43
772 Hz	39.14	3759 Hz	3.25
2737 Hz	25.49	6292 Hz	2.52

Table 3.5: Factors for a clamped-clamped configuration

Bending mode	k_e/k_ω	Torsional mode	$k_{e,\phi}/k_{\omega,\phi}$
1103 Hz	30.90	443 Hz	3.88
2999 Hz	25.14	827 Hz	2.75
5846 Hz	22.40	1220 Hz	2.32

For the clamped-free configuration the ratio between the first two bending modes is determined as $\frac{k_{e,1}/k_{\omega,1}}{k_{e,2}/k_{\omega,2}} = 1.35$ and for the clamped-clamped configuration as 1.23. For non-constant cross sections, the formulation of the ratio between the factors of proportionality from eq. (3.26) is extended to

$$\frac{k_\sigma}{k_\tau} = \frac{k_e}{k_\omega}\frac{k_{\omega,\phi}}{k_{e,\phi}}\sqrt{\frac{2E}{G}}\frac{W_{t,\tau_{max}}\hat{z}_{\sigma_{max}}r_{v_{rot,max}}}{LI_{t,\tau_{max}}} \quad . \tag{3.46}$$

Considering the first bending and torsional modes of the cone yields $\frac{k_{\sigma,1}}{k_{\tau,1}} = 3.45$ for the clamped-free and 4.85 for the clamped-clamped configuration. The inconstant behavior of the factors introduces uncertainty in the relationship between stress and velocity. This effect has to be considered for every system depending on the geometry and the frequency range of interest. However, the previously obtained results for the H-section in table (3.3) indicate a moderate influence on the fatigue damage accuracy.

3.4.2 Geometric Factors Obtained from FE-models

In the last subsections beams with constant and non-constant cross sections were considered within the scope of a preliminary investigation. Geometric factors of real, three-dimensional structures which are usually less symmetric in nature shall be obtained from FE models. Therefore, three example structures are considered: A multi-axis test specimen, a simple automotive component and a complex one. The latter is not shown in detail due to the security of corporate know-how and thus not introduced before subsection 3.4.3.3.

3.4.2.1 Fixed-free multi-axis test specimen

The multi-axis test specimen shown in fig. (3.22) is a typical dummy for hydraulic units of chassis control systems, as described in [61]. The development of its FE model was performed in [70]. The velocities are obtained from positions 1 and 2, the plane stresses from position 3. Position 2 is evaluated in order to calculate the angular velocity. The stress and velocity FRFs from the simulated model are used directly to calculate the geometric factors.

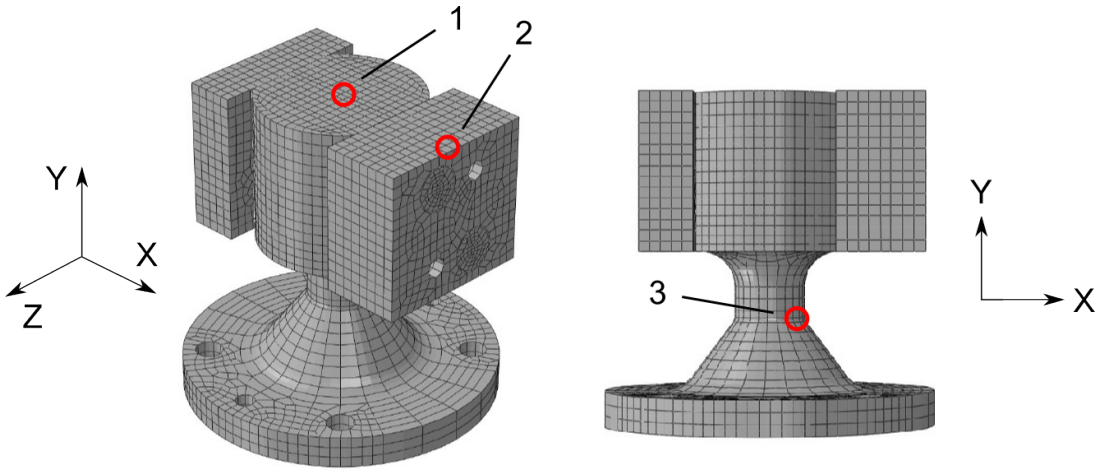

Figure 3.22: Multi-axis test specimen [38], [40]

The sum of the absolute values of all terms that contribute to an equivalent stress are illustrated in fig. (3.23) for a relative comparison. Thereby, a harmonic excitation is applied to all axes simultaneously (superimposition). Due to the similarity of the component to a cantilever beam the factors of proportionality can be obtained separately from the respective directions. The phases of the largest normal stress and the velocity components are shown in fig. (3.24). As mentioned in subsection 3.2.3.1, the phases of the first bending and torsional modes are of the same phase shift.

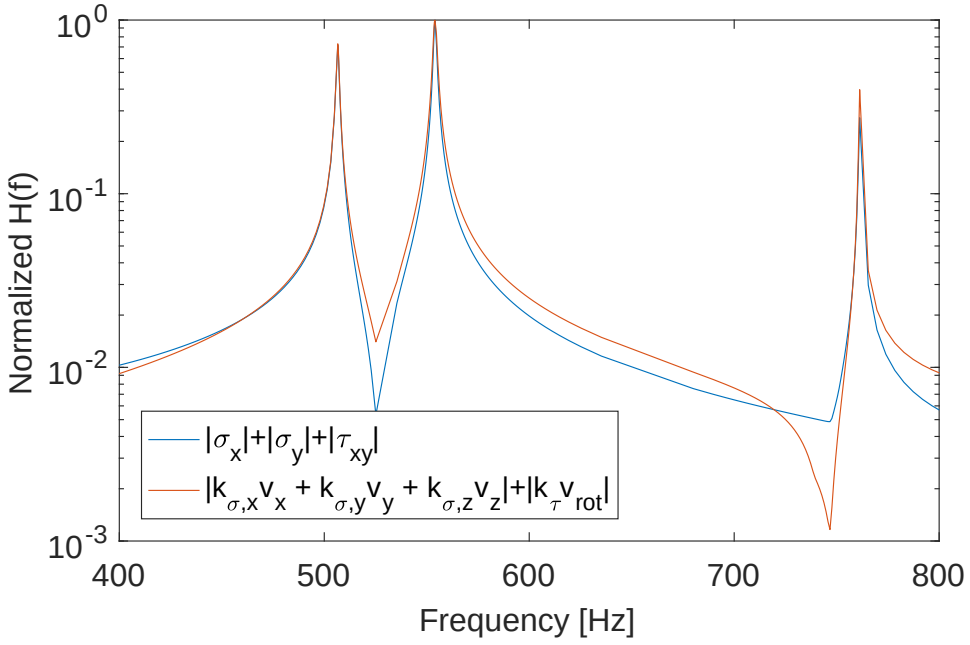

Figure 3.23: Sum of normalized stresses and velocities for the multi-axis test specimen

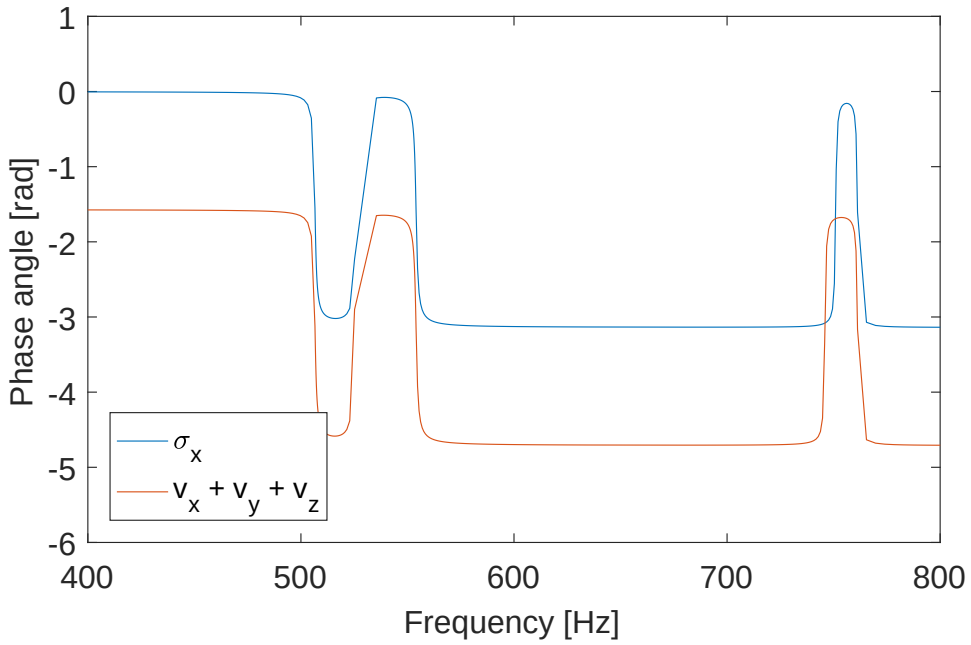

Figure 3.24: Phase of normal stress component and sum of translational velocities for the multi-axis test specimen

Since only a relative estimation of the factors is required, they are normalized to $k_{\sigma,z} = 1$ of the first bending direction. For bending in x-direction a factor of $k_{\sigma,x} = 0.98$ is obtained. The factor for the axial direction is defined as $k_{\sigma,y} = 1$ according to the proposed standard values. The reason is its contributing phase information which will be clarified in the next subsection 3.4.2.2. However, there are no longitudinal modes in the considered frequency range that is typical for automotive applications. The torsional factor is obtained as $k_{\tau} = 0.43$. The estimated factors provide the best relative match between velocities and the stress components.
However, a perfect fit is impossible due to non-constant geometric factors. As shown in fig. (3.25), the second mode is related to a first bending mode while the third mode represents a coupling of a second bending mode and a first torsional mode. If only the bending part is considered for the first two bending modes in the particular z-direction, a ratio of $\frac{k_{e,1}/k_{\omega,1}}{k_{e,2}/k_{\omega,2}} = 1.39$ is obtained which has similarity to the ratio from the example cone given in the previous subsection 3.4.1.3.

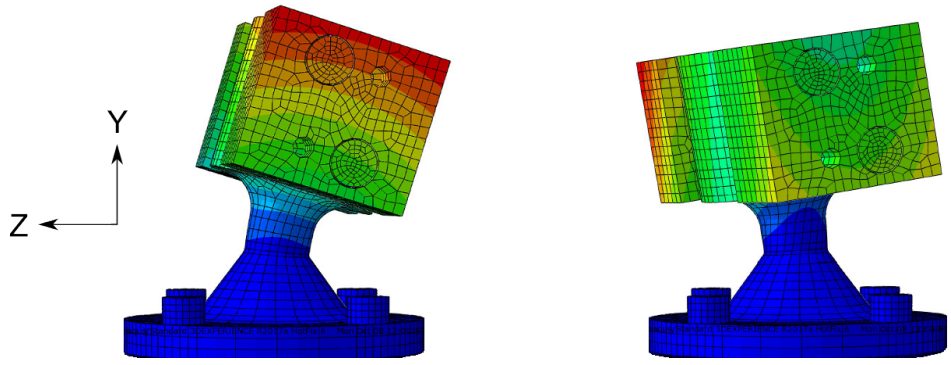

Figure 3.25: Second and third modeshape of the multi-axis test specimen [40]

A fatigue damage calculation according to fig. (3.20) is performed with the normalized stresses and normalized velocities for different S-N curves. The damage ratios D_v/D_σ are given in table (3.6) showing small differences due to the minor deviation at the third mode. Thus, a usage of velocities to perform a fatigue damage evaluation is reasonable.

Table 3.6: Deviation of the fatigue damage values for the multi-axis test specimen

b	3	4	5	6	7	8	9	10	11	12	13
D_v/D_σ	0.96	0.98	1.04	1.11	1.18	1.26	1.33	1.40	1.48	1.57	1.66

For the previous investigations only a single, multiaxial hot spot was considered. As indicated in subsection 3.1.2.2, depending on the excitation different hot spots may occur. If the fatigue calculation shall be based on several locations, different geometric factors have to be obtained for the respective locations (see position $3,1$ and $3,2$ in fig. (3.26)). Again, the uniaxial factors are normalized to $k_{\sigma,z,1D} = 1$ which yields $k_{\sigma,x,1D} = 1.08$ for the uniaxial excitation of the x-direction and $k_{\tau,x,1D} = 0.03$, respectively $k_{\tau,z,1D} = 0.32$. The first value for the shear stress is much lower since the torsional mode is mostly excited in z-direction. The summation of the obtained FRFs of both uniaxial hot spots is given in fig. (3.27) to show the relative match between them.

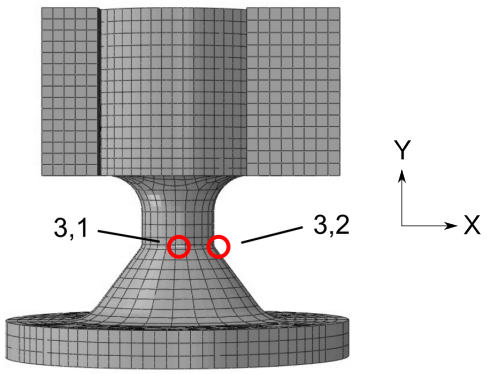

Figure 3.26: Uniaxial hot spots of multi-axis test specimen

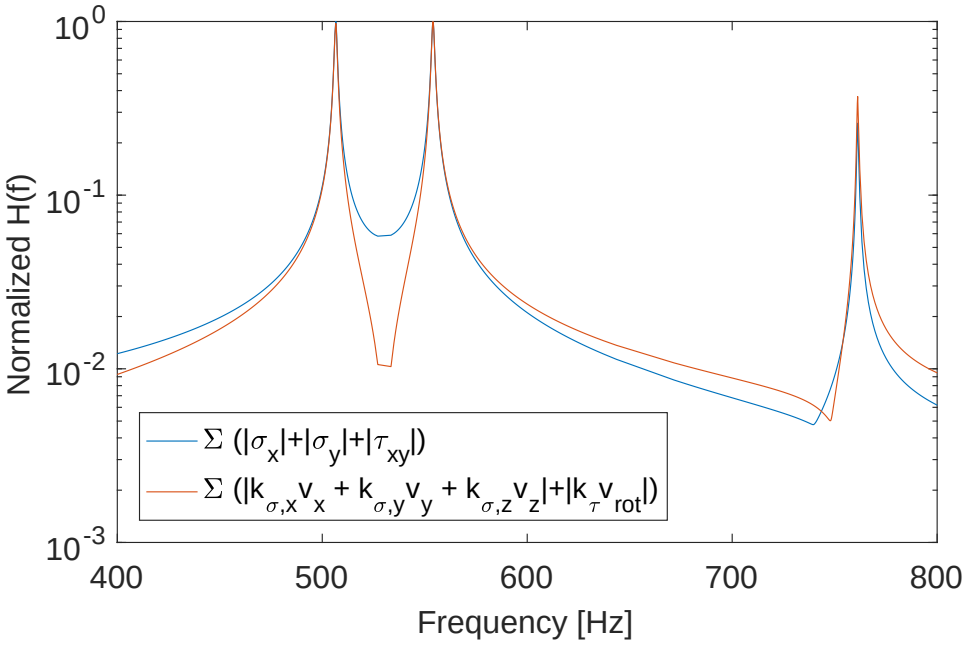

Figure 3.27: Sum of normalized stresses and velocities for the multi-axis test specimen of both uniaxial hot spots together

An experimental verification of fig. (3.27) using strain gauge and laser vibrometry measurements is given in fig. (A2) and (A3) within the appendix. The measurements are obtained from uniaxial shaker tests performed in [70] and evaluated respectively. They confirm the similarity between velocity and stress time signals.

3.4.2.2 Quasi-fixed-free simple automotive component

The second model is a simple automotive component with two boundary constraints realized by two screw connections shown in fig. (3.28). Since the connections are located on the same side, the boundary condition is referred to as quasi-fixed-free. Besides the electronic parts, the component consists of a predominant plastic housing. Due to the from the outside unknowable internal setup it is treated as a black box. The velocities are obtained from the positions 1 and 2, the plane stresses from the maximum stress position 3 in the vicinity of the clamped end. For both uniaxial and simultaneous excitation only one hot spot is considered based on the simulation results. Generally, a simulation model is needed to determine the hot spot positions. To avoid high computing times also coarse models can be used for an approximate detection.

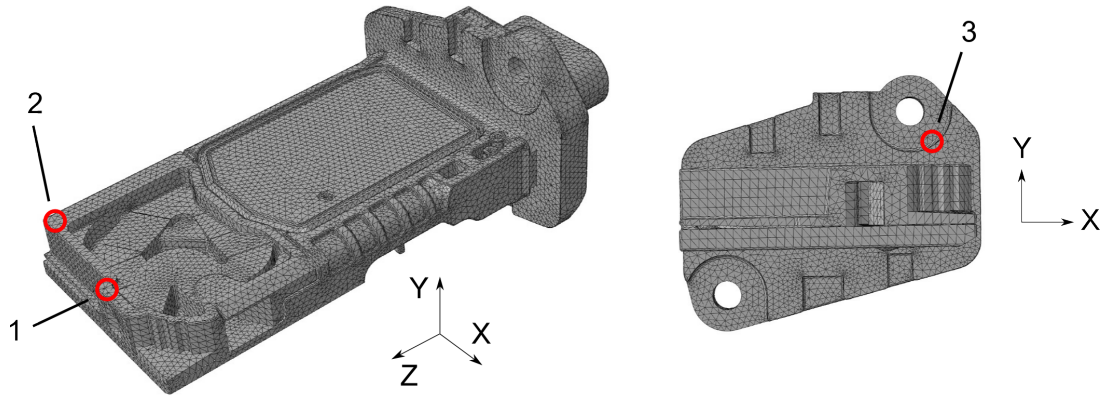

Figure 3.28: Simple automotive component [40]

In opposite to the cantilever beam, the geometric factors cannot be obtained independently of each other anymore due to the superimposition of several velocity components at some modes. Thus, their phase relation has to be considered. Coupling effects between velocity components can also occur when the location of maximum stress which can be treated as the reference point is moving itself. According to the considerations made in subsection 3.3.2, the largest normal stress $\sigma(t)$ is given in the time domain as

$$\sigma(t) \approx k_{\sigma,x} v_x(t) + k_{\sigma,y} v_y(t) + k_{\sigma,z} v_z(t) \quad . \tag{3.47}$$

Considering a single frequency ω_0, eq. (3.47) can be expressed with its respective phase angles as

$$\begin{aligned} \sigma(t) \approx k_{\sigma,x} \hat{v}_x \sin\left(\omega_0 t + \theta_{v_x}\right) + k_{\sigma,y} \hat{v}_y \sin\left(\omega_0 t + \theta_{v_y}\right) \\ + k_{\sigma,z} \hat{v}_z \sin\left(\omega_0 t + \theta_{v_z}\right) \end{aligned} \tag{3.48}$$

To consider occurring phase shifts of $\pm\pi$ between the velocity components, the complex sum of velocities has to be used at a particular frequency. The geometric factors are then assigned with respect to the largest occurrence of each velocity component over all eigenfrequencies. Thereby, only a relative consideration of the factors is accomplished with a normalization to $k_{\sigma,y} = 1$ of the first bending direction (y-axis). For bending in x-direction a factor of $k_{\sigma,x} = 0.43$ is obtained. The factor for the axial direction is defined as $k_{\sigma,z} = 1$ according to the proposed standard values. No longitudinal modes are located within the considered frequency range. The torsional factor is obtained as $k_\tau = 0.05$. Applying the relative factors yields the best relative match between the stress and velocity FRFs, as shown in fig. (3.29). The phases of the largest normal stress and the sum of the velocity components are given in fig. (A4) within the appendix, showing a phase shift of $\pm\pi/2$ at each frequency.

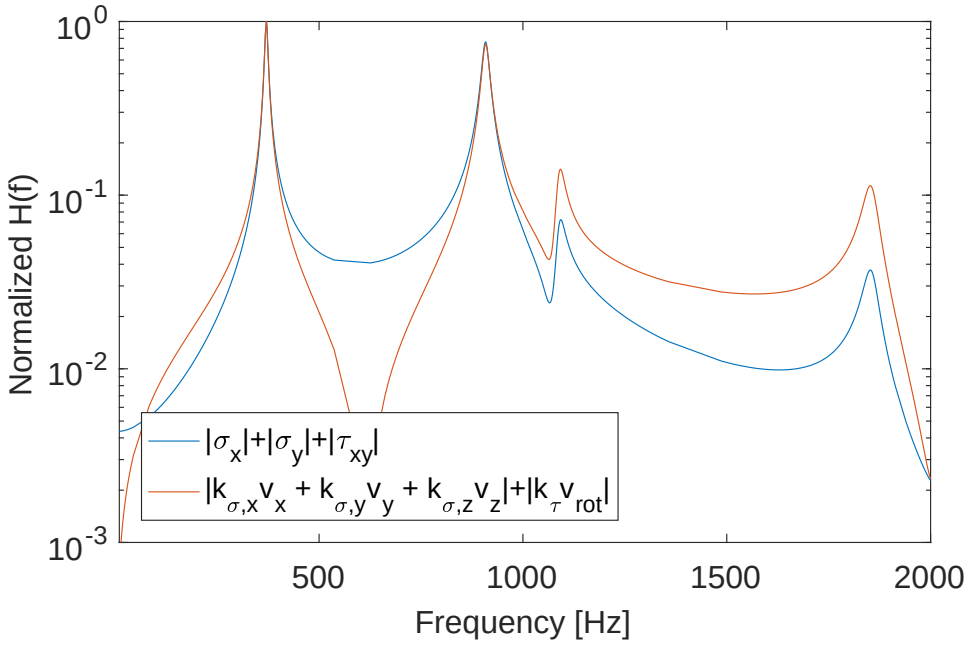

Figure 3.29: Sum of normalized stresses and velocities for the simple automotive component

The results of a respective fatigue damage calculation with normalized stresses and velocities are shown in table (3.7). Within the scope of fatigue damage calculation, the expected deviations are acceptable and reasonable fatigue damage values can be obtained.

Table 3.7: Deviation of the fatigue damage values for the simple automotive component

b	3	4	5	6	7	8	9	10	11	12	13
D_v/D_σ	1.64	1.84	2.08	2.35	2.61	2.87	3.13	3.40	3.72	4.09	4.53

The deviation for larger slope values b is mainly caused by the deviations of the two higher modes above 1000 Hz. However, in real application those modes are usually not excited strongly. For the first two bending modes, a ratio of $\frac{k_{e,1}/k_{\omega,1}}{k_{e,2}/k_{\omega,2}} = 1.30$ is calculated which is also close to the value of the example cone in subsection 3.4.1.3. If the relative geometric factors are obtained independently instead of using the complex sum of velocities, large errors may occur which is indicated by the resulting FRFs in fig. (3.30). As can be seen, a large deviation at the first eigenfrequency is produced. As mentioned previously, the longitudinal velocity term shall be kept to $k_{\sigma,lon} = 1$. Neglecting the term completely results in errors due to too much considered motion of the flexural tip at the second bending mode around 1850 Hz. The resulting FRF is shown in fig. (3.31). Including all terms as proposed leads to a correct cancellation of the out-of-phase velocity components.

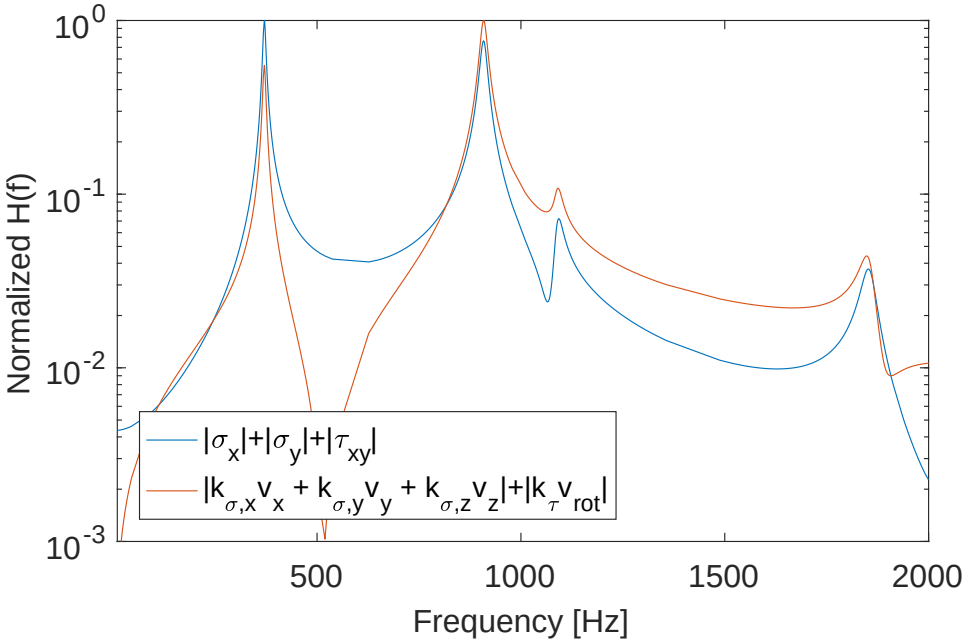

Figure 3.30: Sum of normalized stresses and velocities for the simple automotive component with separately obtained factors

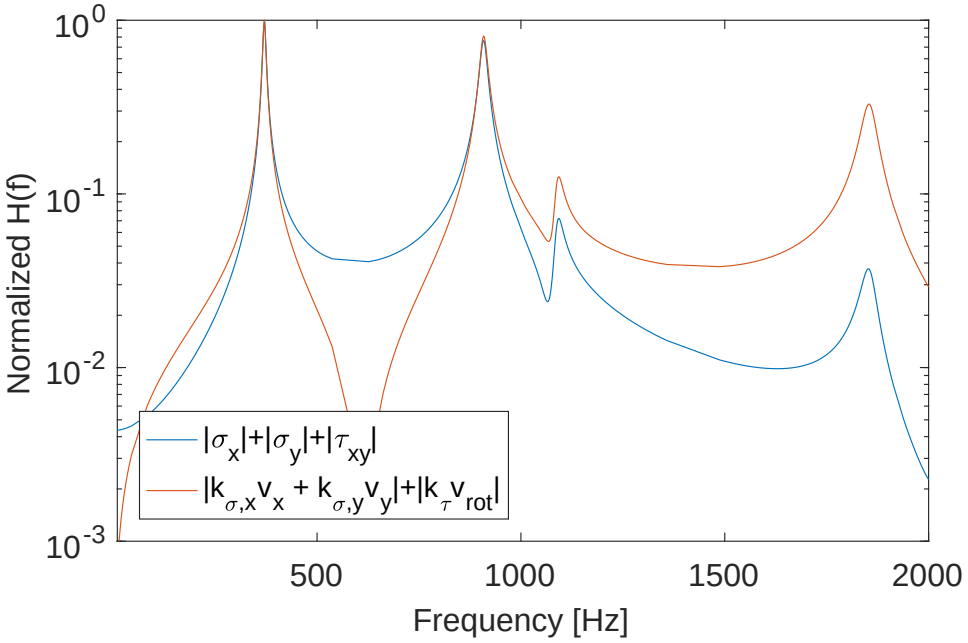

Figure 3.31: Sum of normalized stresses and velocities for the simple automotive component without longitudinal term

3.4.3 Usage of Simplified FE-models

To ensure a fast fatigue damage evaluation process, full simulations are to be avoided. Therefore, geometry information shall be obtained from a strongly simplified model. Apart from obtaining the geometric factors, appropriate velocity measurement position can be determined

using the simplified model. Only simple geometries are used for the manual FE model setup, targeting a strong reduction analogous to a 99% simplification for machined products, as described in [101]. Stress estimation using simple FE models based on an already assumed range for the geometric factors is also mentioned in [83]. The material parameters of the simplified model are to be chosen the same as for the full component. Thereby, the main structural components are considered. Internal structures are unknown and thus still neglected. In order to match the measurable total mass, density values can be adjusted. Concerning the geometrical precision some reasonable limitations are defined: The Center of Gravity (CoG) should not deviate by more than 5% of the respective spatial dimension. The deviation of the principal moments of inertia should be a maximum of $20 - 30\%$ while the products of inertia can be neglected. Furthermore, it is important to maintain the same boundary conditions of the real component. Obviously, the eigenfrequencies of the simplified model usually do not match the real ones. However, to obtain meaningful geometric factors and to propose appropriate measurement locations, a simplified model is qualitatively sufficient.

3.4.3.1 Fixed-free multi-axis test specimen

A simplified model that matches the criteria is built for the multi-axis test specimen, shown in fig. (3.32). As for the full model, the velocities are obtained from positions 1 and 2 and the plane stresses from position 3. The FRFs of the simple model are given in fig. (A5) within the appendix.

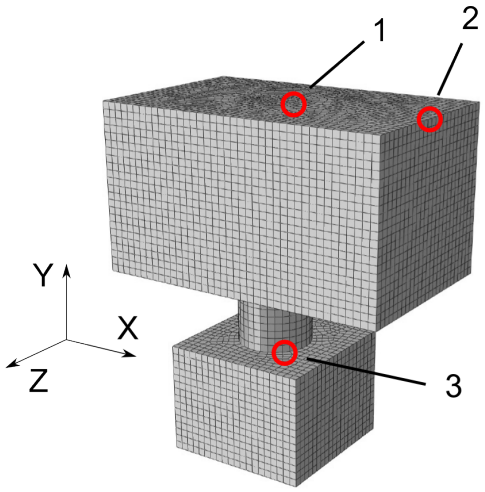

Figure 3.32: Simplified models for the multi-axis test specimen [40]

The model parameters for both the full and the simplified model are given in table (3.8). The volume is estimated considering the models as a block using the largest width, length and height. The obtained relative geometric factors are given in table (3.9) and are in a good agreement. Comparable deviations of the geometric factors can be obtained (see table (3.10)) when relating to the uniaxial hot spots previously shown in fig. (3.26).

Table 3.8: Model parameters for full and simplified example multi-axis test specimen

Parameter	Full model	Simplified model
$m\ [kg]$	1.18	1.17
$\boldsymbol{r}_{\mathrm{CoG}}\ [mm]$	$[0, 6, 30]$	$[0, 4, 30]$
$V\ [mm]$	$80 \times 95 \times 50$	$80 \times 95 \times 50$
$J_x\ [t\ mm^2]$	1.74	1.32
$J_y\ [t\ mm^2]$	1.26	1.02
$J_z\ [t\ mm^2]$	1.06	0.736

Table 3.9: Geometric factors for full and simplified multi-axis test specimen

	Full model	Simplified model
$k_{\sigma,x}$ (bending)	0.98	0.80
$k_{\sigma,y}$ (axial)	1.0	1.0
$k_{\sigma,z}$ (bending)	1.0	1.0
k_{τ} (torsion)	0.43	0.50

Table 3.10: Geometric factors for full and simplified multi-axis test specimen, uniaxial hot spots

	Full model	Simplified model
$k_{\sigma,x,1D}$ (bending), pos. 3,2	1.08	1.09
$k_{\sigma,y,1D}$ (axial), pos. 3,1 and 3,2	1.0	1.0
$k_{\sigma,z,1D}$ (bending), pos. 3,1	1.0	1.0
$k_{\tau,x}$ (torsion), pos. 3,2	0.03	0.00
$k_{\tau,z}$ (torsion), pos. 3,1	0.32	0.39

Applying the factors from the simplified model on the full simulation model yields a good match between the FRFs, shown in fig. (3.33). The deviation between the calculated fatigue damage values in table (3.11) are acceptable within the scope of fatigue damage calculation. The slight deviation at $b = 4$ can be explained by the stronger counteractive effect of the exponent b on the largest amplitude values of both stress and velocity.

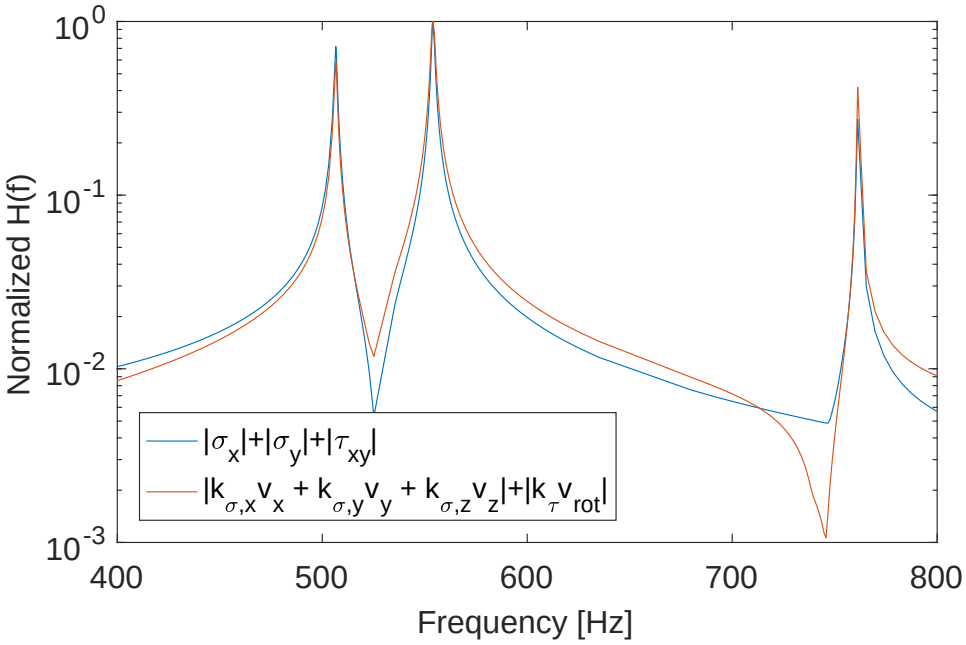

Figure 3.33: Sum of normalized stresses and velocities for the multi-axis test specimen with factors from the simplified model

Table 3.11: Deviation of the fatigue damage values for the multi-axis test specimen with factors from the simplified model

b	3	4	5	6	7	8	9	10	11	12	13
D_v/D_σ	0.97	0.96	0.98	1.03	1.13	1.24	1.35	1.45	1.55	1.65	1.75

3.4.3.2 Quasi-fixed-free simple automotive component

The simplified model of the simple automotive component is shown in fig. (3.34). Again, the velocities are obtained from positions 1 and 2 and the plane stresses from position 3. The FRFs of the simple model are given in fig. (A6) within the appendix.

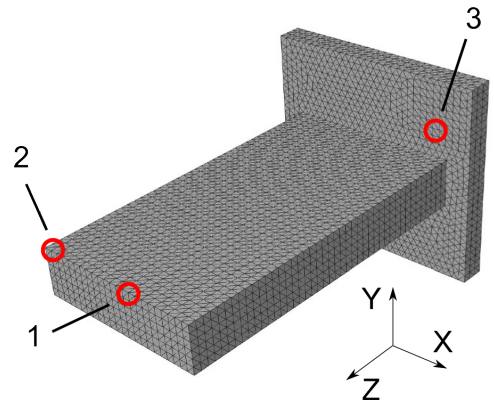

Figure 3.34: Simplified models for the simple automotive component [40]

The model parameters for both the full and the simplified model are given in table (3.12). The obtained relative geometric factors are given in table (3.13) and are also in a good agreement.

Table 3.12: Model parameters for full and simplified model of simple automotive component

Parameter	Full model	Simplified model
$m\ [kg]$	3.19×10^{-2}	3.21×10^{-2}
$\boldsymbol{r}_{\mathrm{CoG}}\ [mm]$	$[16.55, 4.5, 17.9]$	$[17.5, 4.75, 22.2]$
$V\ [mm]$	$45 \times 45 \times 87.5$	$45 \times 40 \times 70$
$J_x\ [t\ mm^2]$	0.0173	0.0176
$J_y\ [t\ mm^2]$	0.020	0.020
$J_z\ [t\ mm^2]$	0.004	0.005

Table 3.13: Geometric factors for full and simplified model of the simple automotive component

	Full model	Simplified model
$k_{\sigma,x}$ (bending)	0.43	0.34
$k_{\sigma,y}$ (bending)	1.0	1.0
$k_{\sigma,z}$ (axial)	1.0	1.0
k_{τ} (torsion)	0.05	0.04

Applying the factors from the simplified model on the full simulation model yields a good match between the FRFs, shown in fig. (3.35). The deviation between the calculated fatigue damage values are given in table (3.14). As mentioned previously, the deviation especially for larger slope values b is due to the two higher modes above 1000 Hz. They are usually not excited strongly and thus the simplified model is still acceptable within the scope of fatigue damage calculation.

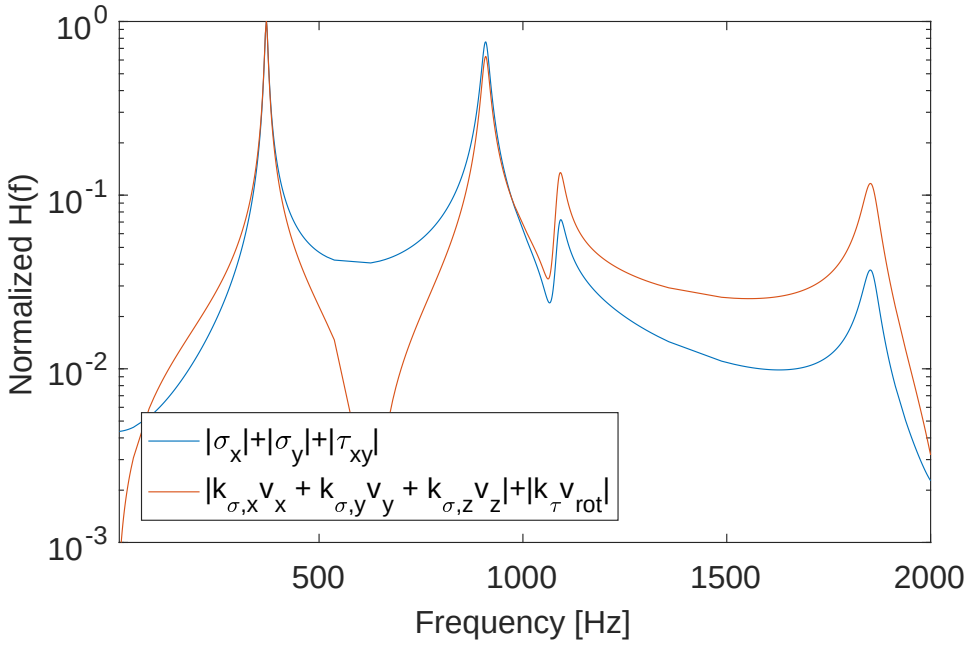

Figure 3.35: Sum of normalized stresses and velocities for the simple automotive component with factors from the simplified model

Table 3.14: Deviation of the fatigue damage values for the simple automotive component with factors from the simplified model

b	3	4	5	6	7	8	9	10	11	12	13
D_v/D_σ	2.01	2.42	2.94	3.56	4.27	5.08	6.01	7.13	8.51	10.27	12.52

3.4.3.3 Complex automotive component

The third model is now introduced as a complex automotive component. Since details cannot be published, only the simplified model is shown in fig. (3.36). For most real products as the complex automotive component, the internal structure is not accessible and thus not measurable. It consists of stringers, circuit boards and further electronics. The focus is put on the exterior locations and the component is treated as black box. The structure is mounted at three locations on its outer edge and is to be considered in a fixed-fixed configuration.
Since the top of the structure being considered as a cap, potentially responding with several plate modes, a measurement location on the edge is to be found more appropriate. Translational velocities are then obtained from position 1. For the given structure no meaningful rotational velocity can be obtained. The plane stresses are measured at position 2 which is considered as the hot spot for both uniaxial and simultaneous excitation regarding the full simulation model. The FRFs of the simple model are given in fig. (A7) within the appendix.

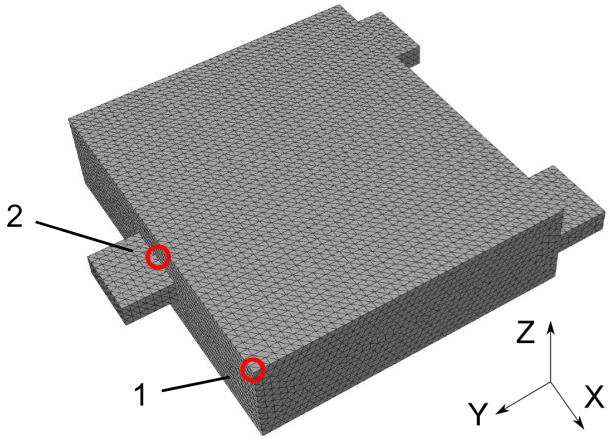

Figure 3.36: Generalized model of a complex automotive component [40]

Since the velocity components of the original FE model being strongly coupled, no meaningful geometric values can be obtained from the full FE model. Therefore, the standard values for a clamped-clamped configuration provided in subsection 3.3.1 are used. The model parameters for the simplified model are given in table (3.15). Hence, the simplified model is mainly used for the determination of an appropriate velocity measurement position.

Table 3.15: Model parameters for full and simplified complex automotive component

Parameter	Full model	Simplified model
$m\ [kg]$	6.99×10^{-2}	6.96×10^{-2}
$\boldsymbol{r}_{\mathrm{CoG}}\ [mm]$	$[2.1, 0.36, 2.1]$	$[0, 0, 1.5]$
$V\ [mm]$	$87 \times 80 \times 17$	$70 \times 80 \times 17$
$J_x\ [t\ mm^2]$	0.0251	0.0241
$J_y\ [t\ mm^2]$	0.0366	0.0303
$J_z\ [t\ mm^2]$	0.0574	0.0512

Applying the factors on the full simulation model yields a good match between the FRFs, shown in fig. (3.37). The deviation between the calculated fatigue damage values in table (3.16) are still acceptable within the scope of fatigue damage calculation.

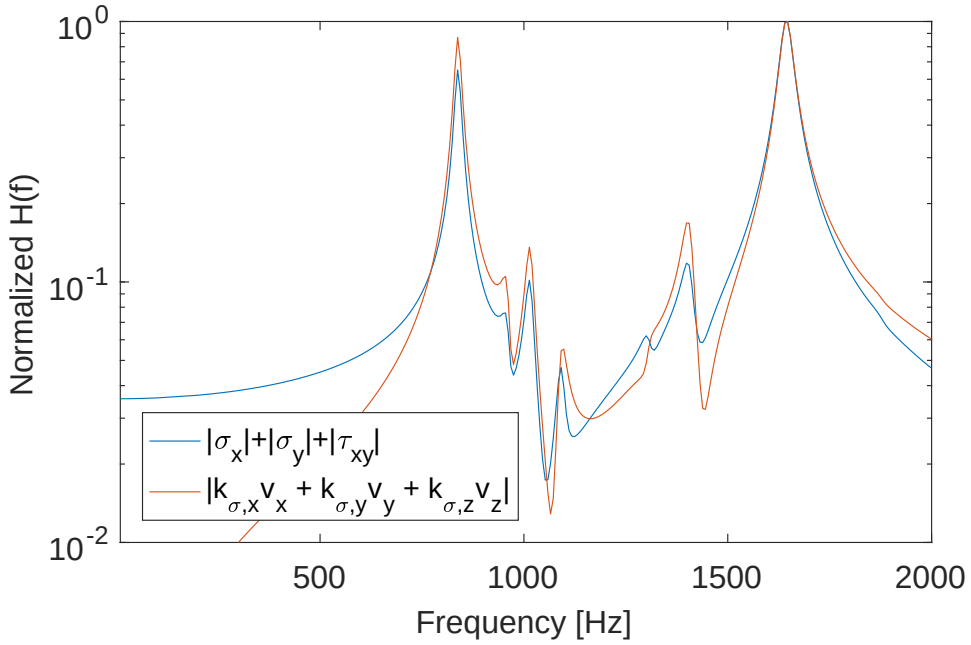

Figure 3.37: Sum of normalized stresses and velocities for the complex automotive component using standard factors

Table 3.16: Deviation of the fatigue damage values for the complex automotive component with standard factors

b	3	4	5	6	7	8	9	10	11	12	13
D_v/D_σ	1.84	2.26	2.74	3.27	3.82	4.34	4.80	5.18	5.49	5.76	6.01

The applicability of the entire method was shown on three example structures. Useful geometric factors that relate velocity measurements to stresses can be obtained efficiently. They can directly be used for an equivalent stress based fatigue damage calculation which will be applied on real test cases in section 6.2 to evaluate the fatigue damage difference between uniaxial and multiaxial excitation.

3.5 Conclusions on Velocity based Fatigue Damage Evaluation

The previous sections introduced a new method to evaluate fatigue damage using relative velocity responses. Geometric factors were obtained from simplified models yielding a good match between stresses and velocities. Within the scope of vibration testing the combined quantity can be used to perform a relative comparison between the severity of different vibration profiles $D_{\text{profile 1}}/D_{\text{profile 2}}$. Fig. (3.38) shows the classification of the new method with respect to already existing approaches. The most complex and accurate approach is naturally the full stress simulation of the component to be tested. Often, the availability of fully developed FE models or the time for its building is limited. On the other hand, the fastest approach is to use standards. A common procedure is explained in subsection 2.3.3 which uses standard vibration profiles and performs a cycle counting directly on the measured acceleration responses. A more complex approach is the FDS which relates the fatigue damage directly to the acceler-

ation excitation profile coupled through the FRF of a SDOF system. The new method combines both the correct measurement quantity and rough geometric information obtained from a fast FE simulation. It is independent of the excitation profiles on contrary to the FDS.

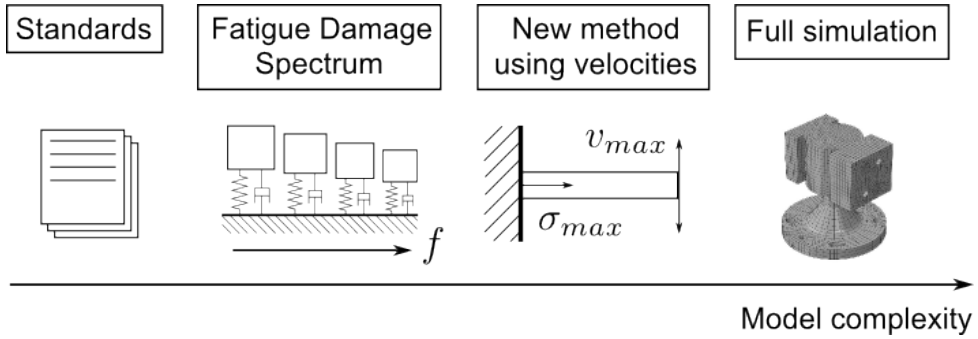

Figure 3.38: Classification of different methods concerning model complexity [40]

Field measurements are widely performed using accelerometers at both the mounting and response locations of a structure. To obtain velocities an integration of the acceleration time signal has to be performed. To avoid errors due to sensor drift, an appropriate integration method according to [102] is used. The method removes drifts by considering the upper and lower envelope of the integrated signal.
Consequently, the flow chart from fig. 3.20 is extended to fig. (3.39) with measured accelerations and geometric factors from simplified FE models as the starting point of the developed method.

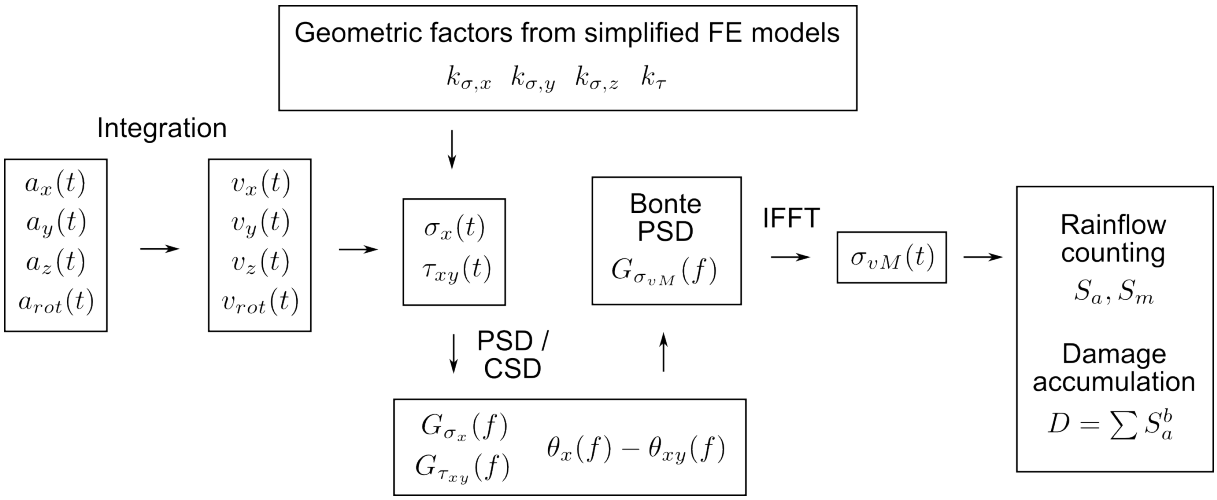

Figure 3.39: Flow chart of fatigue damage calculation using measured accelerations

4 Implementation of the 3D-Shaker System

Subject of this chapter is an electrodynamic 3D-shaker system prototype which is shown in fig. (4.1). The implementation of the system for its proper usage is indispensable for the experimental verification of the difference in fatigue damage between uniaxial and multiaxial excitation. This will be part of chapter 6, where tests are conducted using the introduced structures from the previous subsections 3.4.2 and 3.4.3. Thereby, the tests are designed using realistic scenarios to achieve an overall more realistic testing.
The shaker and its controller are initially treated as black boxes due to the lack of knowledge on both hardware and software. After a preliminary investigation, fixture modifications are accomplished for an effective control of field data based profiles. Different vibration controllers and configurations are then investigated. Parts of this chapter, especially in section 4.1, have been published previously in [39].

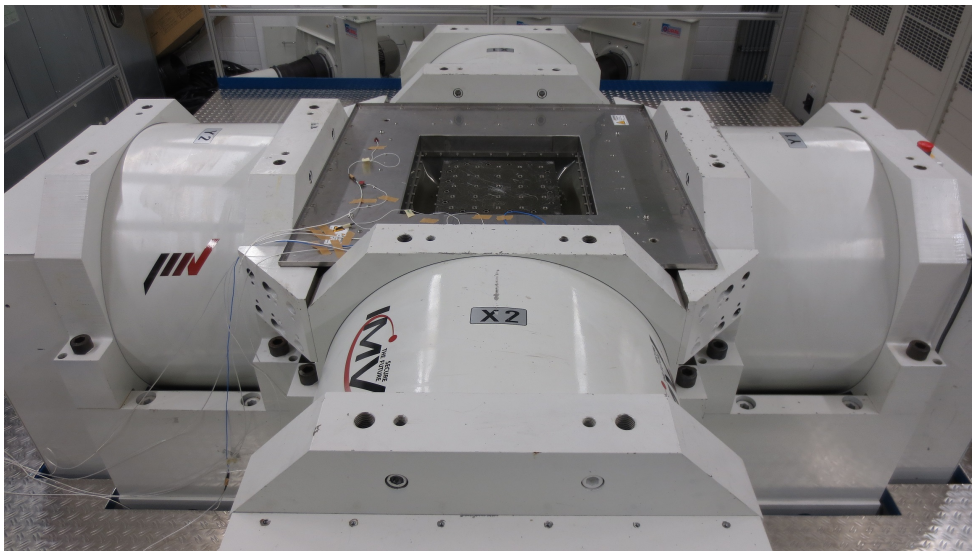

Figure 4.1: 3D-shaker system [39]

4.1 Shaker Characterization

4.1.1 System Description

The system to be investigated is labeled as IMV TS-3000-3.2H-CE. It consists of five independent shakers which are coupled through a bearing unit, as illustrated in fig. (4.2). Both horizontal axes (X and Y) are excited with two 15 kN shakers each, arranged in a push-pull configuration. The vertical Z-axis is realized with a single 30 kN shaker. Due to its quadratic design with an edge length of 320 mm and a number of 25 threaded holes, the usage of the shaker table is limited to smaller Devices Under Test (DUT). Both the IMV K2 and the Dataphysics Signal Star Matrix MIMO controller are used for the subsequent investigations. Measurements are performed with triaxial Dytran 3133 series accelerometers and the control is performed with a triaxial PCB 356A61 accelerometer.

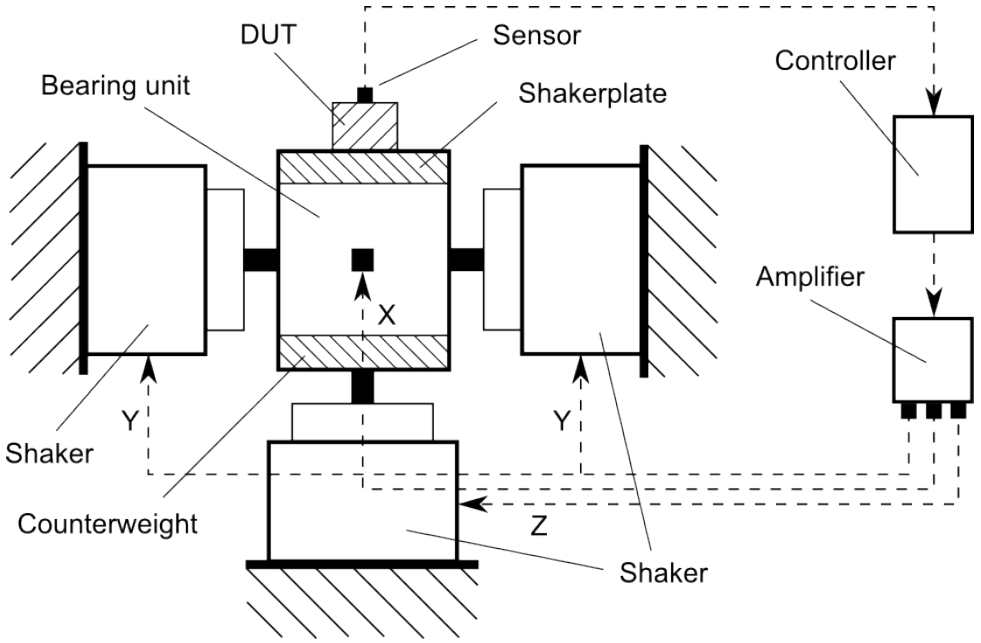

Figure 4.2: Illustration of the 3D-shaker setup

In order to balance the systems bearing unit, a counterweight is mounted at its bottom as shown in fig. (4.2). Especially rotational modes around the horizontal axes, usually occurring at the vicinity of 110 Hz, produce displacements that may cause damage to the bearings. A respective specification for the balancing is provided in [34]. It contains upper and lower limits for the pairing of mass and height of the CoG, as indicated in fig. (4.3) which have to be maintained for extensive testing.

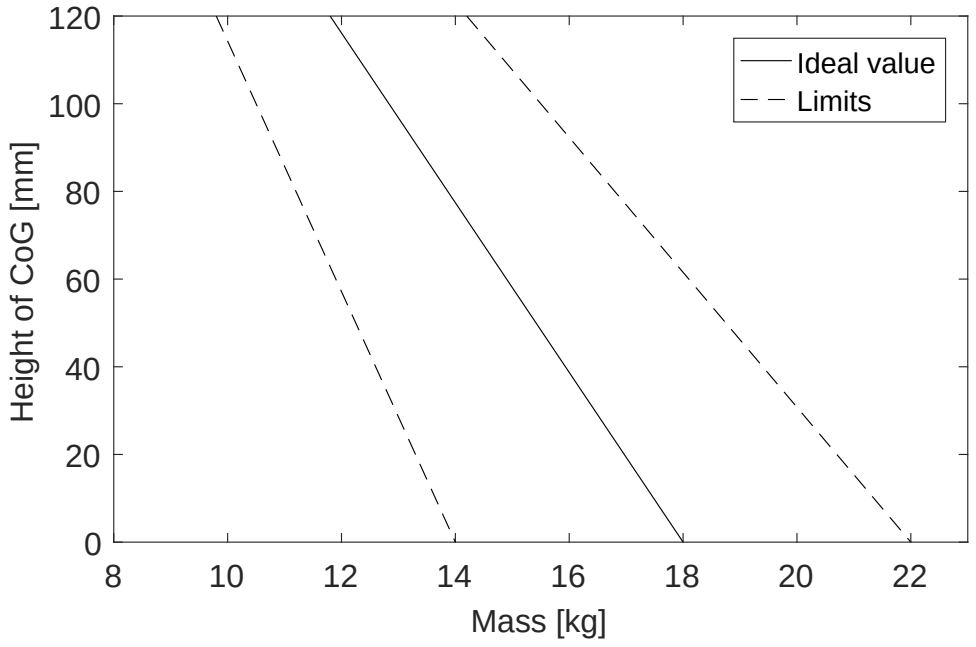

Figure 4.3: Specification for shaker setup

4.1.2 Preliminary Investigation

Initially, the bare table is considered. Five measurement points are determined according to fig. (4.4) with the control sensor being located in the center M1.

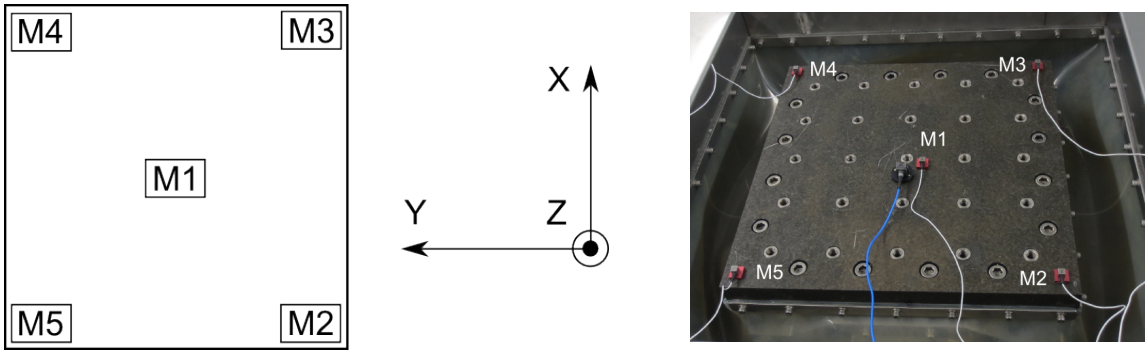

Figure 4.4: Shaker plate [39]

The bearing unit of the 3D-shaker is the main difference to uniaxial shakers, including its dynamic behavior. While most uniaxial shakers only have a low suspension resonance below 10 Hz and an armature resonance around 5000 Hz, a preliminary sine sweep of the 3D-shaker with a bare setup shows roughly 14 resonances in total within a frequency range of 10 Hz to 2000 Hz. Peak hold FFTs for each direction and for uniaxial excitations are given in fig. (4.5). An example phase plot of an Y-excitation and Z-response is shown in fig. (B1) within the appendix. Table (4.1) shows 7 modes that can be described clearly by their distinct peaks and $180°$ phase shifts. Further 7 peaks are detected which do not show a distinct phase shift or which do only develop with a simultaneous XYZ-excitation indicating a nonlinear behavior.

Table 4.1: Detected critical 3D-shaker modes

Mode number	Frequency	Modeshape
1	110 Hz	Rotation around X-axis (Y-excitation), rotation around Y-axis (X-excitation)
2	550 Hz	Rotation around X-axis (Y-excitation), rotation around Y-axis (X-excitation)
3	1120 Hz	Rotation around Z-axis
4	1360 Hz	Rotation around X-axis
5	1500 Hz	Rotation around X-axis and translation in Y-direction, first buckling mode
6	1730 Hz	Rotation around Y-axis and Z-axis
7	1850 Hz	Second buckling mode

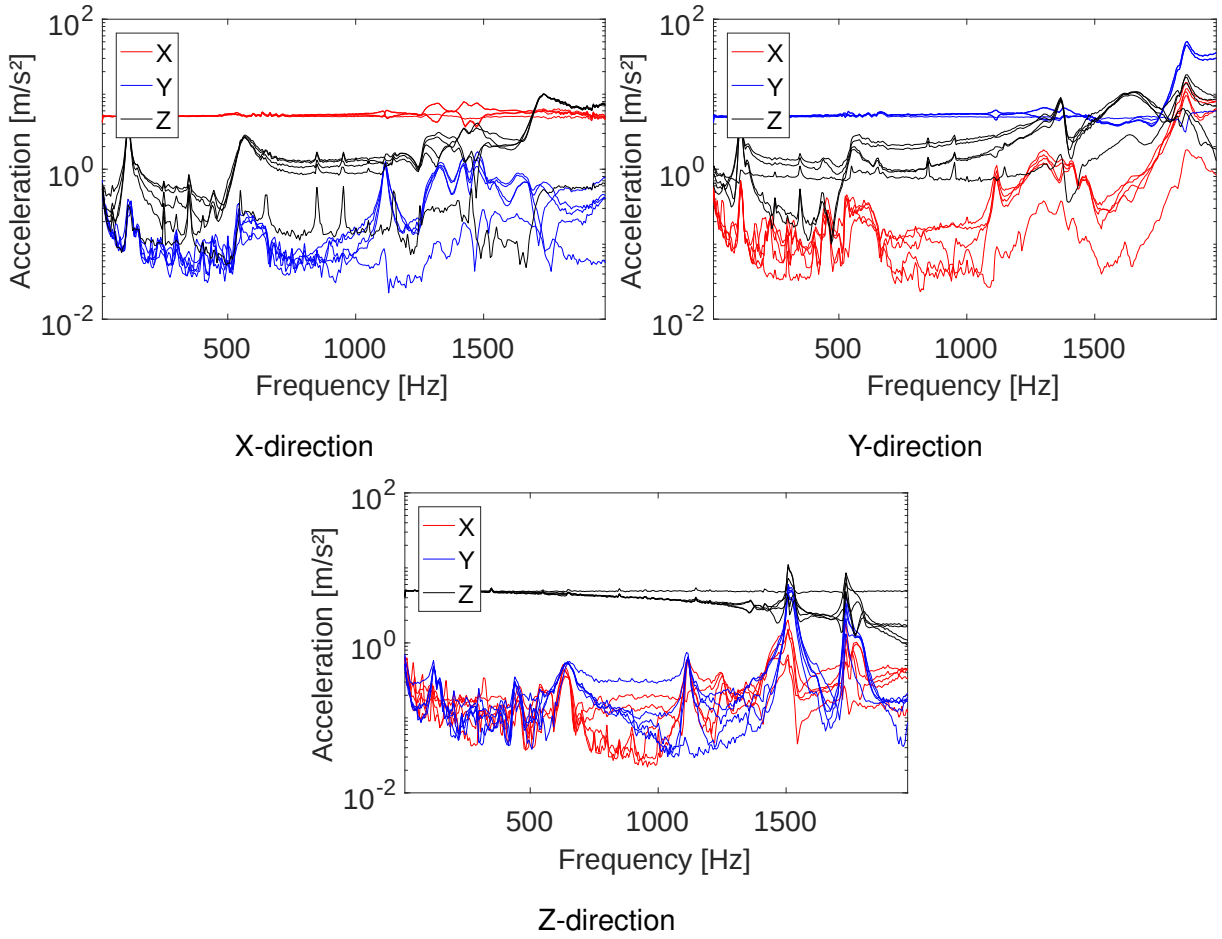

Figure 4.5: Response peak hold FFT of sine sweep

The lower modes below 1000 Hz can be mainly described by a rigid body motion. Modes above 1000 Hz do mostly occur with an additional in-plane bending component. The mode at 1500 Hz is likely to be related to a first buckling mode which is hardly controllable along the Y-edge near to the rotational axis. The second buckling mode occurs in the vicinity of 1850 Hz when exciting in Y-direction. Due to its vibrational node in the center, the second buckling mode is also the most critical modeshape in case of performing the vibration control at this location. An Operational Deflection Shape (ODS) analysis using a Polytech PSV-400 3D-laser scanning system is performed for a better understanding. The result in fig. (4.6) shows clearly a motion that can be described as the second bending mode of the plate in combination with a translation in Y-direction. For its detection an operational analysis has to be accomplished since the mode is not excitable with an impact hammer. A shaker characterization in terms of Experimental Modal Analysis (EMA) or system identification is therefore not meaningful.

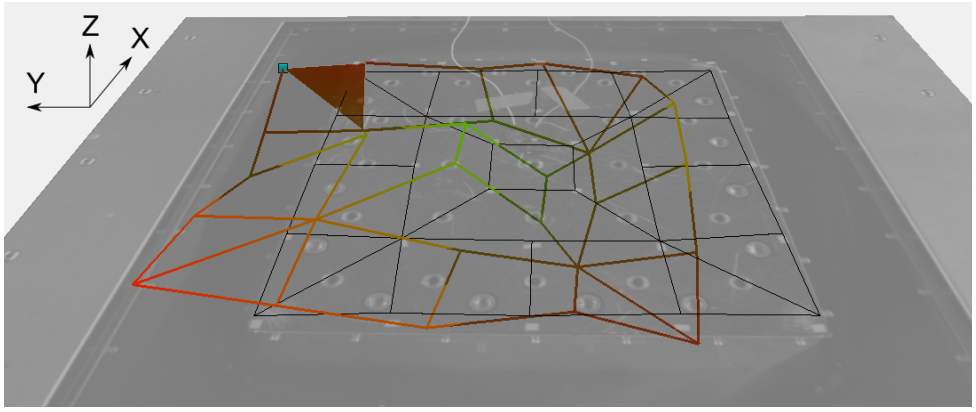

Figure 4.6: Laser vibrometry of second bending mode at around 1850 Hz [39]

As mentioned previously, the 3D-shaker has a nonlinear behavior which can be emphasized by fig. (4.7) showing the responses of a simultaneous 3D-excitation and the sum of the sequentially applied uniaxial excitations. The test is conducted with a random profile from 10 Hz to 2000 Hz with an overall RMS value of 15 m/s². The control of the table is realized at the center using the IMV K2 vibration controller.

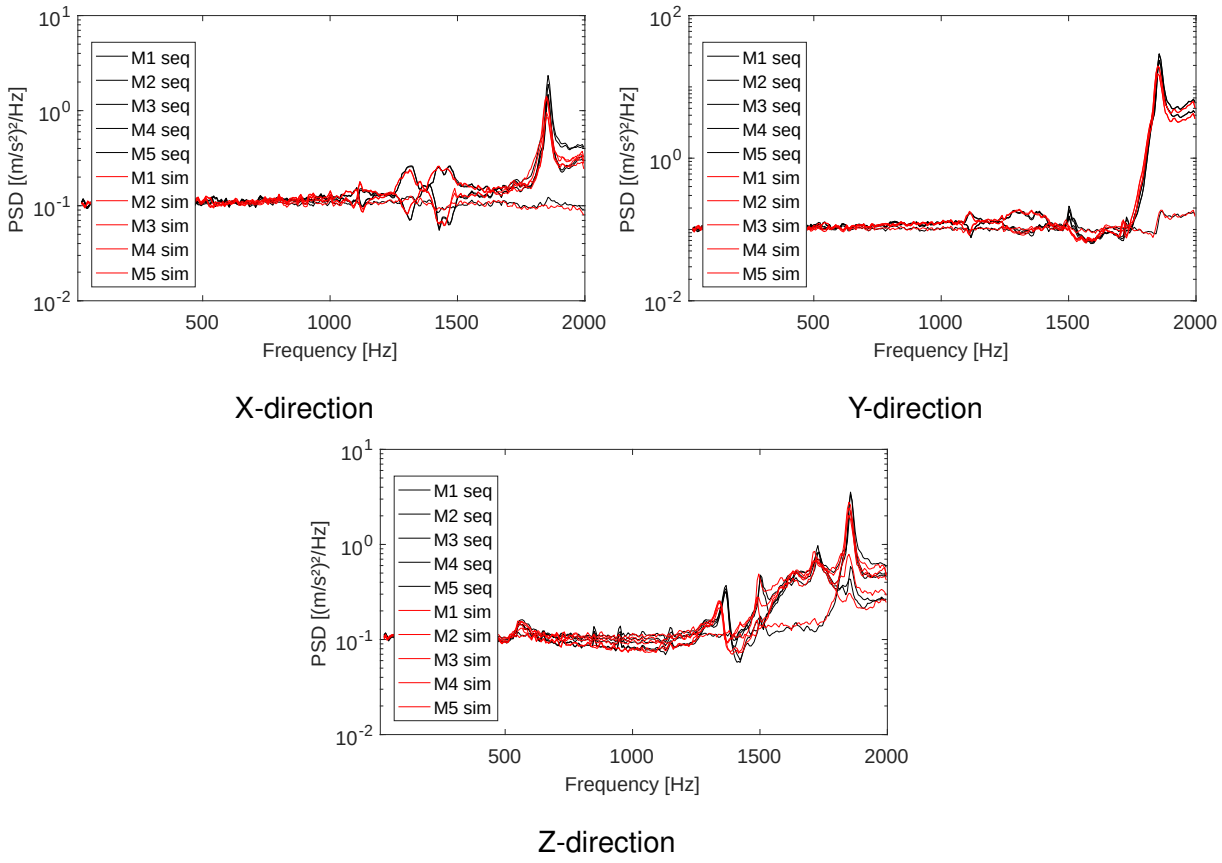

Figure 4.7: Simultaneous and sequential responses [39]

The Z-axis shows minor disturbances which are caused by current noise and is probably explained by insufficient grounding of its amplifier. Furthermore, the system changes its behavior slightly over time which will also be discussed in the next subsection. The shaker axes are not perfectly decoupled due to the nature of the bearing unit and thus excitation always results in cross acceleration. Thereby, the strongest correlation is detected between the Y- and Z-axis. The accuracy of a XYZ-excitation is similar to a YZ-excitation unlike other combinations which show higher accuracies.

4.1.3 Modifications of the Fixture

As a next step, the shaker setup is to be modified in order to decrease the influence of the shaker modes and to perform optimum measurements up to 2000 Hz. For the modification process, different geometries are used and evaluated sequentially to find an improved setup. Thereby, the specimen is supposed to be mounted in the center since asymmetrically mounted masses cause disturbances in the system and may damage the bearings due to the larger displacements. Furthermore, a single-point control in the center near the potential mounting locations of the specimen is to be preferred since the response power at any arbitrary point on the structure usually deviates from the responses at the control location. For the final fixture design, the setup requirements from fig. (4.3) have to be met. Besides mass and both horizontal and vertical positions of the CoG, every setup changes the stiffness and inertia of the bearing unit.
Different setups shall be investigated and evaluated subsequently with respect to their accuracy in running a simultaneous (XYZ) RMS 15 m/s² random profile. Therefore, the mean and maximum deviation of the response PSD value of the most imprecise axis at each frequency is determined. For the sake of reproducibility all screw joints of each setup are always applied with a 20 Nm torque. All tests are then repeated after a total shaker service time of 100 operating hours. The initial measurements were performed with the IMV K2 vibration controller and are slightly corrupted by current noise. The most severe noise peaks usually seem to occur at 850 Hz and 950 Hz. The measurements after 100 operating hours are performed with the Dataphysics Signal Star Matrix. The results are not corrupted by the noise anymore due to the controller's ability of noise compensation.
As a reference, the first evaluation is performed on the bare table controlled in the center. The results are given in table (4.2) below and in table (B1) within the appendix.

Table 4.2: Deviation from reference profile for bare table setup

Frequency range	$10 - 1000$ Hz	$1000 - 1500$ Hz	$1500 - 2000$ Hz
Mean deviation	9.0 % (noisy)	11.4 %	299.3 %
Max deviation	21.1 % (noisy)	44.4 %	2319.3 %

The next structure to be tested is a homogeneous plate of 16.8 kg with a height of 24 mm, shown in fig. (4.8). The resulting accuracies are given in table (4.3) and table (B2) within the appendix. Especially the mode around 1500 Hz causes a higher deviation in Z-direction which lowers the accuracy for the medium frequency range. The response amplitude at the center which is the node location of the particular mode is lowered by the plate and the screws. Thus,

the controllability is reduced. The decrease of the response amplitude is verified with a test controlled on the edge for both bare table and plate. For the second bending mode around 1850 Hz an opposite effect occurs: The response amplitude is higher than on the bare table. This can be explained by an increased stiffness of the plate which leads to an increased rigid body motion in Y-direction at the center and thus a better controllability. The effect is also verified with a test controlled on the edge for both bare table and plate.

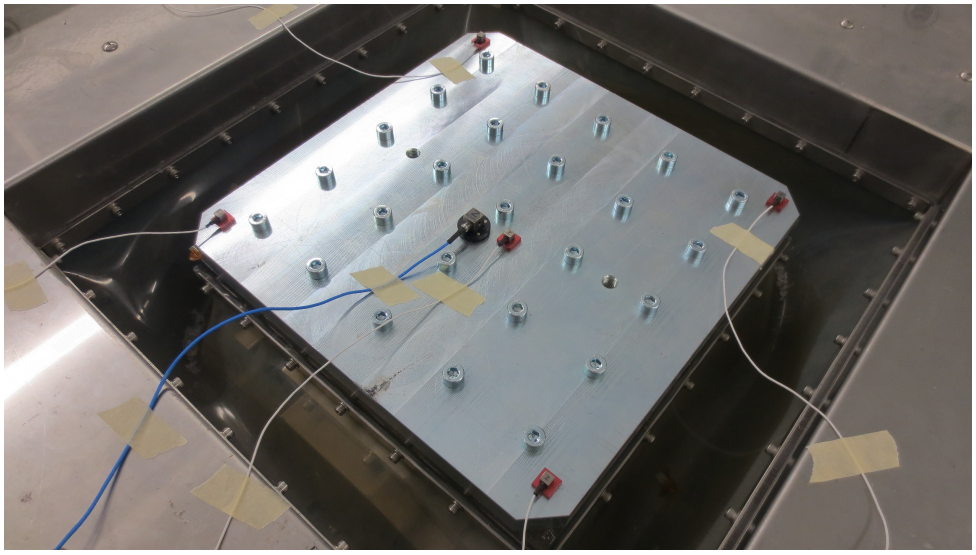

Figure 4.8: Setup with plate [39]

Table 4.3: Deviation from reference profile for plate setup

Frequency range	$10 - 1000$ Hz	$1000 - 1500$ Hz	$1500 - 2000$ Hz
Mean deviation	9.4 % (noisy)	32.8 %	206.3 %
Max deviation	63.7 % (noisy)	310.6 %	794.0 %

Since a plane setup seems not to give accurate results and is furthermore not within the required boundaries of fig. (4.3), a block setup shown in fig. (4.9) is considered. The block consists of two caulked pieces with a total weight of 8.3 kg and a height of 120 mm. It is mounted on the table with 9 screws of a nominal length of 90 mm and a thread length of 30 mm. The accuracies are given in table (4.4) and table (B3) within the appendix. First, the raised position of the control sensor produces an increased response signal for the modes that have a node located around the center. As an example serves the mode around 1500 Hz which is now better controllable. Second, the mode is shifted down below 1500 Hz and contributes to the medium frequency range. Due to the strongly increased modal stiffness of the plate, the second bending mode is shifted to the vicinity of 2000 Hz while its modal participation on the table is lowered. The response PSDs of the block setup are shown in fig. (4.10). The measurement points are arranged similar to the bare table setup except M1 which is now located on top of the block.

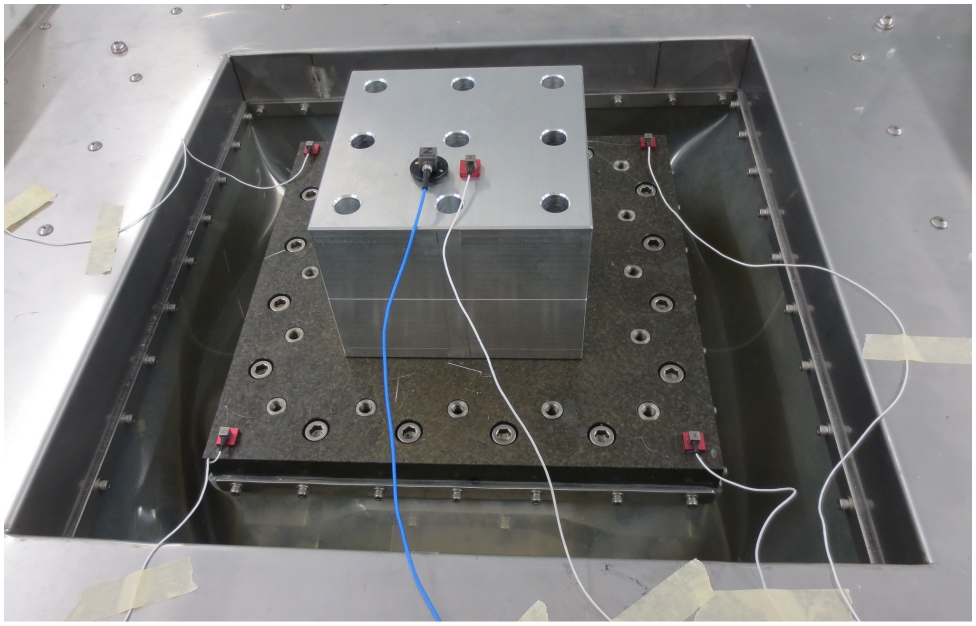

Figure 4.9: Setup with block [39]

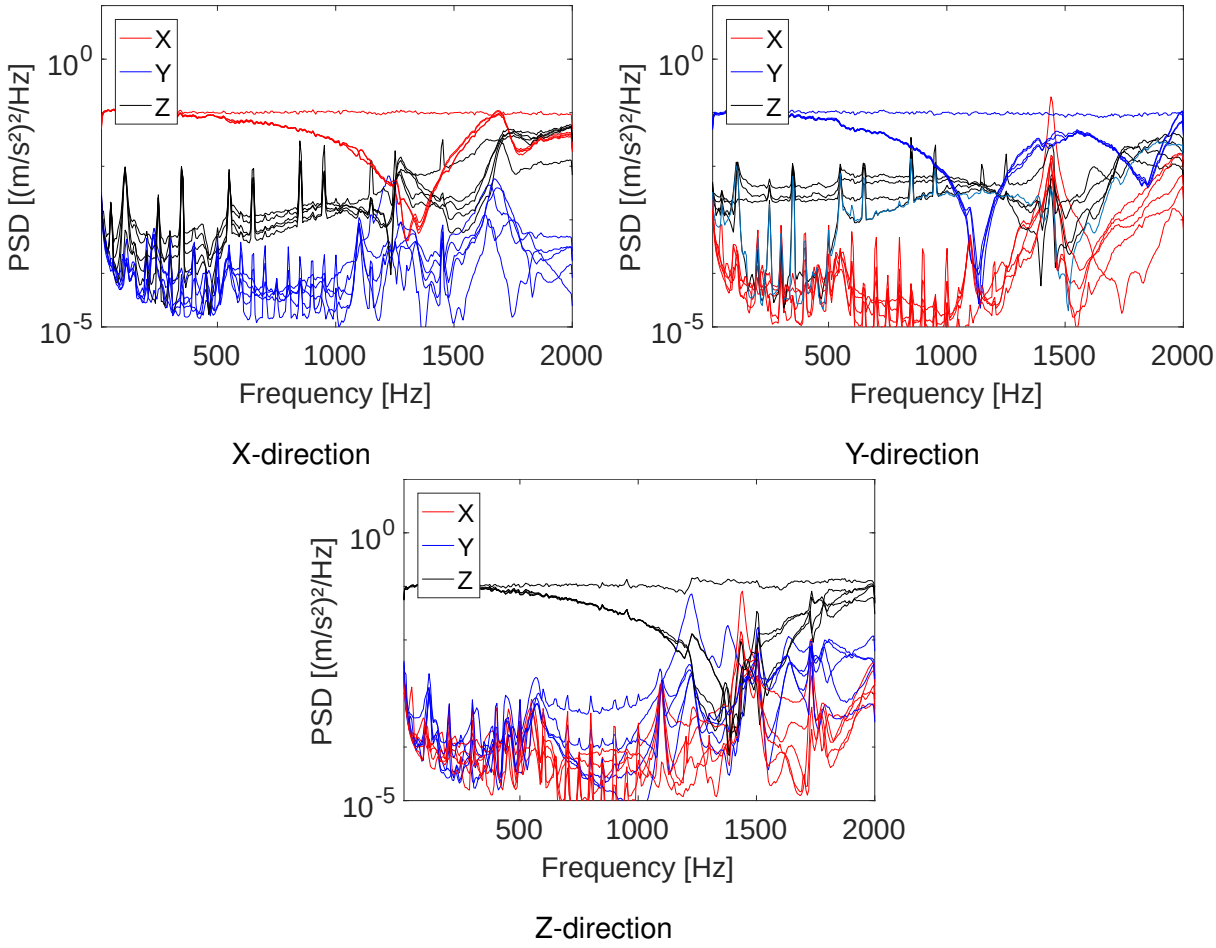

Figure 4.10: Response PSD of random profile for block setup

Table 4.4: Deviation from reference profile for block setup

Frequency range	$10 - 1000$ Hz	$1000 - 1500$ Hz	$1500 - 2000$ Hz
Mean deviation	10.3 % (noisy)	16.4 %	24.0 %
Max deviation	35.2 % (noisy)	30.7 %	37.9 %

Considering table (B3) within the appendix, a slight improvement of the accuracy in the higher frequency range over time can be detected. This can be explained by a minor relaxation of the bearing unit which leads to a higher response in the particular frequency range and therefore a better controllability. The response PSDs of the block setup after 100 hours operating time are given in fig. (B2) within the appendix.

Since the block setup is still not within the required boundaries of fig. (4.3), further mass is added to the table by using two frames around the block as shown in fig. (4.11). Thereby, the setup is enhanced by further stiffness. The response amplitudes along the edge can be reduced for several modes which leads to slightly better accuracies as can be seen in table (4.5) and table (B4) within the appendix. Each frame has a mass of 2.5 kg and a height of 25 mm. The entire setup then has a total mass of 13.3 kg and a CoG height of 46 mm which lies inside the required boundaries. It can be used as an adapter for smaller components as will be seen in the next subsection. The mounting of the frames is realized with 16 screws of a nominal length of 60 mm and a thread length of 30 mm.

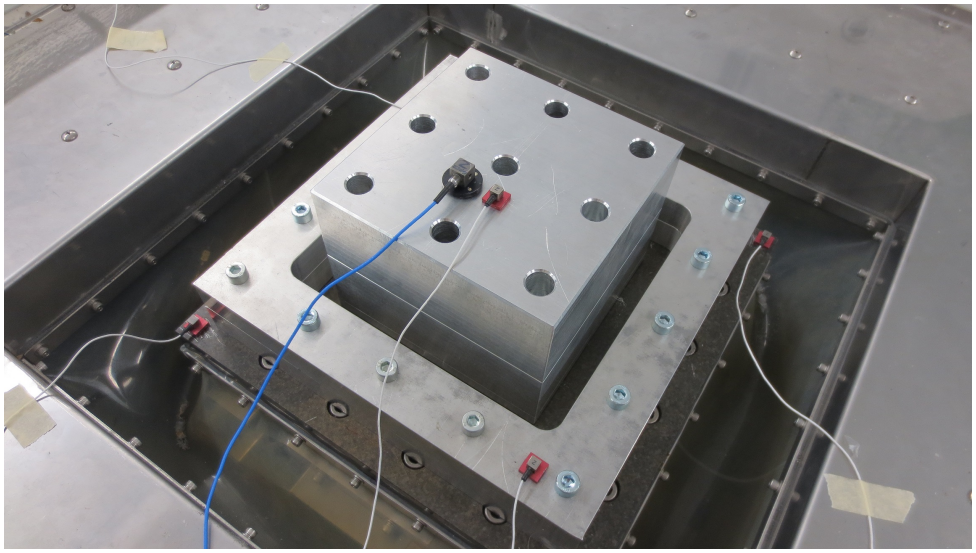

Figure 4.11: Setup with block and frame [39]

Table 4.5: Deviation from reference profile for block with frame setup

Frequency range	$10 - 1000$ Hz	$1000 - 1500$ Hz	$1500 - 2000$ Hz
Mean deviation	10.5 % (noisy)	14.1 %	19.0 %
Max deviation	134.2 % (noisy)	29.2 %	29.8 %

To provide a feasible adapter for larger or broader components, a plane structure is manufactured from a solid block shown in fig. (4.12) and referred to as adapter plate. Cavities are inserted at the bottom to meet the required mass (13.5 kg) and CoG height (45 mm). It is shown in fig. (B3) within the appendix. At the mode around 1850 Hz hardly no response can be measured in the center of the adapter plate which is therefore not appropriate as control location. The effect is verified with a test controlled on the edge. Another peripheral location is then used as a control position which can be seen in fig. (4.12). The accuracies of the test are given in table (4.6) and still leave room for improvement. No measurements after 100 operating hours are available for the adapter plate.

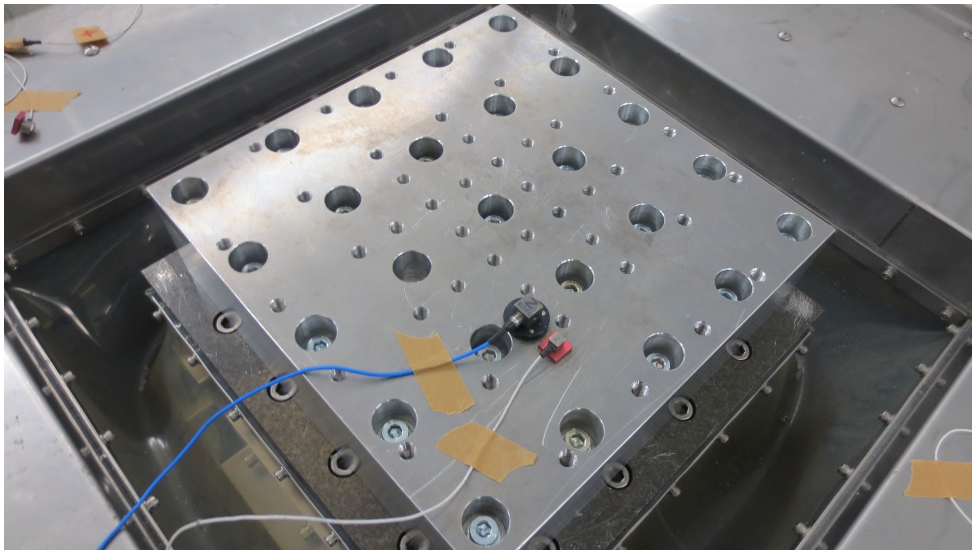

Figure 4.12: Adapter plate

Table 4.6: Deviation from reference profile for adapter plate

Frequency range	$10 - 1000$ Hz	$1000 - 1500$ Hz	$1500 - 2000$ Hz
Mean deviation	4.6 %	10.3 %	46.8 %
Max deviation	13.9 %	20.3 %	191.1 %

4.1.4 Verification with a Simple Automotive Component

The test of both the original and modified fixture is demonstrated with an example DUT. Therefore, the simple automotive component which was introduced in subsection 3.4.2.2 is considered. Its mounting fixture is shown in fig. (4.13) and has a total weight of 1.7 kg. Thereby, the main fixture has a weight of 0.7 kg and the small adapter plate a weight of 1.0 kg. The position of the control sensor generally depends on the mounting location of the DUT and its accessibility provided by the fixture. Within the scope of the verification two scenarios are considered: A control position on the bottom of the fixture as shown in fig. (4.13) and a control position on top as shown in fig. (4.14). For the vibration control the Dataphysics Signal Star Matrix is used. The accuracies are given in tables (4.7) and (4.8). They show an absolutely imprecise accuracy for the control at the bottom as expected[1], and a sufficient accuracy for the control on top due to the raised position which intensifies the measured response amplitude of the second buckling mode.

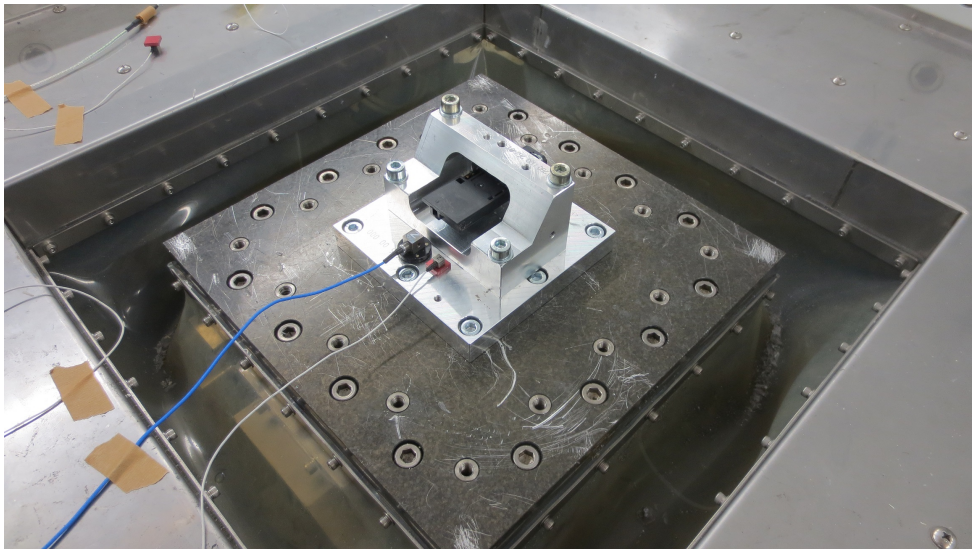

Figure 4.13: Component mounted directly on shaker plate, control at bottom [39]

Table 4.7: Deviation from reference profile for specimen mounted directly on shaker plate, control on bottom

Frequency range	$10 - 1000$ Hz	$1000 - 1500$ Hz	$1500 - 2000$ Hz
Mean deviation	4.2 %	10.0 %	665.3 %
Max deviation	13.4 %	20.7 %	3698.6 %

[1] Position near the vibrational node

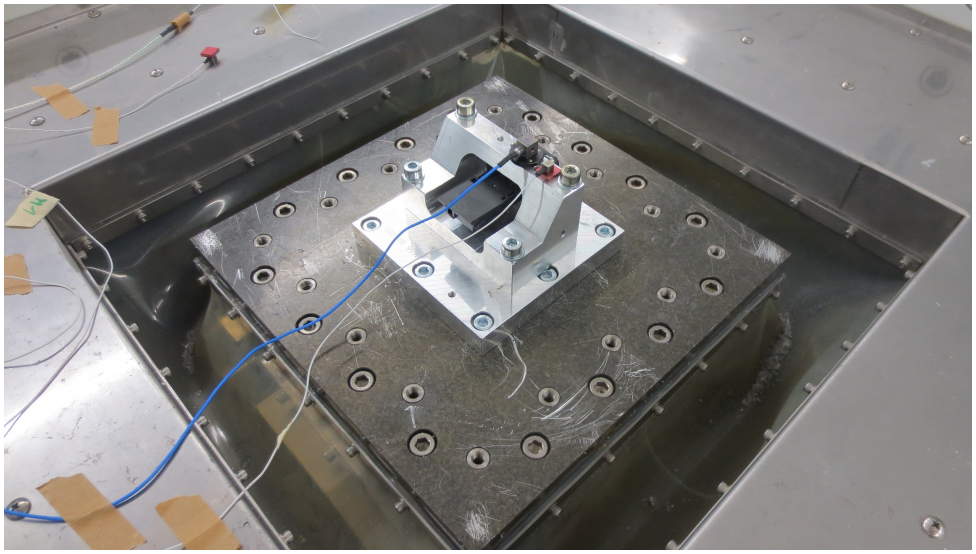

Figure 4.14: Component mounted directly on shaker plate, control at top [39]

Table 4.8: Deviation from reference profile for specimen mounted directly on shaker plate, control on top

Frequency range	$10 - 1000$ Hz	$1000 - 1500$ Hz	$1500 - 2000$ Hz
Mean deviation	$4.2\ \%$	$7.2\ \%$	$16.4\ \%$
Max deviation	$16.6\ \%$	$15.2\ \%$	$35.5\ \%$

To meet the required specifications, the fixture proposed in fig. (4.11) is considered. Furthermore, it is necessary for the case where the control shall be accomplished at the bottom. Threaded holes are brought into the block for the assembly. The configurations are shown in fig. (4.15) and (4.16) for both control scenarios. The resulting accuracies given in tables (4.9) and (4.10) are sufficient. Slightly better results are achieved with the raised position where higher responses occur.

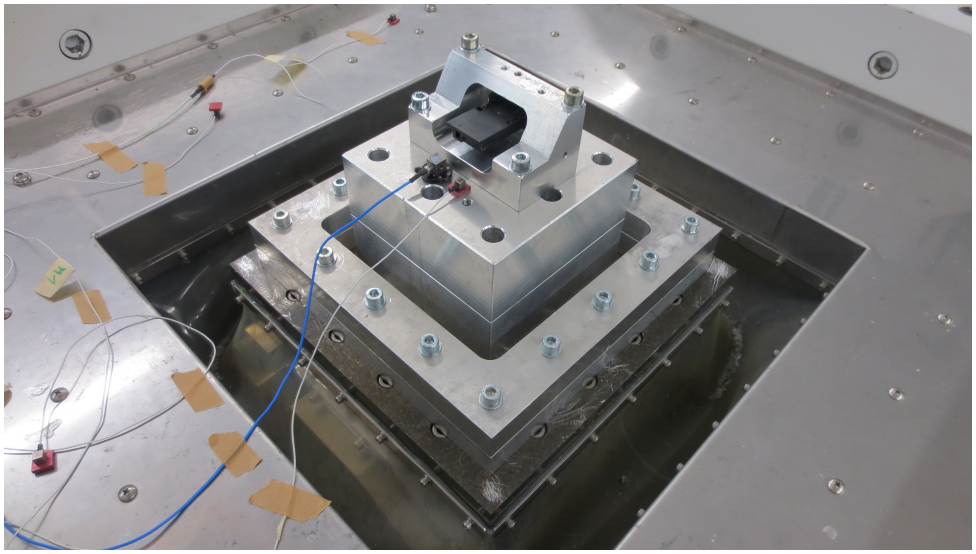

Figure 4.15: Component mounted on block with frame setup, control at bottom [39]

Table 4.9: Deviation from reference profile for specimen mounted on block with frame setup, control at bottom

Frequency range	$10 - 1000$ Hz	$1000 - 1500$ Hz	$1500 - 2000$ Hz
Mean deviation	$5.7\ \%$	$16.3\ \%$	$15.3\ \%$
Max deviation	$18.1\ \%$	$23.6\ \%$	$27.7\ \%$

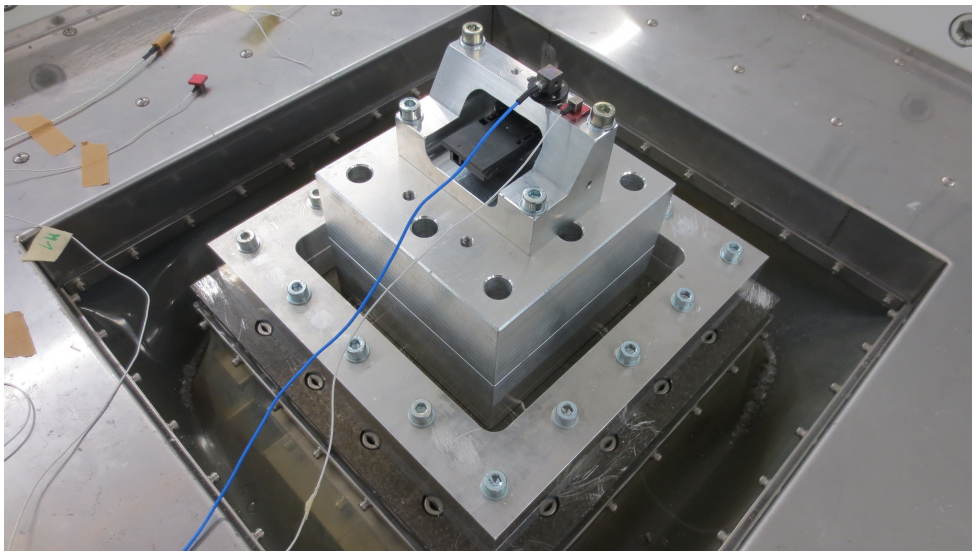

Figure 4.16: Component mounted on block with frame setup, control at top [39]

Table 4.10: Deviation from reference profile for specimen mounted on block with frame setup, control on top

Frequency range	$10 - 1000$ Hz	$1000 - 1500$ Hz	$1500 - 2000$ Hz
Mean deviation	$5.3\ \%$	$9.5\ \%$	$7.6\ \%$
Max deviation	$15.4\ \%$	$19.4\ \%$	$14.6\ \%$

4.1.5 Considerations on Phase Control

So far, only PSD levels were used for the evaluation due to their major influence on the potential fatigue damage of the DUT. However, a full SDM is generally used in order to replicate field data qualitatively, as described in [86]. Further techniques like the control of PSD and coherence only, as mentioned in [33], are not considered. In this subsection the effects and limitations in controlling phases and coherences are discussed.
As already explained in subsection 2.1.1, the reference SDM has to be positive definite. The Silvester's criterion provides an inequality expressed with all three phases and coherences derived by the determinants of the upper left 1×1, 2×2 and 3×3 corner. It is given in [55] and can be expressed as

$$1 - \gamma_{12}^2 - \gamma_{13}^2 - \gamma_{23}^2 + 2\cos(\theta_{12} - \theta_{13} + \theta_{23})\sqrt{\gamma_{12}^2\gamma_{13}^2\gamma_{23}^2} \geq 0 \quad . \tag{4.1}$$

If all phases are consistent ($\theta_{12} - \theta_{13} + \theta_{23} = 0$), the SDM is positive definite for any coherence values. In case of an inconsistent phase relation the coherences have to be reduced in order to obtain a positive definite SDM. The strongest violation can be produced with $\theta_{12} - \theta_{13} + \theta_{23} = \pi$ which leads to the cosine term of eq. (4.1) being $\cos(\theta_{12} - \theta_{13} + \theta_{23}) \geq -1$. In this case the Silvester's criterion in eq. (4.1) holds exactly for coherence values of $\gamma_{12} = \gamma_{13} = \gamma_{23} = 0.5$ or below. A higher coherence value for one axis can be applied if the other coherences are decreased at the same time. The described case with coherence values of 0.5 is tested with the setup of fig. (4.16). As input phases, $\theta_{xy} = -120°$, $\theta_{xz} = 0°$ and $\theta_{yz} = -120°$ are applied which represents a highly inconsistent phase relation. The controlled spectra are given in fig. (4.17) and show a sufficient phase and coherence control without disturbances by the modes. Since the SDM gets nearly negative definite, the controller is assumed to be pushed on its limits which can be detected by the deviation of the respective phases from $-120°$.

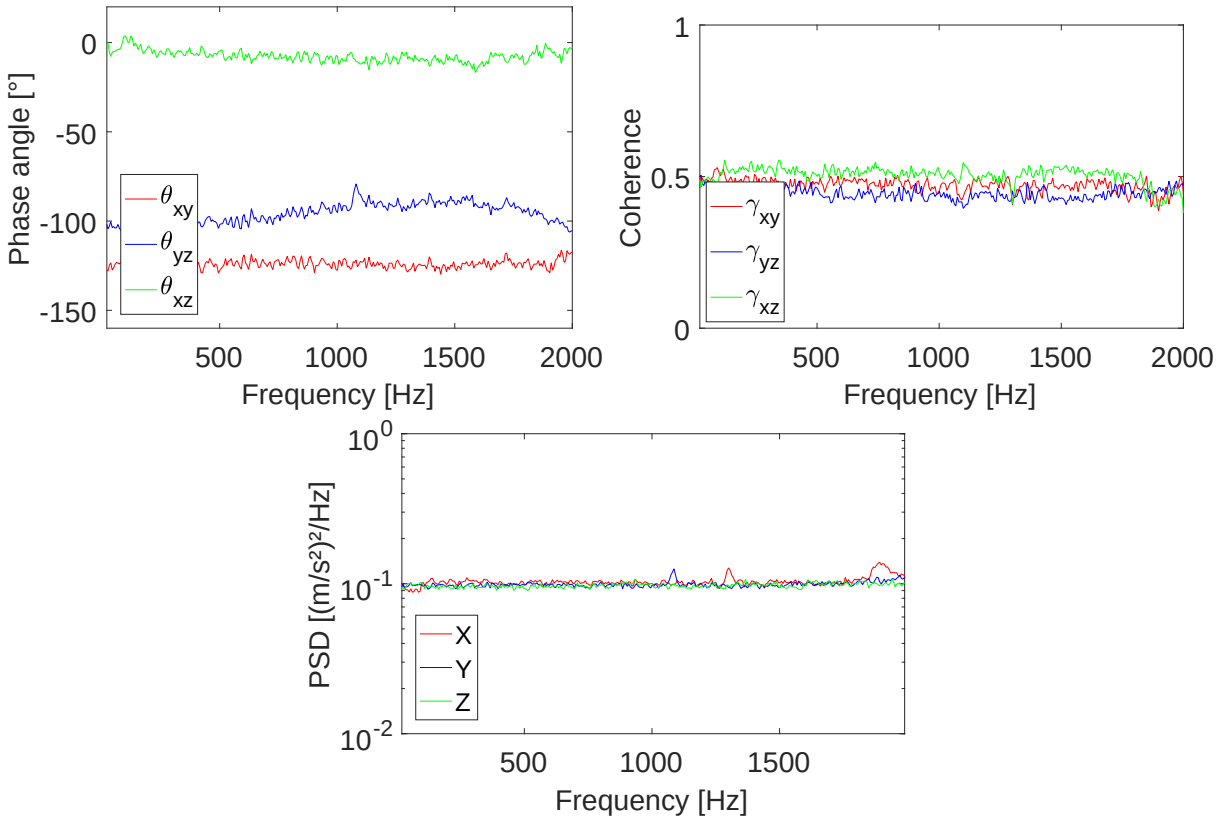

Figure 4.17: PSD, phase and coherence output for input PSD levels 0.1 (m/s²)²/Hz, phases $-120°$, $-120°$, $0°$ and input coherences of 0.5

A forced phase response may also lead to distortions of the PSD responses at particular modes, especially if the test setup is affected by mass inertia. If this issue is to be removed for testing, a reduction of coherences has to be performed until all modes can be controlled sufficiently. Thereby, it is proposed to scale all coherences simultaneously for the entire frequency range to maintain their desired proportions to each other but in a weak form.
Furthermore, care has to be taken of choosing appropriate measurement positions in order to obtain the same phases as controlled due to the influence of the shaker modes (refer to a rotational mode around a particular axes where a phase difference of π occurs between the two sides).

4.2 Vibration Controller Investigation

Apart from the 3D-shaker system itself, the vibration controller is of crucial importance, especially regarding its software component. In this section, different controllers and their particular configuration are compared qualitatively with measurable criteria that are to be defined beforehand. Since no insight into the controller programming is possible, it is treated as a black box. The underlying basics of all MIMO vibration control systems were given previously in subsection 2.3.1. Vibration control actions are especially needed around resonances. The drive signals are decreased respectively to avoid overshoots or increased when being located at a vibrational node. Difficulties may occur if the resulting cross accelerations due to mass inertia counter the target profile, as can be seen exemplary in [24]. Furthermore, nonlinear behavior

such as amplitude sensitive FRFs or unsteady vibrational nodes may lead to overshoots of the defined profile. In a complex system several issues may also occur at the same time.

4.2.1 Definition of Measurable Evaluation Criteria

At first, measurable criteria are to be defined for the comparison since no differences in the front-ends of the considered controllers are observable. Therefore, the control chart for random vibration control of fig. (2.9) is referred and marked respectively in fig. (4.18).
The first defined criterion is the system identification process which gives evidence about the processing of the initial transfer matrix and thus the starting point of the control actions. The accuracy of the system identification can be influenced by the type of random signal generation that is used. Apart from the already introduced pseudo random, the so-called pure random is oftenly used which is basically a random number generator based signal, as described in [22]. The different effects on the system identification are explained in [12], where it is stated that better FRF results can be achieved using pseudo random. Since the drive spectra being usually described in voltage, the transfer matrix $H(f)$ is given in terms of $\left[\frac{m/s^2}{V}\right]$. The second criterion is the stability of the control loop in presence of disturbances as for example hum noise that occurs on the amplifiers as mentioned in subsection 4.1.2. The third detected criterion concerns the configuration of the control process algorithm. Two basic methods are available: Updating the inputs through an error correction and updating the full transfer matrix.

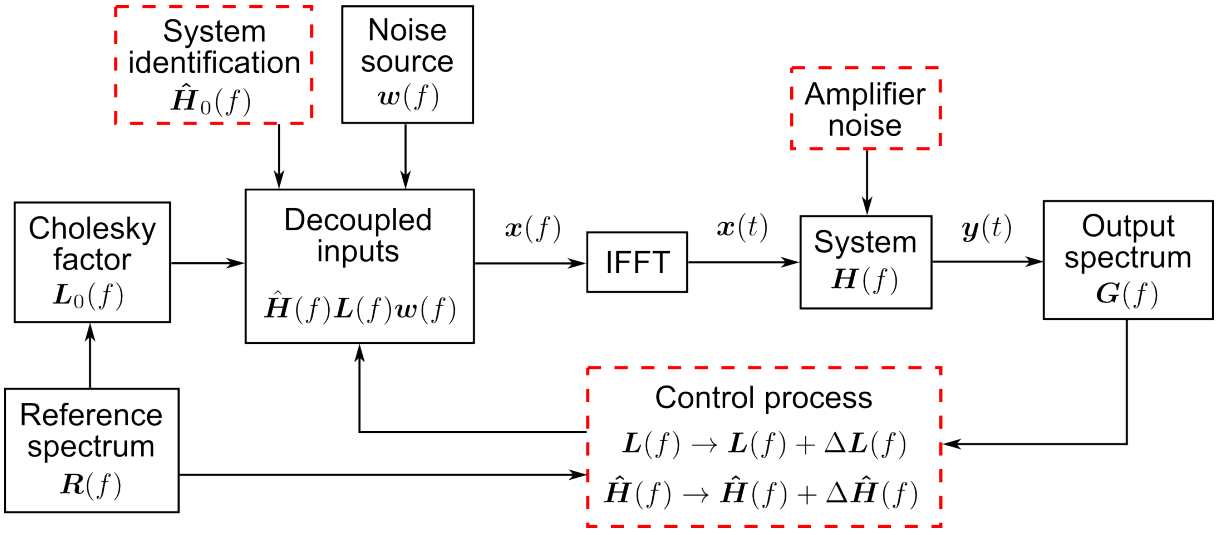

Figure 4.18: Flow-chart of random vibration control algorithm with measurable criteria for controller comparison

4.2.2 Comparison of Different Systems

A qualitative comparison of the respective profile conformity is used to evaluate the differences. Both controllers introduced in subsection 4.1.1 (IMV K2 and Dataphysics Signal Star Matrix) are considered. For all tests the same adjustable parameters are used for signal processing (PSD calculation), control (frequency lines and bandwidth) and initial input voltage (system identification).
The transfer functions of the initial system identifications for both controllers are shown in fig. (4.19) for a bare table setup. It has moderate deviations on the main axes and larger deviations on its cross-axes, especially in the higher frequency range. The most obvious reason appears to be the difference in the excitation. While controller 1 performs a continuous excitation, the excitation of controller 2 is controlled batch-wise. Thereby, the excited resonances are likely to fade while in the other case modes are able to develop. Furthermore, a difference might be caused by the strongly nonlinear behavior of the shaker.

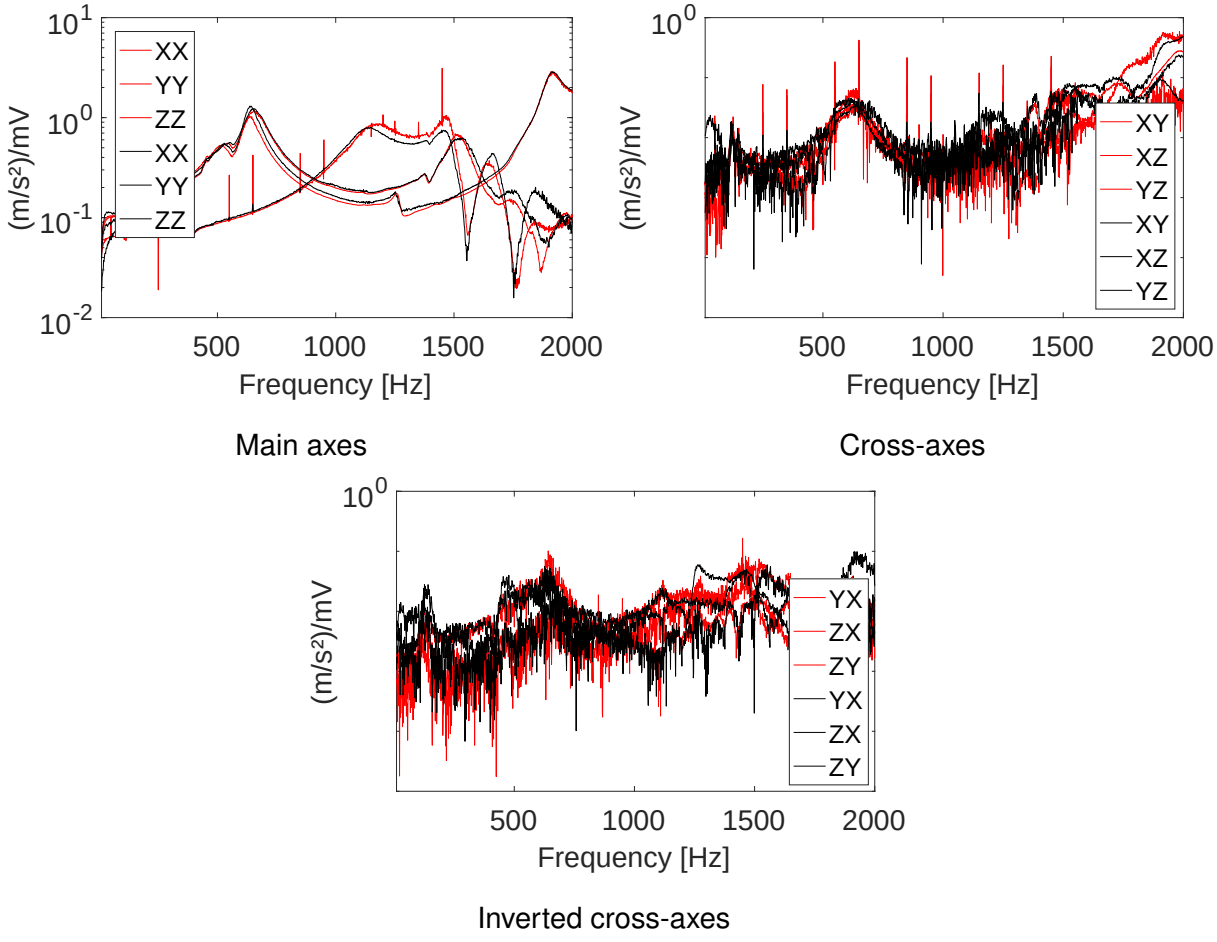

Figure 4.19: Initial transfer functions of controller 1 (red) and controller 2 (black)

The influence of disturbances on the control loop stability is evaluated with the setup from fig. (4.11). The resulting PSD responses in fig. (4.20) show that controller 2 is able to remove the hum noise that is especially present at 850 Hz and 950 Hz. The reason might be a band

stop filter, respectively a notch filter that removes hum noise at every 50 Hz in European power networks[2]. A notch filter is a strongly narrow version of a band pass filter which allows to reduce noise without influencing the desired transfer functions. The results of the initial system identification in fig. (4.19) also show hardly any noise using controller 2.

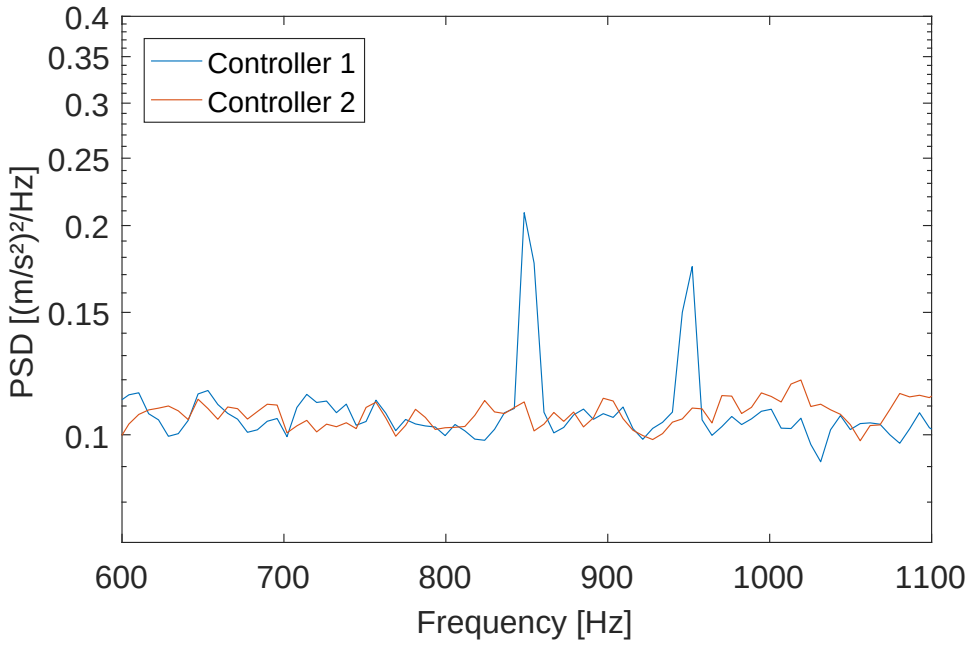

Figure 4.20: Influence of current noise at 850 Hz and 950 Hz on controller 1 and 2

The configuration of the control process is evaluated with the same test setup. While no difference can be detected for a normal random vibration test, major advantages of using a transfer matrix update are detected for deterministic vibration control. Fig. (4.21) shows the PSD responses of different TWR tests using an example signal. As explained in subsection 2.3.1.2, the transfer matrix update during testing is referred to as adaptive control. Besides a peak at 1450 Hz due to hum noise, no difference in accuracy is detected between controller 1 and 2 when omitting the transfer function update[3].

[2] 60 Hz in US and parts of Asia
[3] Controller 1 doesn't provide adaptive control for TWR at all

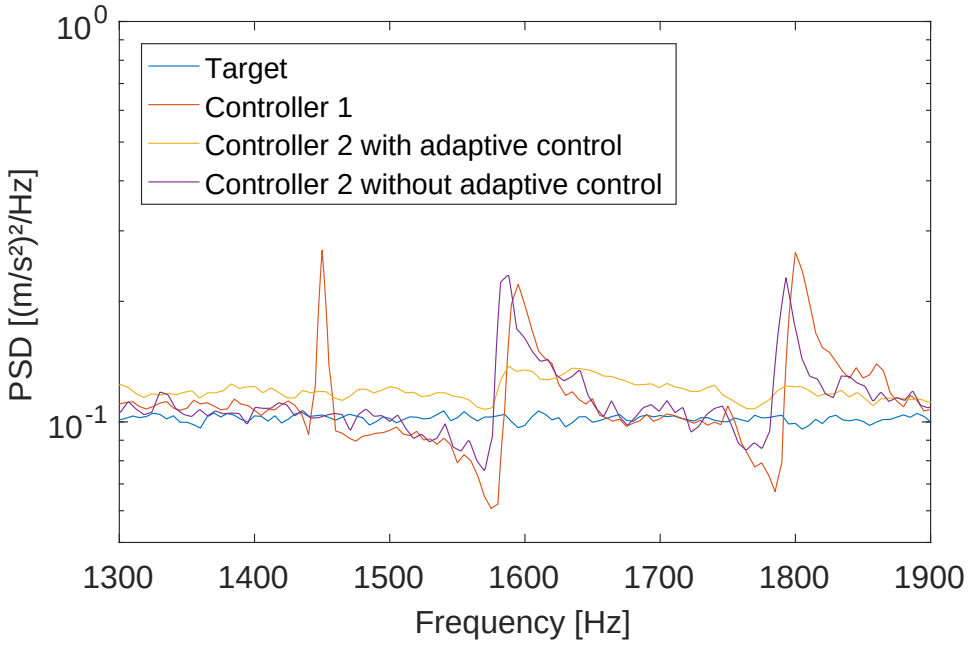

Figure 4.21: Time Waveform Replication of an example signal with different controller configurations

The investigation concludes in the utility of notch filters and adaptive control for an accurate vibration testing. Furthermore, the precision of the initial system identification may influence the vibration control positively with providing reasonable start values.

In this chapter, an entire 3D-shaker system together with its vibration controller was investigated. Thereby, a focus was put on calibration to ensure an effective control for different possible test setups. The work enables accurate multi-axis vibration testing of complex structures which is the base for the evaluation performed in chapter 6.

5 Multi-Axis Vibration Test Definition

The scope of this chapter is the derivation of multi-axis vibration test profiles from available field data. To ensure a realistic multi-axis vibration test, it is important to define a reference that covers all driving scenarios to be considered.
Existing uniaxial and multiaxial methods are reviewed and extended appropriately. Thereby, it is distinguished between methods using field data directly (section 5.1), the FDS approach (section 5.2) and standard profiles (section 5.3). A focus is put on random vibration due to its extensive usage.

5.1 Direct Random Vibration Profile Derivation from Field Data

The averaging method introduced in subsection 2.3.2.1 is applied on an example dataset for random vibration. An enveloping method considering amplitudes, phases and coherences is proposed subsequently. It contains the enveloping process itself, as well as a following manipulation of the resulting profile SDM to maintain positive definiteness. Regarding the latter part, existing methods are discussed and compared with the proposed one.

5.1.1 Composition of the Spectral Density Matrix

Starting point is a set of SDMs obtained from four typical road vibration scenarios, differing in pavement and speed. The raw data is left unprocessed and without the omission of certain time windows. In a first step, mean values of the SDM are calculated according to eq. (2.96) without applying weighting factors. Thereby, mean PSDs, mean phases and mean magnitude squared coherences are obtained, as shown in fig. (5.1). The PSDs are shown on the diagonals (longitudinal, transverse, vertical), the phases in the upper triangle and the magnitude squared coherences in the lower triangle, as illustrated in table (5.1). Within the scope of test profile derivation, usually the magnitude squared form of the coherences are used as simplification. The mean calculation for amplitudes and phases can be performed analogue for sine profiles, as explained in subsection 2.3.2.1.

Table 5.1: SDM profile configuration

G_{11} (longitudinal)	θ_{12}	θ_{13}
γ_{12}^2	G_{22} (transverse)	θ_{23}
γ_{13}^2	γ_{23}^2	G_{33} (vertical)

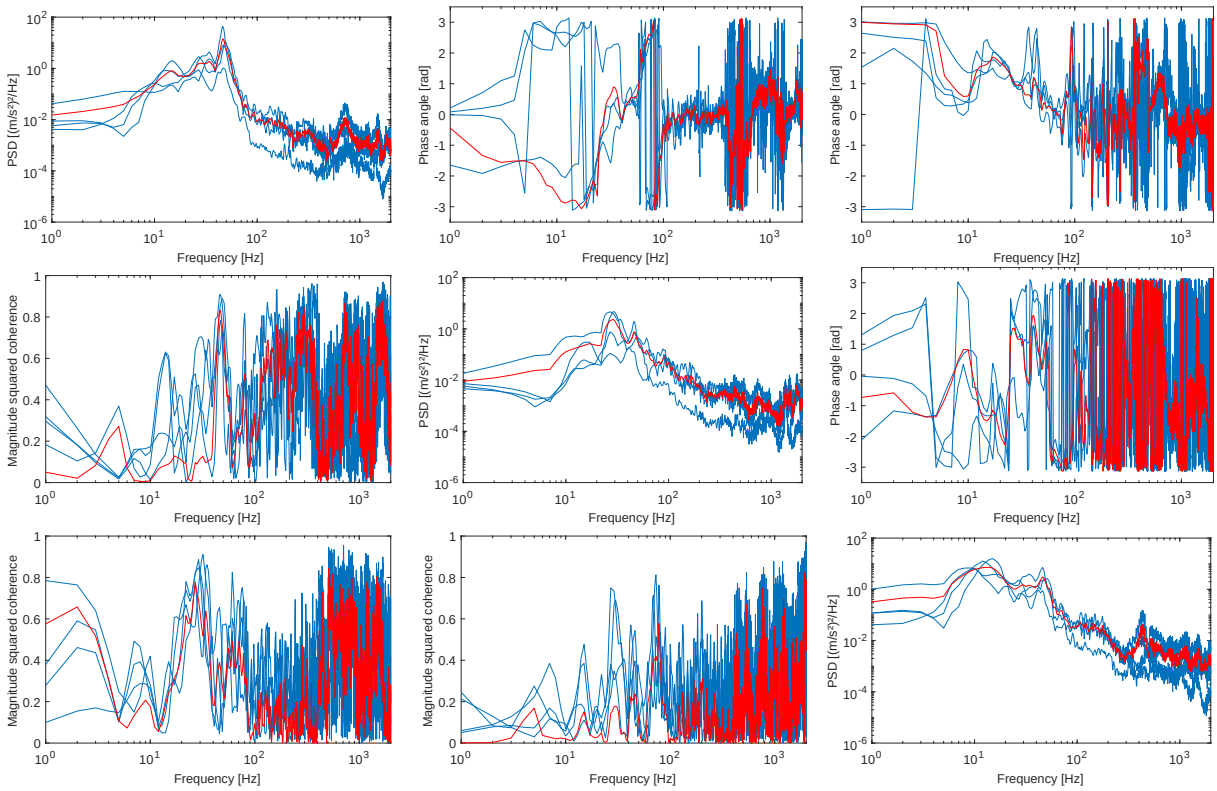

Figure 5.1: Exemplary profile SDMs together with mean values in red, phases on the upper triangle, magnitude squared coherences on the lower triangle

5.1.2 Usage of Straight-line Specifications

As a next step, envelopes are applied to the PSDs, phases and magnitude squared coherences. The PSD terms are still to be covered with respect to their maximum values. The envelope $G_{11,env}(f)$ over a set of PSDs $[G]$ is defined according to eq. (2.100) as

$$G_{11,env}(f) = \text{envelope}\left[\bigcup_{i\in[G]} G_{11,i}(f)\right] \tag{5.1}$$

with an analogue expression for $G_{22,env}(f)$ and $G_{33,env}(f)$. While the PSDs are enveloped in a usual manner, the phase and magnitude squared coherence envelopes $\theta_{12,env}(f)$, $\theta_{13,env}(f)$, $\theta_{23,env}(f)$, $\gamma^2_{12,env}(f)$, $\gamma^2_{13,env}(f)$ and $\gamma^2_{23,env}(f)$ are oriented on the mean values. They are described as

$$\theta_{12,env}(f) = \text{envelope}\left[\bar{\theta}_{12}(f)\right] \tag{5.2}$$

and

$$\gamma^2_{12,env}(f) = \text{envelope}\left[\bar{\gamma}^2_{12}(f)\right] \quad . \tag{5.3}$$

For the sake of perceptibility only mean phases and mean magnitude squared coherences are given on the triangles of fig. (5.2). Again, the phases are shown in the upper triangle, the

magnitude squared coherences in the lower triangle. The nature of the envelopes depends on its aim, on the complexity of the profile to be defined and its desired precision.

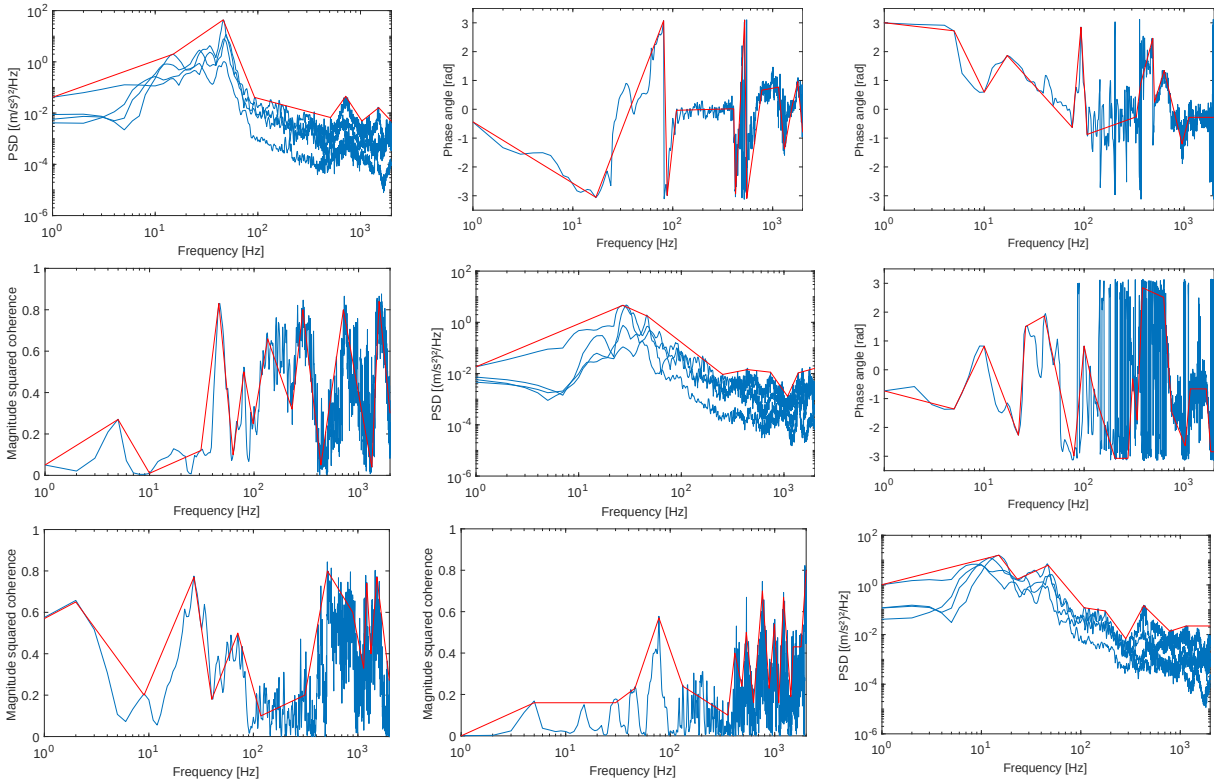

Figure 5.2: Exemplary profile SDMs with envelopes, phases on the upper triangle, magnitude squared coherences on the lower triangle

The corresponding CSD terms have to be recalculated using all envelope values as

$$G_{12,env}(f) = \sqrt{\gamma^2_{12,env}(f)\; G_{11,env}(f)\; G_{22,env}(f)}\; e^{j\theta_{12,env}(f)} \tag{5.4}$$

with an analogue expression for $G_{13,env}(f)$ and $G_{23,env}(f)$. The final profile SDM can then be stated as

$$\boldsymbol{G}_{env}(f) = \begin{bmatrix} G_{11,env}(f) & G_{12,env}(f) & G_{13,env}(f) \\ G_{21,env}(f) & G_{22,env}(f) & G_{23,env}(f) \\ G_{31,env}(f) & G_{32,env}(f) & G_{33,env}(f) \end{bmatrix} . \tag{5.5}$$

Once again, the enveloping of amplitudes and phases can be used analogue for sine profiles. In case of a required scaling, eq. (2.101) can be used for the entire SDM instead of scaling each axis individually as it is proposed by [27]. The scaling ratio is valid for all axes at the same time in order to maintain their relative proportions.

5.1.3 Manipulation of the Spectral Density Matrix

Manipulations on the CSD terms of a SDM are likely to produce a negative definite matrix. Thus, the matrix has to be corrected at the respective frequencies to be physically realizable. Two already existing approaches are described in [33]. The first is the replacement of negative

eigenvalues of the SDM with small positive ones which also may affect the PSD terms. The second approach is the reduction of all coherences until the resulting SDM gets positive definite which may strongly decrease the coherence values. Another possible approach is using the phase relationship $\theta_{23} = \theta_{13} - \theta_{12}$, described in subsection 4.1.5. For each frequency the phase value with the lowest corresponding coherence can be chosen. It is then adjusted according to the given relationship. Thereby, the least important phase information is manipulated strongly. Besides the methods using all relations, also one coherence or phase-coherence pairing can be changed solely. Latter one is described in [50] using the constraint defined by the Silvester's criterion and is not considered further.
The introduced methods (see table (5.2) including the proposed optimization method) have either strong influence on individual phases and coherences or violate the PSD terms which has to be avoided in any case.

Table 5.2: Changed parameters of different manipulation methods

Manipulation method	Changed parameters
Coherence reduction	$\gamma_{12}, \gamma_{13}, \gamma_{23}$
Eigenvalue replacement	$G_{11}, G_{22}, G_{33}, \theta_{12}, \theta_{13}, \theta_{23}, \gamma_{12}, \gamma_{13}, \gamma_{23}$
Phase change	$\theta_{12}, \theta_{13}, \theta_{23}$
Optimization	$\theta_{12}, \theta_{13}, \theta_{23}, \gamma_{12}, \gamma_{13}, \gamma_{23}$

A method is needed which changes all phases and coherences at the same time and in an optimum way. Therefore, an optimization of the envelope SDM $\boldsymbol{G}_{env}(f)$ is performed using so-called Semidefinite Programming (SDP). As described in [93], the SDP is the generalized form of the Linear Programming (LP). The minimization problem on the SDM can be expressed using the Frobenius norm as

$$\begin{aligned} \text{minimize} \quad & \left\| \boldsymbol{G}_{env}(f) - \boldsymbol{B}(f) \right\|_F \\ \text{subject to} \quad & \boldsymbol{B}(f) \succ 0 \end{aligned} \tag{5.6}$$

with the optimized matrix $\boldsymbol{B}(f)$, that is to be positive definite. The constraint $\succ$ denotes the positive definiteness of the matrix. Optimization problems can only be formulated on real values by nature. Since the SDM being a complex valued matrix, a modified optimization formulation has to be used which can be achieved by so-called Complex Semidefinite Programming (CSDP). The n-dimensional matrix has to be mapped from $\mathbb{C}_n$ to $\mathbb{R}_{2n}$ in a way that yields a symmetric matrix, as described in [23]. A transformation $\mathcal{J}$ is therefore used which is stated as

$$\mathcal{J}\left(\boldsymbol{B}(f)\right) = \begin{bmatrix} \mathrm{Re}\left(\boldsymbol{B}(f)\right) & -\mathrm{Im}\left(\boldsymbol{B}(f)\right) \\ \mathrm{Im}\left(\boldsymbol{B}(f)\right) & \mathrm{Re}\left(\boldsymbol{B}(f)\right) \end{bmatrix} . \tag{5.7}$$

The SDP minimization problem in eq. (5.6) is then performed with symmetric 6×6 matrices. For the optimization, a software package provided by CVX Research is used. It includes interior-point methods as numerical solver.
The optimization has to be accomplished on the phases and coherences only. Therefore, additional constraints for the PSD terms have to be applied according to

$$\begin{aligned} \text{subject to} \quad & B_{11}(f) = G_{11,env}(f) \\ \text{subject to} \quad & B_{22}(f) = G_{22,env}(f) \\ \text{subject to} \quad & B_{33}(f) = G_{33,env}(f) \quad . \end{aligned} \tag{5.8}$$

The results of the optimization algorithm on the example envelopes are given in fig. (5.3). The changes on the coherences appear qualitatively larger than on the phases, however their effects are generally not comparable. While the optimized phase profiles deviate by an angle of up to 0.76 rad, the magnitude squared coherences show deviations of at most 0.34 (in terms of coherence the maximum deviation is 0.58).

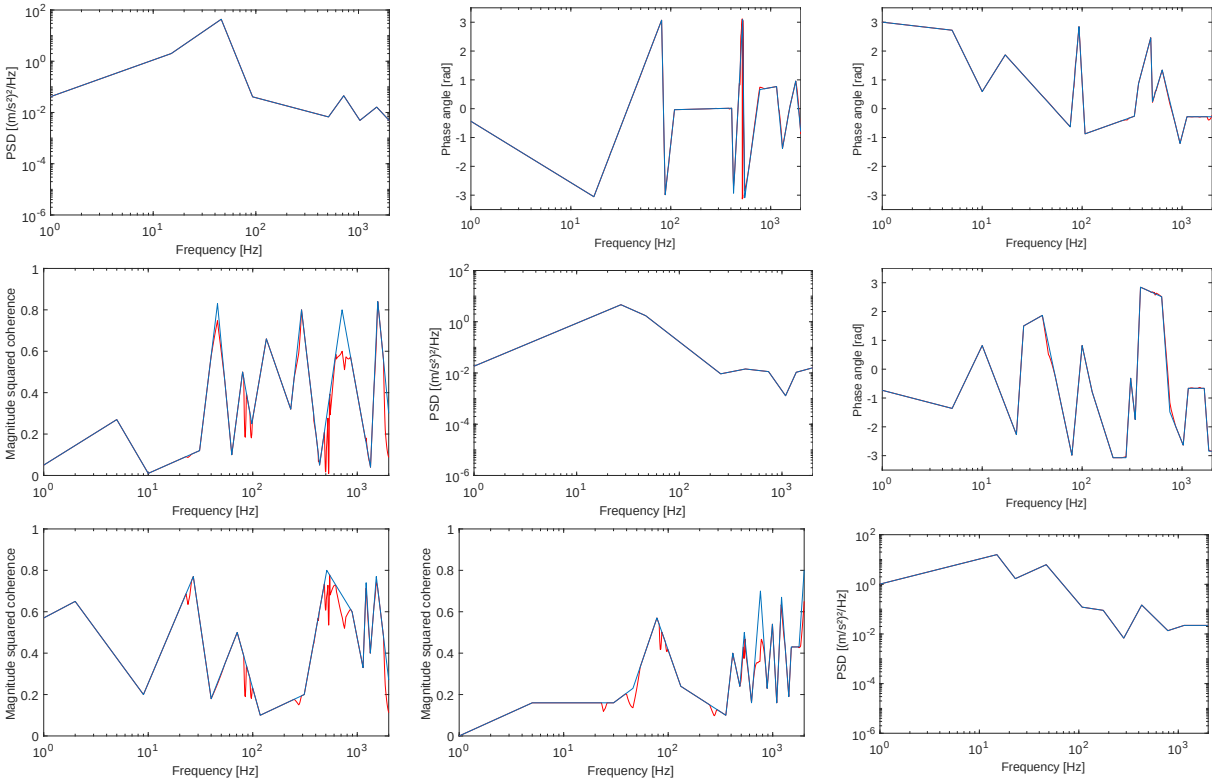

Figure 5.3: Exemplary SDM profile with optimized envelopes marked in red, phases on the upper triangle, magnitude squared coherences on the lower triangle

The difference of the optimization approach to other methods shall be demonstrated with an example. Therefore, the multi-axis test specimen previously given in fig. (3.22) (position 3) is used for a fatigue damage calculation according to the stress based method given in fig. (3.1). The specimen is excited with each of the modified multiaxial profiles derived from the four different manipulation methods given in table (5.2). In order to perform a qualitative comparison, the resulting fatigue damage values are normalized with respect to the results of the coherence reduction approach and are given in table (5.3). The optimization appears to be close to the coherence reduction method, slightly higher deviations are calculated for the phase changing method. The eigenvalue replacement results in higher deviations, partly due to the violation of the PSD terms. The calculated values are only a demonstration using the example structure

and the results may change strongly with other structures and their respective eigenfrequencies. Rotating the mounting orientation of the multi-axis test specimen already causes a larger deviation between the different methods, however it is not a realistic case anymore.

Table 5.3: Fatigue damage values resulting from the different modification approaches for the multi-axis test specimen, normalized to the results of the coherence reduction

b	3	4	5	6	7	8
Coherence reduction	1.00	1.00	1.00	1.00	1.00	1.00
Eigenvalue replacement	1.04	1.05	1.06	1.07	1.08	1.09
Phase change	1.02	1.03	1.04	1.05	1.05	1.05
Optimization	0.99	0.99	0.98	0.98	0.98	0.98
b	9	10	11	12	13	
Coherence reduction	1.00	1.00	1.00	1.00	1.00	
Eigenvalue replacement	1.11	1.13	1.16	1.19	1.22	
Phase change	1.06	1.07	1.08	1.09	1.11	
Optimization	0.99	0.99	1.00	1.02	1.04	

The biggest advantage of the optimization approach is the manipulation of all phases and coherences at the same time. Even small deviations of the phase may avoid strong manipulations on the coherences and thus maintain its physical meaning. The method provides the geometric optimum without violating the PSD terms. The method will be used in the next chapter.

5.2 Applicability of the Fatigue Damage Spectrum

In this section, the FDS is examined regarding its applicability to multiaxial problems. Parts of this subsection have been investigated in [94]. The FDS is an explicit uniaxial profile derivation method. For a three-dimensional case, one would thus obtain three independent FDS.
An attempt to include the cross coupling of the entire SDM can be made using a SDOF system with a variable orientation $\boldsymbol{r}$. Thereby, the vector length is maintained as $|\boldsymbol{r}| = 1$. The Miles eq. (2.34) can then be rewritten as

$$\tilde{\sigma}_{aa}(\boldsymbol{r}) = \sqrt{\frac{\pi}{2}\, f_n\, Q\, \boldsymbol{r}^T \boldsymbol{G}(f) \boldsymbol{r}} \quad . \tag{5.9}$$

The term $\boldsymbol{r}^T \boldsymbol{G}(f) \boldsymbol{r}$ is known as quadratic form and can be geometrically described as an ellipsoid. Eq. (2.104) for the DP can then be rewritten as

$$DP(f, T, \boldsymbol{r}) = f_n T \left[\frac{2Q\, \boldsymbol{r}^T \boldsymbol{G}(f) \boldsymbol{r}}{f_n} \right]^{b/2} \tag{5.10}$$

which yields the DP for every direction including all coupling phase relations. The extreme case is a fully coherent in-phase excitation of all three directions. In the two-dimensional case this leads to a maximum damaging direction of $45°$ as shown in fig. (5.4).

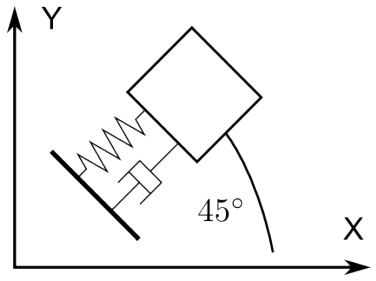

Figure 5.4: SDOF rotated by $45°$

The profile derivation methodology of fig. (2.13) can then be extended accordingly, as shown in fig. (5.5). After merging together the individual fatigue spectra, again a single PSD profile is obtained which includes all potential damaging effects of the coupling. An entire profile SDM cannot be obtained due to the inherent uniaxiality of the FDS.

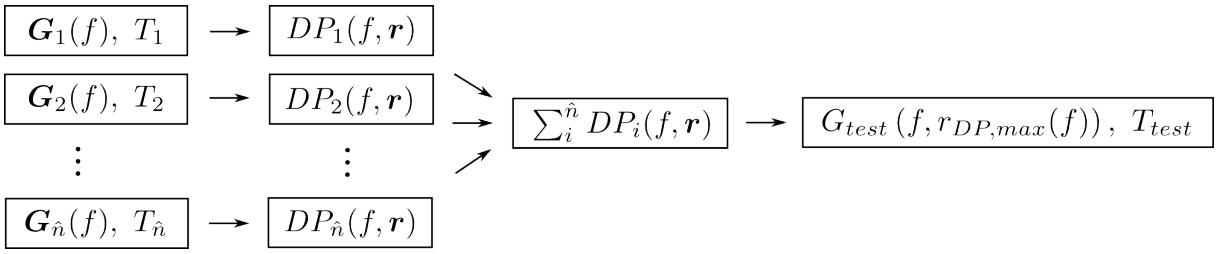

Figure 5.5: Profile derivation using a modified FDS approach

The four profile SDMs from subsection 5.1.1 are used as an example. They are merged together by summing up their fatigue damage spectra using the assumption of equal exposure times. The test profile is accelerated by a factor of 200. As proposed in [100], exemplary values of $b = 8$ and $Q = 10$ are used for the FDS calculation. The PSD profile following the original FDS approach is obtained by taking the maximum value out of all three directions at each frequency $G_{test}(f) = \max\left[G_{x,test}(f), G_{y,test}(f), G_{z,test}(f)\right]$, yielding an uniaxial worst case profile. For the modified FDS, fatigue damage calculations are performed for all possible directions using the fully populated SDM as given in eq. (5.10). The damages of the different profiles are then summed up for each direction. The resulting PSD profile is obtained using the maximum damaging direction for every frequency. The modified FDS yields always higher values for the PSD profile than the original approach, shown in fig. (5.6). This can be explained by the partly coherent in-phase excitation at particular frequencies.

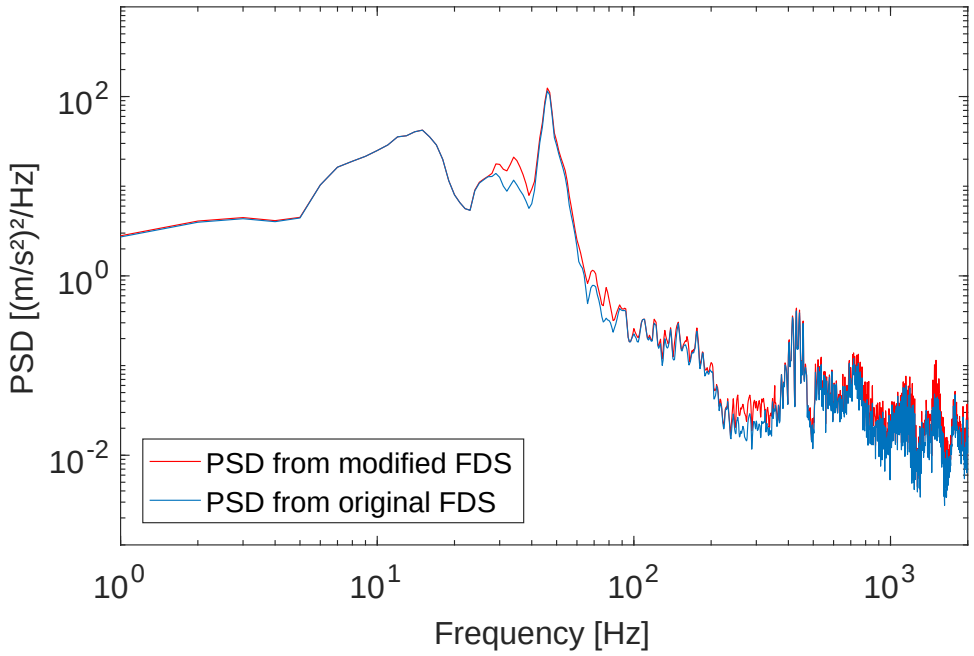

Figure 5.6: PSD profiles obtained from modified and original FDS $(Q = 10,\ b = 8)$

The difference between the original FDS approach and the modified one regarding its influence on fatigue damage is demonstrated with an example. Again, the multi-axis test specimen from fig. (3.22) (position 3) is used for a fatigue damage calculation according to the stress based method given in fig. (3.1). Thereby, the x-axis points in the transverse, the y-axis in the longitudinal (driving) and the z-axis in the vertical direction. As inputs, the profiles from fig. (5.6) are used. The deviations between the fatigue damage results for different slope values b are given in table (5.4).

Table 5.4: Deviation factors of the fatigue damage values resulting from the modified and original FDS for the multi-axis test specimen (modified divided by original)

b	3	4	5	6	7	8	9	10	11	12	13
dev.	1.19	1.28	1.40	1.54	1.69	1.87	2.05	2.23	2.41	2.60	2.82

The expression in eq. (5.10) can also be formulated for sine excitation. Therefore, the amplitude of the sine $\hat{A}(f) = QS_a(f)$ from the original eq. (2.106) is extended to the complex sine form $X(f)$. Then, the spatial direction $\boldsymbol{r}$ is included using the scalar product $\boldsymbol{r}^T X(f)$. To obtain a real value, the norm of a complex vector has to be used. For any complex vector $\boldsymbol{v}$ its norm can be stated as $\|v\| = \sqrt{\sum v_i v_i^*}$. The final expression for the coupled sine based DP then becomes

$$DP(f, T, \boldsymbol{r}) = f_n T \left[\frac{\sqrt{(\boldsymbol{r}^T\ X(f))\,(\boldsymbol{r}^T\ X(f))^*}}{f_n^2} \right]^b . \tag{5.11}$$

5.3 Development of a Standard Random Vibration Profile

As indicated in subsection 2.3.3, the current state of the art does barely provide standards for multiaxial testing. Especially within the automotive industry standard profiles are usually not available. An example standard profile shall be derived for random vibration, based on a comparatively large dataset. Thereby, a focus is put on the assembly group named sprung masses, as considered in [35]. Parts of this section have been investigated in [16].
A total of 65 datasets from 5 different vehicles are considered. At first, a verification of the dataset using the respective uniaxial norm given in [35] is accomplished. The underlying accelerometer orientations of the measurements are unordered and not rotated in a common coordinate system, as it is assumed for the reference standard. The first step is a preprocessing of the available data. All time windows with an RMS value lower than 25% of the maximum RMS value are neglected. This process eliminates the influence of the time intervals with weak excitation. The resulting PSD curves of all individual measurements are shown in fig. (5.7) together with the respective standard profile. Thereby, all axes are plot together.

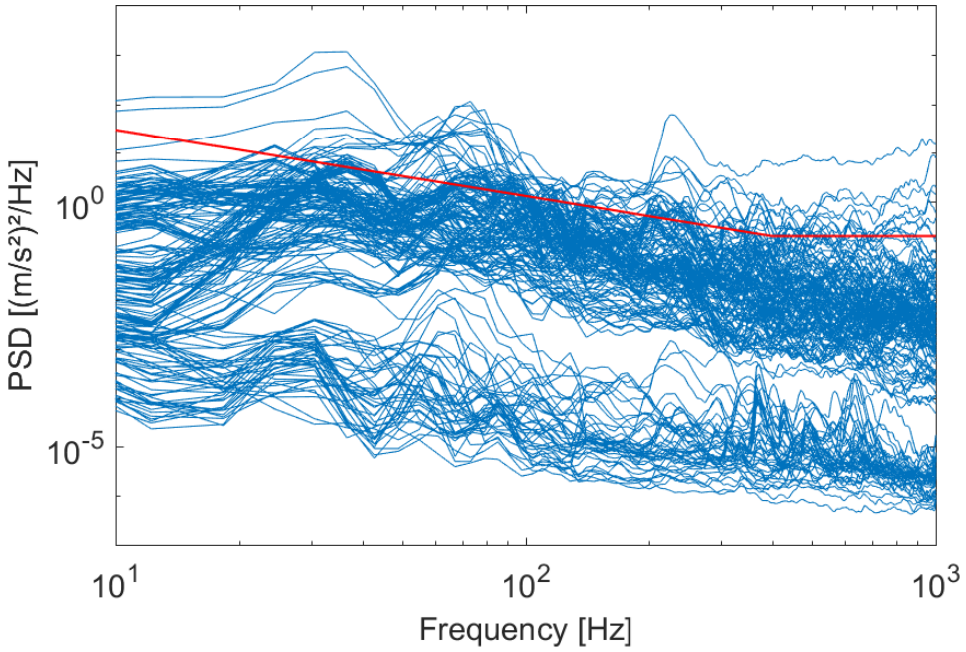

Figure 5.7: Database with all directions and ISO standard profile for sprung masses

Apart from certain outliers, the database is appropriate for further considerations. In the next step, each measurement is split direction specifically. Coordinate transformations of the raw acceleration signals are performed into a common global coordinate system using the longitudinal (driving), transverse and vertical direction of a vehicle. The resulting PSDs are given in fig. (5.8) together with proposed envelopes. The envelopes are chosen arbitrarily following the nature of the original standard. Thereby, the attempt is made not to overshoot the original profile. In higher frequency ranges larger values occur for the transverse direction which is due to the coordinate system rotation of the respective time signals.

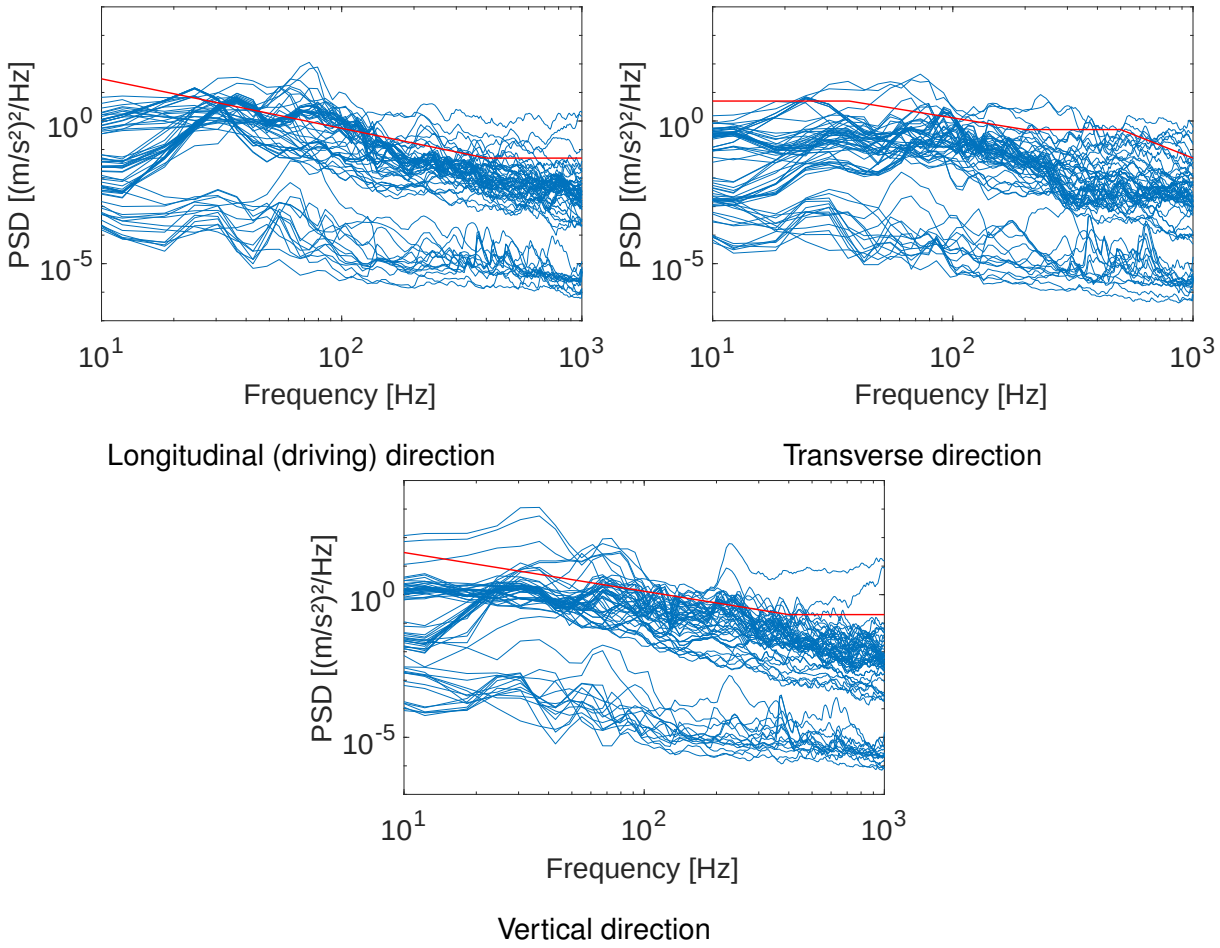

Figure 5.8: Proposed standard profiles

Phase and coherence profiles are not obtained due to the lack of any tendencies. The reason is combining data from different measurement positions of different vehicles. The resulting profiles for the longitudinal, transverse and vertical direction are given in fig. (5.9) and in table (5.5). The standard profile will be used in the next chapter.

Table 5.5: Values for standard profiles obtained from database

Longitudinal		Transverse		Vertical	
Freq. [Hz]	PSD [(m/s²)²/Hz]	Freq. [Hz]	PSD [(m/s²)²/Hz]	Freq. [Hz]	PSD [(m/s²)²/Hz]
10	30	10	5	10	30
400	0.05	37	5	400	0.2
1000	0.05	200	0.5	1000	0.2
		500	0.5		
		1000	0.05		

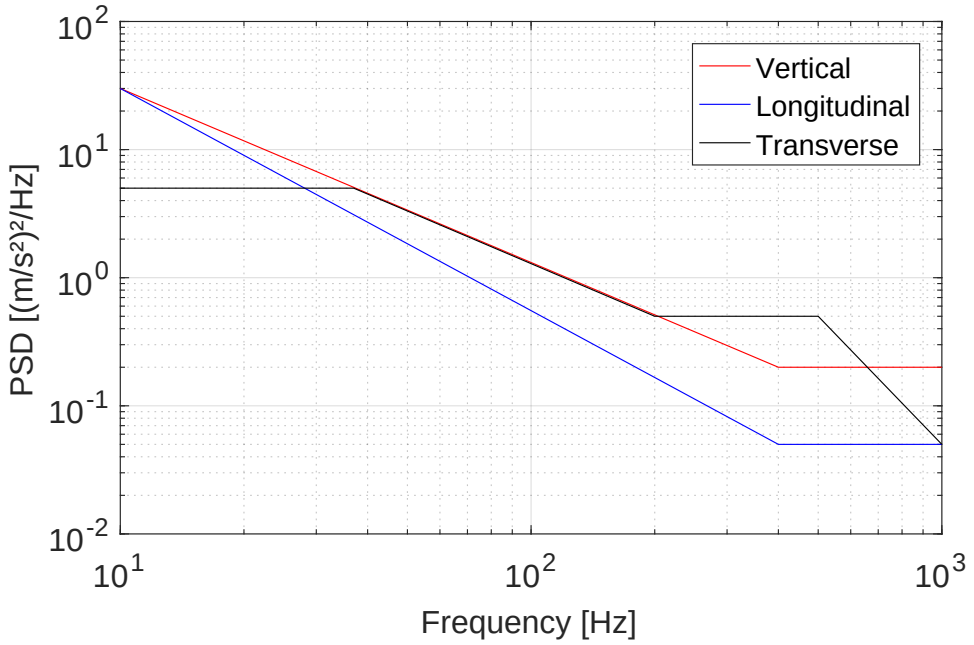

Figure 5.9: Standard profiles obtained from database

In case of a known mounting orientation in the vehicle, the test time of 8 hours can be maintained. Otherwise, a case dependent fatigue life estimation has to be accomplished beforehand.
Since no general phase information can be obtained from the given dataset, an uncorrelated excitation of the standard profiles is proposed. Another option is to use a minimum drives approach which determines the phases to reduce the shaker voltage and the stresses on the shaker system. The approach is explained and applied to an example shaker setup within the appendix (see fig. (C1)). A main drawback is the application of unrealistic phase information on the DUT. Furthermore, the shaker transfer functions have to be well determined and are not supposed to shift over time or being affected somehow else through nonlinearities.

In this chapter, different approaches for a multiaxial vibration test profile derivation were developed. A field data based method using envelopes and a subsequent optimization, as well as a concrete random vibration standard profile are the primary outcome that will be used in the next chapter. Furthermore, the FDS approach was investigated and found to be very limited and thus not appropriate for the definition of multiaxial profiles. However, an advanced FDS approach for uniaxial test profiles was proposed.

6 Verification of the Multi-Axis Testing Methodology

The verification chapter serves two major goals. The first is to experimentally prove the direct relation between velocities and fatigue damage. So far, conclusions have only been drawn on the preceding relationship between velocities and stresses. EOL tests are performed using simple specimens and evaluated with velocity measurements to emphasize their validity. The second goal is to confirm and determine the existing difference in fatigue damage between uniaxial and multiaxial vibration tests based on realistic scenarios. Thereby, the developed methods for velocity measurement evaluation (chapter 3), shaker fixture design (chapter 4) and profile derivation (chapter 5) are applied. Three automotive components with different complexity levels are used for the fatigue damage evaluation.

6.1 Fatigue Failure Test using a Simple Specimen

The preceding relationship between velocities and fatigue damage is based on single numerical models and a continuum mechanics approach. Fracture mechanics based calculations were not included to maintain generality. Considerations on natural imperfections varying with material behavior, which is mostly due to fabrication inconsistencies, are not included. Therefore, EOL tests are performed to determine the fatigue life for both uniaxial and multiaxial excitation. Fatigue damage calculations are then accomplished using velocities and accelerations for a qualitative and quantitative comparison. Parts of this section have been published previously in [41].

6.1.1 Design of a Test Setup

The design of the test specimens is inspired by the work on multiaxial fatigue testing published in [20]. The geometry of the specimens introduced in [20] are changed to obtain two different eigenfrequencies to highlight the frequency independence of the velocities and their relation to fatigue damage. A rectangular cross section of 5×10 mm² is chosen which introduces two damaging first bending modes at different frequencies. While the first eigenfrequency is located around 29 Hz and can be excited in the X-direction of the shaker, the second eigenfrequency is located around 58 Hz and responds to an excitation in the Y-direction. The length of the specimen is 390 mm, cut from AlMgSi0.5 stocks. As shown in fig. (6.1), a round notch is placed on the long edge with a depth of 1.65 mm and a tolerance of ± 0.05 mm.

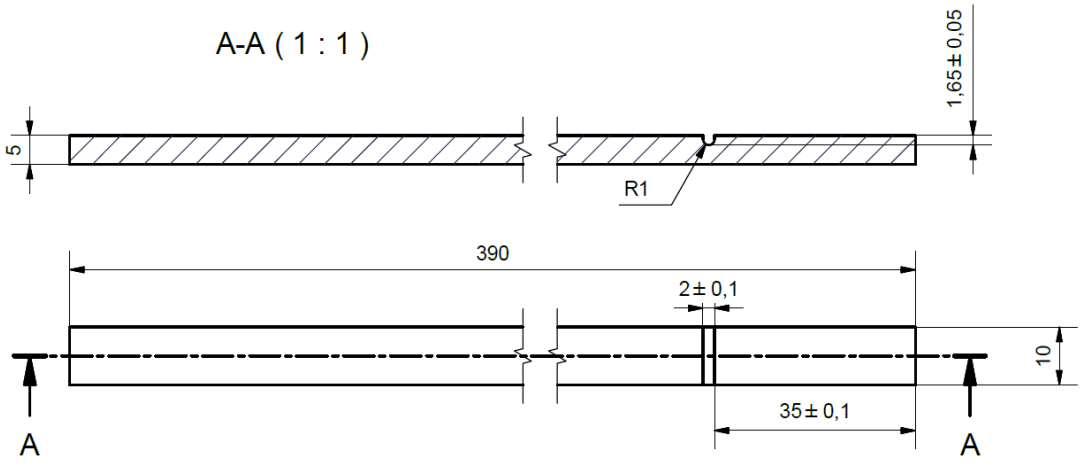

Figure 6.1: Technical drawing of specimen [41]

A fixture is designed to mount a maximum of eight specimens at the same time. However, only four specimens are placed in a staggered fashion due to the large response amplitudes. Accelerometers are placed on top of each specimen. The full test setup is shown in fig. (6.2). The tests are performed with a Dataphysics Signal Star Matrix controller, a tri-axial PCB 356A61 accelerometer for the control and tri-axial Dytran 3133 series accelerometers for the response measurements.
To measure the transfer functions for acceleration and velocity, given in fig. (6.3), an initial sine sweep is performed. The velocity FRF shows a relative difference between the peak values at the eigenfrequencies, as it is also expected for the normal stresses. A random excitation of $20 - 80$ Hz with a PSD level of 5 (m/s²)²/Hz is then applied as test profile. For the multiaxial test, the horizontal axes (X and Y) are excited in an uncorrelated manner. A Time Waveform Replication (TWR) is used to ensure an equal test environment for all specimens.

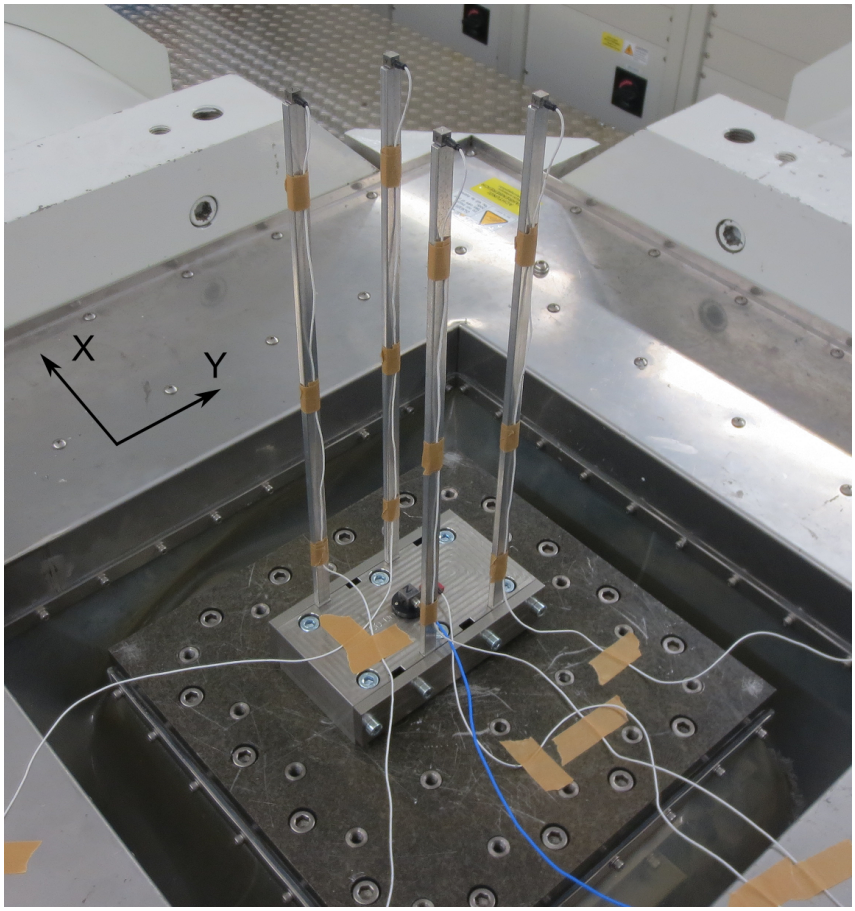

Figure 6.2: Test setup with fixture and four specimens [41]

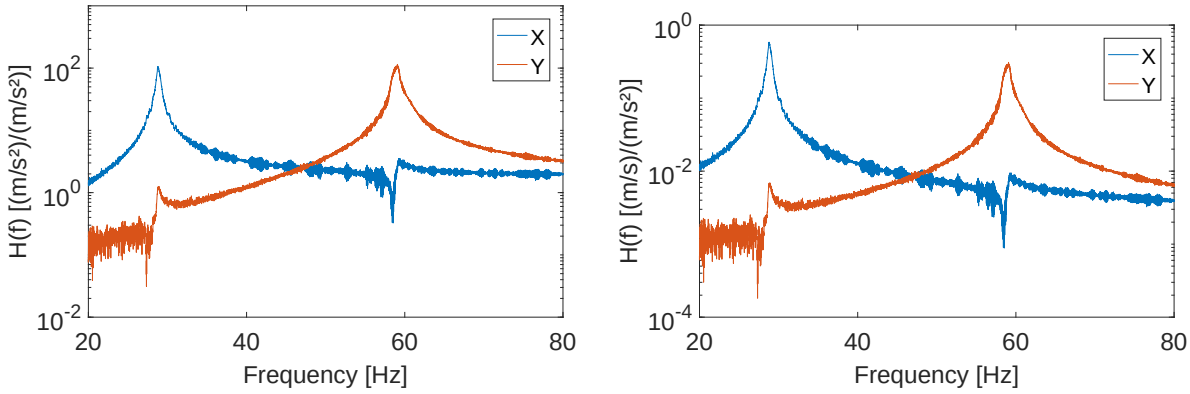

Figure 6.3: Transfer functions for relative acceleration response (left) and relative velocity response (right) [41]

6.1.2 Fatigue Damage Evaluation

A pool of 24 specimens is tested for both the uniaxial (only X-direction) and the multiaxial case to ensure a robust estimation of the fatigue life. Thereby, the fatigue life is determined if the first eigenfrequency decays by 10% which is below 26 Hz. The amplitudes decrease at the same time and thus a limitation of the structural functionality is assumed. The uniaxial test results are

shown in fig. (6.4) and (6.5), the multiaxial test results in fig. (6.6), (6.7) and (6.8). As expected, a faster fatigue failure can be detected under multiaxial loading. The mean fatigue lives are 562.8 s for the uniaxial and 496.7 s for the multiaxial case. The uniaxial fatigue lives roughly range between 500 s and 700 s, while the multiaxial fatigue lives roughly range between 400 s and 600 s. Both results are assumed to follow an approximate normal distribution.

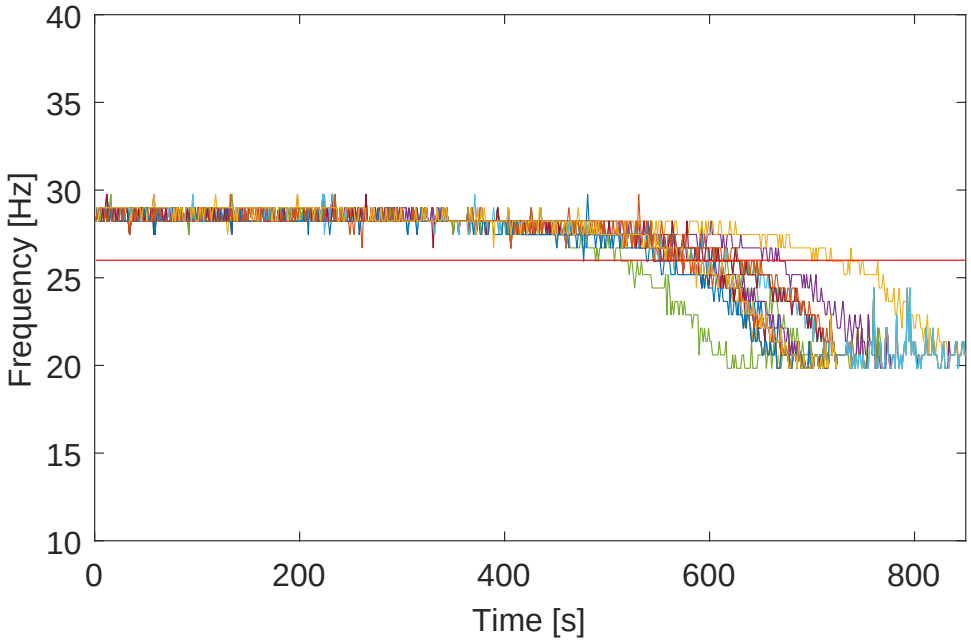

Figure 6.4: Frequency decay of 24 specimens under uniaxial loading, first eigenfrequency, failure criterion at 26 Hz [41]

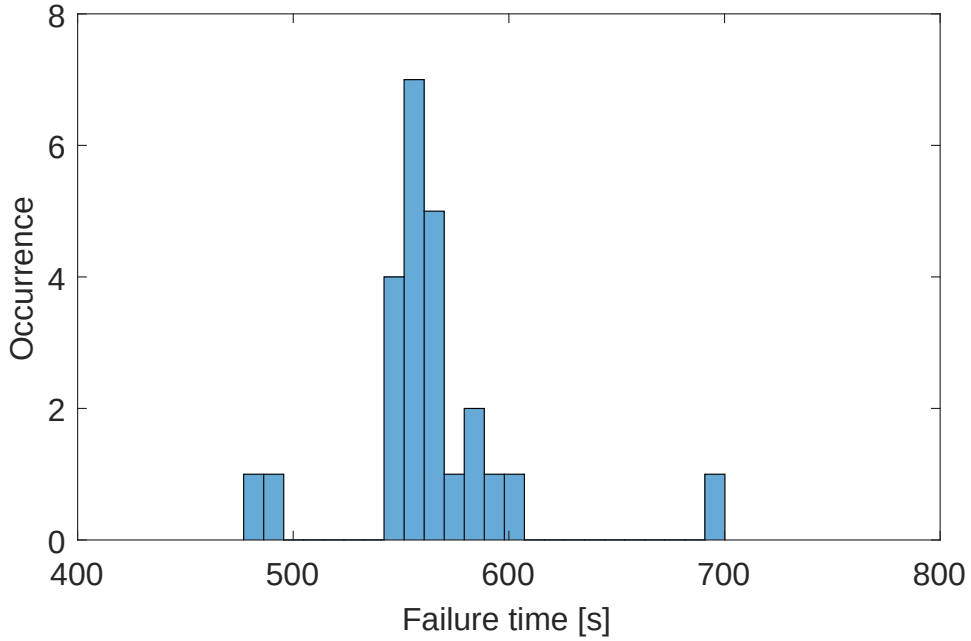

Figure 6.5: Fatigue life of 24 specimens under uniaxial loading [41]

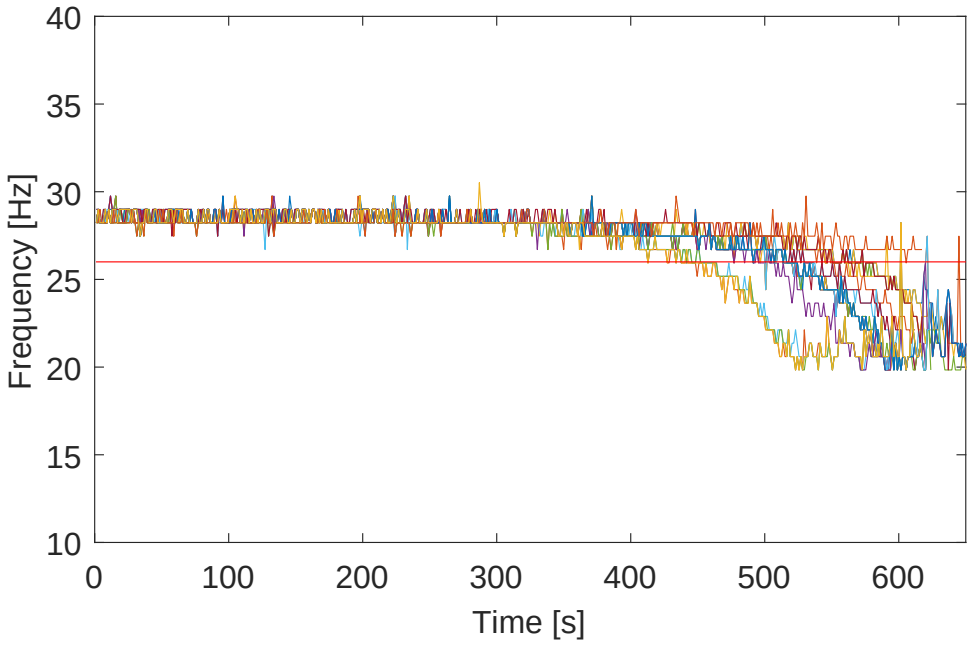

Figure 6.6: Frequency decay of 24 specimens under multiaxial loading, first eigenfrequency, failure criterion at 26 Hz [41]

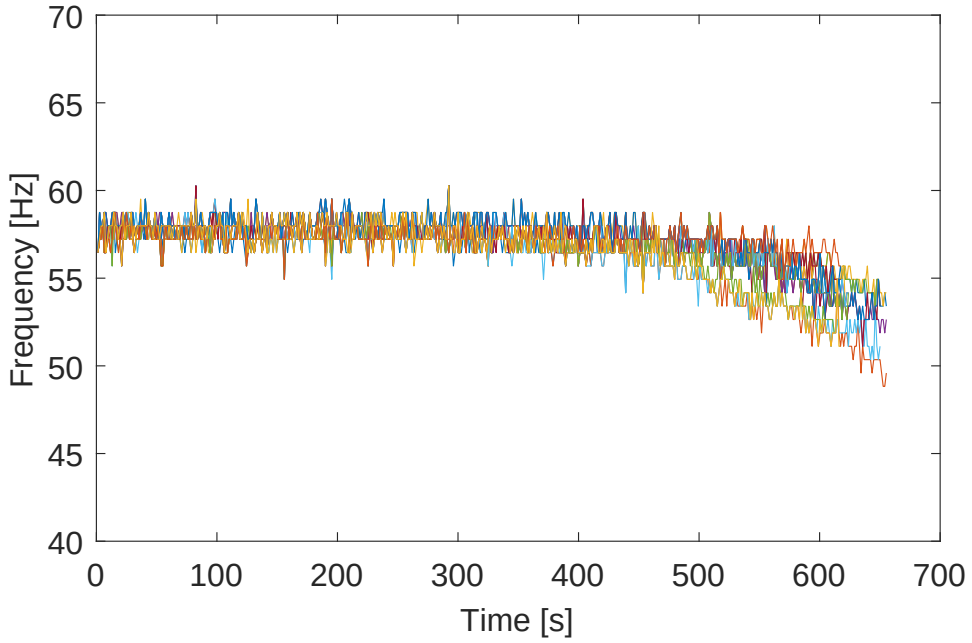

Figure 6.7: Frequency decay of 24 specimens under multiaxial loading, second eigenfrequency [41]

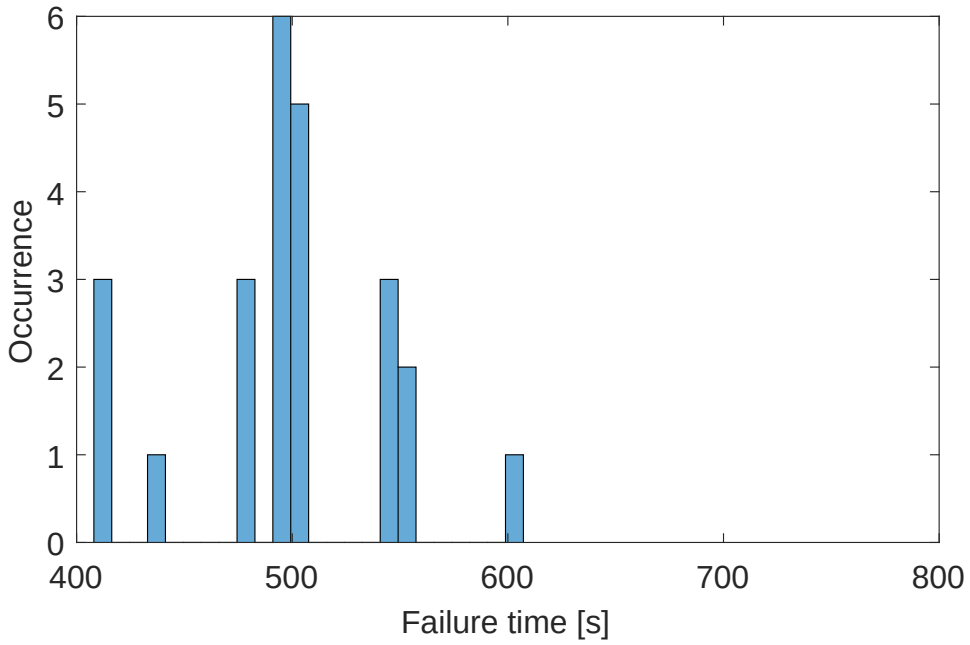

Figure 6.8: Fatigue life of 24 specimens under multiaxial loading [41]

According to [9], the HCF range for unnotched round AlMgSi0.5 specimens begins with 10^4 cycles. A failure within the HCF range is also assumed to be ensured for the notched specimens, since the lowest fatigue failure is detected at around a total of 1.5×10^4 cycles (29 Hz times 500 s). A typical crack due to fatigue is shown in fig. (6.9). It propagates along the entire notch root of the specimen where the highest stresses occur.

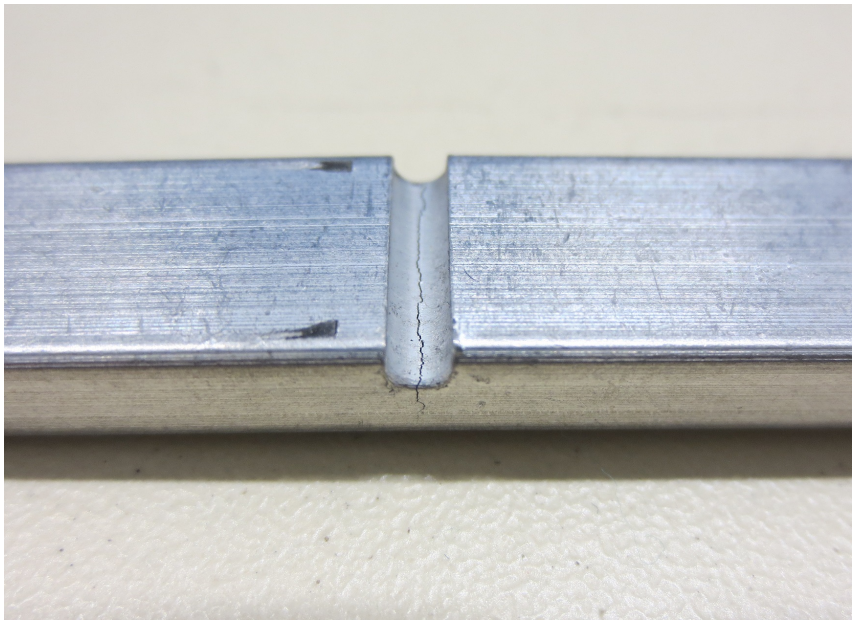

Figure 6.9: Crack formed in the notch [41]

Fatigue damage values are calculated for each test. The relative acceleration signals are obtained from accelerometer measurements with a subsequent integration according to [102]. Both relevant velocity components are summed up as $v(t) = v_x(t) + v_y(t)$ in order to obtain a time signal proportional to the normal stress. Thereby, the geometric factors are the same for both directions and thus can be neglected. A Rainflow counting is then performed on the combined velocity signal and the resulting cycle amplitudes are exponentiated with the slope b of the S-N curve and summed up, as explained in subsection (2.2.4). For unnotched round AlMgSi0.5 specimens a slope value of 16 is commonly used (according to [9]). However, a notch usually lowers the slope value to $b = 5$ for metallic specimens, as stated in [26]. In further procedure all evaluations are thus performed for values of $b = 5$ and $b = 8$. The values are also proposed as standards in [35].
All calculated fatigue damage values should be in the same order of magnitude regardless of whether a uniaxial or multiaxial excitation was applied. To perform a qualitative comparison, also relative accelerations are used for the fatigue damage calculation. They are processed analogously to the relative velocity components. The combined signal is thereby calculated as $a(t) = a_x(t) + a_y(t)$. As a comparable quantity, also relative displacements can be used. In the case of the given specimen, the displacements at the second mode are neglectable and do not influence the overall fatigue calculation. Hence, they are not suitable as a counterexample. The results are shown in fig. (6.10) and (6.11) for both slope values respectively.

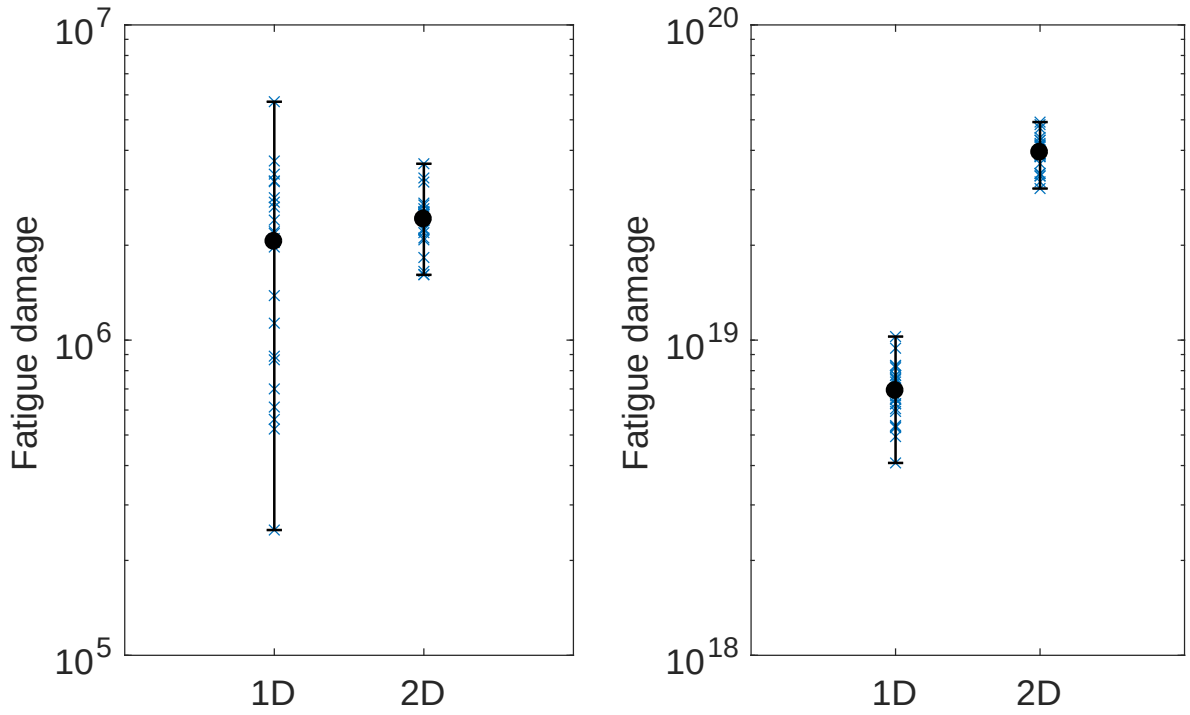

Figure 6.10: Uniaxial and multiaxial fatigue damage evaluation of 24 specimens using $b = 5$, velocity based (left) and acceleration based (right) [41]

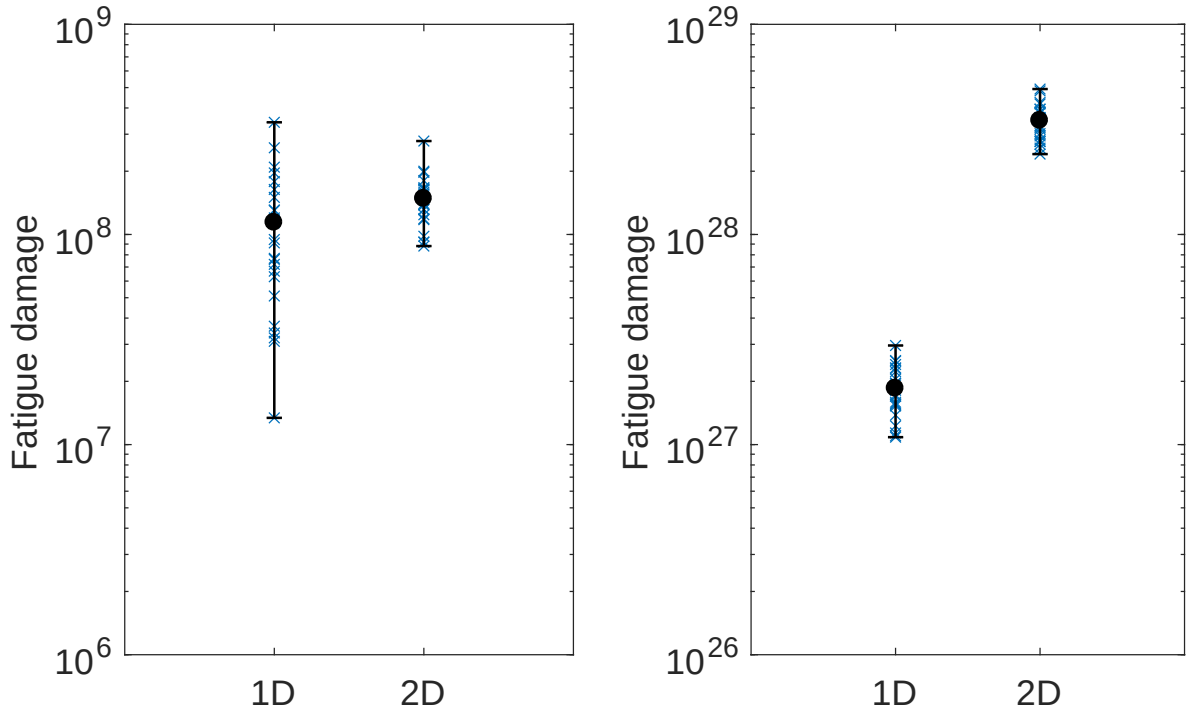

Figure 6.11: Uniaxial and multiaxial fatigue damage evaluation of 24 specimens using $b = 8$, velocity based (left) and acceleration based (right) [41]

The velocity calculation results in similar values for uniaxial and multiaxial (pseudo) fatigue damage around 2×10^6 for $b = 5$ and 1×10^8 for $b = 8$. Due to the limitation in the number of specimens, the slight deviation by a factor of 1.2 for $b = 5$ and of 1.3 for $b = 8$ is assumed to be statistical in nature. On the contrary, calculations based on acceleration result in a large deviation between uniaxial and multiaxial fatigue damage values at fatigue failure, as can be seen in fig. (6.10) and (6.11). The deviation factors are 5.6 for $b = 5$ and 19.4 for $b = 8$. Furthermore, the uniaxial fatigue damage values appear to deviate more than the multiaxial ones. This can be explained by the slightly varying anisotropic nature of the extruded specimens which were probably cut from different stocks.
The experimental results confirm the relationship between velocities and fatigue damage sufficiently and conclude in the exclusive consideration of velocities for the purpose of fatigue damage calculation in further procedure.

6.2 Application of Method to Automotive Components

The introduced methods for 3D-shaker testing and the calculation of multiaxial fatigue damage are used to evaluate the difference between conventional uniaxial shaker testing and three-dimensional multi-axis shaker testing. Thereby, three realistic case scenarios are considered which are summarized in table (6.1). The first is a standard random vibration test on a multi-axis test specimen (see subsection 3.4.2.1). The structure serves as dummy model for hydraulic units of chassis control systems. To maintain generality, no application-specific vehicle measurements are used to create a profile. Instead, the developed standard profile from section

5.3 is considered. Geometric factors are obtained from both the simplified model introduced in subsection 3.4.3.1 and from the original one. Thereby, three potential hot spots are considered, depending on uniaxial and multiaxial excitation. The second scenario is a random vibration test of a complex automotive component. An application-specific test profile is derived from vehicle measurements according to the method explained in section 5.1. Standard values as proposed in subsection 3.3.1 are used as geometric factors. The third case scenario is a sine sweep test of a simple automotive component which is mounted near the engine. An application-specific test profile is derived from vehicle engine run-up measurements. Geometric factors are obtained from the simplified model given in subsection 3.4.3.2 and compared with the original ones.
All fatigue damage evaluations are performed according to fig. (3.39). All tests are performed with a Dataphysics Signal Star Matrix controller, a tri-axial PCB 356A61 accelerometer for the control and tri-axial Dytran 3133 series accelerometers for the response measurements.

Table 6.1: Test scenarios for application of the multi-axis testing methodology

Scenario	Multi-axis test specimen	Complex automotive component	Simple automotive component
Test type	Standard random profile	Derived random profile	Derived sine sweep profile
Geometric factors	Full / simplified model	Standard	Full / simplified model
Evaluation	2 uniaxial hot spots, 1 multiaxial hot spot	1 hot spot	1 hot spot
Test fixture	Setup with block and frame	Adapter plate	Setup with block and frame

6.2.1 Standard Random Vibration Test

The setup in fig. (4.11) serves as fixture for the multi-axis test specimen that has a weight of 1.18 kg. A small adapter (0.73 kg) is used to connect the specimen with the fixture block, as shown in fig. (6.12). Thereby, the entire setup complies with the specification in fig. (4.3). Two accelerometers are placed on the specimen to determine both translational and rotational velocities. All tests are controlled on the small adapter near the fixation. The standard profiles are run 200 minutes for each uniaxial test, as well as for the simultaneous test. Referring to the coordinate system in fig. (3.22), the vertical profile from fig. (5.9) is applied on the z-axis, the longitudinal on the y-axis and the transverse on the x-axis. The reason is the respective assumed mounting orientation, as indicated in [61]. Fig. (6.13) shows the controlled profiles together with their respective targets for a simultaneous test. The controlled profiles of the uniaxial tests are shown in fig. (D1) within the appendix. Apart from the axis to be excited, both cross-axis excitations are kept as low as possible by the vibration controller.

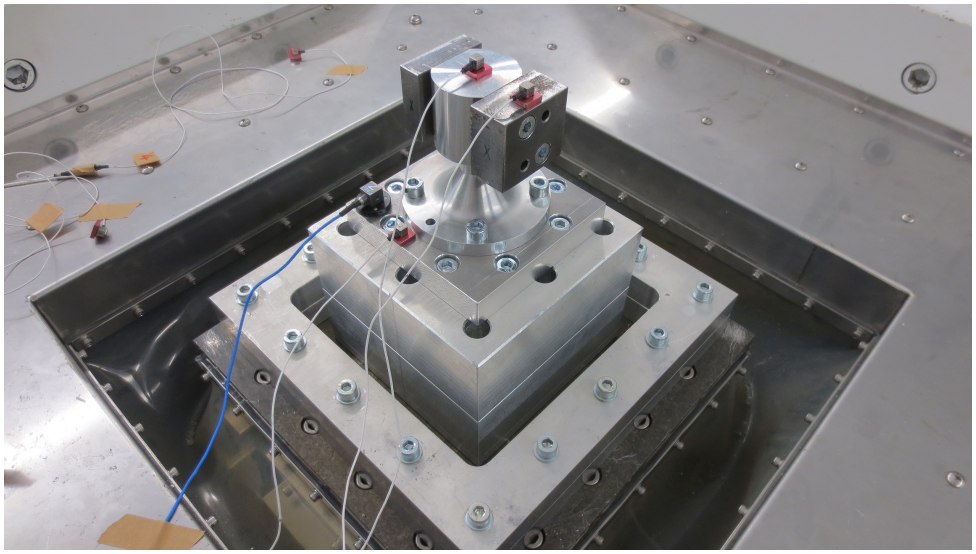

Figure 6.12: Setup for multi-axis test specimen

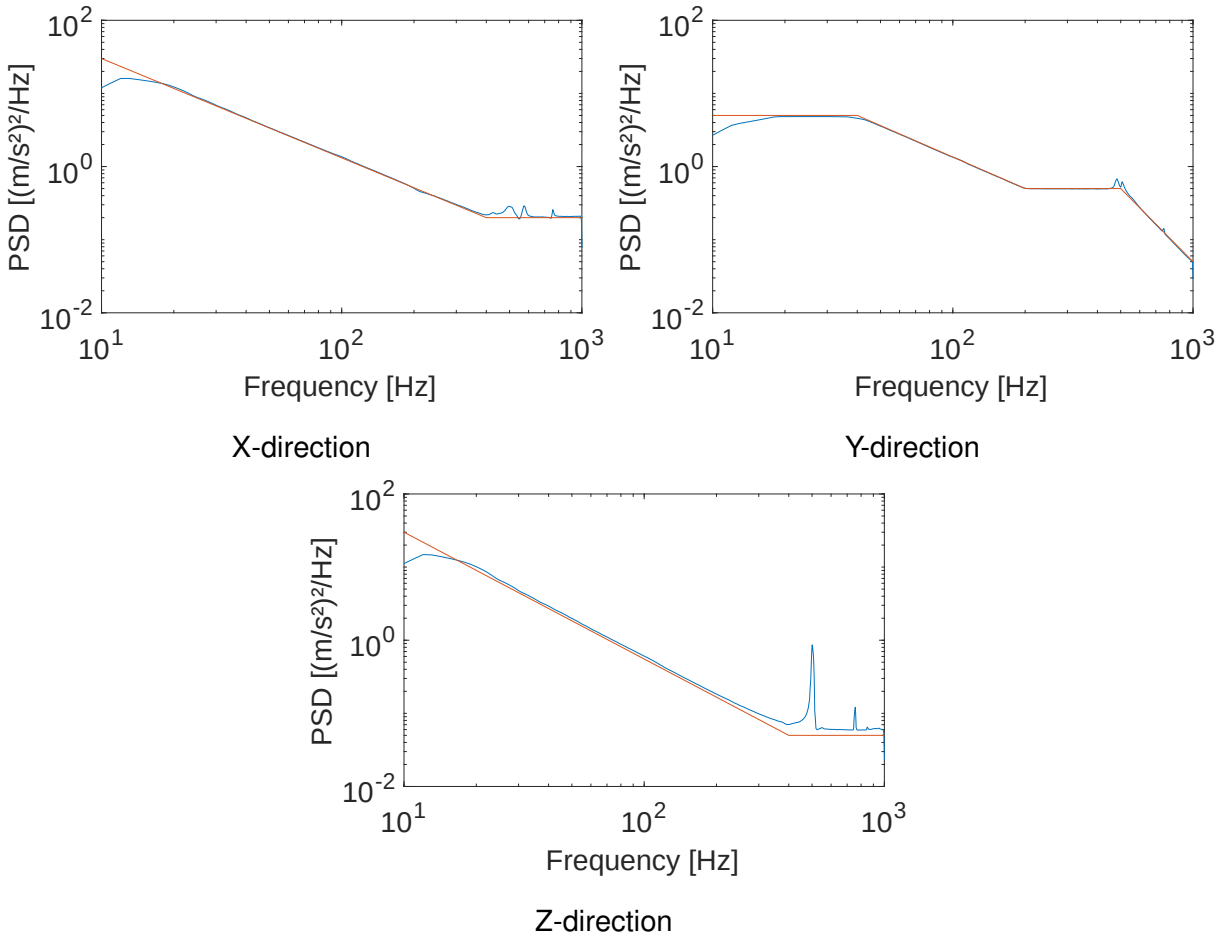

Figure 6.13: Measured 3D-test excitation on multi-axis test specimen (3D-shaker coordinate system)

The deviations are a result of the cross accelerations due to mass inertia which counter the target profile, as described in section 4.2. Thus, the control accuracy may also influence the final results of the fatigue damage evaluation. However, due to the relatively long testing time and the linear system behavior of the multi-axis test specimen (and also of the subsequent examples to be tested), the influence is neglected if an accurate test execution can be ensured. Fig. (6.14) shows the stress related velocity response PSDs of the simultaneous test with highest values occurring on the Y-axis of the shaker due to the relatively high excitation level of the transverse profile. No geometric factors are applied in this figure.

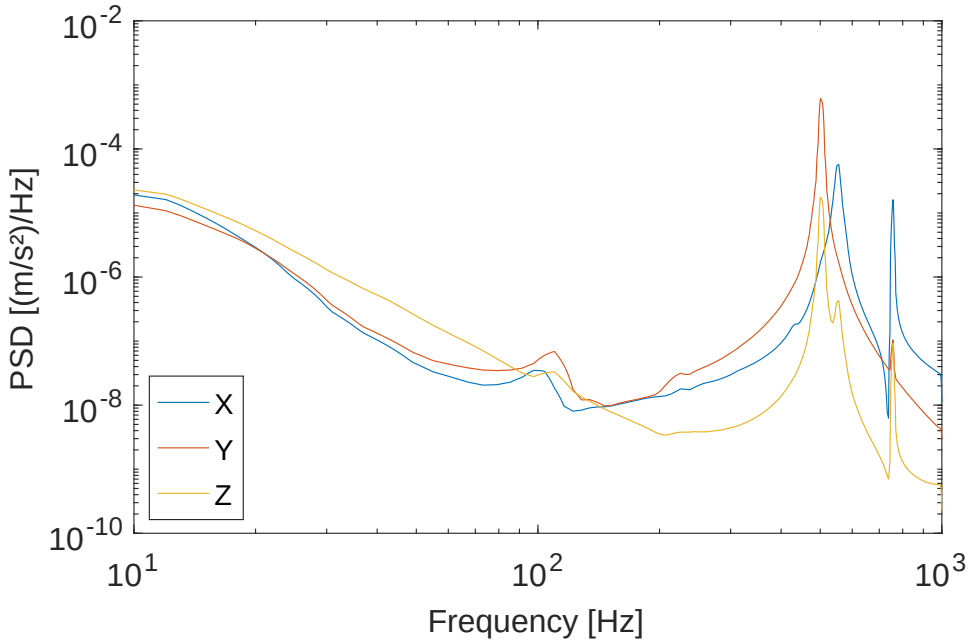

Figure 6.14: Response velocity PSDs from 3D excitation of the multi-axis test specimen (3D-shaker coordinate system)

6.2.1.1 Evaluation of the multiaxial hot spot

At first, the multiaxial hot spot (position 3 in fig. (3.22)) is considered. Therefore, the respective geometric factors from the full and the simplified model in table (3.9) are applied. The results using the full model are given in table (6.2), the results using the simplified model in (6.3). Both show a higher fatigue damage with a multiaxial excitation. The simplified model overestimates the fatigue damage ratio by a factor of around 2. However, the tendency is correct and the deviation within an acceptable range.

Table 6.2: Ratio between 3D- and 1D-fatigue damage results for multi-axis test specimen excited with standard profile (velocity measurement, geometric factors from full model), multiaxial hot spot

b	3	4	5	6	7	8	9	10	11	12	13
$D_{v,3D}/D_{v,1D}$	1.13	1.32	1.49	1.64	1.79	1.94	2.09	2.26	2.43	2.61	2.80

Table 6.3: Ratio between 3D- and 1D-fatigue damage results for multi-axis test specimen excited with standard profile (velocity measurement, geometric factors from simplified model), multiaxial hot spot

b	3	4	5	6	7	8	9	10	11	12	13
$D_{v,3D}/D_{v,1D}$	1.21	1.52	1.84	2.18	2.55	2.93	3.35	3.81	4.31	4.87	5.49

6.2.1.2 Evaluation of the uniaxial hot spots

As a next step, the uniaxial hot spots (positions 3,1 and 3,2 in fig. (3.26)) are considered. The respective geometric factors from the full and simplified model are used which were given in table (3.10). The uniaxial damage $D_{v,1D}$ is calculated as the sum of damages from both uniaxial hotspots, as performed in subsection 3.1.2.2 or fig. (3.27) to obtain a comparable quantity. It is set in ratio to the multiaxial damage obtained from the respective hotspot (position 3). Thereby, the damage caused by excitation in Y-direction strongly dominates. The results using the full model are given in table (6.4), the results using the simplified model in table (6.5). While the full model leads to nearly equal fatigue damage values for both uniaxial and multiaxial excitation, the simplified model results in lower fatigue damage values with a multiaxial excitation. The simplified model underestimates the fatigue damage ratio by a factor of around 5 which is not reliable since a clear tendency is obtained in contrary to the results based on the full model. It appears that the simplified model is rather not appropriate for the evaluation of several locations. To make predictions on the fatigue damage, a more detailed model is thus required.

Table 6.4: Ratio between 3D- and 1D-fatigue damage results for multi-axis test specimen excited with standard profile (velocity measurement, geometric factors from full model), sum of damages from uniaxial hot spots

b	3	4	5	6	7	8	9	10	11	12	13
$D_{v,3D}/D_{v,1D}$	0.93	0.98	1.01	1.02	1.02	1.01	1.00	0.99	0.98	0.98	0.97

Table 6.5: Ratio between 3D- and 1D-fatigue damage results for multi-axis test specimen excited with standard profile (velocity measurement, geometric factors from simplified model), sum of damages from uniaxial hot spots

b	3	4	5	6	7	8	9	10	11	12	13
$D_{v,3D}/D_{v,1D}$	0.64	0.60	0.55	0.49	0.43	0.38	0.33	0.29	0.25	0.22	0.19

6.2.2 Random Vibration Test based on Field Data

The second case scenario to be evaluated is the random test of a complex automotive component with the test setup being shown in fig. (6.15)[1]. It consists of the adapter plate from fig. (4.12) and a typical fixture for the complex automotive component which enables the mounting of two units at the same time. However, only one DUT is used for the evaluation. The test setup has a total weight of 18.3 kg and a total CoG height of around 50 mm and is thus compliant with the specifications in fig. (4.3). All tests are controlled near the single mounting location M1.

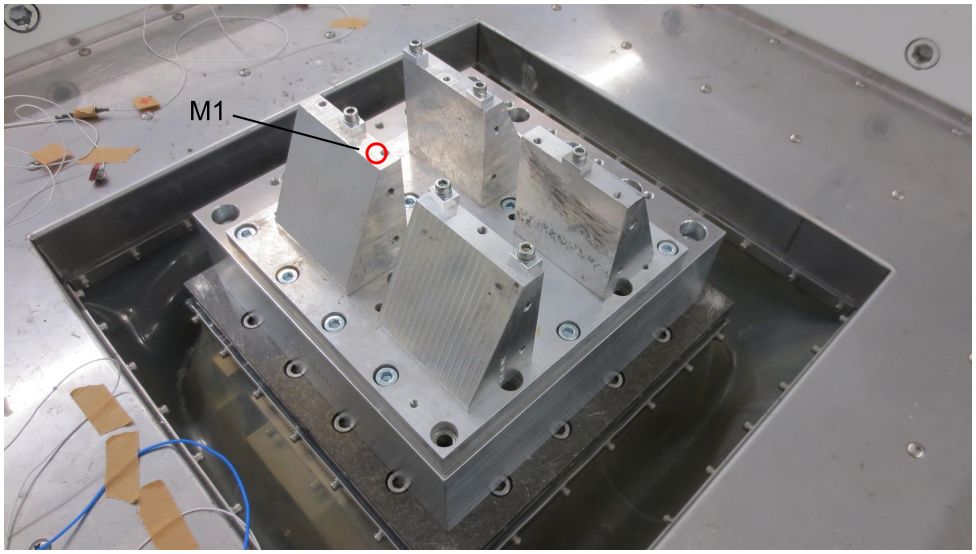

Figure 6.15: Setup for complex automotive component (not shown in picture, two units can be mounted)

The profile is derived from two vehicle measurements according to the method described in section 5.1, resulting in an optimized profile given in fig. (6.16). The preceding mean SDM and its envelopes are given in fig. (D3) and (D4) within the appendix. As usual, the arrangements of the SDM profiles are accomplished according to table (5.1). While the optimized phase profiles deviate by an angle of up to 0.31 rad, the magnitude squared coherences show deviations of at most 0.45 (in terms of coherence the maximum deviation is 0.67).

[1]The DUT cannot be shown due to security of corporate know-how

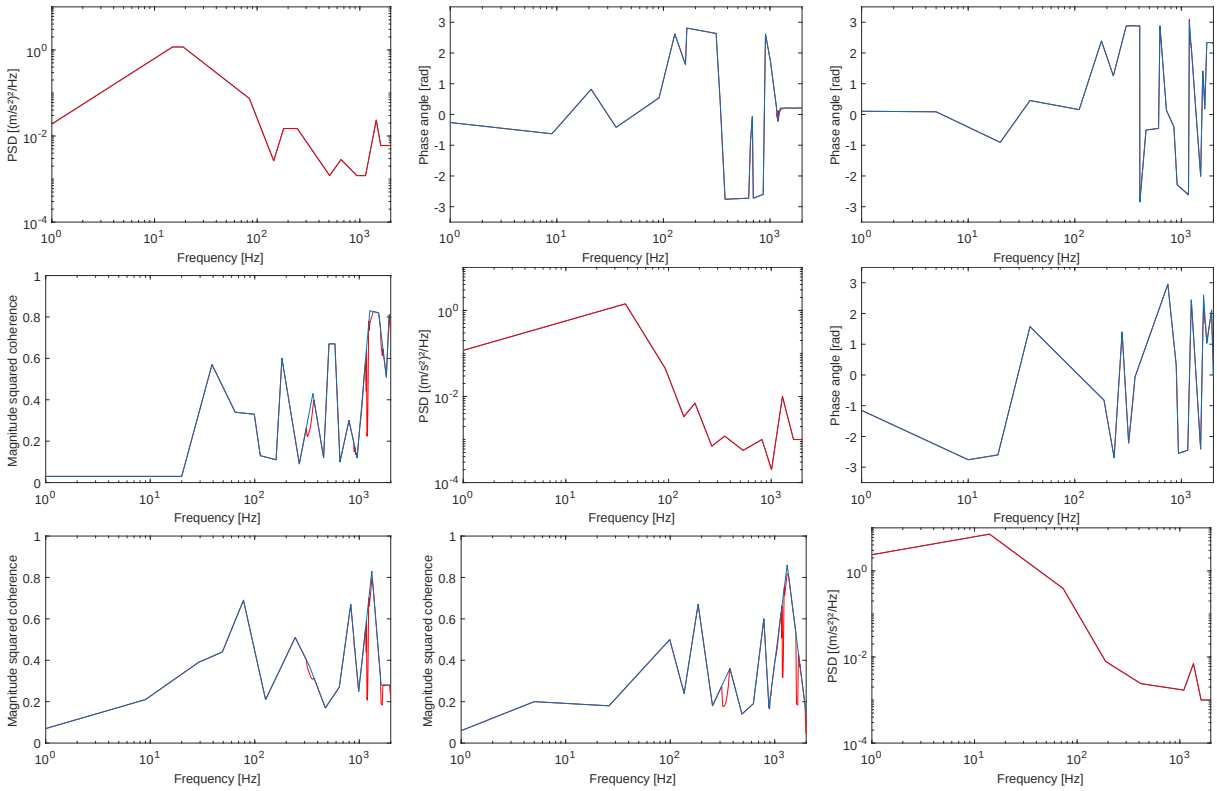

Figure 6.16: Exemplary optimized values of SDM for the complex automotive component, phases on the upper triangle, magnitude squared coherences on the lower triangle

For the DUT, a critical frequency range of $10 - 1700$ Hz is specified which defines the frequency range of the tests. Since the shaker and DUT modes occur in the vicinity of each other, care has to be taken to ensure a sufficient control. As also stated before, the different control actions between uniaxial and multiaxial tests may also have an influence on the final results which is neglected due to the assumed linearity and the long testing time. The derived profiles are run 200 minutes for each uniaxial test, as well as for the simultaneous test. Referring to the coordinate system in fig. (3.36), the vertical profile is applied on the y-axis, the longitudinal on the z-axis and the transverse on the x-axis. Fig. (6.17) shows the controlled profiles together with their respective targets for a simultaneous test. The controlled profiles of the uniaxial tests are shown in fig. (D2) within the appendix. Apart from the axis to be excited, both cross-axis excitations are kept as low as possible by the vibration controller.

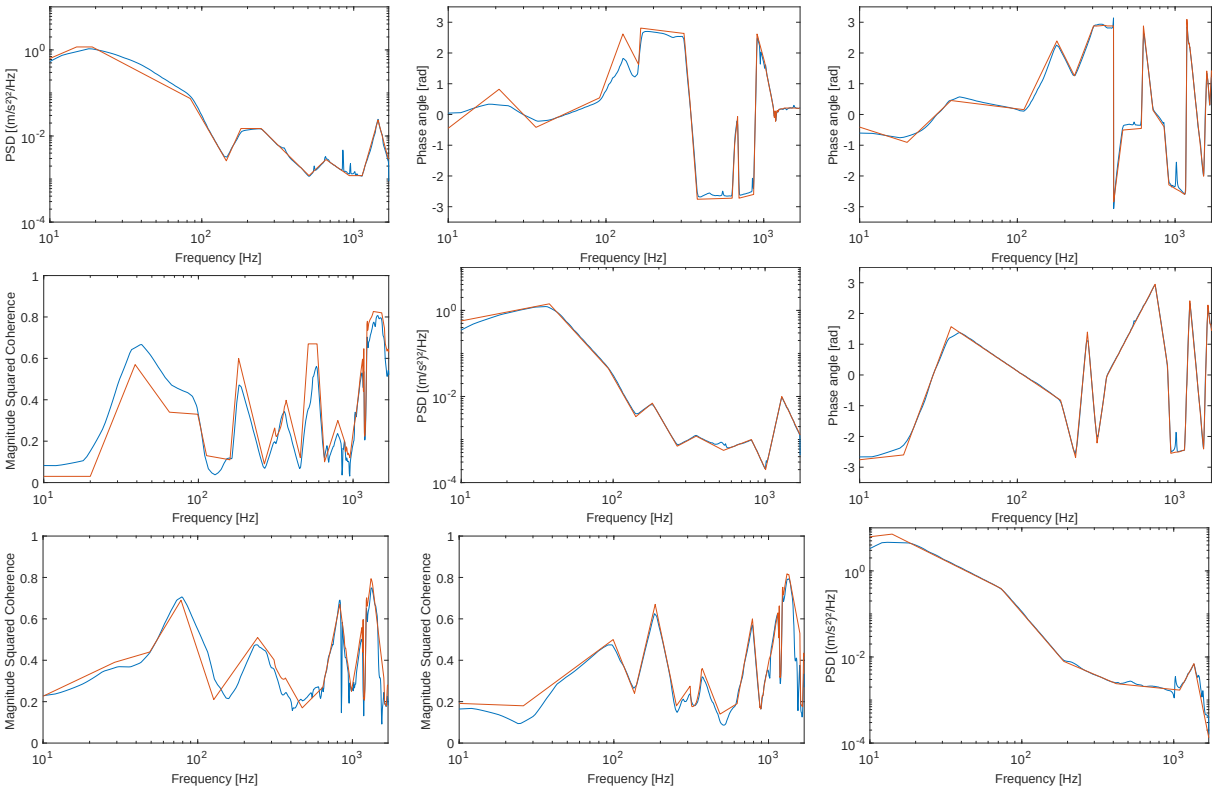

Figure 6.17: Measured test values of SDM for the complex automotive component, phases on the upper triangle, magnitude squared coherences on the lower triangle

Fig. (6.18) shows the stress related velocity response PSDs. No geometric factors are applied in this figure. The overlap of several modes in the higher frequency range indicates a stronger potential influence of the phase control on the resulting fatigue damage.

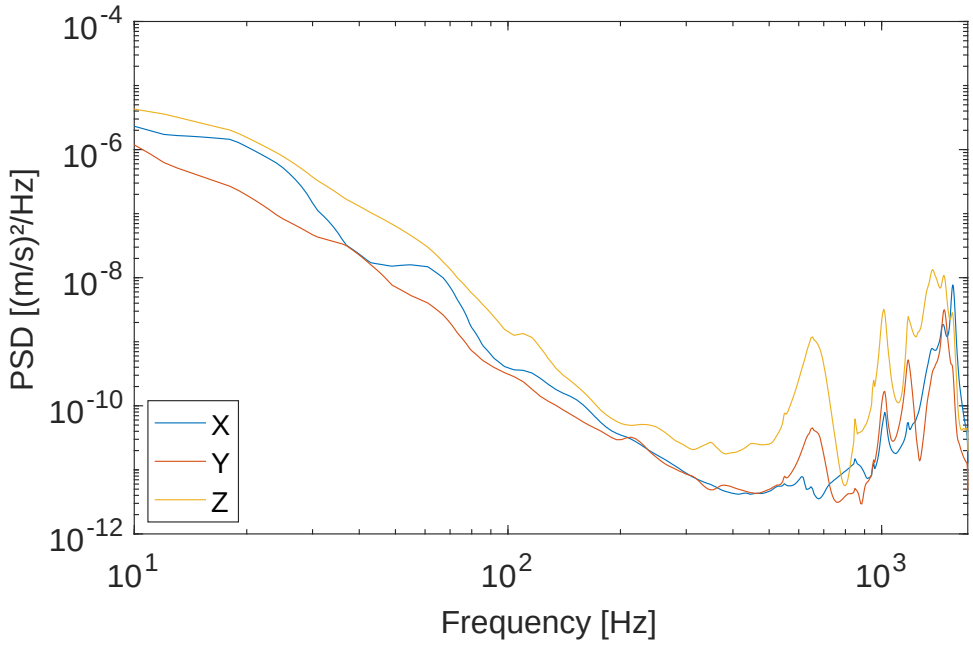

Figure 6.18: Response velocity PSDs from 3D excitation of the complex automotive component (3D-shaker coordinate system)

Fatigue damage calculations are performed for the uniaxial and multiaxial tests. Standard values are used for the geometric factors according to subsection 3.4.3.3. The velocities refer to a single determined hot spot which is used for the quantitative comparison. The results in table (6.6) show a higher multiaxial fatigue damage which increases with increasing slope values. The deviation can be explained by the large number of eigenfrequencies that are differently excited by the derived profile and likely to be influenced by the excitation phase.

Table 6.6: Ratio between 3D- and 1D-fatigue damage results for complex automotive component excited with derived profile (velocity measurement, geometric factors from simplified model)

b	3	4	5	6	7	8	9	10	11	12	13
$D_{v,3D}/D_{v,1D}$	1.28	1.81	2.47	3.25	4.16	5.21	6.44	7.89	9.63	11.76	14.43

6.2.3 Sine Sweep Test based on Field Data

For the test of the simple automotive component, the setup was already given in fig. (4.16). Thereby, a control at the top is chosen because of its location near the mounting. Two accelerometers are placed on the specimen to determine both translational and rotational velocities.

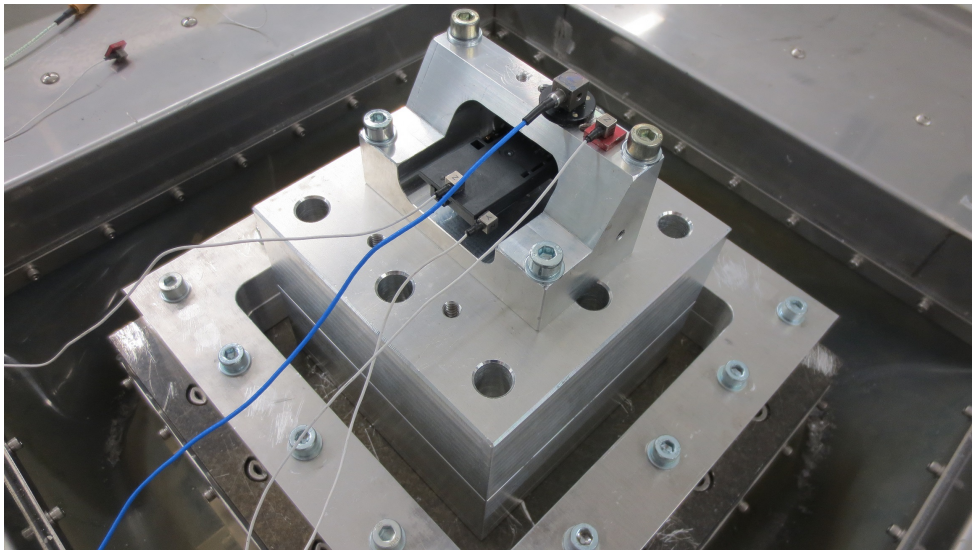

Figure 6.19: Setup for example automotive component

The profile is derived from three vehicle engine run-up measurements. Therefore, envelopes are drawn according to subsection 2.3.2.1 resulting in three sine sweep profiles given in fig. (6.20). Sine sweep profiles that cover engine run-ups typically range from 100 Hz to around 450 Hz, as can be seen in [35]. Thus, a single, logarithmic sweep with 1 octave per minute from 100 Hz to 450 Hz is chosen. The phases are selected randomly since no trends can be obtained from the vehicle measurements and constant phases may lead to highly unrealistic excitations. To overcome the shaker resonances accurately, a TWR is used as sine sweep control. Referring to the coordinate system in fig. (3.28), the vertical profile (orientation in vehicle) is applied on the x-axis, the longitudinal on the y-axis and the transverse on the z-axis. The measured excitations for the uniaxial and simultaneous test are shown in fig. (6.21).

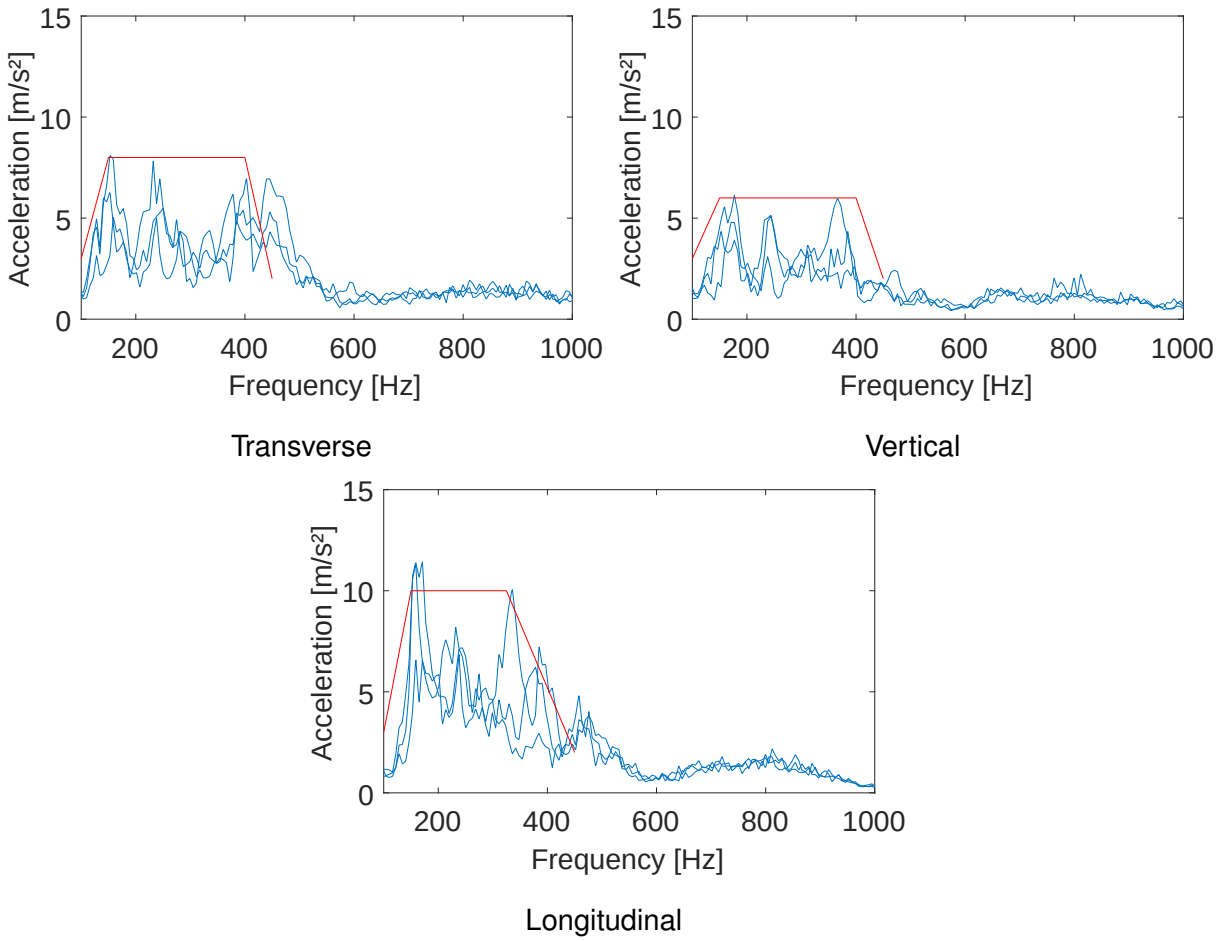

Figure 6.20: Derived sine sweep profile for example automotive component

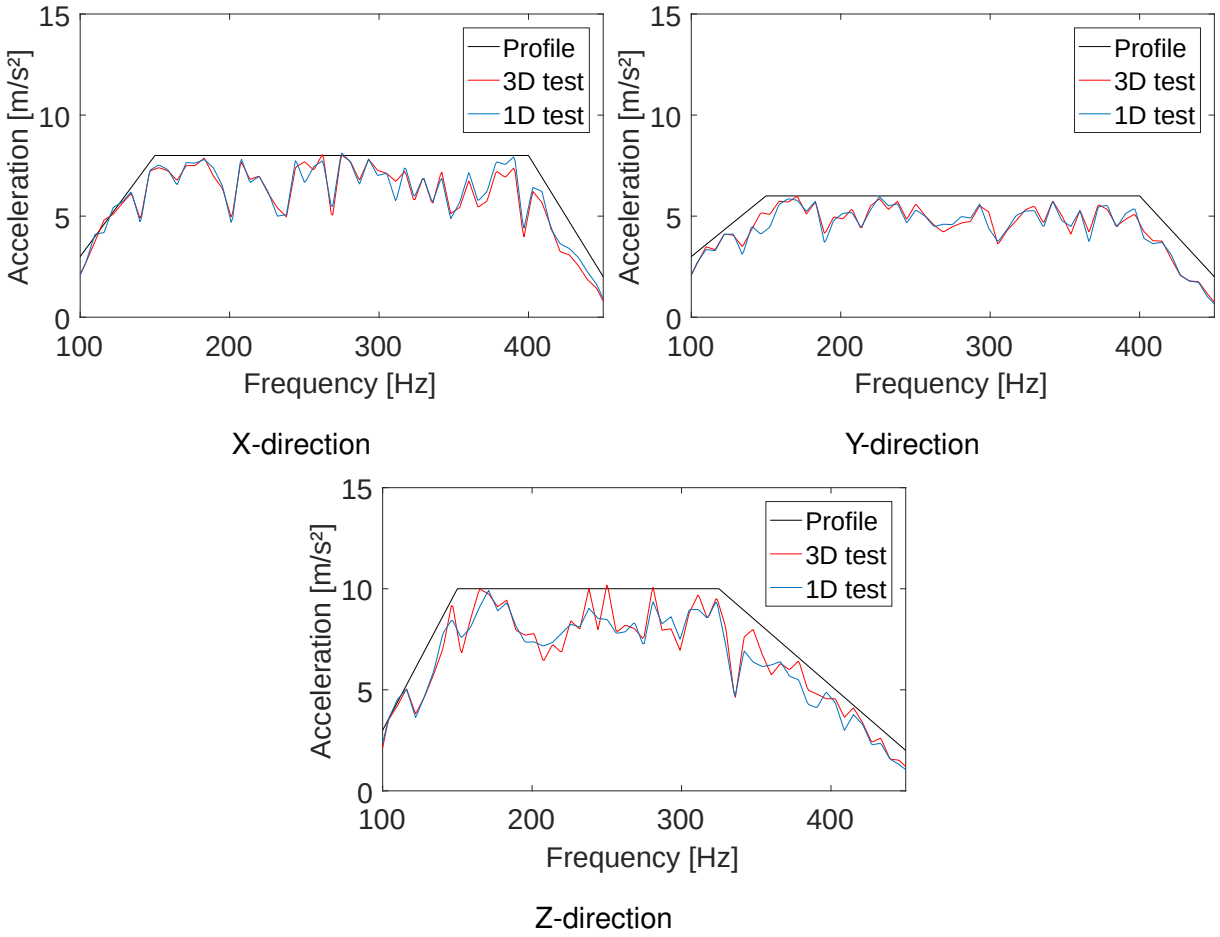

Figure 6.21: Measured test excitation on example automotive component (3D-shaker coordinate system)

Fig. (6.22) shows the stress related velocity response amplitudes. No geometric factors are applied in this figure. The responses are clearly dominated by the first mode at around 390 Hz which appears to be the only excited one.

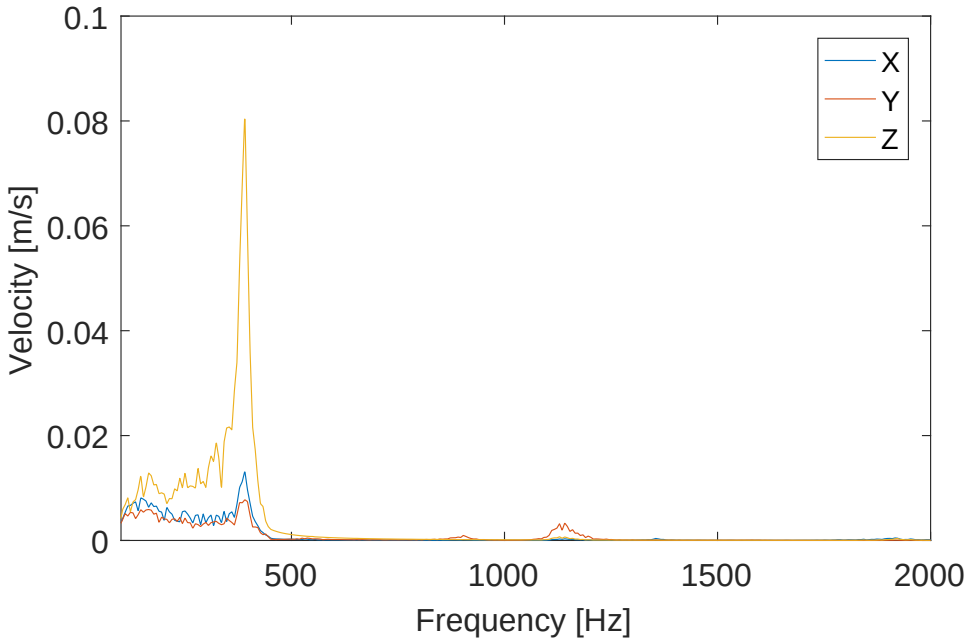

Figure 6.22: Response velocity from 3D excitation of the example automotive component (3D-shaker coordinate system, position 1 according to fig. 3.28)

Fatigue damage calculations are performed for the uniaxial and multiaxial tests. Therefore, the proposed geometric factors of the simplified model are applied. The velocities refer to a single determined hot spot which is used for the quantitative comparison. The results in table (6.7) show slightly larger fatigue damage values for a multiaxial excitation. The reason is a small difference in the vibration control which performs a slightly higher Z-excitation during the multi-axis testing, as indicated in fig. (6.21). Thus, an equal fatigue damage $D_{v,3D}/D_{v,1D} = 1$ is stated since only one mode is excited which responds in the same manner.

Table 6.7: Ratio between 3D- and 1D-fatigue damage results for example automotive component excited with derived profile (velocity measurement, geometric factors from simplified model)

b	3	4	5	6	7	8	9	10	11	12	13
$D_{v,3D}/D_{v,1D}$	1.06	1.16	1.20	1.23	1.24	1.26	1.28	1.32	1.36	1.42	1.48

6.2.4 Conclusions out of Test Results

The results of the testing scenarios are briefly compared in table (6.8). The information of the occurring hot spots is predefined by the FE simulations using either a full or simplified model. Thereby, the locations are chosen reasonable since the selection depends on the refinement of the mesh. Regarding the fatigue damage, the results obtained from the tests are used for a final evaluation.
For realistic example profiles, an equal or higher fatigue damage is expected with multiaxial excitation which could be shown definitely for both the multi-axis test specimen and the complex automotive component. Due to the limited frequency range of interest no difference could be detected for the simple automotive component at all. However, considering a wider frequency range a much higher sensitivity is assumed as indicated in subsection 3.4.2.2.
Generally, all results highly depend on the chosen excitation profile. Changes in amplitudes, mounting orientation, frequency range, as well as excitation phase may influence the results more or less strongly. Furthermore, slight differences in control actions may also take influence.

Table 6.8: Comparison of automotive component tests regarding the difference of sequential uniaxial and multiaxial excitation

Scenario	Result
Multi-axis test specimen	Different hot spot, same fatigue damage
Complex automotive component	Same hot spot, different fatigue damage
Simple automotive component	Same hot spot, same fatigue damage

As already stated in the literature review (see subsection 1.2), differences between uniaxial and multiaxial excitation may occur on both the hot spot location and the fatigue damage. However, this is always case dependent as confirmed by three different realistic scenarios.

7 Summary, Conclusion and Outlook

In this thesis, a methodology for multi-axis testing was developed that aims at comparing the severity of sequential uniaxial and multiaxial vibration tests. Thereby, the work focused on the application within the automotive industry. At the beginning, an initial chapter addressed theoretical aspects of signal processing, structural dynamics, structural durability calculation and vibration testing which all contribute to the multi-axis testing methodology.

A major goal of the thesis was the definition of a measurement quantity that sufficiently relates to fatigue damage which was extensively discussed in chapter 3. Thereby, the usage of strain gauges was to be avoided due to its complexity and the lack of accessibility to potential hot spots. As a first step, a general methodology for fatigue damage evaluation was proposed which had to be extendable to the quantity sought-after. Furthermore, general effects that may occur with multiaxial excitation were discussed. Different vibrational quantities were investigated with regard to their relation to local stresses. The relevant quantity was found to be modal velocity and an expression of an established equivalent stress using velocities multiplied with geometric factors was derived. The general influence of the geometry was at first analytically described using an Euler Bernoulli beam with a non-constant cross section. Then, geometric factors were obtained from example FE-models. To avoid time-consuming simulations, the usage of strongly simplified FE-models was proposed. Thereby, the geometric information can be preserved and appropriate measurement positions can be found, while the simulation effort is reduced down to a minimum. For three example structures, the results indicated a good qualitative match between stresses obtained from the full simulation and velocity measurements multiplied by geometric factors obtained from the simplified models. The new fatigue damage methodology based on modal velocities is less time consuming since neither full simulations nor strain gauges are necessary for the proposed relative evaluation of vibrational environments. For complex equipment, the method may be limited to the determination of appropriate measurement locations. A major drawback is obviously the lack of knowledge about the internal structures. Only linear parts were considered in order to maintain generality. Any non-linear effects can be investigated individually in future work. Since the slender beam theory was used for the derivation of the equivalent stress, the method is rather not appropriate for structures with a dominating shear stress induced by shear force. In chapter 6, EOL tests were performed on simple rods in order to experimentally prove the general relationship between velocities and fatigue damage due to local stresses. The EOL tests might be extended by different excitation phases.

In chapter 4, a focus was put on the investigation and fixture modification of the given electrodynamic triaxial shaker prototype. Since all tests were performed on this system, detailed work on this subject was mandatory. Preliminary investigations of the system showed a complex and changing behavior. Bearing unit resonances, especially between 1000 Hz and 2000 Hz, lead to worse controllability and can be severe to the system. Thus, the efforts done in this chapter aimed at the modification of the test setup in order to ensure an effective control. Different se-

tups and control positions were examined sequentially which led to a test setup that meets all given requirements and enables more accurate testing conditions than on the bare shaker table. Especially for large shakers which are used within the automotive industry, a standardized modification of the test setup might be necessary. Apart from the mechanical shaker system, investigations were performed on different vibration controllers in order to define an optimum control strategy. Thereby, a focus was put on noise suppression and real time control. Further investigations can be conducted on multipoint control strategies, especially for tests with several specimens that are distributed on the table.

Apart from the fatigue damage evaluation and the shaker setup design, the derivation of meaningful vibration test profiles is an essential part of the multi-axis testing methodology which was treated in chapter 5. Generally, there are three different approaches which were all examined and extended for its proper usage in automotive testing. The first method uses field data directly to obtain a single test profile. An application of envelopes, which is often used to create worst case profiles, was considered also including the phase and coherence terms. Since a manipulation of the phases and coherences often results in a negative definite SDM, which is not physically meaningful, a further processing is needed. Therefore, an optimization on the drawn phase and coherence envelopes was proposed which finds the closest geometrical positive definite SDM. The second method, which is the FDS approach, uses an SDOF system for each frequency to simulate a simplified structural response which directly relates the individual road profiles to fatigue damage. Since all phase information is neglected within the FDS, an attempt was made to extend the original approach. Thereby, a new formulation was found for the inclusion of the damaging effects due to a specific excitation phase. However, the improvement only addresses uniaxial profile derivation due to its inherent uniaxiality. The third method is the usage of standard profiles which is only available for uniaxial tests within the current automotive industrial standards. Based on a comparatively large dataset, a multi-axis standard random profile was derived for a specific assembly group. Thereby, no standard phase information could be obtained from the available dataset.

The previous results and methods were used for the specification of three individual test setups in chapter 6: A standard random vibration test of a multi-axis test specimen which serves as a dummy for certain automotive components, a field data based random test of a complex automotive component and a field data based sine sweep test of a simple engine mounted automotive component. In order to quantitatively compare the fatigue damage between multiaxial and sequential uniaxial excitation, vibration tests were conducted on the respective examples under a realistic test condition. A fatigue damage evaluation was performed for all components using velocity measurements and geometric factors obtained from both a full and a simplified FE model. The respective hot spots were defined by a preceding simulation. The tests combined with the simulation showed different results in fatigue damage and hot spot location for each test. Thus, it can be concluded that a multi-axis test is in general of a different nature than sequential uniaxial tests and a general trend may not be stated. It is assumed that complex components with a lot of eigenfrequencies show stronger differences between the fatigue damage of uniaxial and multiaxial tests than simple components. This is mainly due to the su-

perimposition of the stress cycles and the excitation phase. The usage of simplified FE models yields a good estimate for geometric factors but is rather limited to models with a single hotspot and may not be appropriate to evaluate several locations at the same time.

The thesis provides an overall methodology for the evaluation of multi-axis vibration testing with a focus on automotive components. Thereby, fatigue damage is considered as the major failure mechanism. In future work, similar investigations can be accomplished for components where primarily abrasion occurs, such as for example in connectors.

The objectives defined in section 1.3 are accomplished as follows:

- The difference in fatigue damage between multiaxial and sequential uniaxial testing using realistic scenarios were evaluated on three automotive examples resulting in differences in both the hot spot location and the fatigue damage
- As appropriate measurement quantity, an equivalent stress based on relative velocities multiplied with geometric factors from both full and simplified FE models was chosen
- The specific 3D-shaker system was characterized and modified by different fixtures to enable accurate testing up to a frequency of 2000 Hz
- Established profile derivation methods for random vibration testing were investigated and a new method was presented which includes the usage of envelopes and a subsequent optimization towards a feasible, complete 3D-test profile
- All three outcomes (velocity based fatigue damage evaluation, fixture modification of the 3D-shaker system, 3D-test profile derivation) basically describe new aspects and improvements of multi-axis shaker testing. Thereby, a balance between effort and accuracy was found which is valuable for a possible future standardization

References

[1] Abrate S., *Vibration of Non-Uniform Rods and Beams*, Journal of Sound and Vibration, vol. 185, no. 4, pp. 703-716, 1995.

[2] Alessio S.M., *Digital Signal Processing and Spectral Analysis for Scientists*, Springer, first ed., 2016.

[3] Altenbach H., *Kontinuumsmechanik*, Springer Vieweg, third ed., 2015.

[4] ASTM International, *ASTM E1049-85: Standard Practices for Cycle Counting in Fatigue Analysis*, ASTM, 2017.

[5] Benasciutti D., Cristofori A., Tovo R., *Analogies between Spectral Methods and Multiaxial Criteria in Fatigue Damage Evaluation*, Probabilistic Engineering Mechanics, vol. 31, pp. 39-45, 2013.

[6] Benasciutti D., Sherratt F., Cristofori A., *Recent Developments in Frequency Domain Multi-Axial Fatigue Analysis*, International Journal of Fatigue, vol. 91, pp. 397-413, 2016.

[7] Bergmann J.W., Heuler P., *Übertragbarkeit - ein zentrales Problem der Lebensdauervorhersage schwingbelasteter Bauteile*, Mat.-wiss. u. Werkstofftech., vol. 25, pp. 3-10, 1994.

[8] Beste A., et. al., *Multiaxial Rainflow: A Consequent Continuation of Professor Tatsuo Endo's Work*, The Rainflow Method in Fatigue, First. ed., pp. 31-40, 1992.

[9] Boller C., Seeger T., Vormwald M., *Materials Database for Cyclic Loading*, Fachgebiet Werkstoffmechanik, TU Darmstadt, 2008.

[10] Bonte M.H.A., de Boer A., Liebregts R., *Determining the von Mises Stress Power Spectral Density for Frequency Domain Fatigue Analysis Including Out-of-phase Stress Components*, Journal of Sound and Vibration, vol. 302, no. 1-2, pp. 379-386, 2007.

[11] Canfield-Dafilou E.K., Abel J.S., *On Restoring Prematurely Truncated Sine Sweep Room Impulse Response Measurements*, Proc. 20th International Conference on Digital Audio Effects, pp. 375-380, 2017.

[12] Cornelis B., et. al., *Improved MIMO FRF Estimation and Model Updating for robust Time Waveform Replication on durability test rigs*, Proc. 26th ISMA including USD, pp. 737-752, 2014.

[13] Crandall S.H., *Relation between Strain and Velocity in Resonant Vibration*, Journal of the Acoustical Society of America, vol. 34, no. 12, pp. 1960-1961, 1962.

[14] Cui S., Chen H., He X., *Time-domain Approach for Multi-exciter Random Environment Test*, Journal of Sound and Vibration, vol. 398, pp. 52-69, 2017.

[15] D'Elia G., et. al., *Drives Power Reduction Procedure to Fill in the Multiple-Input Multiple-Output Random Control Reference Matrix*, Proc. 28th ISMA including USD, pp. 1259-1270, 2018.

[16] Ekanayaka V., *Extension of a Method for Designing 3D Vibration Test Profiles*, Master's Thesis, Universität Duisburg-Essen, 2020.

[17] Ernst M., et. al., *Comparison of Electronic Component Durability Under Uniaxial and Multiaxial Random Vibrations*, Journal of Electronic Packaging, vol. 137, no. 1, 2015.

[18] Feldmann M., *Hilbert Transform Applications in Mechanical Vibration*, Wiley, first ed., pp. 37-49, 2011.

[19] Finnveden S., Pinnington R.J., *A Velocity Method for Estimating Dynamic Strain and Stress in Pipes*, Journal of Sound and Vibration, vol. 229, pp. 147-182, 2000.

[20] French R.M., Handy R., Cooper H.L., *A Comparison of Simultaneous and Sequential Single-Axis Durability Testing*, Experimental Techniques, vol. 30, no. 5, pp. 32-37, 2006.

[21] Gaberson H.A., Chalmers R.H., *Modal Velocity as a Criterion of Shock Severity*, Shock and Vibration Bulletin, vol. 40, no. 2, pp. 31-40, 1969.

[22] Gatto M., Peeters B., Coppotelli G., *Flexible Shaker Excitation Signals for Improved FRF Estimation and Non-Linearity Assessment*, Proc. 24th ISMA including USD, pp. 2475-2488, 2010.

[23] Goemans M.X., Williamson D.P., *Approximation Algorithms for Max-3-Cut and Other Problems Via Complex Semidefinite Programming*, Journal of Computer and System Sciences, vol. 68, pp. 442-470, 2004.

[24] Gregory D., Bitsie F., Smallwood D.O., *Comparison of the Response of a Simple Structure to Single Axis and Multiple Axis Random Vibration Inputs*, Proc. 79th Shock and Vibration Symposium, 2008.

[25] Guan G., et. al., *Generation of Time Domain Drive Signals in MIMO Random Vibration Control System*, Proc. 7th JFPS International Symposium on Fluid Power, pp. 295-300, 2008.

[26] Haibach E., *Betriebsfestigkeit*, Springer, third ed., 2006.

[27] Hale M.T., *A 6-DOF Vibration Specification Development Methodology*, Journal of the IEST, vol. 54, no. 2, 2011.

[28] Halfpenny A., *Methods for Accelerating Dynamic Durability Tests*, Proc. 9th International Conference on Recent Advances in Structural Dynamics, 2006.

[29] Hanselka H., Sonsino C.M., *Betriebsfestigkeit und Zuverlässigkeit von komplexen und intelligenten Strukturen*, Mat.-wiss. u. Werkstofftech., vol. 34, no. 9, 2003.

[30] Henderson G.R., Piersol A.G., *Fatigue Damage Related Descriptor for Random Vibration Test Environments*, Sound and Vibration, vol. 29, no. 10, pp. 20-24, 1995.

[31] Himmelblau H., Hine M.J., *Effects of Triaxial and Uniaxial Random Excitation on the Vibration Response and Fatigue Damage of Typical Spacecraft Hardware*, Proc. 66th Shock and Vibration Symp., 1995.

[32] Hunt F.V., *Stress and Strain Limits on Attainable Velocity in Mechanical Vibration*, Journal of the Acoustical Society of America, vol. 32, no. 9, pp. 1123-1128, 1960.

[33] Hunter N.F., Cross K.R., Nelson G., *The Cross Spectrum in Multiple Input Multiple Response Vibration Testing*, Proc. 36th IMAC, 2019.

[34] IMV Corporation, *Operation Manual*, Internal document, 2015.

[35] International Organization for Standardization, *ISO 16750-3: Road Vehicles - Environmental Conditions and Testing for Electrical and Electronic Equipment - Mechanical Loads*, IHS, third ed., pp. 37-43, 2012.

[36] Irgens F., *Continuum Mechanics*, Springer, first ed., 2008.

[37] Karczub D.G., Norton M.P., *Correlations between Dynamic Stress and Velocity in Randomly Excited Beams*, Journal of Sound and Vibration, vol. 226, pp. 645-674, 1999.

[38] Kersch K., Schmidt A., Woschke E., *Multiaxial Fatigue Damage Evaluation: A new Method based on Modal Velocities*, Journal of Sound and Vibration, vol. 476, 2020.

[39] Kersch K., Woschke E., *Fixture Modifications for Effective Control of an Electrodynamic 3D-Shaker System*, Sound and Vibration, vol. 54, no. 2, 2020.

[40] Kersch K., Woschke E., *Modal Velocity based Multiaxial Fatigue Damage Evaluation using Simplified Finite Element Models*, Journal of Applied Mechanics, vol. 87, 2020.

[41] Kersch K., Woschke E., *Multiaxial and Uniaxial Fatigue Failure Evaluation using Modal Velocities*, Experimental Techniques, DOI: 10.1007/s40799-020-00403-7, 2020.

[42] Kim C.J., *Accelerated Sine-on-Random Vibration Test Method of Ground Vehicle Components over Conventional Single Mode Excitation*, Applied Sciences, vol. 7, no. 8, 2017.

[43] Kley M., *Einflüsse auf die Lebensdauer von Bus-Automatgetriebegehäusen*, Institut für Maschinenkonstruktion und Getriebebau Universität Stuttgart, 2004.

[44] Lagoda T., Macha E., Pawliczek R., *The Influence of the Mean Stress on Fatigue Life of 10HNAP Steel under Random Loading*, International Journal of Fatigue, vol. 23, pp. 283-291, 2001.

[45] Lalanne C., *Mechanical Vibration and Shock Analysis - Fatigue Damage*, Wiley, second ed., 2009.

[46] Lalanne C., *Mechanical Vibration and Shock Analysis - Random Vibration*, Wiley, second ed., 2009.

[47] Lalanne C., *Mechanical Vibration and Shock Analysis - Specification Development*, Wiley, second ed., 2009.

[48] Läpple V., *Einführung in die Festigkeitslehre*, Vieweg+Teubner, third ed., 2011.

[49] Li Q.S., *Exact Solutions for Free Longitudinal Vibrations of Non-Uniform Rods*, Journal of Sound and Vibration, vol. 234, no. 1, pp. 1-19, 2000.

[50] Liu Z. et. al., *Complex Coherence Constraint for the Definition of the Spectral Density Matrix*, Journal of the IEST, vol. 61, no. 1, 2018.

[51] Maia N.M.M., e Silva J.M.M., *Theoretical and Experimental Modal Analysis*, Wiley, first ed., 1997.

[52] McNeill S.I., *Implementing the Fatigue Damage Spectrum and Fatigue Damage Equivalent Vibration Testing*, Proc. 79th Shock and Vibration Symposium, pp. 1-20, 2008.

[53] Merritt R.G., *Harris Shock and Vibration Handbook*, McGraw-Hill, sixth. ed., pp. 7.1-7.29, 2009.

[54] Mrsnik M., Slavic J., Boltezar M., *Frequency Domain Methods for a Vibration Fatigue Life Estimation - Application to Real Data*, International Journal of Fatigue, vol. 47, pp. 8-17, 2013.

[55] Musella U., et. al., *A Minimum Drives Automatic Target Definition Procedure for Multi-axis Random Control Testing*, Mechanical Systems and Signal Processing, vol. 107, pp. 452-468, 2018.

[56] Musella U., et. al., *Analyses of Target Definition Processes for MIMO Random Vibration Control Tests*, Proc. 35th IMAC, 2017.

[57] Musella U., et. al., *Tackling the Target Matrix Definition in MIMO Random Vibration Control Testing*, Proc. 30th Aerospace Testing Seminar, 2017.

[58] Nasdala L., *FEM-Formelsammlung Statik und Dynamik*, Vieweg+Teubner, first ed., 2010.

[59] NATO, *AECTP-200-3, Category 240: Mechanical Conditions*, NATO Standardisation Agency, third ed., 2006.

[60] Nelson G., Jacobs-O'Malley L., *Comparison of Multi-Axis and Single Axis Testing on Plate Structures*, Proc. 85th Shock and Vibration Symposium, 2014.

[61] Nguyen N.B., *Entwicklung einer numerisch gestützten Methodik zur betriebsfesten Vorauslegung von Fahrzeugkomponenten unter stochastischer und mehrachsiger Vibrationsbelastung*, Shaker, first ed., pp. 49-52, 2015.

[62] Nieslony A., Boehm Michal, *Frequency-domain Fatigue Life Estimation with Mean Stress Correction*, International Journal of Fatigue, vol. 91, pp. 373-381, 2016.

[63] Papuga J., Vargas M., Hronek M., *Evaluation of Uniaxial Fatigue Criteria Applied to Multiaxially Loaded Unnotched Samples*, Engineering Mechanics, vol. 19, no. 2/3, pp. 99-111, 2012.

[64] Peeters B., Debille J., *Multiple-Input-Multiple-Output Random Vibration Control: Theory and Practice*, Proc. 20th ISMA, pp. 507-516, 2002.

[65] Piersol A.G., *Preliminary Design Procedures for Equipment Exposed to Random Vibration Environments*, Journal of the IEST, vol. 44, pp. 23-27, 2001.

[66] Pitoiset X., Preumont A., *Spectral Methods for Multiaxial Random Fatigue Analysis of Metallic Structures*, International Journal of Fatigue, vol. 22, pp. 541-550, 2000.

[67] Pouyet J.M., Lataillade J.L., *Torsional Vibrations of a Shaft with Non-Uniform Cross Section*, Journal of Sound and Vibration, vol. 76, no. 1, pp. 13-22, 1981.

[68] Qiu H., et. al., *Study on Multi-axis Sine Vibration Test Control Techniques*, Vibroengineering Procedia, vol. 28, pp. 46-51, 2019.

[69] Sanger D.J., *Transverse Vibration of a Class of Non-Uniform Beams*, Journal Mechanical Engineering Science, vol. 10, no. 2, pp. 111-120, 1968.

[70] Schmidt A., *Betriebsfestigkeit unter stochastischen Belastungen*, Veröffentlichung des Instituts für Stahlbau und Werkstoffmechanik der Technischen Universität Darmstadt, 2020.

[71] Schmidt A., *Ermittlung der Beanspruchungskollektive bei stochastischer Vibrationsbelastung als Basis eines Betriebsfestigkeitsnachweises*, Effiziente Auslegung und Absicherung in der Betriebsfestigkeit - Berichtsband der 45. Tagung, 2018.

[72] Smallwood D.O., *A Random Vibration Control System for Testing a Single Test Item with Multiple Inputs*, SAE Technical Paper 821482, pp. 55-61, 1982.

[73] Smallwood D.O., *Matrix Methods for Estimating the Coherence Functions from Estimates of the Cross-Spectral Density Matrix*, Shock and Vibration, vol. 3, no. 4, pp. 237-246, 1996.

[74] Smallwood D.O., *Minimum Input Trace for Multiple Input Multiple Output Linear Systems*, Journal of the IEST, vol. 56, no. 2, 2013.

[75] Smallwood D.O., *Multiple-Input Multiple-Output (MIMO) Linear Systems Extreme Inputs/Outputs*, Shock and Vibration, vol. 14, no. 2, pp. 107-131, 2007.

[76] Smallwood D.O., *Multiple Shaker Random Vibration Control - An Update*, Technical Report, Sandia National Laboratories, 1999.

[77] Smallwood D.O., Gregory D., *Evaluation of a Six-DOF Electrodynamic Shaker System*, Proc. 79th Shock and Vibration Symposium, 2008.

[78] Smallwood D.O., Paez T.L., *A Frequency Domain Method for the Generation of Partially Coherent Normal Stationary Time Domain Signals*, Shock and Vibration, vol. 1, no. 1, pp. 45-53, 1993.

[79] Smallwood D.O., Woodall T.D., Buksa E.J., *Minimum Drive Requirements for a Multiple Input Multiple Output Linear System*, Proc. 32th Environmental Technology: Coming of Age, 1986.

[80] Steinberg D.S., *Vibration Analysis for Electronic Equipment*, Wiley, third ed., pp. 166-175, 2000.

[81] Straka O., et. al., *Aspects and Comparison of Matrix Decompositions in Unscented Kalman Filter*, Proc. American Control Conference 2013, pp. 3075-3080, 2013.

[82] Strommen E.N., *Structural Dynamics*, Springer, first ed., 2014.

[83] Sweitzer K.A., Hull C.A., Piersol A.G., *Harris Shock and Vibration Handbook*, McGraw-Hill, sixth ed., pp. 40.6-40.20, 2009.

[84] Underwood M., Ayres R., Keller T., *Filling in the MIMO Matrix, Part 1 - Performing Random Tests Using Field Data*, Sound and Vibration, vol. 45, no. 3, pp. 8-14, 2011.

[85] Underwood M., Ayres R., Keller T., *Filling in the MIMO Matrix, Part 2 - Time Waveform Replication Tests Using Field Data*, Sound and Vibration, vol. 45(9), pp. 8-17, 2011.

[86] Underwood M., Ayres R., Keller T., *Some Aspects of using Measured Data as the Basis of a Multi-Exciter Vibration Test*, Proc. 28th IMAC, 2010.

[87] Underwood M., Keller T., *Rectangular Control of Multi-Shaker Systems: Theory and Practical Results*, Journal of the IEST, vol. 47, pp. 80-86, 2004.

[88] Underwood M., Keller T., Ayres R., *Multi-Shaker Control*, Sound and Vibration, vol. 51, no. 8, pp. 8-16, 2017.

[89] Ungar E.E., *Maximum Stresses in Beams and Plates Vibrating at Resonance*, Transactions of the ASME. Journal of Engineering for Industry, vol. 82B, pp. 149-155, 1962.

[90] U.S. Department of Defense, *MIL-STD-810H, Part 2: Laboratory Test Methods, Paragraph 514.8*, U.S. Department of Defense, 22th ed., 2019.

[91] van Baren J., *Fatigue Damage Spectrum - A New Tool to Accelerate Vibration Testing*, Sound and Vibration, vol. 49, no. 3, pp. 15-17, 2015.

[92] van Tongeren J.H., Maas R., *Derivation of Shaker Spectra for Structural Certification from Helicopter Flight Test Vibration Measurements*, Proc. 24th ISMA including USD, pp. 1759-1774, 2010.

[93] Vandenberghe L., Boyd S., *Semidefinite Programming*, SIAM Review, vol. 38, no. 1, pp. 49-95, 1996.

[94] Wagner A., *Implementierung einer Methode zur Berechnung schädigungsäquivalenter Vibrationstestprofile*, Master's Thesis, Universität Stuttgart, 2019.

[95] Wagner M., *Lineare und Nichtlineare FEM*, Springer Vieweg, first ed., 2017.

[96] Wandji D., *Entwicklung einer Methodik zur Berücksichtigung der Bauteilgeometrie bei Auslegung von Vibrationstests*, Bachelor's Thesis, Hochschule Heilbronn, 2019.

[97] White G., *Relationship between Strain and Velocity for Ground Vehicle Vibration*, Journal of the IEST, vol. 55, pp. 57-67, 2012.

[98] Whiteman W.E., Berman M., *Inadequacies in Uniaxial Stress Screen Vibration Testing*, Journal of the IEST, vol. 44, no. 4, pp. 20-23, 2001.

[99] Wijker J., *Random Vibrations in Spacecraft Structures Design*, Solid Mechanics and its Applications, vol. 165, pp. 37-70, 2009.

[100] Wijker J.J., Ellenbroek M.H.M., de Boer A., *Characterization and Synthesis of Random Acceleration Vibration Specifications*, Proc. 4th ECCOMAS Thematic Conference on Computational Methods in Structural Dynamics and Earthquake Engineering, 2013.

[101] Woo Y., *Automatic Simplification of Solid Models for Engineering Analysis Independent of Modeling Sequences*, Journal of Mechanical Science and Technology, vol. 23, pp. 1939-1948, 2009.

[102] Yang Y., Zhao Y., Kang D., *Integration on Acceleration Signals by Adjusting with Envelopes*, Journal of Measurements in Engineering, vol. 4, no. 2, pp. 117-121, 2016.

[103] Zheng R., Chen H., He X., *Control Method for Multi-Input Multi-Output Non-Gaussian Random Vibration Test with Cross Spectra Consideration*, Chinese Journal of Aeronautics, vol. 30, no. 6, pp. 1895-1906, 2017.

Appendix

A Chapter 3: Multiaxial Fatigue Damage Calculation

3.2 Relationship between Stresses and Different Vibrational Quantities

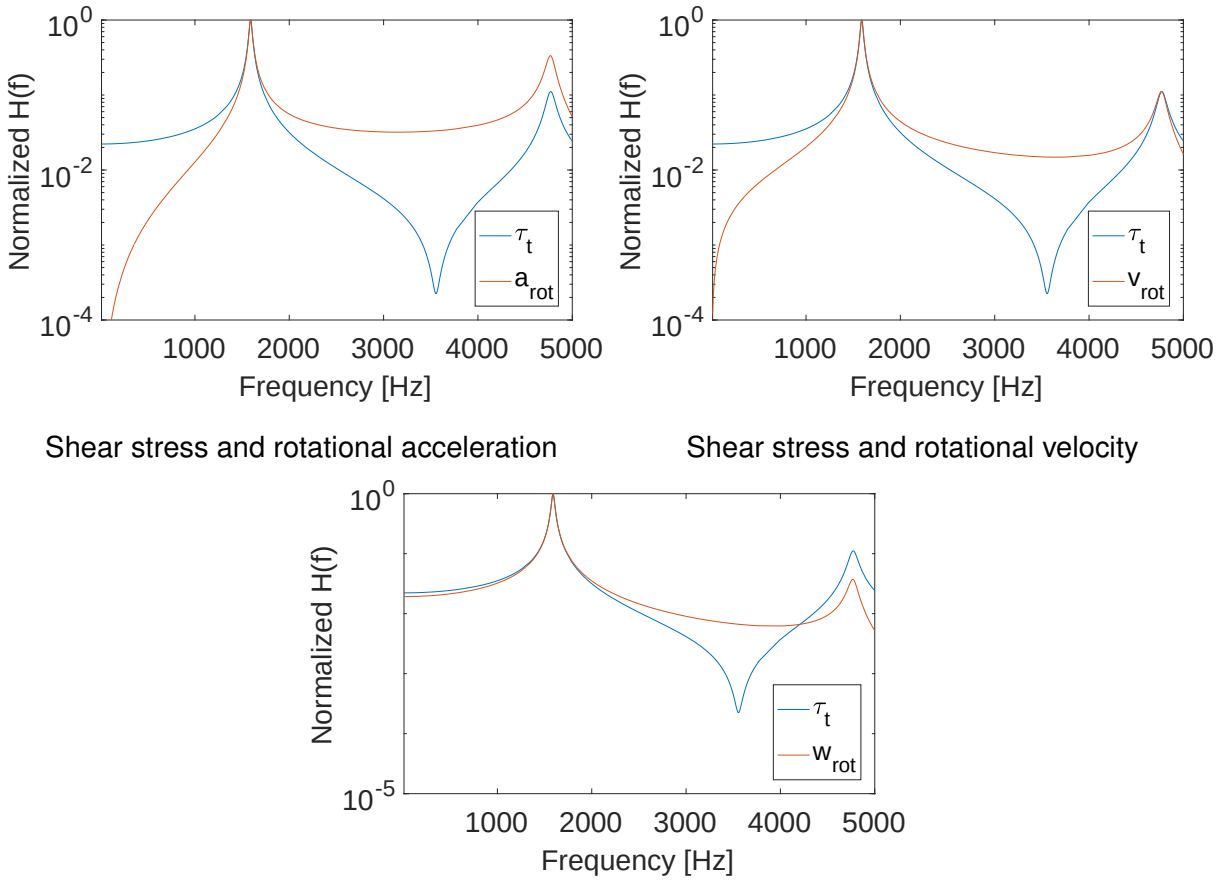

Shear stress and rotational acceleration

Shear stress and rotational velocity

Shear stress and rotational displacement

Figure A1: Frequency responses of normalized shear stress and different vibrational quantities

3.4 Geometry Influence on the Stress-Velocity Relationship

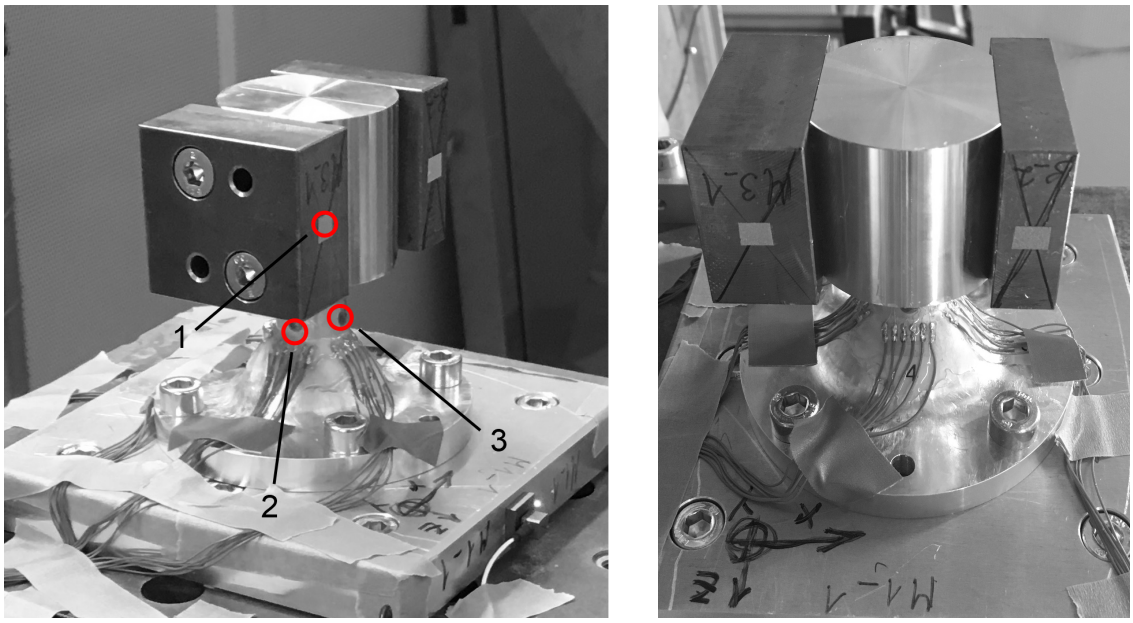

Figure A2: Experimental setup of multi-axis test specimen [38]

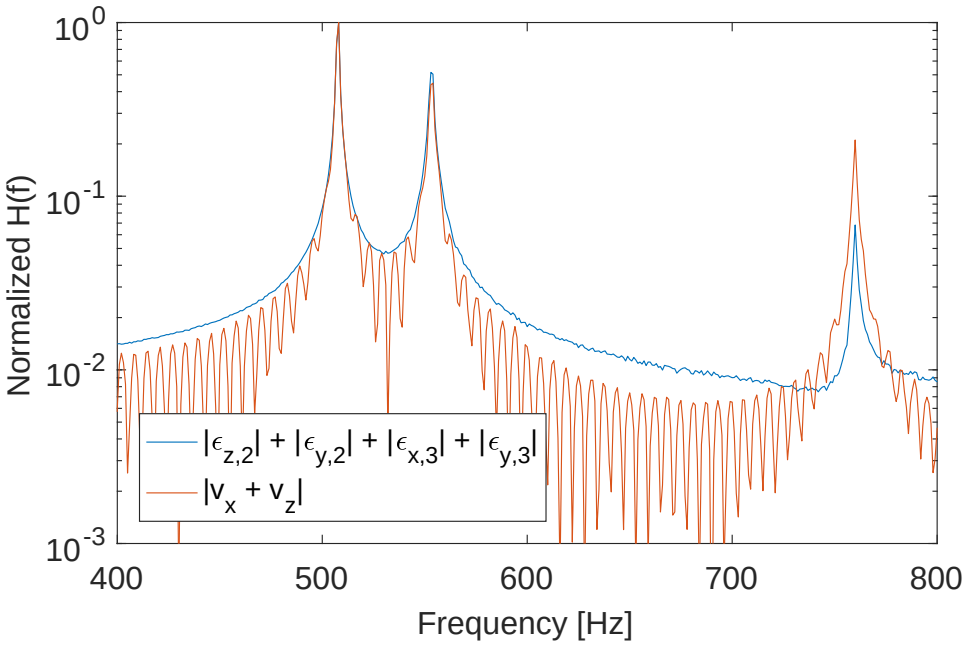

Figure A3: Normalized sum of absolute strains and velocities [38]

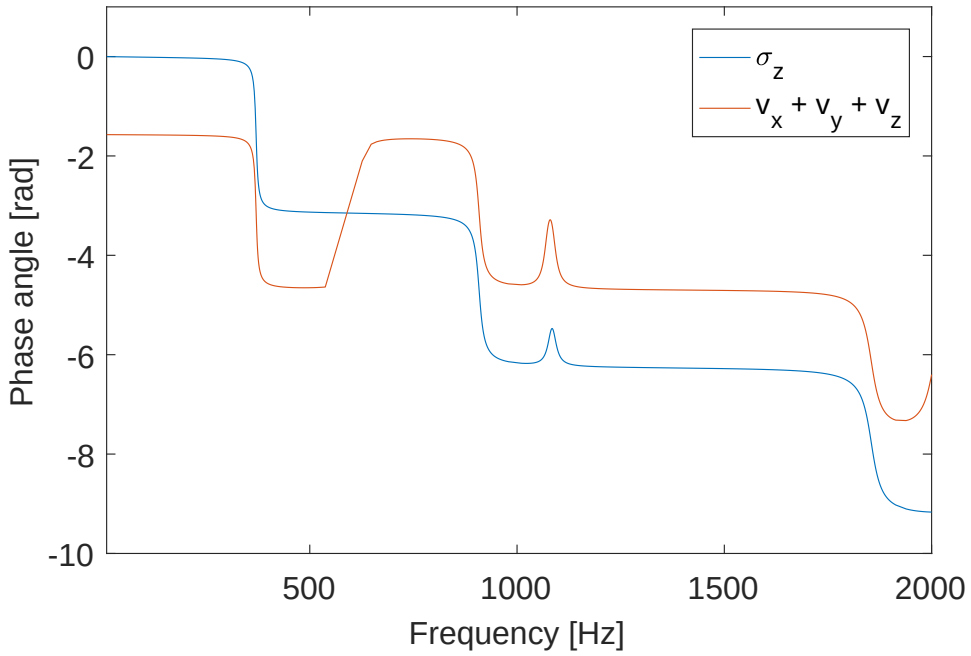

Figure A4: Phase of normal stress component and sum of translational velocities for the simple automotive component

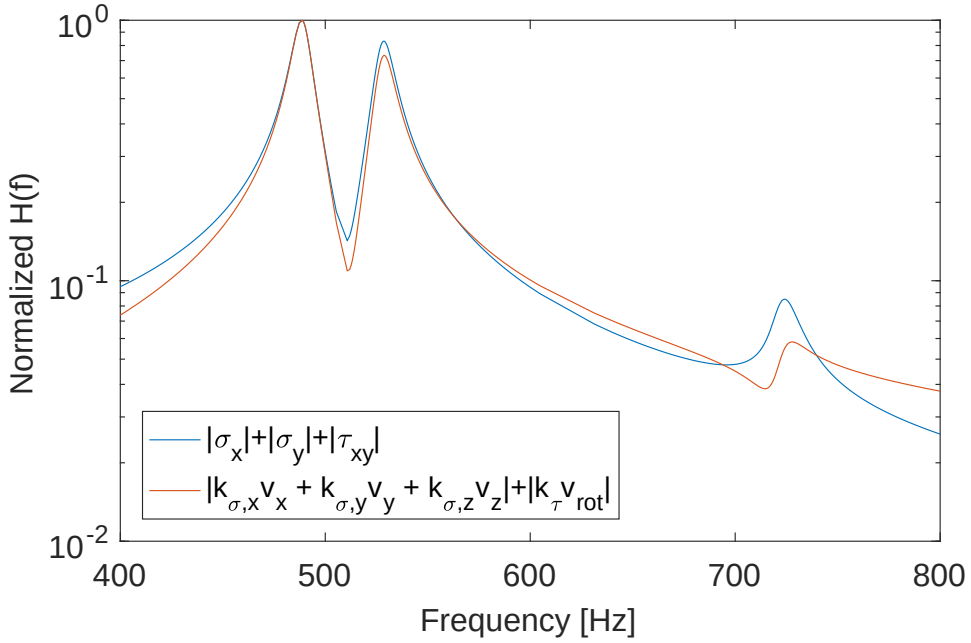

Figure A5: Sum of normalized stresses and velocities for the simplified multi-axis test specimen

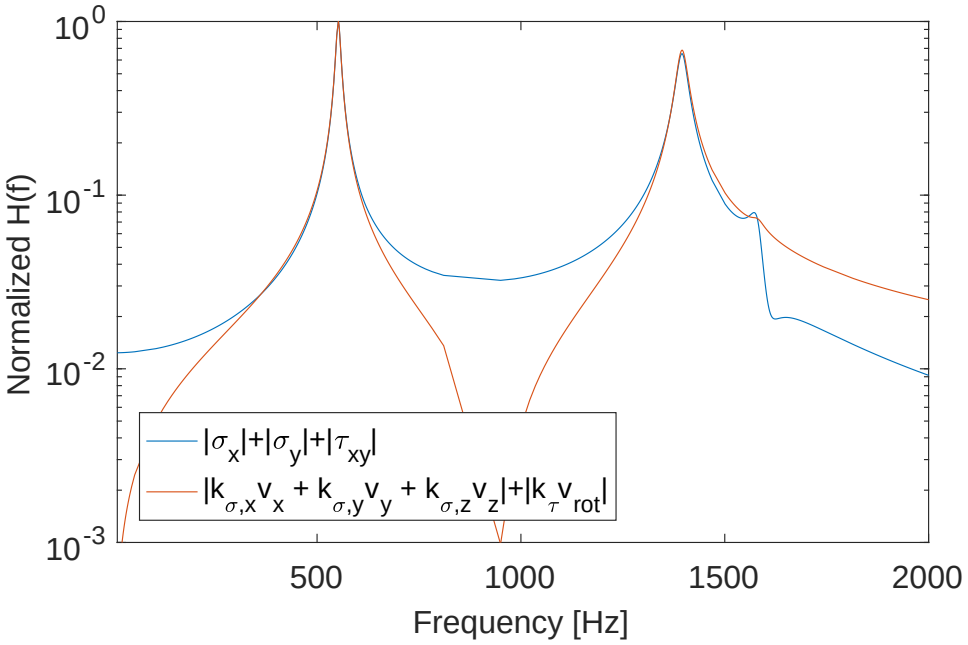

Figure A6: Sum of normalized stresses and velocities for the simplified model of the simple automotive component

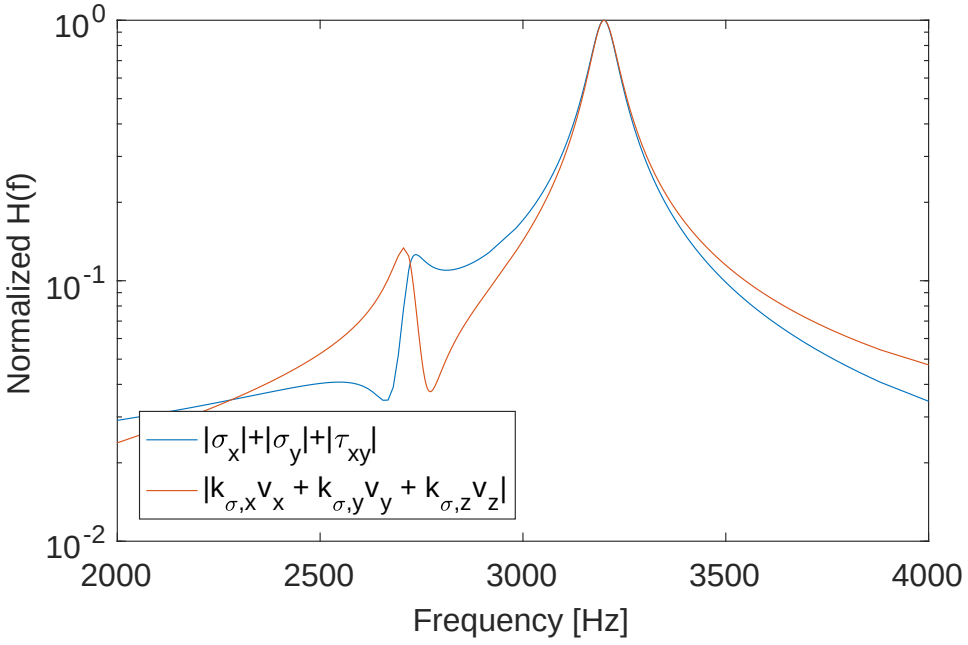

Figure A7: Sum of normalized stresses and velocities for the simplified complex automotive component

B Chapter 4: Implementation of the 3D-Shaker System

4.1 Shaker Characterization

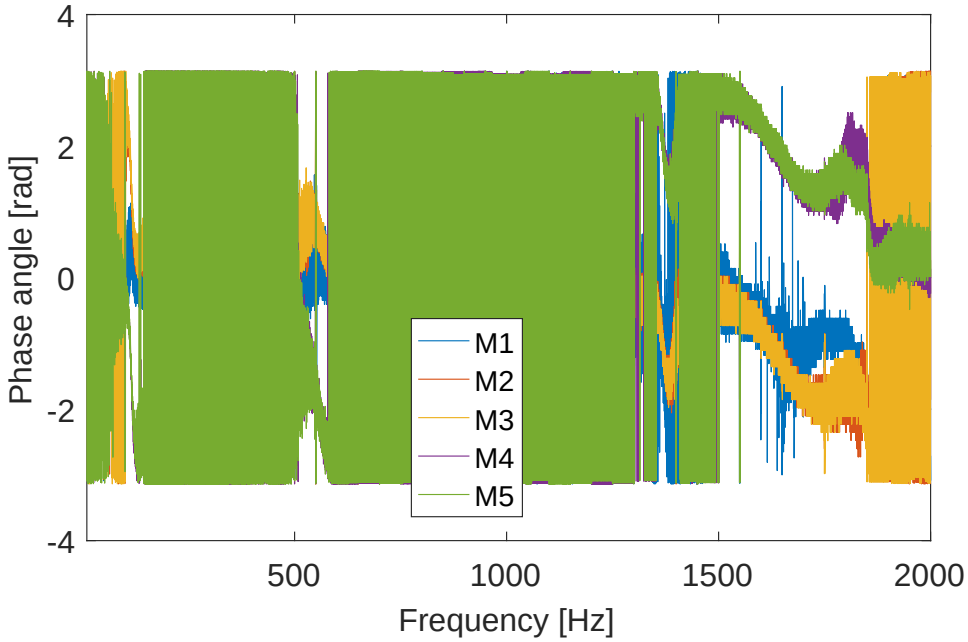

Figure B1: Phases of transfer function $\angle H_{23}(f)$ (Y-excitation, Z-response)

Table B1: Deviation from reference profile for bare table setup after approx. 100 operating hours

Frequency range	$10 - 1000$ Hz	$1000 - 1500$ Hz	$1500 - 2000$ Hz
Mean deviation	$6.0\ \%$	$8.9\ \%$	$348.9\ \%$
Max deviation	$14.0\ \%$	$22.6\ \%$	$2126.4\ \%$

Table B2: Deviation from reference profile for plate setup after approx. 100 operating hours

Frequency range	$10 - 1000$ Hz	$1000 - 1500$ Hz	$1500 - 2000$ Hz
Mean deviation	$6.3\ \%$	$33.6\ \%$	$249.4\ \%$
Max deviation	$26.4\ \%$	$152.3\ \%$	$991.5\ \%$

Table B3: Deviation from reference profile for block setup after approx. 100 operating hours

Frequency range	$10 - 1000$ Hz	$1000 - 1500$ Hz	$1500 - 2000$ Hz
Mean deviation	$8.1\ \%$	$21.7\ \%$	$14.8\ \%$
Max deviation	$21.7\ \%$	$33.2\ \%$	$32.2\ \%$

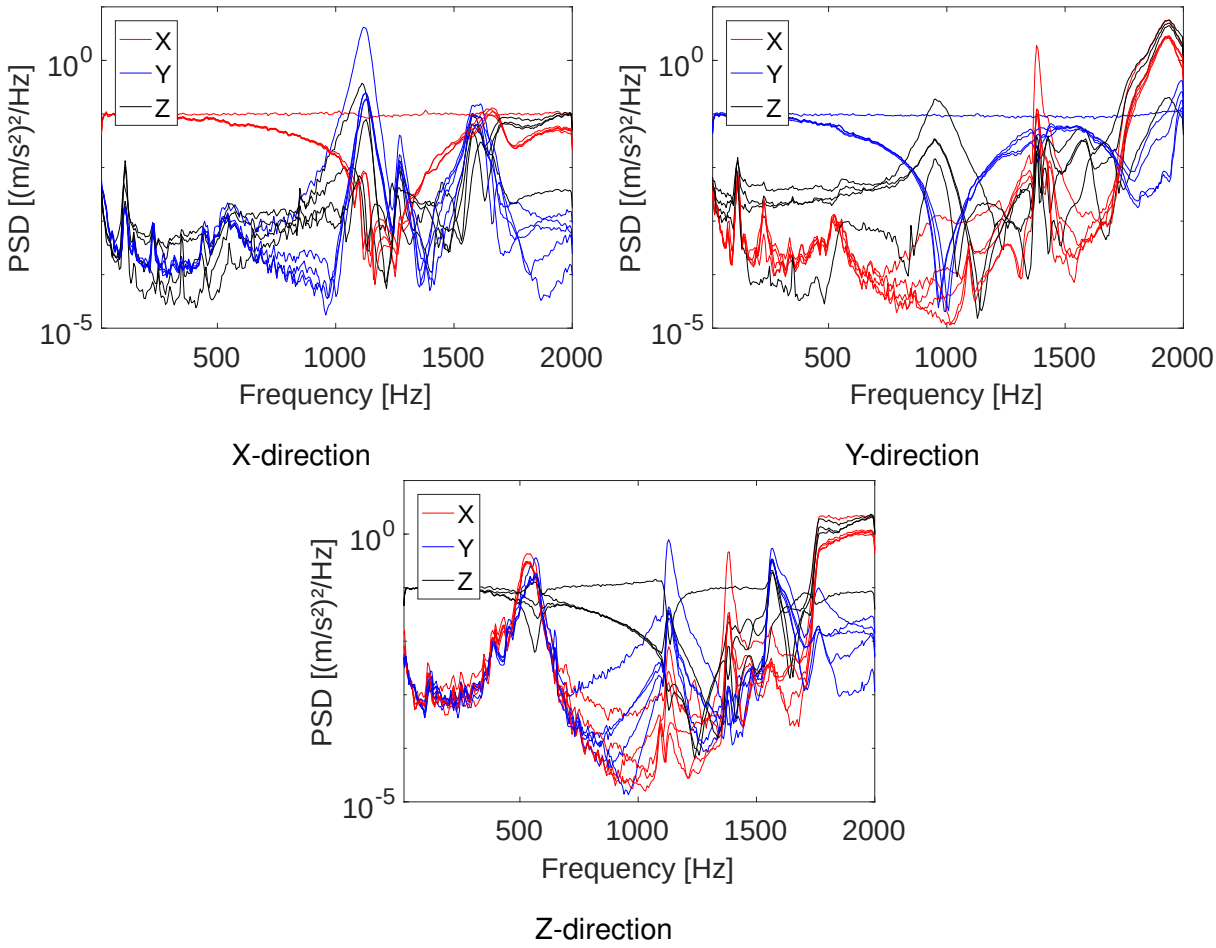

Figure B2: Response PSD of random profile for block setup after approx. 100 operating hours (Z-response at M4 not available)

Table B4: Deviation from reference profile for block with frame setup after approx. 100 operating hours

Frequency range	$10 - 1000$ Hz	$1000 - 1500$ Hz	$1500 - 2000$ Hz
Mean deviation	$6.6\ \%$	$16.2\ \%$	$11.9\ \%$
Max deviation	$18.1\ \%$	$31.7\ \%$	$37.0\ \%$

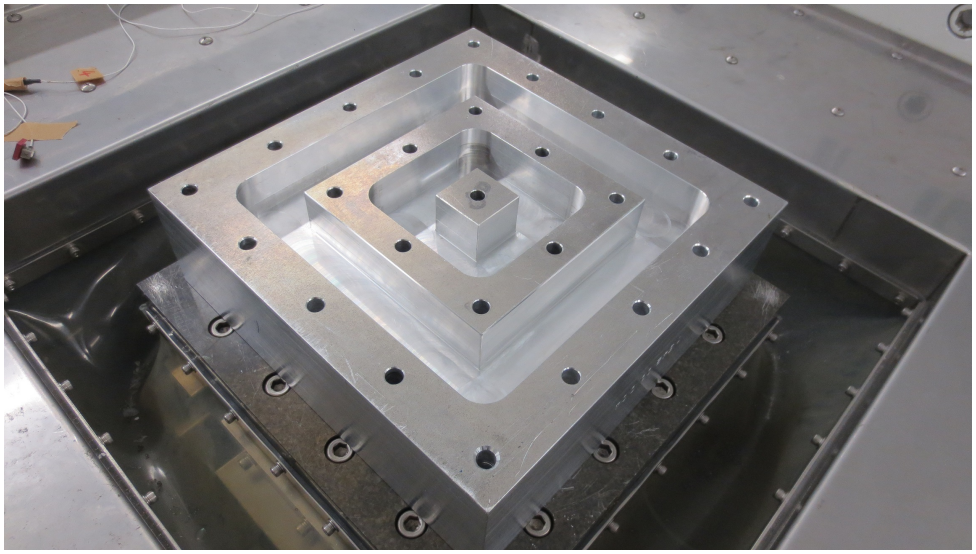

Figure B3: Bottom of adapterplate

C Chapter 5: Multi-Axis Vibration Test Definition

Application of a minimum drives approach

The minimum drives approach was originally introduced in [75] and [74]. Further amendments are proposed in [55], [57], [56] and [15]. The basic principle is a selection of phases and coherences in way that reduces the drive voltages. As input, only the PSD profiles and the shaker transfer matrix have to be known. Starting point is the drives SDM $\boldsymbol{D}(f)$ which can be described using the system relationship of eq. (2.18) as

$$\boldsymbol{D}(f) = \boldsymbol{Z}(f)\ \boldsymbol{R}(f)\ \boldsymbol{Z}^*(f) \tag{A.1}$$

where $\boldsymbol{Z}(f)$ is the inverse transfer matrix of voltage to acceleration. The aim is to define the entire reference matrix $\boldsymbol{R}(f)$ appropriately. Therefore, the trace of the drives matrix $P(f)$ is defined. In case of a square controlled $n \times n$ SDM the trace can be written as

$$P(f) = \sum_{i=1}^{n} D_{ii}(f)\hat{F}_{ii}(f) + 2\sum_{i=1}^{n-1}\sum_{k=i+1}^{n} \sqrt{\gamma_{ik}^2(f)}\sqrt{D_i(f)D_k(f)}\ |\hat{F}_{ik}(f)|\cos\left(\theta_{ik}(f) - \varphi_{ik}(f)\right) \tag{A.2}$$

with the hermitian matrix out of transfer functions $\hat{\boldsymbol{F}}(f)$ and its related angles φ. It is defined as

$$\hat{\boldsymbol{F}}(f) = \boldsymbol{Z}^*(f)\boldsymbol{Z}(f) \tag{A.3}$$

with the valid relationship $\hat{\boldsymbol{F}}(f) = |\hat{F}_{jk}(f)|\ e^{j\varphi_{ik}(f)}$. The trace in equation (A.2) has to be minimized. Therefore, the two largest terms from $\sqrt{D_i(f)D_k(f)}\ |\hat{F}_{ik}(f)|$ are obtained for each frequency. The related frequency terms are minimized as $\cos\left(\theta_{ik}(f) - \varphi_{ik}(f)\right) = -1$ which is equal to $\theta = \varphi + \pi$. The third phase is then determined according to the phase relation $\theta_{23} = \theta_{13} - \theta_{12}$. All coherences are determined as $\gamma_{12} = \gamma_{13} = \gamma_{23} = 1$ in order to fulfill the Silvester's criterion. In the same manner, the maximum drives can be obtained by selecting the

first two phases using $\theta = \varphi$.
The transfer functions from fig. (4.11) are considered for an example application. Both the minimum and maximum drives are calculated and the resulting traces $P(f)$ are given in fig. (C1) in terms of voltage PSDs. Furthermore, a compromise is calculated defining all coherence values as 0.5. Since the reference SDM always being positive definite for this case, all three phase terms are minimized as $\cos(\theta_{ik}(f) - \varphi_{ik}(f)) = -1$.

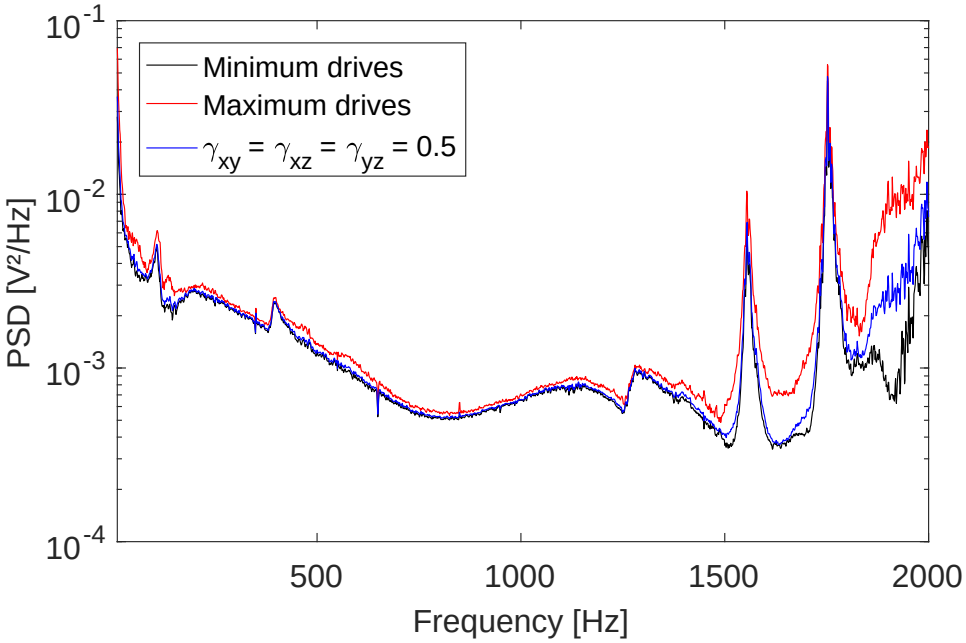

Figure C1: Different feasible drives spectral densities for setup with block and frame

D Chapter 6: Verification of the Multi-Axis Testing Methodology

6.2 Application of Method to Automotive Components

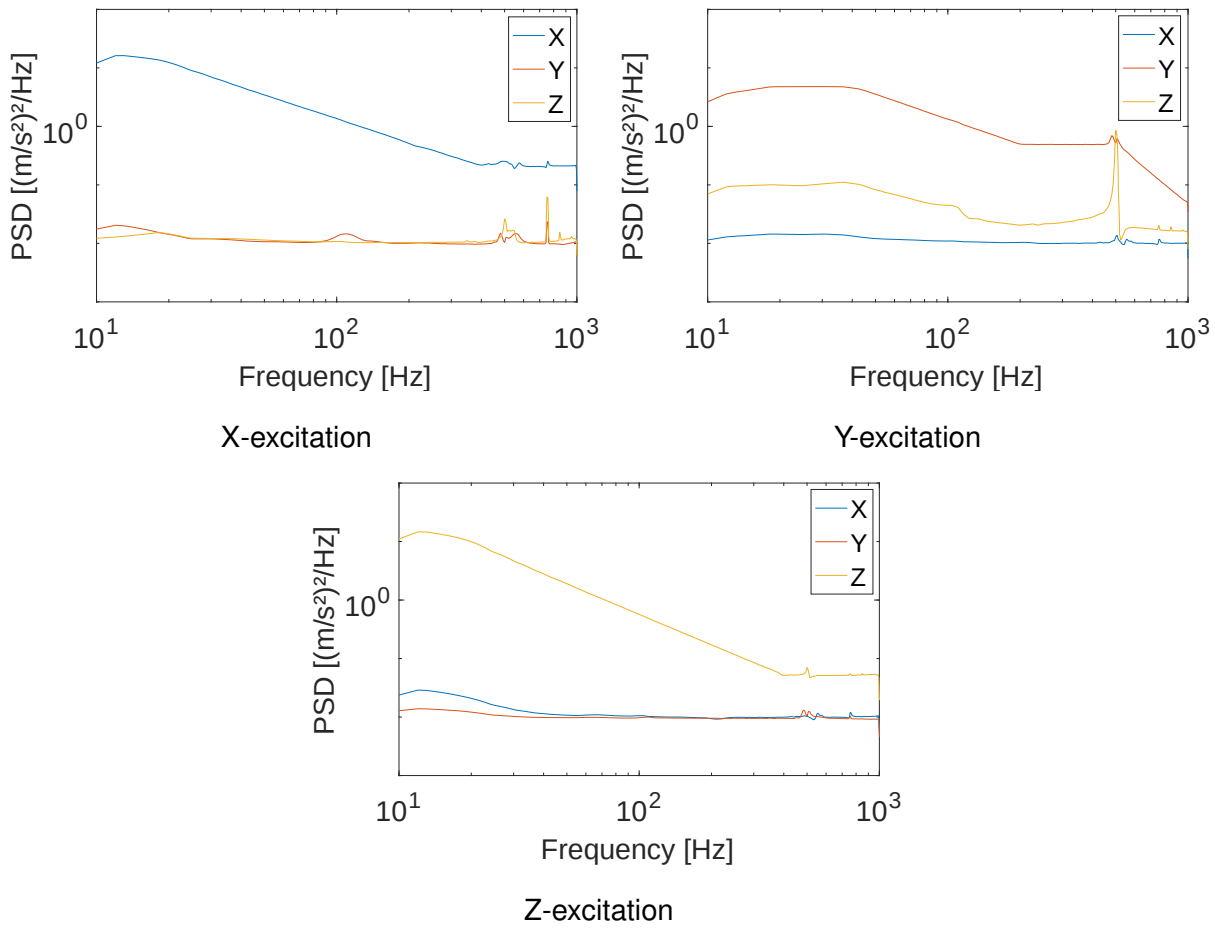

Figure D1: Measured uniaxial test excitations on multi-axis test specimen (3D-shaker coordinate system)

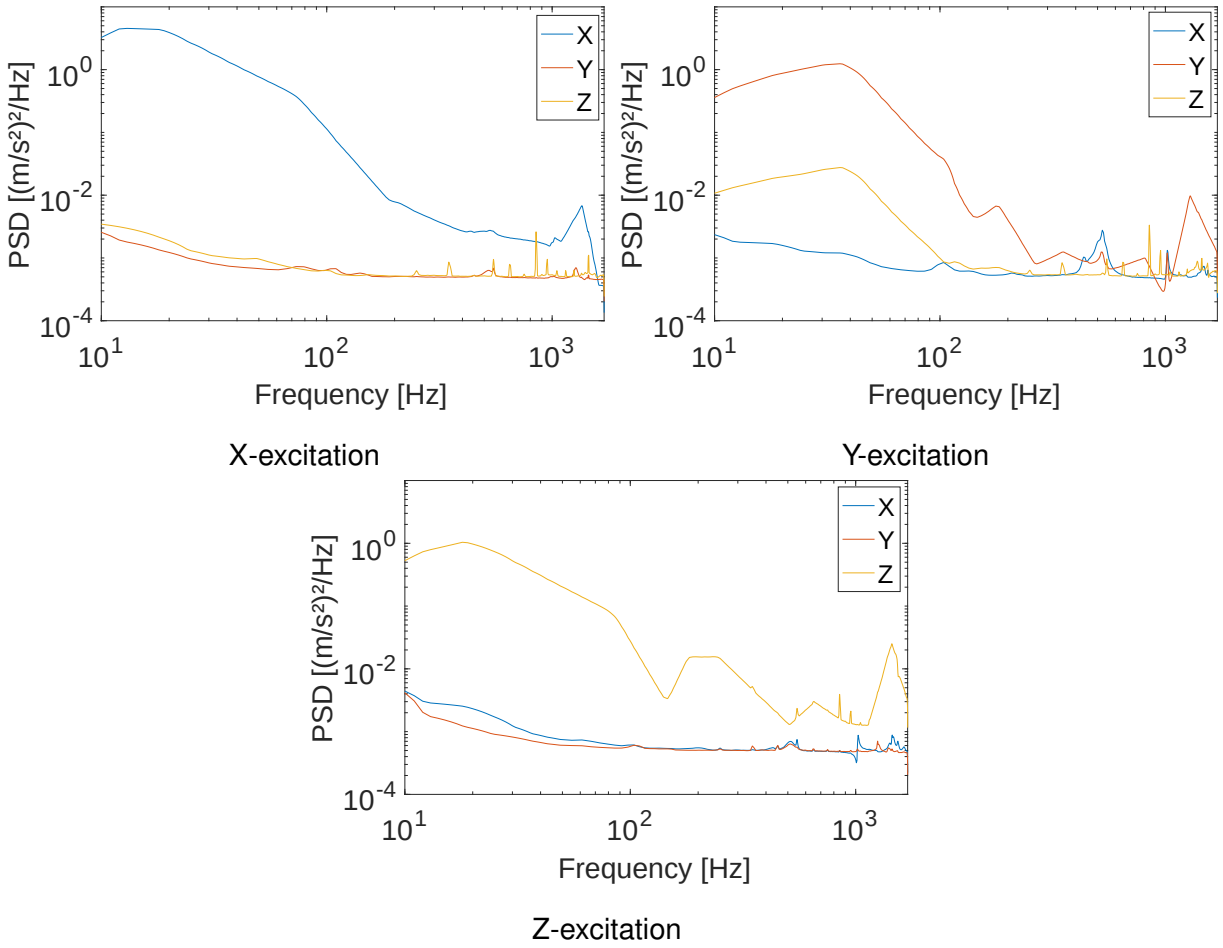

Figure D2: Measured uniaxial test excitations on complex automotive component (3D-shaker coordinate system)

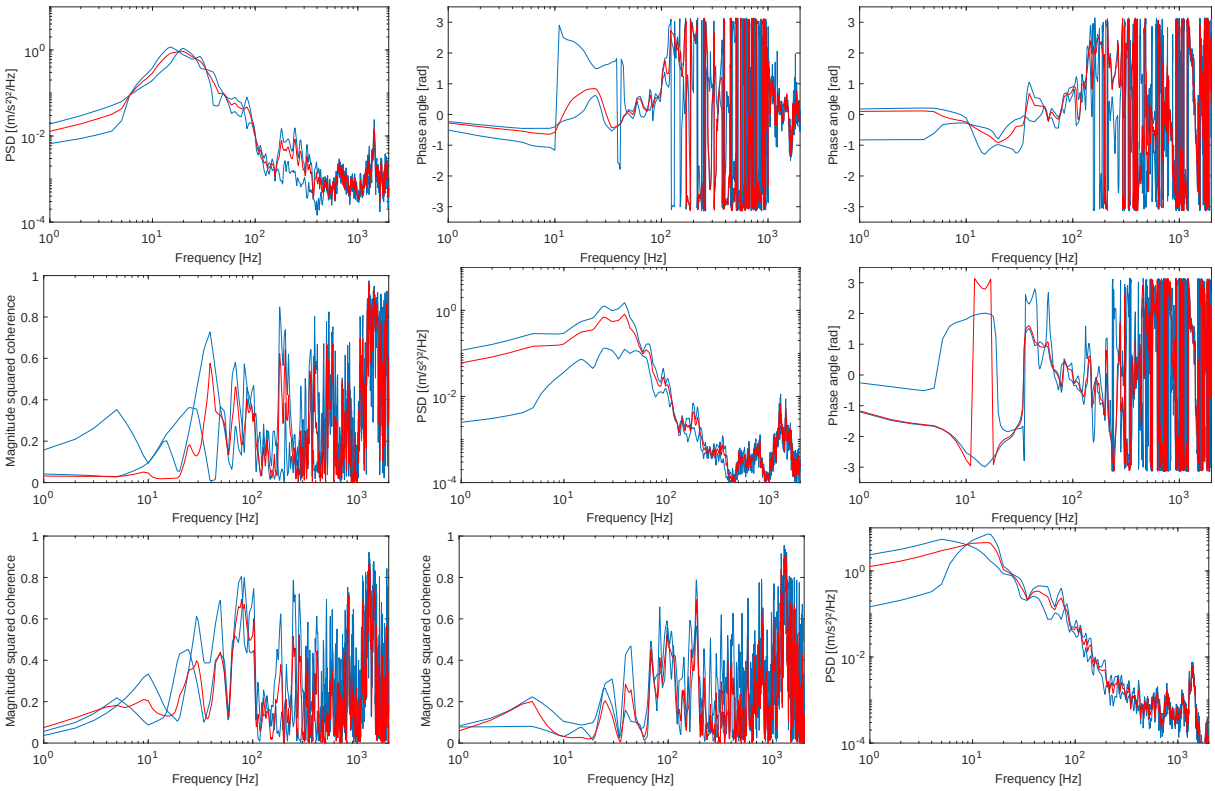

Figure D3: Exemplary mean values of SDM for the complex automotive component, phases on the upper triangle, magnitude squared coherences on the lower triangle

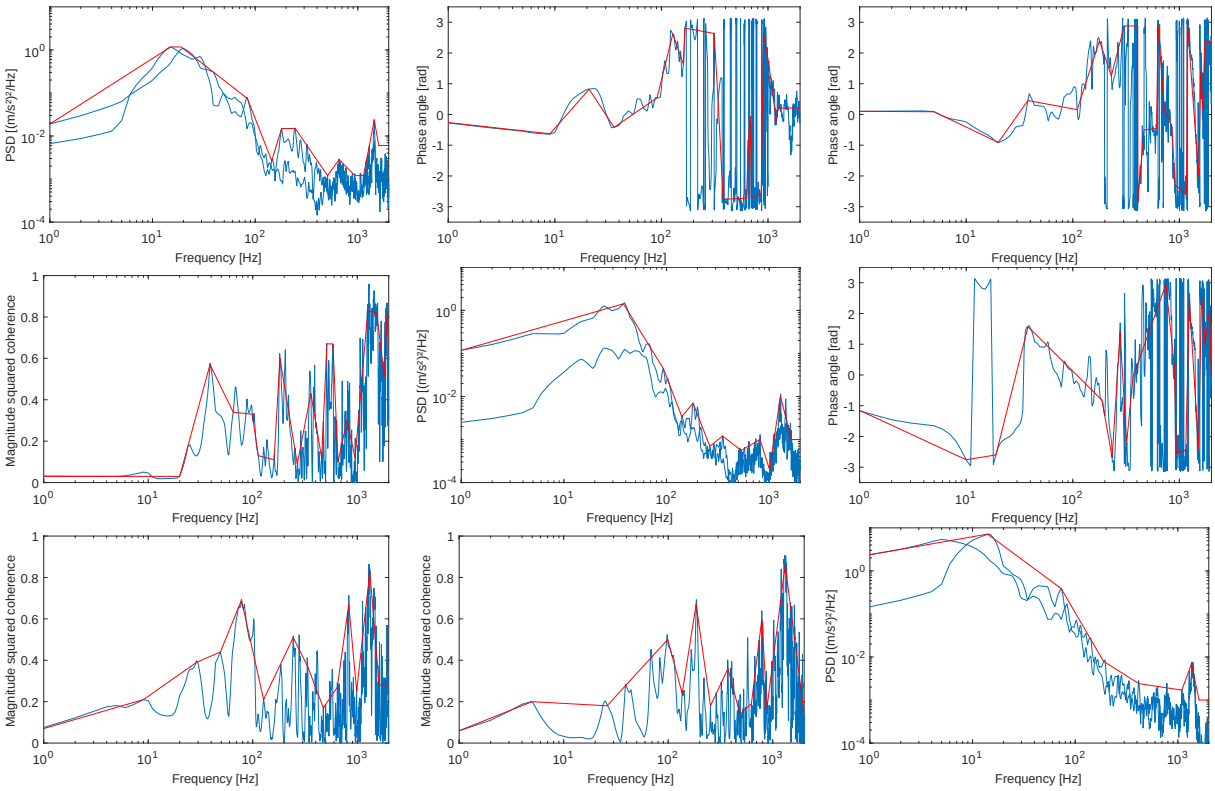

Figure D4: Exemplary enveloped values of SDM for the complex automotive component, phases on the upper triangle, magnitude squared coherences on the lower triangle